SOFT, ORGANIC, CARRIER-SELECTIVE CONTACTS AT INORGANIC SEMICONDUCTOR INTERFACES ENABLED BY LOW-DEFECT COVALENT BONDING

Alexander D. Carl
In partial requirements for the
Degree of Doctor of Philosophy, Ph.D. in Chemistry
submitted to the Faculty of
WORCESTER POLYTECHNIC INSTITUTE
100 Institute Road, Worcester, Massachusetts 01609

Committee: Professors Arne Gericke (CBC, chair), Shawn C. Burdette (CBC),
Pratap M. Rao (Mech. E.), Ronald L. Grimm (CBC, advisor)

CONTENTS

LIST OF FIGURES

LIST OF TABLES

PREFACE

The integration of covalent, organic, carrier-selective monolayers on semi-conductor surfaces will enable efficient electron transfer in perovskite single and tandem-junction perovskite photovoltaic devices. This work details the functionalization and characterization of semiconductor surfaces and the electronic measurements of relevant devices. In chapter 3, we synthesized oxide-free, covalently-bound alkylamine terminated Si(111) surfaces. These surfaces demonstrated low recombination velocities and resistance to oxidation under ambient conditions. The NH_3^+-terminated monolayers also showed increased adhesion toward $MAPbI_3$ thin films and the photovoltaic performance of the perovskite on functionalized n^+-Si was increased compared to the native oxide. Chapter 4 details the covalent functionalization of oxidized Si(111) and TiO_2 surfaces with perylene derivatives. Secondary functionalizations enabled surface coverage quantification relevant to the surface density ammonium groups that might later be utilized in $MAPbI_3$ devices. Chapter 5 utilizes the chemical strategies developed in Chapter 4 to prepare NH_3^+-terminated, perylene monolayers on TiO_2 for the testing of their viability as electron transport layers in $MAPbI_3$-based PV devices. We characterized the band-energy levels as the TiO_2 was functionalized and found the surface's conduction band was well matched for use as an

ETL in perovskite PV. Functionalized TiO_2 devices showed increased performance compared to baseline, silane-functionalized TiO_2-perovskite devices. Chapter 6 summarizes our latest work and future directions on perylene-functionalized TiO_2 perovskite devices and our exploration of oxide-free, ammonium-terminated, perylene monolayers on Si(111) surfaces for their viability in perovskite/silicon hetero-junction PV.

ACKNOWLEDGMENTS
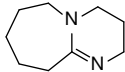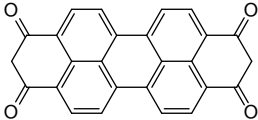
First and foremost, I need to thank my advisor Ron Grimm for bringing me into his lab and teaching me to be a real scientist. I couldn't have chosen a better lab where I could explore not only surface chemistry, but the electronics and fancy instrumentation that goes along with it. From the Grimmgroup: I want to thank all the undergrads that have come through our lab in the last 5 years, it's been a pleasure working alongside you all. Roghi, thank you for showing me photoelectrochemistry of perovskites, which turned into a huge part of my project. Ken, thank you for running the lab with me in the beginning when there was an army of people in that half a pod. I especially want to thank Julia, who has been a great friend since she joined our lab and is always around to chat about science and food. I'd also like to thank the other members of my committee: Arne Gericke, Shawn Burdette, and Pratap Rao.
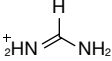
I want to thank my family, Nick, Mackenzie, and especially Mom and Dad, for being incredibly supportive through my chemistry career. I wouldn't have the same drive and interests without you.

To Maggie, I can't describe how grateful I am for you to have been in my life these last eight years, and how excited I am to start our lives together in a few short weeks. I love you.

GLOSSARY

DBU   1,8-diazabyclo[5.4.0]undec-7-ene

fwhm   Full-width-at-half-maximum

IRRAS   Infrared reflection-absorption spectroscopy

PTCDA   Perylene tetracarboxylic dianhydride

XPS   X-ray photoelectron spectroscopy

UPS   Ultraviolet photoelectron spectroscopy

KE   Kinetic energy

BE	Binding energy
$h\nu$	Photon energy – Planck's constant (h) × frequency (ν)
d	Depth or length
ρ	Density
I_x	Photoelectron intensity
I_0	X-ray flux
$T(E_x)$	Analyzer transmission function
$D(E_x)$	Detector efficiency
N_A	Number density
λ	Attenuation length
SF	Sensitivity Factor
EA	Electron affinity
IP	Ionization potential
PV	Photovoltaic(s)
OPV	Organic photovoltaic(s)
ETL	Electron transport layer
ETM	Electron transport material
HTL	Hole transport layer
HTM	Hole transport material
MA	Methylammonium
FA	Formamidinium

$$^+_2HN \diagup\!\!\!\overset{\overset{\displaystyle H}{|}}{}\!\!\!\diagdown NH_2$$

HOMO	Highest-occupied molecular orbital
LUMO	Lowest-unoccupied molecular orbital

SYMBOLS

Φ   Work function (energy)

E$_F$ Fermi Level

E$_{VBM}$ Valence band maximum

E$_{CBM}$ Conduction band minimum

E$_g$ band gap

E$_{vac}$ Vacuum level energy

θ Angle of detector with respect to the surface normal

δ Angle of incoming radiation with respect to the surface normal

γ Angle of incoming radiation with respect to the detector

ϕ Azimuthal angle of incoming radiation with respect to the detector (UV source)

Φ   Fractional surface coverage

$\sigma_{Si(111)}$ Si(111) Surface density

a_{Si} Silicon cubic unit cell length

τ Carrier recombination lifetime

S Surface recombination velocity

CHAPTER 1

SOLAR MOTIVATION, CARRIER-SELECTIVE MATERIALS, AND TANDEM-JUNCTION PHOTOVOLTAICS

As of 2018, the world's total energy consumption reached ~165,000 TWh per year, more than 400 EJ (Exajoules = EJ = 10^{18}), and over 80% of that energy is generated by non-renewable resources such as coal, natural gas, and oil.[1] Of the many renewable energy sources such as hydropower, wind, geothermal, and solar; solar provides the greatest potential energy and highest extractable efficiency.[2-3] The average solar flux incident upon the Earth's surface, accounting for atmospheric scattering, absorption, and changes in latitude, is ~150 W m^{-2}. This equates to roughly 80,000 TW of solar power hitting the Earth's surface at any given moment. In 1.5 hours, roughly 430J of energy illuminates the Earth, more than the total energy consumed across all sectors of the globe in 2018. The excess solar energy, not utilized in photosynthetic processes by plants and bacteria or reflected from the Earth, presents a vast resource of obtainable, renewable energy.

There are three practical methods to extract viable energy from sunlight: solar-thermal, solar-chemical, and solar electrical.[3-9] In the solar-thermal process, sunlight is extracted as thermal energy. In low-temperature systems, typically found in residential buildings, water is pumped to the roof, heated by the incoming sunlight, and routed to the heating/hot water system. High-temperature systems utilize optical concentrators to focus the sunlight on a material capable of absorbing and conducting extremely high temperatures.[9-10] This thermal energy is used directly, stored, converted to electricity via thermoelectric generators or steam-turbines, or converted to chemical energy. There is significant research into materials for the storage of latent heat including molten salts and metals, organics, and rocks.[11] Unfortunately, thermal energy must be used where it was extracted or converted to other forms nearby, or else costs of insulating and maintaining

high-temperature transport over long distances deter the wide-spread implementation.

The solar-chemical method utilizes energy from the sun to convert molecules into energy-dense, chemical fuels. Natural solar-chemical conversion has been occurring for billions of years as photosynthesis in plants and bacteria, where photons from the sun provide the required activation energy to convert H_2O and CO_2 into complex carbohydrates.[12] Research into artificial photosynthesis focuses on a simpler chemical reactions: the splitting of H_2O into H_2 and O_2, combining protons to form H_2, and the reduction of CO_2 into simple hydrocarbons like methanol.[2,4–5,13] Hydrogen and other chemical fuels enable the storage of excess solar energy, with energy densities 2-3 orders of magnitude greater than current Li-ion technologies.[2,14] There is still much research to be done in finding robust photoanodes with suitable photocatalytic conversion efficiencies,[15] however, pairing more traditional catalytic materials with discrete photovoltaic systems presents a straightforward path to storing excess solar energy.

The solar-electrical process utilizes appropriate materials to absorb photon energy and directly convert it to electrical energy. The photovoltaic effect was first observed in selenium in the 19th century but despite extensive research, remained little more than a novelty at only conversion 0.5% efficiency by the 1950's.[16–17] The photovoltaic effect was also observed in copper oxide[18] and cadmium sulfide[19] during the 20th century but it wasn't until 1954 that Chapin, Fuller, and Pearson demonstrated the first practical solar cell.[20] A p-n junction, further discussed in Chapter 2, was formed when a gallium-doped, p-type silicon sample was dipped in molten lithium to create a thin p-type layer near the surface.[17] This cell exhibited a 6% efficiency,[20] dwarfing the established efficiencies of available commercial devices. Today, in addition to silicon, many other photovoltaic materials are finally achieving efficiencies to offset the materials-cost, challenge fossil-fuels, and enable wide-spread adoption and grid utilization.

Under AM1.5G standard illumination, which is ~1000 W m^{-2} at sea level after atmospheric losses, and utilizing modern, commercial solar panels (20% efficient),[21] we would need a 100,000 km^2 sized solar panel to provide 20 TW of continuous power, or just over the global average, continuous usage, 18 TW, in 2018.[1] This area is roughly the size of Virginia or 0.067% of the Earth's landmass. These are ideal values, assuming no cloud-cover and with the sun almost directly overhead but are still useful when trying to put into context the space required and available to house large grid-installations. A more realistic value for average solar flux on the surface, accounting for the time of day, atmosphere, and scattering, is ~150 W m^{-2}, requiring a solar cell roughly the size of Texas, 670,000 km^2, to power the globe. While a single solar field that size is unrealistic, it still only covers 0.1% of the Earth's land-area, which realistically would be spread across the world in locations

with ideal geographies. To help further visualize the areas mentioned above, all the paved roadways in the U.S. cover close to 40,000 km^2 and the roof real estate of 95 million homes adds up to ~10,000 km^2. There is a massive amount of space to integrate PV, on existing structures or in open spaces, without disrupting natural environments. However, the number of panels, materials, and area required is significantly reduced by more efficient PV.

In 2018, the record efficiency for an NREL-certified, crystalline silicon solar cell was set by ISFH, which has efficiency of 26.1%.[22] New, commercial solar modules now exceed 20% efficiencies[23] and the price of commercial silicon modules has fallen to the point where its $ W^{-1} is competitive with that of fossil fuels.[24–25] Beyond silicon, non-concentrating GaAs single crystal and thin films have yielded 27.8% and 29.1% efficiencies.[26] Unfortunately, III–V materials, such as GaAs, are expensive to fabricate large single-crystals and defect-free thin-film deposition requires expensive metal-organic precursor chemical vapor deposition (MOCVD) instrumentation to yield material in relevant amounts.[4,27] Other well-studied direct-gap, thin film materials include copper indium gallium selenide (CIGS) and CdTe, where researches have recently achieved efficiencies between 22 and 23%.[26] The direct band gap of these materials enables their thin film designs as majority of the light is absorbed in the first few microns and the cost of the rare-earth metals is offset by the small amounts required.[28] The large-scale adoption of photovoltaics in power generation is still hindered by the cost of synthesizing high-quality, inorganic materials. Organic photovoltaics (OPV) present an appealing option to circumvent the requirement of pristine growth of inorganic crystals, defect-free thin films, and the costs of rare elements by utilizing solution-processable, abundant, organic precursors. The utilization of small-molecule donor-acceptor polymers have helped OPV-based devices jump almost 50% in efficiency during the last 3 years alone, from ~12% to ~17%.[26,29–30] OPV materials can also be deposited on conductive, flexible substrates, desirable for wearable devices and non-planar surfaces. As the technology is still in its infancy, high-efficiency devices are still limited to small active areas and there is still much research required to increase device stability under ambient conditions.[31] As more viable donor-acceptor molecules are discovered and synthesized, material and processing costs will continue to fall. Presently, the expensive, difficult-to-synthesize small molecule precursors render scale utilization of OPV cost-prohibitive. In the short term, a dramatic change to single-crystal silicon dominated, commercial PV will require efficient, inexpensive, robust, and defect-tolerant material.

The last decade has seen an enormous amount of academic research poured into the discovery, testing, and enhancement of organic-inorganic metal halide hybrid perovskites.[32–35] The earliest PV-relevant perovskite materials were methylammonium lead halides, MAPbX$_3$ where X is I, Br, or Cl and The first NREL certified MAPbI$_3$ device had an efficiency near 14%.[26,32] Besides the high efficiency, these perovskites employ simple thin film de-

position methods including spin-coating, doctor-blading, vapor deposition, and printing.[36−37] Their inherent defect-tolerance and inexpensive precursors make them extremely appealing as a new generation of photovoltaic devices. Unfortunately, they suffer from instability in the presence of elevated temperatures (>60 °C) and even small amounts of humidity.[38−39] The temperature stability is enhanced by incorporation of formamidinium (FA) in place of the cation, MA, and the stability against moisture is increased by the addition of Cs as the cation.[40] Mixtures of halide anions yield dramatic changes to the optical and electronic properties such as increasing the proportion of Br to I to widen the band gap.[41−43] Such fine control over these properties is necessary to extract the uttermost efficiency from solar materials. $(FAPbI_3)_{0.92}(MAPbBr_3)_{0.08}$ perovskites have shown efficiencies ~23%,[44] and record-breaking, NREL-certified perovskite cells have recently reached 25.2%,[26] with the composition still yet to be revealed.

Carrier-selective transport is a critical component in the design of high-performance perovskite devices, which unlike silicon devices, do not contain a p-n junction to separate charges upon illumination. Fortunately, carrier diffusion distances for most hybrid perovskites range between 100 nm and 1 μm and the carriers can travel long distances before recombining.[45−45] These electrons and holes generated in the absorbing layer must be collected at opposing ends where they are selectively extracted by carrier-selective materials. There are two types of carrier-selective materials: electron transport materials (ETM) and hole transport materials (HTM), which as their names suggest, conduct electrons and holes to be collected at their respective contact.[47−48] These carrier-transport materials can be organic or inorganic semiconductors with energy levels aligned to facilitate the flow of electrons or holes. Figure 1.1 illustrates the band energy alignment of the HTM, active layer, and ETM. For the efficient transfer of electrons through the ETM, the conduction band minimum (CBM) of the ETM must be closely aligned to the CBM of the active layer to allow electrons to fall from the CB of the active layer to the CBM of the ETM. Additionally, the valence band maximum (VBM) of the ETM must be located far below the VBM of the active layer to block the falling "upward" of holes. The opposite is true for the HTM where it is desired to increase the transfer of holes and mitigate the flow of electrons.

In a single junction photovoltaic device, there are two configurations of the ETLs and HTLs surrounding the active layer with respect to the incoming light. In p-i-n cells, the light first passes through the HTL and in n-i-p devices, the ETL is illuminated first.[46] The choice is highly dependent on the materials employed for the active layer and the transport layer and their respective deposition method's chemical compatibility. If the processing of one transport layer harms the integrity of the active layer, it is desirable to deposit that transport layer before the active layer. For example, perovskite devices utilizing TiO_2 as an ETL, the high-temperature anatase annealing process would destroy a typical perovskite material, thus the TiO_2 layer
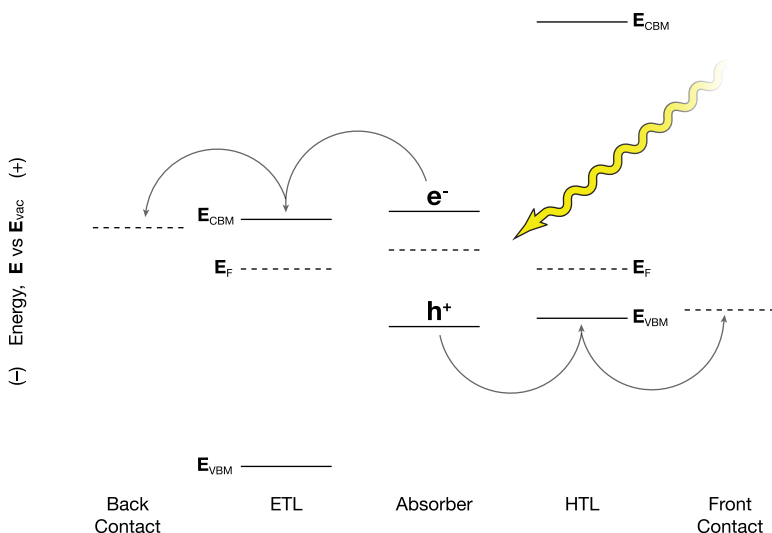
Figure 1.1   Band energy diagram illustrating the alignment of energy levels in the front contact, HTL, active layer, ETM, and back contact. The valence band maxima (E_{VBM}) and conduction band minima (E_{CBM}) are represented by solid lines while the Fermi levels (E_F) are represented by dashed lines. Electrons, e⁻, fall down through the aligned conduction bands while holes, h⁺, fall up via the valence bands.
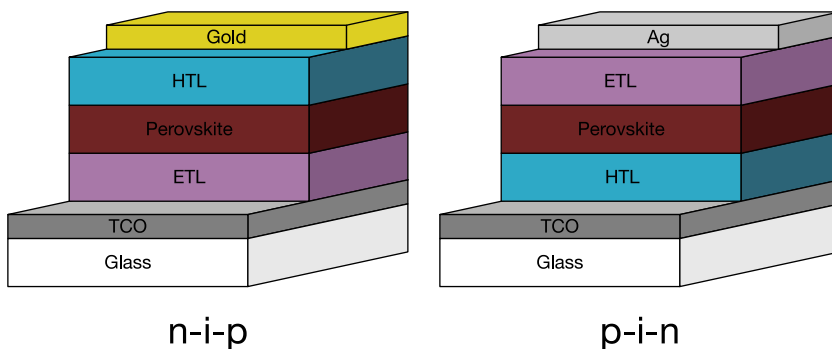
Figure 1.2   General n-i-p and p-i-n perovskite devices. Devices are illuminated from the bottom through the glass substrate.

is deposited on a transparent conductive oxide (TCO), followed deposition of the perovskite, and finally careful formation of the HTL. Light is first transmitted through the TCO and TiO$_2$, making this an n-i-p type device. Examples of p-i-n and n-i-p configurations are given below in Fig. 1.2.

The efficiency of a single-junction solar cell is limited by the Shockley-Queisser limit.[49–51] Accounting for losses due to transmission, thermalization, reflection, and recombination, the theoretical, maximum efficiency under one-sun illumination is ~30%. Silicon-, III–V-, and perovskite-based devices have exceeded 25% efficiencies and are closing in on the theoretical single-junction limits. To limit the losses due to transmission and thermalization, where energy is lost due to below and above band gap light, semiconductors are stacked to form tandem-junction or multi-junction solar cells.[51–53] There are two popular configurations of hetero-junction, perovskite/silicon devices: four-terminal and two-terminal.[54] Four-terminal systems are simply two discrete photovoltaic devices that have been built or stacked mechanically on one another but remain electronically discrete. In the two-terminal configuration, there are only connections to the front and back contacts of the device, therefore, current generated in the top cell must be passed through the bottom cell before collection. Four-terminal cells are less constrained by the perfect band gap matching, required to optimize two-terminal configurations, and can yield higher overall efficiencies but are more complicated in their design. While the ideal band gap for a single-junction device is ~1.45, a hetero-junction device contains a top cell with a 1.60 eV band gap and a bottom cell band gap of 0.94 eV. This configuration yields a theoretical maximum efficiency of 46%.[54] Figure 1.3 illustrates the current-matching relationship of band gaps between absorbers in a tandem-junction device and resulting theoretical maximum efficiencies.

Perovskite/silicon-based solar cells are a promising configuration for tandem-junction solar cells, combining efficient, low-cost perovskites with the mature, robust silicon technology. Silicon's band gap of 1.12 eV paired with a 1.73 eV band gap perovskite may theoretically yield a >40% efficient device.[54–56] Hybrid organic-inorganic perovskites have wide, tunable band gaps and the compositions are easily adjusted to achieve 1.73 eV. Figure 1.4 presents the AM1.5G spectrum where higher energy light is first absorbed in the perovskite layer and the lower end of the spectrum is absorbed by or transmitted through the silicon. Perovskite/c-Si devices are almost exclusively p-i-n type devices because the conduction bands of both materials are already closely aligned for electrons to flow from the perovskite into the silicon through a suitably chosen electron transport material.[57]

Electron transport materials are essential to the performance of tandem-junction perovskite/silicon devices which utilize many of the same carrier-selective transport layers used in single-junction perovskite solar cells.[57–62] Metal-oxide ETMs, including TiO_2 and SnO_2, are often sputtered or deposited directly onto the Si substrate or onto a transparent conductive oxide buffer layer.[57,62] The perovskite layer is then spin-coated, printed, or doctor bladed on. The HTM, typically spiro-OMeTAD, PEDOT:PSS, CuSCN, NiO, or thiophene-based organics is then carefully deposited on the perovskite before thermal evaporation of a metal contact.[60,63] The engineering of these
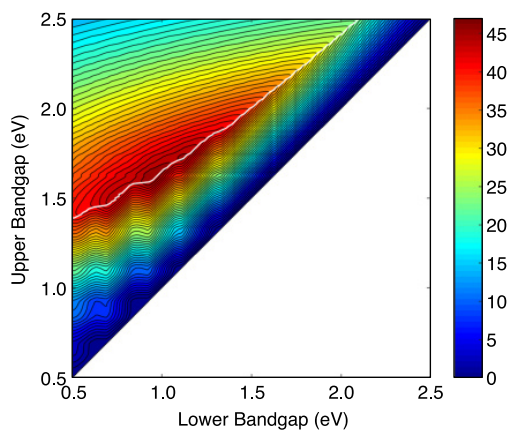
Figure 1.3 A contour map of the theoretical efficiencies yielded by hetero-junction photovoltaic cells. Maximum efficiencies are dependent on the band gaps of both materials. Peak efficiencies of 45.8% occur when the lower band gap is 0.94 eV and the upper material's band gap is 1.60 eV. Adapted from Garrison, R.; Kleiman, R. Opt. Express. **2019**, 27, A543-A571.[54] Copyright **2019**, OSA Publishing.
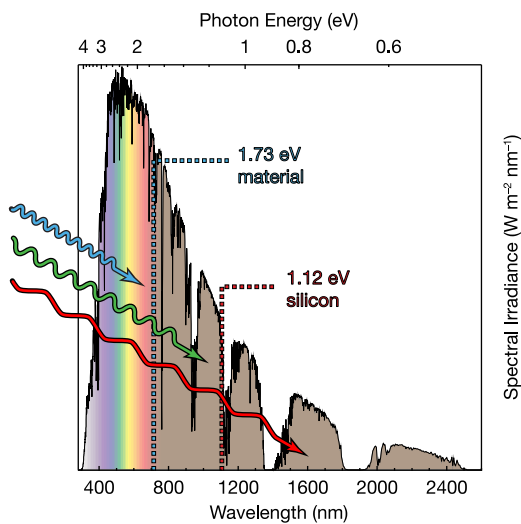
Figure 1.4 AM1.5G spectrum. The blue, green, and red waves represent varying wavelengths of light of which the higher energy is absorbed by a 1.73 eV material that is relevant for an optimal paring with a 1.12 eV band gap material such as silicon.

interfaces, especially between the Si and perovskite, is vitally important to the performance of two-terminal, monolithic tandem-junction photovoltaic devices.[47]

Trap-state defects on the silicon surface deleteriously reduce the overall performance of a tandem-junction solar cell.[64-65] Many previously reported devices, some examples shown in Fig. 1.5, utilize metal-oxide ETLs.[57] However, despite a metal-oxide's ability to "passivate" the surface, the deposition procedures, high annealing temperatures, and prolonged exposure to light during operation will eventually induce oxidative defects.[66-68] Additionally, metal-oxides are limited by the tunability of their energy levels and a specific metal-oxide will not maximize the current-density in all heterojunction systems. An important element to forming ideal hetero-junctions is lattice matching.[69-71] Lattice mismatch is introduced when joining two materials with dissimilar lattice constants, yielding high densities of dislocations at the interface of the metal-oxide and semiconductor which contribute to recombination.[62-74] In ideal lattice-matched, multi-junction devices, such as GaInP/GaAs//InGaAs, the materials are grown directly on top of one another, seamlessly integrating their crystal structures without stress or defects.[75] The lattice constants of the $MAPbI_3$,[76] and the Si(111)[77] surface are not well matched to many metal-oxide lattices, including the prevalent anatase TiO_2 ETL material.[78] The consequent lattice strains induced by direct contact with TiO_2 surfaces will result in efficiency losses due to electron traps at stress and dislocation defects sites.[79] Covering metal-oxides with soft, flexible, organic layers help to alleviate the lattice mismatch and yield increased power conversion efficiencies.[80-82]

Among organic electron-transport layers, C_{60}, PCBM, and other fullerene derivatives are popular owing to their desirable HOMO and LUMO energies and their electronic tunability.[83-86] Fullerenes may be used as the sole ETM but are often coupled with a metal-oxide ETL like TiO_2.[81-82] In addition to mitigating the consequences of lattice mismatch, effected by direct contact of TiO_2 and the perovskite, the organic layer passivates terminal trap-states on the TiO_2 surface.[82,87-88] Most fullerene species, however, are only weakly bound to the surface and uniform, pinhole-free, ultrathin films of pure fullerenes are difficult to produce via solution-processing.[80,88] Deposition of materials on top of thin fullerene layers may also disturb or delaminate patches of material, introducing holes in the material that act as shunts and decrease overall performance.[89-90] This can be countered by thicker fullerene layers but at the cost of increased series resistance of the ETL. Surface-tethered organic molecules with optimal energy levels would make for ideal transport layers in heterojunction devices and metal-oxide capping layers in single-junction devices.

Rylene-based molecules, shown in Fig. 1.6, offer many appealing characteristics in their utilization as an ETL. Of particular interest are the perylene di-
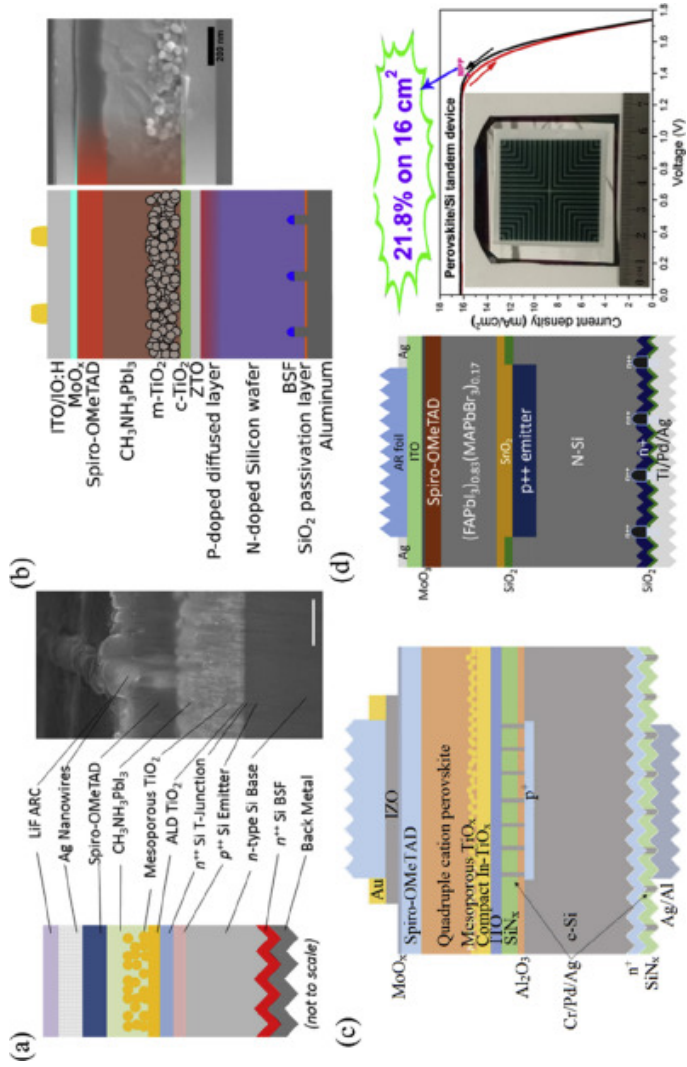
Figure 1.5 Examples of reported monolithic, two-terminal perovskite/silicon tandem-junction devices. Adapted from Yan, L. L.; Han, C.; Shi, B.; Zhao, Y.; Zhang, X. D. *Mater. Today Nano.* **2019**, *7*, 100045.[57] Copyright **2019**, Elsevier.

| Napthalene | Perylene | Terrylene | Perylene dianhydride | Perylene diimide |
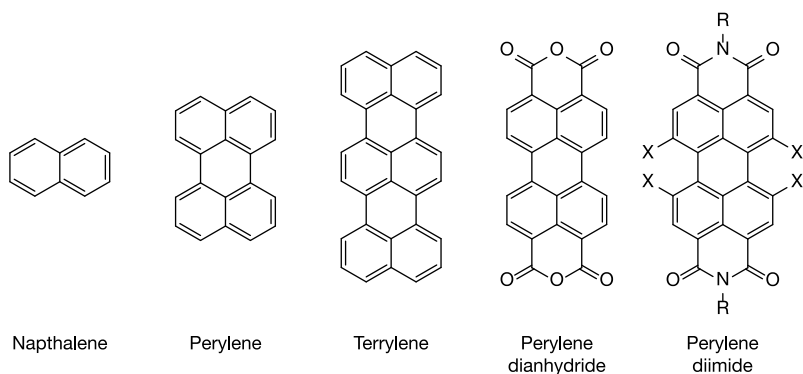
Figure 1.6   Chemical structures of rylene-based molecules.   Among perylene derivatives, bay-position functionalization at –X affords electronic tuning, while imide functionality at –R enables tunable solubility, chemical compatibility, and possible surface-attachment strategies.

imide (PDI) for their flexible functionalizations, favorable HOMO and LUMO energies, high charge-carrier mobility, and low-cost.[91–93] The imide groups offer a pathway toward covalent, chemical attachment to a variety of surfaces, given suitable chemical strategies. Further, wet-chemical processing of PDI monolayers will enable monolayer control of the surface coverage, whereas spin-coating procedures are more likely to produce multilayer films.[94] Typical HOMO/LUMO energies for generic the PDI depicted in Fig. 1.6 are about –5.8/–3.7 eV.[95] Functionalization of the bay positions, –X, with electron donating/withdrawing groups offers precise control over the energy levels and charge-carrier mobility, whereas the imide's –R group effects changes to the solubility.[91,96–98] The electron mobility of PDIs are generally found to be within an order of magnitude of PCBM and other fullerenes.[62,95,99] The –R group of the imide opposite the surface is also readily functionalized with a variety of species. In the context of PDIs as an ETL for MAPbI$_3$, incorporation of terminal ammonium groups should increase the adhesion. During solution phase deposition and crystallization of MAPbI$_3$, a surface-bound ammonium group should be "recognized" by the perovskite film and incorporated during crystallization.

In summary, covalently-bound, organic monolayers of carrier-selective molecules will provide the passivation, adhesion, and charge-carrier selectivity at perovskite/semiconductor interfaces for increased performance of relevant photovoltaic devices.

CHAPTER 2

SILICON, SEMICONDUCTOR FUNCTIONALIZATION, AND CHARACTERIZATION

2.1 Introduction

The advent of modern electronics including transistors, diodes, integrated circuits, and photovoltaics semiconductors.[100] Human-sized boules of silicon are grown nearly impurity-free for sensitive integrated electronics, with purities exceeding 99.999999999% silicon by weight. In comparison, photovoltaic grade silicon requires only 99.9999% purity to yield the appropriate charge-carrier lifetimes.[101] Pure, crystalline silicon is an intrinsic semiconductor with an indirect band gap of 1.12 eV and a Fermi level found directly mid-gap.[100] Dopants are intentionally added during the growth or afterward by ion implantation[102] and thermal diffusion processes.[103] Doping control the density of free electrons or holes which determine the location of the Fermi level in the gap. Phosphorous and arsenic, n-type dopants for silicon, have one additional valence electron and the increase free-electron density shifts the Fermi level, E_F, closer to the conduction band. Boron, a p-type dopant, contains one less electron and brings E_F toward to the valence band. A p-n junction is formed at the interface of p-type and n-type regions.

The p-n junction is integral to nearly all semiconducting, electronic devices.[100] Figure 2.1 presents a diagram of a p-n junction before and after thermal equilibration. In equilibrium, electrons flow from the n-type region into the p-type region, leaving behind a positive charge. At the same time, holes from the p-type region flow into n-type region, leaving behind a negative charge. This region, the depletion width, now devoid of free charge-carriers, contains static ions which repel the flow electrons and holes from both the n and p regions. Under illumination, free charge-carriers are generated and separated within the p-n junction, producing current depended on by photovoltaic cells. Despite the ability to synthesize ultrahigh purity silicon and precisely control
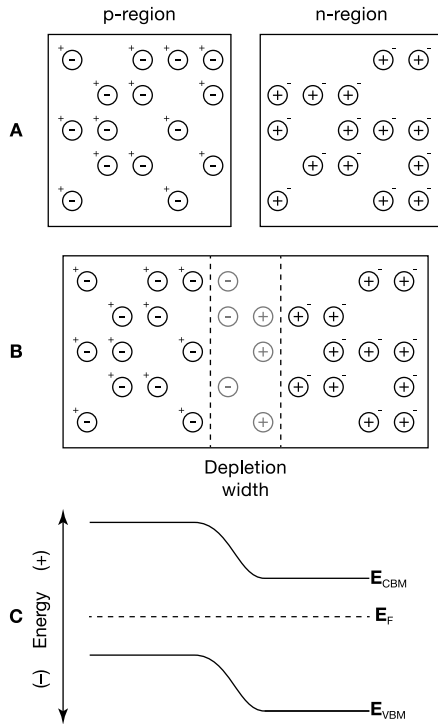
Figure 2.1   Silicon p-n junction. The $\oplus$ and $\ominus$ denote the static donor/acceptor dopants while free electrons and holes are represented by – and +. Frame **A** presents both an n- and p-type semiconductor regions. Frame **B** presents the p-n junction under thermal equilibrium and the generation of a depletion width. Frame **C** presents the band bending diagram of the equilibrated p-n junction.

the dopant depths and densities, the Si surface is prone to oxidation and the formation of defects under ambient conditions undermines the performance of silicon solar devices.

The degradation of performance in silicon devices dominated by trap-state defects formed at the surface.[64,104–105] Silicon will rapidly oxide in the presence of O_2 and H_2O under atmospheric conditions.[106–107] Unlike thick, thermal oxides, native oxides form randomly, breaking Si–Si back bonds, introducing dangling bonds that form mid-gap trap states.[108] Passivation of defects can be achieved by formation of a thermal oxide, SiO_2,[109–110] or deposition of silicon nitride, Si_3N_4,[111] layers and both are often used in optoelectronic applications. However, the insulating properties of these materials preclude their utilization at the interface of two-terminal, tandem-junction solar devices. Other metal-metal oxide passivation strategies such as Al_2O_3, HfO_2, Ga_2O_3, and Ta_2O_5 present similar passivation properties but are better suited
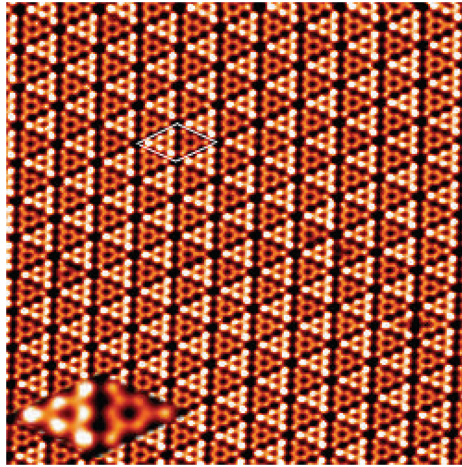
Figure 2.2 STM image of Si(111) 7×7 surface. The image represents at 30 x 30 nm surface area. Adapted from Wang, Y.-L.; Guo, H.-M.; Qin, Z.-H.; Ma, H.-F.; Gao, H.-J. *J. Nanomater.* **2008**, 874213.[116] Copyright **2008**, Hindawi Publishing Corporation.

as high-κ dielectric materials for metal-oxide-semiconductor field-effect transistors (MOSFETs).[112–114] These passivation methods all require either high temperatures, to oxidize and anneal, or vacuum chambers for atomic layer deposition (ALD), limiting the cost-scalability factor. However, silicon surfaces can be etched and functionalized employing benchtop, wet-chemistry methods at modest temperatures to chemically and electronically passivate the surface against oxidation.

2.2 The H–Si(111) Surface

The Si(111) face is of particular interest due to its ability to form long, atomically smooth surfaces along the crystal plane. High-temperature processing of this surface in an ultrahigh vacuum chamber removes the oxide layer and yields the Si(111) 7×7 reconstructed surface.[115] Figure 2.2 presents the STM of a Si(111) 7×7 surface.[116] It contains few defects and is atomically clean after heating, making it an ideal surface for imaging and gas-phase adsorption experiments and other fundamental surface studies on silicon. However, it is limited to UHV studies and will rapidly oxidize once introduced to air.[117]

Fluoride ion containing solutions are capable of etching SiO_x layers.[118–120] Acidic solutions of hydrogen fluoride, HF, will quickly through the oxide layer before slowing down at the bulk Si. Intrinsic and lightly doped silicon is unaffected by aqueous HF solutions in the absence of light.[121] However, the silicon surface left behind after HF etching is extremely rough compared to the atomically smooth, UHV-prepared samples.[122] Buffered HF solutions,
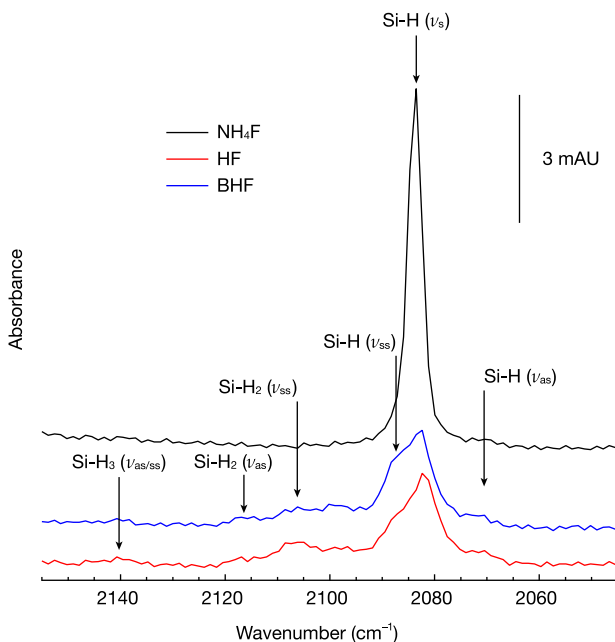
Figure 2.3   Transflection IR spectra of the Si(111) surface after etching with different fluoride solutions a 2 cm^{-1} resolution. 40% NH$_4$F (black), 10% HF (red), and pH 5.5 BHF (blue). The higher order Si–H$_x$ stretching modes are difficult to distinguish from the baseline due to the inherent uniformity of Si(111) surfaces and their low surface densities. The assignments of these modes are based on those determined by Dumas *et al.*[126]

BHF, contain ammonia which raises the pH, slowing down the etch rate through the oxide layer while increasing the rate through the bulk silicon. 40% ammonium fluoride solutions, NH$_4$F(aq), anisotropically etch Si(111), yielding atomically smooth surfaces with terraces that stretch over hundreds of nanometers, depending on the miscut angle of the wafer.[118,123–126] Unlike UHV-prepared Si(111), the surface is not terminated by dangling bonds. Instead, Si–H bonds oriented perpendicular to the surface are left behind by the fluoride etching process. Figure 2.3 presents the transflection IR spectra of HF, BHF, and NH$_4$F etched Si(111). Fluoride solution etched surfaces contain Si–H vibrational modes between 2060 and 2150 cm^{-1}: 2070, 2083, 2088, 2106, 2117, and 2140 cm^{-1}, which were reported an assigned by Dumas *et al.*[126] Briefly, the monohydride stretch, v_s, at 2083 cm^{-1} represents by the isolated Si–H group found within smooth terraces. The symmetric and asymmetric coupling modes, v_{ss} and v_{as} , of adjacent monohydrides at step sites are found at 2088 and 2070 cm^{-1}.[127] The symmetric and asymmetric Si–H$_2$ stretching modes, occur at dihydride step sites around 2106 and 2117 cm^{-1}. Trihydride
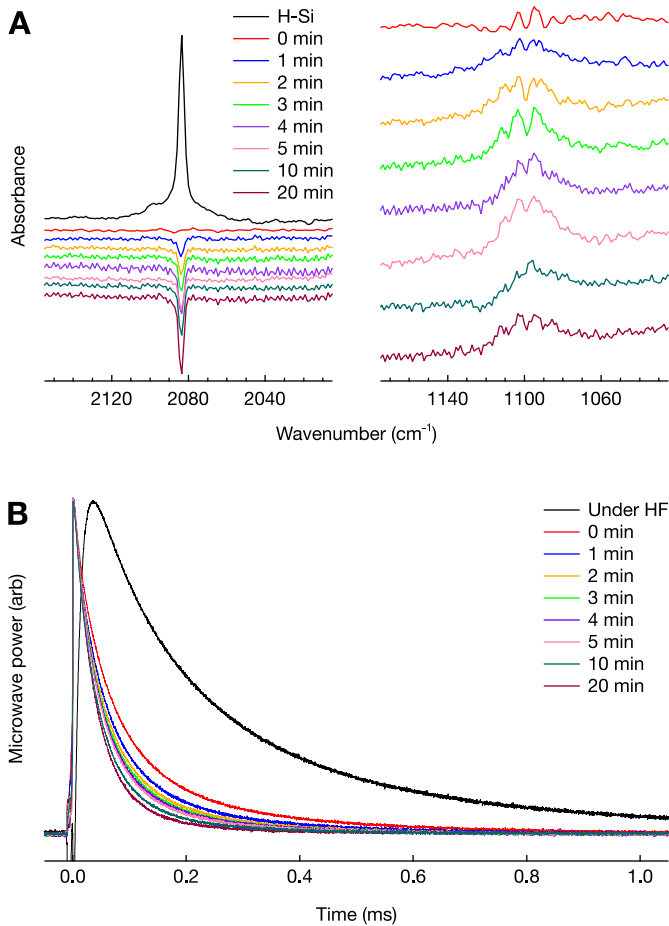
Figure 2.4   Onset of oxidation on the H–Si(111) surface. Frame **A** presents two regions of the transflection IR spectra left in air for 20 minutes. On the left is the Si–H stretching modes and the right region contains the SiO$_x$ TO mode. The black H-Si trace is referenced to the chemically oxidized silicon surface and the remaining traces are referenced to the Si–H surface. Frame **B** presents the charge-carrier lifetimes a hydrogen-terminated, intrinsic Si sample.

sites are represented by the small peak at 2140 cm^{-1}. The presence of SiH$_2$ and SiH$_3$ species in the HF and BHF etched surfaces indicates an increased density of step edges and general surface roughness while the NH$_4$F trace is dominated by a single peak at 2083 cm^{-1}, representing the back-bonded, perpendicular Si–H stretching mode.[125–127] The homogeneity of Si–H bonds at the surface is necessary to effect high coverage, defect-free, functionalized surfaces.

In aqueous acid, HF solutions, and organic redox solutions, atomically smooth H–Si(111) surfaces yield long charge-carrier lifetimes or surface recombination velocities (SRV), implying electronic passivation.[104,128–129] In contact with these solutions, an inversion layer is formed which forces electrons away from the surface into the bulk, away from surface defects, yielding long carrier lifetimes, >1 ms, and decreased SRV values <1 cm s^{-1}.[104,128,130–131] However, a native oxide quickly develops after only a few minutes in air,[107] as evidenced by the increasingly negative Si–H peak and the appearance of SiO_x transverse optical (TO) mode[132] in the IR spectrum in frame **A** of Fig. 2.4. Time-resolved microwave photoconductivity (TRMPC) experiments, frame **B** of Fig. 2.4, also measure an immediate reduction of carrier lifetimes. The semiconductor-liquid interfaces that maintain silicon's excellent electronic properties are not conducive to the design of high-performance devices and are limited to laboratory-scale studies.

The functionalization of H–Si(111) surfaces with organic groups has been shown to increase the stability toward oxidation.[133] A variety of methods have yielded the direct attachment of alkyl and aromatic species to the surface including, but not limited to, silanization,[134–135] methanolic reactions,[136–137] hydrosilylation,[138–139] aryl diazonium functionalization,[140–142] anodic grafting,[143–145] and halogenation-alkylation.[104,146–153] Figure 2.5 presents the methods mentioned above for attaching organic species to Si(111) surfaces. The silanization method typically requires an –OH group from the surface which precludes use in oxide-free strategies, but procedures yield well-defined and well-characterized monolayers for various surface applications.[134] H–Si(111) surfaces are typically inert toward non-aqueous solvents but alcohols, particularly methanol, have reported reactions under ambient and electrochemical conditions.[136] The hydrosilylation reaction is still a very popular method to quickly graft a relatively high fraction of organic groups onto hydrogen terminated surfaces. UV light is employed to generate a radical on the silicon surface followed by its addition to the double bond of the alkene in solution. Another proposed mechanism is the UV radiation causes the photoemission of an electron from the silicon's valence band, leaving behind a positive charge which is attacked by the alkene's π-electrons.[154–155] A wide variety of surfaces can be prepared via hydrosilylation and coverages are precisely controlled by the radiation energy, concentration, and time. The aryl diazonium reaction provides a method for the direct attachment of the phenyl ring to the surface. An N_2 group leaves the molecule after injection of an electron from the silicon, leaving behind the aryl radical. The next step is a two-step process, one aryl radical abstracts a hydrogen from the surface and another aryl radical attaches itself by way of the newly generate dangling bond.[141,156] This surface reaction is limited to only phenyl diazonium molecules, limiting its applications and effectiveness at surface passivation. Anodic grafting has also been employed to effect high surface coverages on H–Si(111) with Grignard reagents. The anodic grafting process begins with
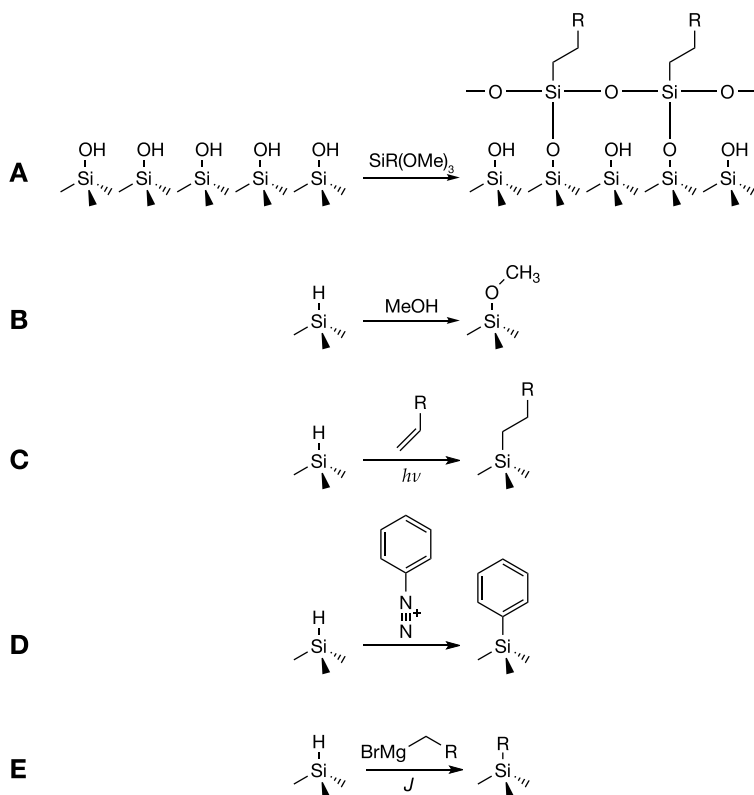
Figure 2.5 Various other methods of organic functionalization of Si(111) surfaces. (A) silanization with a pre-oxidized surface, (B) methanolic reaction, (C) hydrosilation in the presence of UV light, (D) radical diazonium reaction, and (E) anodic grafting of Grignard reagents, where *J* is anodic current.

the generation of a radical at the silicon surface in the presence of anodic current or indirectly by hydrogen abstraction by a radically cleaved Grignard. The Si dangling bond then reacts with the Grignard to form a covalent bond with the alkyl group.[145,157] While useful for altering the hydrophobicity/hydrophilicity of the surface, tuning the electronic properties, and providing chemical hooks for further reactions, these strategies do not fully passivate the terminal silicon atoms which leaves space for oxidation. However, the halogenation-alkylation method is capable of functionalizing a high fraction of the surface with a wide variety of alkyl and functional groups.

2.3   Halogenation-Alkylation of Si(111)

Halogenation of the silicon surface enables versatile, efficient, alkylation re-
actions. The atomic distances between atoms on the Si(111) surface, 0.384
nm,[77] enables the total surface termination by –Cl and –Br atoms,[158–160] how-
ever, iodine atoms are too large and unreactive to cover every adatom.[161–162]
The termination of chlorine atoms can be achieved with Cl_2 gas, although
the reactive gas has been shown to etch Si(111) surfaces in UHV.[163] The more
typical reagent employed is PCl_5, which when used with a radical initiator
such as benzoyl peroxide, generates Cl· in solution to react at modestly low
temperatures and ambient pressure.[159] Br_2 gas from the vapor headspace of
liquid bromine also halogenates Si(111) surfaces and yields total coverages
at room temperature.[160,164] Frame **A** of Fig. 2.6 presents the Si 2p and Br 3d
spectra of an H–Si(111) surface after a two-minute reaction with Br_2 gas. The
Si^0 $2p_{3/2}$ peak is located at 99.83 eV, shifted 0.27 eV compared to the H-term
surface, indicating the presence of a dipole effected by the –Br surface ter-
mination. The location of the Br $3d_{5/2}$ peak at 69.43 eV is consistent with Br
bound to Si.[160–161] Frame **B** of Fig. 2.6 presents the IR spectra of brominated
H–Si(111) with an H–Si(111) background. The area of the monohydride H–Si
peak at 2083 cm^{-1} implies the total conversion of hydride Si sites to Br–Si.
Like H–Si, halogen terminated surfaces are also prone to rapid oxidation after
a short amount of time in air. Alkylation of the halogenated Si(111) surface
provides the much-needed chemical stability against oxidation and further
alteration of the electronic properties.

Halogenated Si(111) surfaces are submerged in Grignard or lithium solutions
for short amounts of time at modest temperature to effect the attachment of
organic species.[104,146–153] Due to its small Van der Waal's radius, 0.22 nm,[165]
methyl groups are the only alkyl group that will terminate every Si(111)
site. The passivated CH_3–Si surface shows stability toward oxidation for
weeks in air with no observable increase in oxidized Si 2p features.[104,165–166]
The SRV values remain unchanged indicating the silicon is also electronically
passivated.[104] However, methyl terminated silicon's robust passivation limits
the secondary chemistry that may be conducted to further modify the surface.

The attachment of organic species such as allyl groups, butenes, thiophenes,
and substituted benzenes offer the chemical reactivity necessary to conduct
secondary derivatizations.[151–152,167–169] Unlike methyl groups, bulky func-
tional groups, such as benzenes and long-chain alkyl groups, are hindered
by sterics and only capable of functionalizing 50–90% of Si atop sites.[133,150]
Fortunately, mixed monolayers with methyl groups can increase the overall
surface coverage to >90%.[151–152,167,170–171] IR, XPS, and SRV studies reveal
slight oxidation of mixed monolayer surfaces after extended periods of time
in air, with oxidation plateauing ~0.1 monolayers, and minimal detriment
to the electronic properties.[152,167] The disordered nature of longer, bulkier
alkyl groups prevent direct access of O_2 and H_2O to the surface, limiting
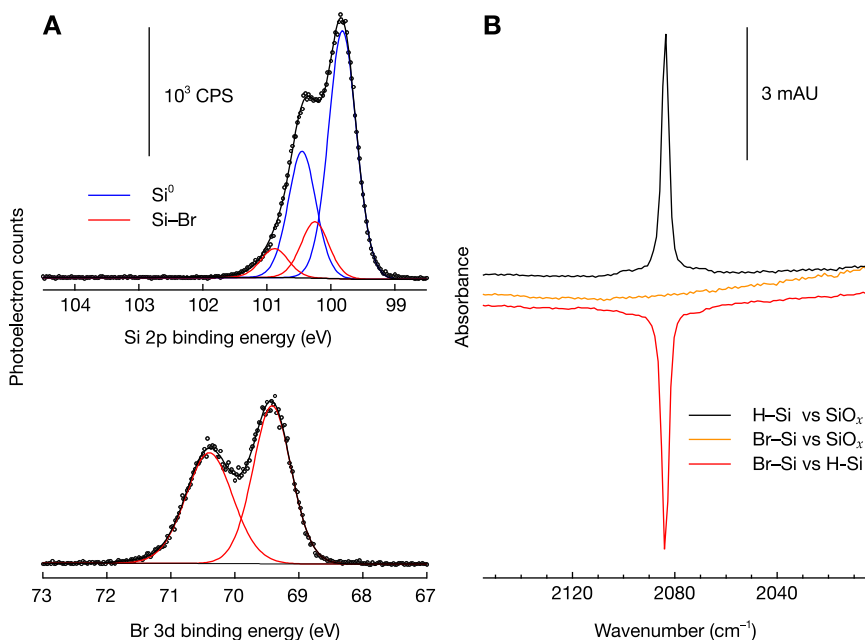
Figure 2.6   XPS and transflection IR spectra of Br–Si(111). Frame **A** shows Si 2p and Br 3d XP spectra. The Si 2p spectrum consists of a pair of doublet peaks. The blue Si peaks represent the Si^0 substrate and the red peaks represents interfacial Si–Br. The Br 3d spectrum contains one doublet representing Br-Si. Frame **B** presents the Si–H stretching region of the transflection IR spectrum of H–Si(111) before and after bromination. The H–Si IR spectrum (black) is referenced to an oxidized, piranha cleaned surface and the Br–Si samples are referenced to the SiO_x (blue) and H–Si (red).

the rate of oxidation. Bromination, Heck-coupling, and cross-coupling reactions have been previously utilized in the secondary functionalization of allyl/methyl monolayer to effect chemical handles for further derivatization and the attachment of practical moieties, including bipyridines, metallocenes, and porphyrins.[152,167,169,172–174]

While simple alkyl groups provide chemical passivation, the small dipole moment at the surface effects only small changes to the positions of band-energies, compared to H–Si, which are integral to the design and performance of water-splitting, optical, and photovoltaic devices.[153,160,164,168,171,175–177] Redox-active metal complexes, such as ferrocene, have previously been attached to Si(111) surfaces and exhibit redox potentials similar to their respective redox species solutions, indicating the linker between the surface and active group has little effect on the charge-transfer characteristics.[151,173] Similar methods have been employed to tether catalytic molecules to the surface for the generation of chemical fuels.[169,172] Terminal aldehydes have

also been covalently attached as precursors in the first steps of well-defined TiO_2 and Al_2O_3 growth in ALD experiments.[178] It is also possible to tune the energy levels of the surface with electron withdrawing and donating groups that contribute to the overall surface dipole moment.[160,171,176–177,179] To probe the surface coverages and electronic properties of these functionalized surfaces requires a variety of surface-sensitive, analytical techniques which are described in the following sections.

2.4   X-ray Photoelectron Spectroscopy

X-ray photoelectron spectroscopy (XPS) was extensively utilized to identify the chemical species and states on semiconductor surfaces. XPS determined the surface coverage of covalently attached organic molecules on Si(111) and the extent of oxidation due to reactions and long periods of time in air.

In a typical XPS experiment, soft X-rays with energies between 1 and 5 keV, irradiate surfaces which then emit photoelectrons via the photoelectric effect.[180] Aside from synchrotron and beamline light sources, the narrowest X-ray lines are attained with the aid of a monochromator. Al Kα X-rays are directed toward a bent quartz crystal and reflected according to Bragg's Law.[181–182] These reflected X-rays are monochromated and highly focused, yielding narrow line widths and photoelectron peaks. These X-rays travel through the first 1–10 μm of a surface and are absorbed by many-electron orbitals. If the photon energy is greater than the binding energy of that electron, it is emitted from the atom. Equation 2.1 gives the kinetic energy (**KE**) of an emitted photoelectron.

$$\mathbf{KE} = h\nu - \mathbf{BE} - \mathbf{\Phi}_D \tag{2.1}$$

$$\mathbf{BE} = h\nu - \mathbf{KE} - \mathbf{\Phi}_D \tag{2.2}$$

In eq 2.1 **KE** is the kinetic energy of the photoelectron, $h\nu$ is the photon energy, **BE** is the binding energy, and $\mathbf{\Phi}_D$ is the inherent spectrometer work function. Photoelectrons that escape the sample surface pass through the entrance slit of the analyzer where they are focused by a series of electrostatic lenses which discriminate electrons by their kinetic energies before funneling them into the spherical capacitor analyzer (SCA). Within the SCA hemisphere are two concentric electrodes biased at an energy referred to as the pass energy. Electrons passing through the hemisphere are further filtered by their kinetic energy. After exiting the hemisphere, the photoelectrons pass through an electron multiplier to amplify the signal before they are counted by a position-sensitive 16-channel detector. Photoelectrons generated in XPS experiments are typically presented by their binding energy, thus eq 2.1 can be rewritten as eq 2.2.

Because each element has a unique nuclear charge and electronic structure, the BE of a core-level electron is specific to its orbital and the nucleus it is bound to, allowing for compositional analysis of the sample surfaces. Further, XPS can resolve different oxidation states and chemical species of the same element due to changes in electronegativity effected by the atoms surrounding the element of interest.

XPS is a highly surface sensitive experiment. Unlike photons, photogenerated electrons can only travel a short distance through a material, about 1–4 nm, before experiencing an inelastic scattering event.[183–186] The average distance this electron can travel is referred to as the attenuation length, λ. Figure 2.7 presents the empirically derived attenuation lengths of photoelectrons based on their kinetic energies.[183] At low kinetic energies, <50 eV, photoelectrons do not interact with atoms in the substrate and can travel comparably far through materials. However, these electrons are extremely susceptible to stray magnetic and electric fields. Above 50 eV, the attenuation length increases with increasing kinetic energy. A materials density and electronic properties will also affect an electron's attenuation length, thus semi-empirical models based on specific materials are required. The models used in determining the attenuation lengths for this work are further discussed in §2.4.1.
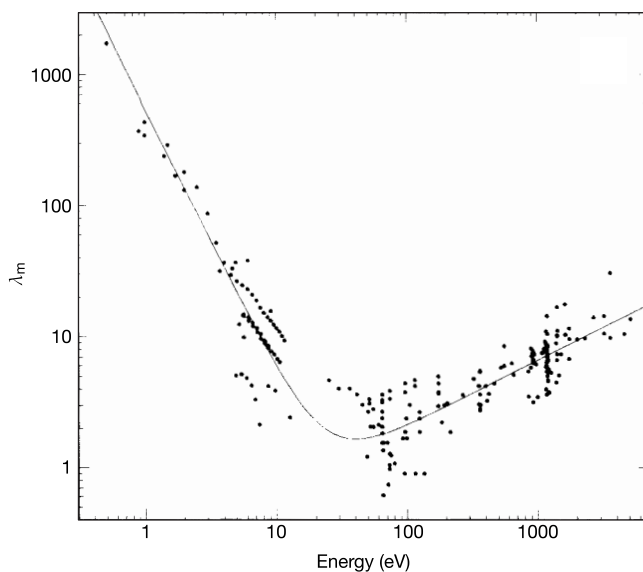
Figure 2.7   Attenuation length vs the kinetic energy of photoelectrons. Adapted from Seah, M. P.; Dench, W. A. *Surf. Interface Anal.* **1979**, *1*, 2-11.[183] Copyright **1979**, John Wiley & Sons, Ltd.

A Incoming X-ray radiation: Al K_α $h\nu$

$\phi = 0°$
$\gamma = \delta + \theta$
$\quad = 54.7°$ (Twin)
$\quad = 90°$ (Mono)

Sample normal

e^- Detector

+z

+x   +y

Stage adjustment   Effective θ ($\phi = 0°$) that varies from 0–90°

B Incoming UV radiation ("flat" puck):

$\phi \approx 31°$
$\gamma \approx 51°$
$\delta \approx 79°$
$\theta = 45°$

Sample normal

e^- Detector

He I $h\nu$

+z

+x   +y

C Incoming He I radiation (as acquired):

$\theta = 0°$
$\phi = 0°$
$\gamma = \delta \approx 51°$

Sample normal,
e^- Detector

$\gamma = \delta \approx 51°$

He I $h\nu$

+z

+x   +y
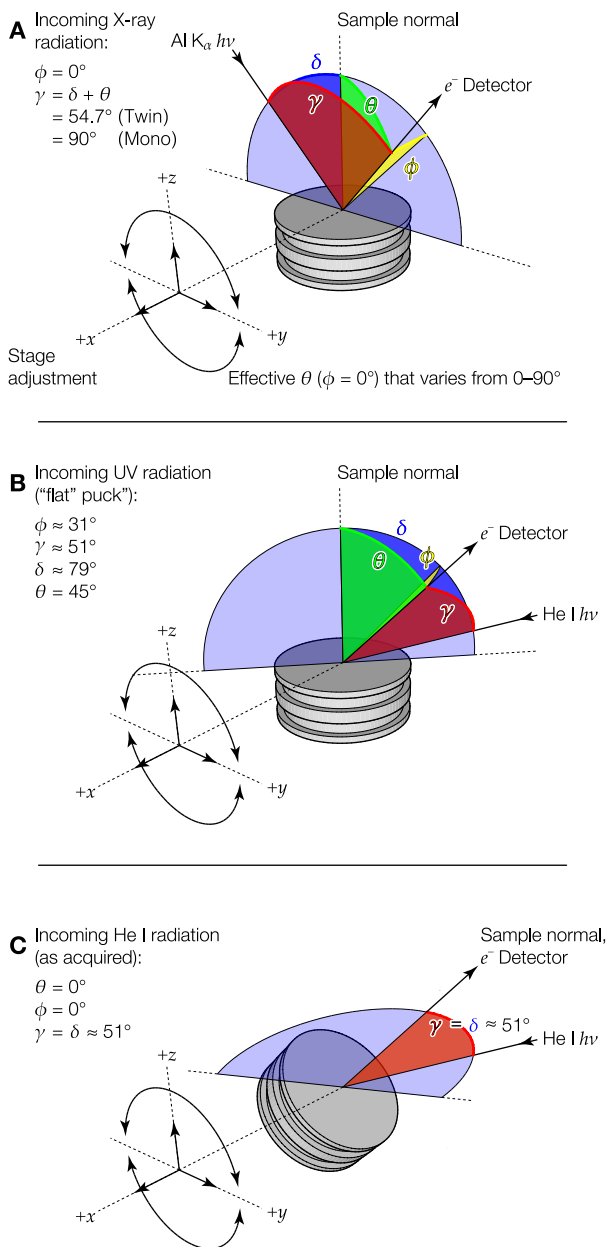
Figure 2.8   Configuration of the Phi 5600 XPS system and labelling of angles pertinent to quantification. Frame **A** presents the typical orientation of the sample with respect toward incoming X-rays and the detector. Frame **B** and **C** present the sample in its normal and tilted positions with respect to the UV light source and detector.

X-ray photoelectron spectra were acquired with a PHI 5600 multitechnique system. To interface with modern computer and software, the system was fitted with a third-party data acquisition system (RBD Instruments, Bend Oregon). All analyses were conducted with a chamber base pressure of $< 2 \times 10^{-9}$ Torr. Figure 2.8 presents the optics configuration of the PHI 5600. The instrument utilized two x-ray sources: A monochromated Al source and a twin-anode source containing Al and Mg anodes. The incident angle of the monochromated X-rays were positioned at 45° with respect to the surface normal, δ, while the twin anode was positioned at 9.7°. Here θ is the angle between the surface normal and electrons emitted to the detector. So, γ is the sum of δ and θ yielding 90° for the monochromated source and 54.7° for the twin-anode. Kinetic energy discrimination of photoelectrons was accomplished by a hemispherical analyzer (also called a spherical capacitor analyzer, SCA) and 16-electrode multi-channel detector (MCD). Survey spectra utilized a pass energy of 117 eV, a 0.5 eV step size, and a 50 ms dwell time. High-resolution "multiplex" spectra utilized a pass energy of 23.5 eV, a 0.025 eV step size, and a 50 ms dwell time. The fermi-edge of the spectrometer was periodically calibrated with gold and copper to align the Au $4f_{7/2}$ and Cu $2p_{3/2}$ features to exactly 84.00 and 932.67 eV.

Post-acquisition data fitting utilized an in-house-developed LabVIEW-based program. Spectral background shapes that describe the contribution from inelastically scattered electrons include a linear background, Shirley-shaped background, or the integration of a Tougaard shape based on $B = 2900 \, eV^2$ and $C = 1643 \, eV^2$ within a universal function that is scaled to the height of the photoelectron data.[187−188] A pseudo-Voight-style function, $GL(x)$, describes each peak shape where x scales nonlinearly from 0 as a pure Gaussian form to 100 as a pure Lorentzian shape. Optimization routines utilize the built-in LabVIEW implementation of the Levenberg–Marquardt algorithm for multiparameter fitting. Fitting of the Si 2p and I $3d_{5/2}$ employed Tougaard style backgrounds. C 1s, Ti 2p, and Pb 4f features utilized a Shirley-shaped background. The N 1s, O 1s, Br 3d, and F 1s regions were fit with linear background. All features were fit with $GL(30)$ functional peaks shapes except the I $3d_{5/2}$ and Pb 4f peaks which required more Lorentzian $GL(70)$ peaks. When Br 3d, C 1s and F 1s regions necessitated multiple fitted peaks, such peaks were constrained to have identical full-width-at-half-maximum (fwhm) values. Features in the Si 2p spectral region were constrained to utilize identical fwhm values for peaks ascribed to bulk and interfacial silicon, while the width of features attributed to SiO_x remained unconstrained.

2.4.1 Substrate-Overlayer Model

The quantification of functionalized silicon surfaces employed a substrate-overlayer model. The substrate-overlayer model employed in this work is based on the models established by Seah, Briggs, Ebel, Fadley, and Sturzneg-

ger *et al.*[185,189–192] Briefly, our model establishes relationship of overlayer species that attenuate the photoelectrons emitted in the underlying substrate.

Before we can quantify fractional coverages of organic monolayers, we need to consider several terms and parameters that form the basis of our model. The total photoelectron intensity of a pure, uncovered substrate, I_A, may be determined by eq 2.3.

$$I_A = I_0 \, \sigma_A \, T(E_A) \, D(E_A) \int_0^\infty N_A(z) \exp \frac{-z}{\lambda_A \cos \theta} \, dz \qquad (2.3)$$

In eq 2.3, the first of these terms is x-ray flux, I_0, or the density of photons striking the surface area per second, σ_A is the photoionization cross-section for a specific core-level electron from element A at energy hv. $T(E_A)$ is the analyzer transmission function or ratio of electrons of energy E that enter the lens system and those that ultimately reach the detector. $D(E_A)$ is the detector efficiency for electrons of energy E. N_A is the number density of atom A within the analyzed material and λ_A is the attenuation length of an electron from atom A traveling through pure material A. The exponential term describes the attenuation of photoelectrons from depth z before being emitted from the surface. Again θ is the emission angle of electrons with respect to the surface normal, which is 45° for all XPS data collected in this work.

We integrate eq 2.3 down from the surface, $z = 0$, through ∞, as substrates are typically thicker than the X-ray penetration depth and far thicker than the attenuation lengths of typical photoelectrons. Integration of eq 2.3 yields eq 2.4 when N_A is not a function of z, or is uniform through the electron escape depth.

$$I_A = I_0 \, \sigma_A \, T(E_A) \, D(E_A) \, N_A \, \lambda_A \cos \theta \qquad (2.4)$$

Equations 2.4 is rarely used alone to quantify surfaces. Instead, an intensity ratio between two different atoms of a matrix or layered system is often utilized. For the purposes of quantifying a substrate-overlayer system, we also need an equation for determining the intensity from an element in the overlayer, I_B. We integrate eq 2.3 from $z = 0$ to a defined depth, d, via eq 2.5 where B is the atom of interest in the overlayer.

$$I_B = I_0 \, \sigma_A \, T(E_B) \, D(E_B) \int_0^d N_B(z) \exp \frac{-z}{\lambda_B \cos \theta} \, dz \qquad (2.5)$$

Integration of eq 2.5 yields 2.6:

$$I_B = I_0\,\sigma_B\,T(E_B)\,D(E_B)\,N_B\,\lambda_B \cos\theta \left(1 - \exp\frac{-d}{\lambda_B \cos\theta}\right) \tag{2.6}$$

Before dealing with the substrate-overlayer intensity ratio, we must first we must consider λ, the attenuation length. Seah and Cumpson developed an empirical model,[184] eq. 2.7, derived from an element's solid-state density, its atomic number, molar mass, and the emitted photoelectron's kinetic energy.

$$\lambda = 3.16 \times 10^{11}\ \text{nm}\ \left(\frac{A}{\rho N}\right)^{1/2}\left[\frac{E}{Z^{0.45}\,(3 + \ln\frac{E}{27})} + 4\right] \tag{2.7}$$

In eq 2.7 A is the molar mass in g mol^{-1}, ρ is the density of the elemental material in g cm^{-3}, N is Avogadro's number, E is the photoelectron kinetic energy, and Z is the atomic number. While useful for calculating attenuation lengths for pure and binary materials, the determination of λ values of electrons passing through organic overlayers are better described by an equation reported by Laibinis *et al.*,[193] derived eq 2.8 from their analysis of gold photoelectrons traveling through thiols.

$$\lambda = 0.090\ \text{nm} + 0.0022\ \text{nm} \times E \tag{2.8}$$

The substrate-overlayer systems of interest require these equations be used in tandem to accurately quantify the depths or fractional coverages of overlayers on substrates. Figure 2.9 presents first and the simplest application of these equations which will quantify the depth of a uniform overlayer on a substrate. In this scenario, the substrate A intensity equation, eq 2.3, is instead integrated from depth $z = d_B \to \infty$, yielding eq 2.9.

$$I_A = I_0\,\sigma_A\,T(E_A)\,D(E_A)\,N_A\,\lambda_A \cos\theta \exp\frac{-d_B}{\lambda_{A,B} \cos\theta} \tag{2.9}$$

In eq 2.9, d_B is the depth of overlayer B and $\lambda_{A,B}$ is the attenuation length of an electron ejected from substrate A travelling through overlayer B. Now we can combine eqs 2.6 and 2.9 to determine 2.10, the expected I_B/I_A ratio for a defined overlayer B on substrate A.
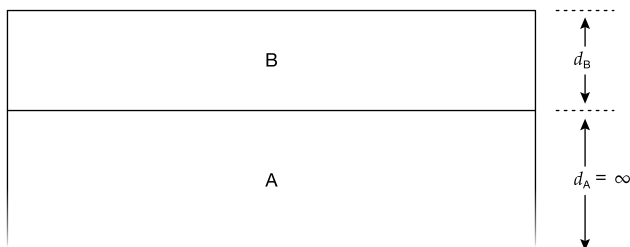
Figure 2.9   Model of a uniform overlayer, **B**, of on top of a semi-infinite substrate, **A**.

$$\frac{I_B}{I_A} = \frac{I_0\,\sigma_B\,T(E_B)\,D(E_B)\,N_B\,\lambda_B \cos\theta}{I_0\,\sigma_A\,T(E_A)\,D(E_A)\,N_A\,\lambda_A \cos\theta}\;\frac{1 - \exp\frac{-d_B}{\lambda_B \cos\theta}}{\exp\frac{-d_B}{\lambda_{A,B}\cos\theta}} \tag{2.10}$$

Fortunately, this eq 2.10 may be simplified by the cancellation several terms. Our analyzer is configured to acquire photoelectrons in the Fixed Analyzer Transmission mode, FAT, where all electrons reaching the detector arrive with similar kinetic energies. This is accomplished by retarding the kinetic energy of electrons at the beginning of the lens system to a specific energy and adjusting the retard voltage stepwise to scan the entire photoelectron spectrum. To the detector, the kinetic energies of detected photoelectrons are all the same, even between different elements, and we can remove the energy-dependent $T(E)$ and $D(E)$ terms. Additionally, the I_0 and first $\cos\theta$ terms are also removed from the intensity ratio because the spectra acquired in these systems occur at the same time, in the same instrument, and under the same conditions of takeoff angle, θ. Finally, the σ and λ terms (not λ terms in the exponentials) are combined into one term referred to as the sensitivity factor, SF, a value that is tabulated for elements analyzed by a specific instrument configuration.[194–195] Taken together, simplification of eq 2.10 yields eq 2.11.

$$\frac{I_B}{I_A} = \frac{N_B\,SF_B}{N_A\,SF_A}\;\frac{1 - \exp\frac{-d_B}{\lambda_B \cos\theta}}{\exp\frac{-d_B}{\lambda_{A,B}\cos\theta}} \tag{2.11}$$

For substrate overlayer systems where $\lambda_{A,B} \approx \lambda_{A,B}$ eq 2.11 rearranges in the following two steps to further simplify the calculation of d_B from an experimental ratio I_B/I_A as in eq 2.13.
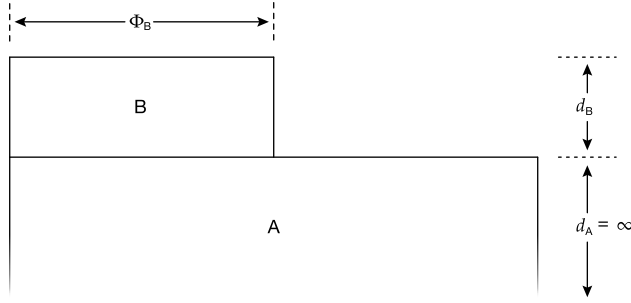
Figure 2.10   Model of surface coverage by a fractional monolayer, **B**, over substrate, **A**.

$$\frac{I_B N_A\, SF_A}{I_A N_B\, SF_B} = \exp \frac{d_B}{\lambda_{A,B} \cos \theta} - \exp \left(\frac{d_B}{\lambda_{A,B} \cos \theta} - \frac{d_B}{\lambda_B \cos \theta} \right) \tag{2.12}$$

$$d_B = \ln \left(\frac{I_B N_A\, SF_A}{I_A N_B\, SF_B} + 1 \right) \lambda_{A,B} \cos \theta \tag{2.13}$$

In section 2.4.2, we discuss the utilization of eq 2.13 in the determination of oxide depths in silicon. It may also be employed for oxide depths in other materials and substrate-overlayer systems that share similar λ values.

Now that we can determine the depth of thin, uniform overlayers, we can expand our substrate-overlayer equations to quantify fractional overlayers. Figure 2.10 presents the a fractional overlayer model with the pertinent variables.

The intensity of signals originating from the fractional overlayer and substrate in Fig. 2.10 are given in eqs 2.14 and 2.15, respectively.

$$I_B = N_B\, SF_B\, \Phi_B \left(1 - \exp \frac{-d_B}{\lambda_B \cos \theta} \right) \tag{2.14}$$

$$I_A = N_A\, SF_A \left(1 - \Phi_B + \Phi_B \exp \frac{-d_B}{\lambda_{A,B} \cos \theta} \right) \tag{2.15}$$

In eqs 2.14 and 2.15, Φ (not to be confused with the $\mathbf{\Phi}$ for work function) is the fractional coverage by the overlayer per surface substrate atom. Briefly, electrons from the substrate A are only attenuated when obscured by the fractional monolayer B, Φ_B. Electrons from bare substrate, $1 - \Phi_B$, do not experience attenuation. Combining eqs 2.14 and 2.15 yields the following intensity ratio in eq 2.16.

$$\frac{I_B}{I_A} = \frac{N_B \, SF_B}{N_A \, SF_A} \frac{\Phi_B \left(1 - \exp \frac{-d_B}{\lambda_B \cos \theta}\right)}{\left(1 - \Phi_B + \Phi_B \exp \frac{-d_B}{\lambda_{A,B} \cos \theta}\right)} \tag{2.16}$$

Equation 2.16 is utilized to determine the fractional coverage of an overlayer on a substrate, however, a value for d_B must be defined prior to quantifying Φ_B. Some example systems described by eq 2.16 include incomplete organic monolayers, sub-monolayer metal coatings, and patterned, photolithographic films.[190–191] However, the surfaces studied in this thesis are not accurately represented by a single, fractional overlayer and usually contain a thin surface-oxide with multiple fractional overlayers. Figure 2.11 presents a substrate covered by both a uniform and fractional overlayer.
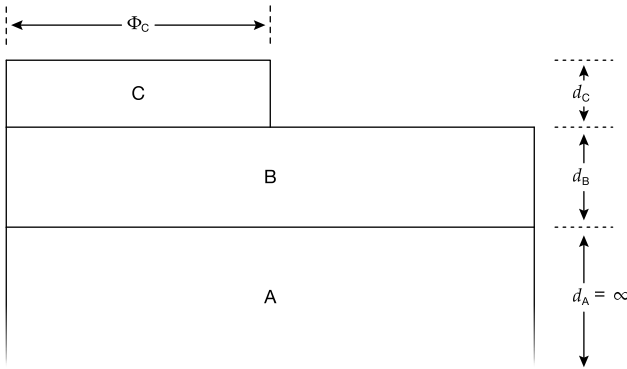
Figure 2.11   Model of surface coverage by a fractional monolayer, **C**, and uniform thin-film, **B**, covering a substrate, **A**.

In the Fig. 2.11 model, photoelectrons from the substrate, **A**, experience attenuation through the uniform overlayer, **B**, then additional attenuation through areas covered by the fractional overlayer, **C**. The intensity ratio equation comprised of both attenuation by the uniform and fractional overlayer is given by eq 2.17.

$$\frac{I_C}{I_A} = \frac{N_C \, SF_C}{N_A \, SF_A} \frac{\Phi_C \left(1 - \exp \frac{-d_C}{\lambda_C \cos \theta}\right)}{\exp \frac{-d_B}{\lambda_{A,B} \cos \theta} \left(1 - \Phi_C + \Phi_C \exp \frac{-d_C}{\lambda_{A,C} \cos \theta}\right)} \tag{2.17}$$

In eq 2.17, d_B is the depth of the uniform overlayer **B**, which has been calculated with eq 2.13 prior to determining the fractional coverage of overlayer **C**.
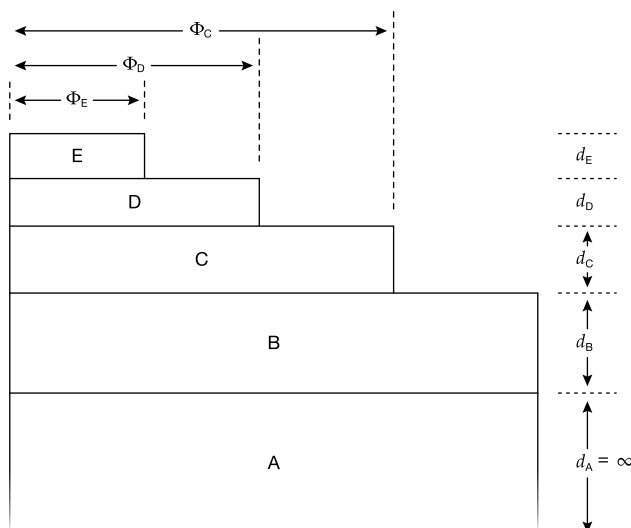
Figure 2.12   Model of surface coverage by three fractional monolayers and uniform thin film over a substrate.

The surfaces functionalized in this work require more rigorous equations accounting for two and even three fractional overlayers due to the step by step reactions yielding less than complete conversion at each step of the surface functionalization. Figure 2.12 presents a model surface with multiple fractional and a uniform overlayer. Equations 2.18 and 2.19, on the next page, build on eq 2.17 by representing surfaces with two and three total fractional overlayers, on a uniform overlayer, all atop a semi-infinite substrate:

For eqs 2.18 & 2.19 to work, the coverage by Φ_C must be determined before Φ_D and so on and so forth as the surface is functionalized. Armed with these equations, we can begin to apply them to real, functionalized Si(111) surfaces relevant to the ongoing organic attachments of interest. The following sections will describe these substrate-overlayer model equations in the context of specific overlayer systems which require only slight variations.

2.4.2   Modeling Alkylamine-functionalized Si(111) Surfaces

The substrate-overlayer model described in this section to quantify the surface coverages of alkylamine groups on Si(111) slightly differs from the one published in *Applied Materials and Interfaces*.[196] Figure 2.13 presents a layered model of the desired alkylamine functionalized Si(111) surface. This model depicts the substrate, silicon, an ultrathin-oxide layer, d_{Ox}, a mixed monolayer of allyl/methyl groups, d_{Org}, fractional coverage by Br-atoms, Φ_{Br}, with

$$\frac{I_D}{I_A} = \frac{N_D\,SF_D}{N_A\,SF_A}\,\frac{\Phi_D\left(1 - \exp\frac{-d_D}{\lambda_D\cos\theta}\right)}{\exp\frac{-d_B}{\lambda_{A,B}\cos\theta}}\,\frac{1}{\left(1 - \Phi_C + (\Phi_C - \Phi_D)\exp\frac{-d_C}{\lambda_{A,C}\cos\theta} + \Phi_D\exp\frac{-d_D-d_C}{\lambda_{A,D}\cos\theta}\right)}$$

(2.18)

$$\frac{I_E}{I_A} = \frac{N_E\,SF_E}{N_A\,SF_A}\,\frac{\Phi_E\left(1 - \exp\frac{-d_E}{\lambda_E\cos\theta}\right)}{\exp\frac{-d_B}{\lambda_{A,B}\cos\theta}} \times$$

$$\frac{1}{\left(1 - \Phi_C + (\Phi_C - \Phi_D)\exp\frac{-d_C}{\lambda_{A,C}\cos\theta} + (\Phi_D - \Phi_E)\exp\frac{-d_D-d_C}{\lambda_{A,D}\cos\theta} + \Phi_E\exp\frac{-d_E-d_D-d_C}{\lambda_{A,E}\cos\theta}\right)}$$

(2.19)

A Atomic arrangement   **B** Photoelectron model
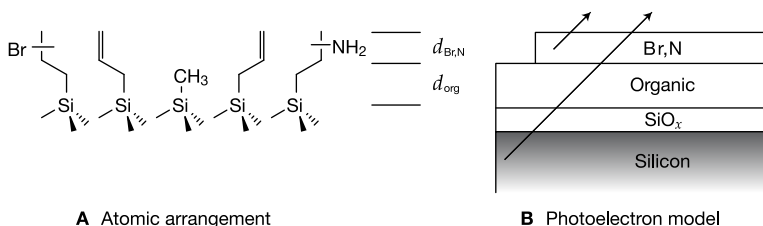
Figure 2.13   Bromine and nitrogen localization on mixed allyl/methyl Si(111) surfaces (Frame **A**) as related to the substrate overlayer model (Frame **B**) that ascribes surface coverages from experimental XPS intensities.

a depth d_{Br}, and fractional coverage by $-NH_2$ terminal groups, Φ_N, with a depth d_N.

As shown in Fig. 2.13, the values for d_{Br} and d_N are 0.18 nm and 0.12 nm, respectively. These values were determined from the length of a cubic volume, d_{Br}^3, that is equal to the spherical atomic volume for a given covalent atomic radius, i.e. $4\pi r_{Br}^3 \equiv d_{Br}^3$, therefore $d_{Br}^3 = 2\sqrt[3]{\pi/6}\, r_{Br}$. The mathematical overlayer model treats photoelectrons as travelling through layers that are uniform throughout their depth. Thus, we believe that using the spherical-to-equivalent-cubic-volume calculation for d is preferable to simply doubling a radius as would be a model for a layer of close-packed hard spheres with void space. From $r_{Br} = 0.114$ nm and $r_N = 0.075$ nm, the volumetric conversion yields $d_{Br} = 0.18$ nm and $d_N = 0.12$ nm. After bromination of the allyl group with HBr, it is unknown where whether bromine binds to the primary, terminal carbon or at the lower, secondary carbon. For this reason, we utilize $d_{Org} = 0.24$ nm based on positioning the Br or N atom in the middle of the double bond and a C–C bond length of 0.154 nm and an angle of 109.5°. Figure 2.14 includes a sensitivity analysis of the overlayer model which compares overlayer coverages of Br while varying the d_{Org} and d_{Br} values. Changes to d_{Br} have a significant effect on surface coverage whereas variation of d_{Org} yields only small changes. Thus, the reliance on the bromine or nitrogen group being found in the middle of the double bond is not unfounded.

The intensity of the bromine signal, I_{Br}, relies upon the density of bromine atoms in the monolayer, N_{Br}, the bromine sensitivity factor, $SF_{Br} = 0.895$, the depth of the bromine layer, d_{Br}, described above, and the attenuation length, $\lambda_{Br} = 2.9(45)$ nm, of a Br 3d photoelectron traveling through the bromine layer itself. The value of λ_{Br} was calculated with eq 2.7, as the bromine atom is assumed to be at the top of the monolayer and didn't travel through additional organic layers. I_{Br} is given by eq 2.20:
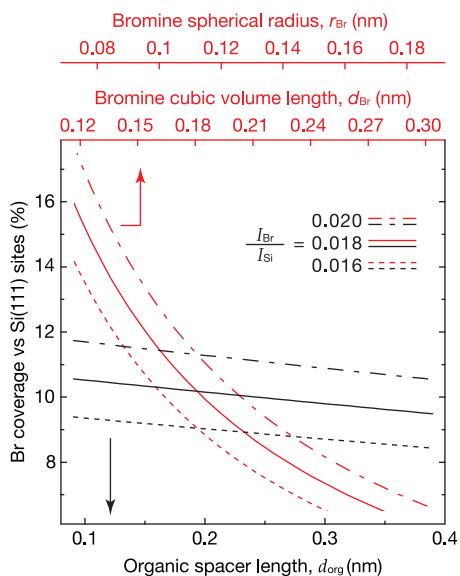
Figure 2.14   A sensitivity analysis explores how changes in the value of the organic spacer length, d_{Org} (black traces, bottom axis) for a fixed value of bromine size, and how changes in the bromine size (red traces, top axes) for a fixed value of d_{Org} change the calculated bromine coverage in the XPS overlayer model. The bromine size is represented two axes of the spherical radius of a bromine atom, r_{Br}, as well as the length d_{Br} of a cubic volume equal to the sphere for a given r_{Br} value. The dotted, solid, and dash-dotted traces represent experimentally relevant photoelectron intensity ratios, $I_{\text{Br}}/I_{\text{Si}}$ of 0.016, 0.018, and 0.020. This analysis demonstrates that the calculated coverage has a very weak dependence on the organic spacer length, d_{Org}, but a more direct dependence on the choice of the atomic radius value that determines d_{Br}.

$$I_{\text{Br}} = N_{\text{Br}} \, SF_{\text{Br}} \left(1 - \exp \frac{-d_{\text{Br}}}{\lambda_{\text{Br}} \cos \theta}\right) \tag{2.20}$$

The fractional bromide coverage, Φ_{Br}, is found within N_{Br}. Realistically, any alkylbromide found on the surface is covalently attached and we relate surface density with respect to the surface packing density of Si(111). Therefore, we express $N_{\text{Br}} = \sigma_{\text{Si}(111)} \Phi_{\text{Br}}/d_{\text{Br}}$ where the surface density of silicon sites, $\sigma_{\text{Si}(111)}$, is 7.830 sites nm^{-2}, coming from the cubic unit cell length, a_{Si}, $\sigma_{\text{Si}(111)} = 4 a_{\text{Si}}^{-2} 3^{-1/2}$. Thus N_{Br} is rewritten as $\frac{4}{a_{\text{Si}}^2 \sqrt{3} \, d_{\text{Br}}} \Phi_{\text{Br}}$ and eq 2.20 may be restated as eq 2.21.

$$I_{Br} = \frac{4}{a_{Si}^2 \sqrt{3}\, d_{Br}} SF_{Br} \Phi_{Br} \left(1 - \exp \frac{-d_{Br}}{\lambda_{Br} \cos \theta}\right) \tag{2.21}$$

Based on a report by O'Leary *et al.*,[152] the total C–Si coverage of mixed allyl/methyl monolayers approaches >90%. To simplify the model, we assume 100% Si coverage by organic groups. That same report showed that allyl groups react with a surface at a faster rate than methyl groups and based on the molar fractions employed in the our Grignard solution (0.2 M Allyl, 0.8 M Methyl), we assume the ratio of allyl to methyl groups is 60:40.

Silicon photoelectrons will experience four different layers of attenuation on alkylbromide surfaces. The first is the oxide layer, d_{Ox}, which we treat as a uniform, ultrathin film. Next, are the allyl groups, with depth d_{Allyl} and a fractional coverage of $0.60 - \Phi_{Br}$, as Φ_{Br} groups are based on the existing allyl groups. Methyl groups cover the remaining Si(111) sites, a 0.40 fractional coverage, and depth d_{Me}. The final attenuation term is given by the brominated allyl groups where the height is sum of $d_{Br}/2$ and d_{Org}. The d_{ox} is divided by 2 as we assume the d_{Ox} extends to the center of the terminal group. Combining these attenuation terms yields eq 2.22:

$$I_{Si} = N_{Si}\, SF_{Si} \exp \frac{-d_{Ox}}{\lambda_{Si,Ox} \cos \theta} \times$$

$$\left((0.60 - \Phi_{Br}) \exp \frac{-d_{Allyl}}{\lambda_{Si,Org} \cos \theta} + \right.$$

$$\left. 0.40 \exp \frac{-d_{Me}}{\lambda_{Si,Org} \cos \theta} + \Phi_{Br} \exp \frac{-d_{Br}/2 - d_{Org}}{\lambda_{Si,Org} \cos \theta}\right) \tag{2.22}$$

When N_{Si} can be expressed as $8a_{Si}^{-3}$, eq 2.22 yields 2.23:

$$I_{Si} = 8a_{Si}^{-3}\, SF_{Si} \exp \frac{-d_{Ox}}{\lambda_{Si,Ox} \cos \theta} \times$$

$$\left((0.60 - \Phi_{Br}) \exp \frac{-d_{Allyl}}{\lambda_{Si,Org} \cos \theta} + \right.$$

$$\left. 0.40 \exp \frac{-d_{Me}}{\lambda_{Si,Org} \cos \theta} + \Phi_{Br} \exp \frac{-d_{Br}/2 - d_{Org}}{\lambda_{Si,Org} \cos \theta}\right) \tag{2.23}$$

Throughout, silicon's sensitivity factor $SF_{Si} = 0.283$. Si 2p photoelectrons have an attenuation length of $\lambda_{Ox} = 3.4(85)$ nm when traveling through the oxide layer that is less than 8 nm thick[197–198] and a $\lambda_{Si,Org} = 3.945$ nm through

the organic layer. The values d_{Allyl}, d_{Me}, and d_{Org} have depths of 0.17, 0.11, and 0.24 nm, respectively.

As depicted in Fig. 2.13, we describe the oxide layer as uniform, sub-monolayer depth. Equation 2.24 expounds on eq 2.13 and applies it to silicon oxide layer depths:

$$d_{Ox} = \ln\left(\frac{I_{Ox}N_{Si}\,SF_{Si}}{I_{Si}N_{Ox}\,SF_{Ox}} + 1\right)\lambda_{Si,Ox}\cos\theta \tag{2.24}$$

Number densities and sensitivity factors are combined into an experimentally derived, instrument-dependent, normalization factor $I_{Si}^{\infty}/I_{Ox}^{\infty}$ to yield 2.25.

$$d_{Ox} = \lambda_{Si,Ox}\cos\theta\,\ln\left(\frac{I_{Ox}I_{Si}^{\infty}}{I_{Si}I_{Ox}^{\infty}} + 1\right) \tag{2.25}$$

The term $I_{Si}^{\infty}/I_{Ox}^{\infty}$ for our PHI 5600 was determined to be 1.41, by taking the raw peak intensity of pure Si^0 over pure SiO_2 as measured sequentially on adjacent samples under otherwise identical sample conditions. To simplify the equation as written as eq 2.25, it is rewritten as eq 2.26.

$$d_{Ox} = 2.464\text{ nm }\ln\left(1.41\frac{I_{Ox}}{I_{Si}} + 1\right) \tag{2.26}$$

Oxide depths d_{Ox}, in nm, are now determined simply by plugging in the peak-intensity ratio of I_{Ox}/I_{Si} of any silicon sample.

Equations 2.21 and 2.23 are combined to form eq 2.27 that is solvable after determining d_{Ox} via eq 2.26. Though the negative exponents may be eliminated with rearrangement, eq 2.27 maintains Br-related terms in the numerator and Si-related terms in the denominator for consistency.

$$\frac{I_{Br}}{I_{Si}} = \frac{3^{-\frac{1}{2}}d_{Br}^{-1}}{2a_{Si}^{-1}}\frac{SF_{Br}}{SF_{Si}}\frac{\Phi_{Br}\left(1 - \exp\frac{-d_{Br}}{\lambda_{Br}\cos\theta}\right)}{\exp\frac{-d_{Ox}}{\lambda_{Si,Ox}\cos\theta}} \times$$
$$\frac{1}{(0.6 - \Phi_{Br})\exp\frac{-d_{Allyl}}{\lambda_{Si,Org}\cos\theta} + 0.4\exp\frac{-d_{Me}}{\lambda_{Si,Org}\cos\theta} + \Phi_{Br}\exp\frac{-\frac{d_{Br}}{2} - d_{Org}}{\lambda_{Si,Org}\cos\theta}} \tag{2.27}$$

The predicted I_{Br}/I_{Si} ratio of a monolayer of alkylbromide groups, or more specifically 60% of silicon sites based on available allyl groups, was determined to be 0.144. In practice, a Wolfram *Mathematica* worksheet was programmed with eq 2.27 and the experimental I_{Ox}/I_{Si} ratios yielded Φ_{Br} values,

which are reported in §3.3.1. The Φ_{Br} signal included the sum of the Br 3d peak areas located at 70.5 eV, which represented the signal coming from Br–C. The I_{Si} signal originated from Si^0 2p photoelectron peaks around 99 eV while the I_{Ox} employed the integrated the area under the peaks centered around 103 eV.

With Φ_{Br} determined, we can calculate Φ_N to determine the coverage of terminal amine groups converted from terminal bromides. An additional attenuation term for Φ_N is added to the denominator to account for the altered layer depth attenuating Si 2p photoelectrons. The fractional attenuation by the Φ_{Br} term is then subtracted by Φ_N due to the conversion of alkylbromide to alkylamine. Quantification of Φ_N in this manner necessitates the a priori determination of Φ_{Br} before amination. The NN density is expressed in the same way as similarly to N_{Br} in eq 2.21, $SF_N = 0.477$, and $\lambda_N = 3.8(12)$ nm. Equation 2.28 calculates coverage of alkylamine surfaces.

$$\frac{I_N}{I_{Si}} = \frac{3^{-\frac{1}{2}} d_N^{-1}}{2 a_{Si}^{-1}} \frac{SF_N}{SF_{Si}} \frac{\Phi_N \left(1 - \exp \frac{-d_N}{\lambda_N \cos \theta}\right)}{\exp \frac{-d_{Ox}}{\lambda_{Si,Ox} \cos \theta}} \frac{1}{\alpha + \beta + \gamma + \delta} \tag{2.28}$$

$$\alpha \equiv (0.6 - \Phi_{Br}) \exp \frac{-d_{Allyl}}{\lambda_{Si,Org} \cos \theta}$$

$$\beta \equiv 0.4 \exp \frac{-d_{Me}}{\lambda_{Si,Org} \cos \theta}$$

$$\gamma \equiv (\Phi_{Br} - \Phi_N) \exp \frac{-\frac{d_{Br}}{2} - d_{Org}}{\lambda_{Si,Org} \cos \theta}$$

$$\delta \equiv \Phi_N \exp \frac{-\frac{d_N}{2} - d_{Org}}{\lambda_{Si,Org} \cos \theta}$$

The fraction of purely allyl groups on the surface remains unchanged as amination only occurs at the alkylbromide species. Thus, $0.60 - \Phi_{Br}$ for the attenuation by allyl groups is still valid. Fractional surface coverages of alkylamine groups were again calculated from experimental I_N/I_{Si} ratios with *Mathematica* and reported in §3.4.2. Table D.1 contains the sensitivity factors and relevant attenuation lengths for Si 2p, Br 3d, and N 1s photoelectrons.

2.4.3 Modeling Perylene-functionalized substrates on Si(111) Surfaces

The model used for interpreting the photoelectron spectra of perylene mono-layers on oxidized Si(111) substrates resembles the one utilized in the previous section for covalent alkyl monolayers. Figure 2.15 presents our model of the physical arrangement of silicon, silicon oxide, phenylaminosilane, perylene, and terminal imide. The first assumption we make with this model is
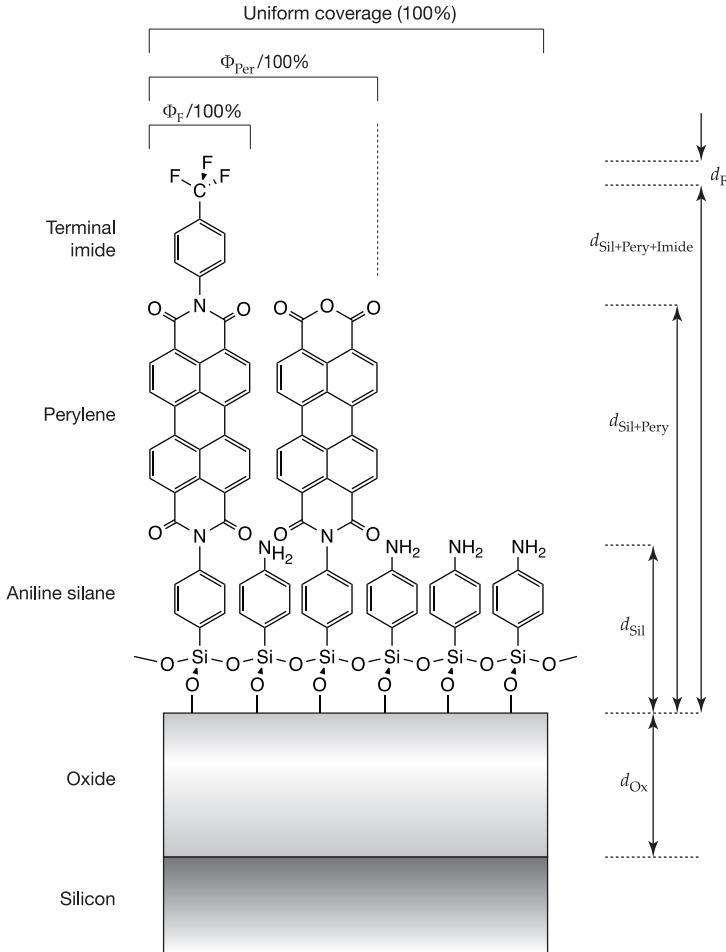
Figure 2.15   Cartoon model of the physical arrangement of silicon, silicon oxide, aniline, perylene, and terminal functional groups. Height or thickness values include the thickness of the chemical oxide d_{Ox}, the thickness of the aniline silane d_{Sil}, the thickness of an aniline–perylene backbone $d_{Sil+Pery}$, the thickness of the backbone with an attached imide that does not include terminal fluorines $d_{Sil+Pery+Imide}$, and the thickness of a fluorine atom layer d_F. We assume a complete coverage of the oxide and aniline silane layers, or a coverage value of unity (100%). Fractional coverage of the perylene layer is Φ_{Per}, and the coverage of the complete imide is Φ_F.

the that the coverage of the oxide is uniform and >1 ML deep. Similarly, we assume the phenylaminosilane layer covering the oxide is also uniform and is ≥1 ML. The depths, d, of the various organic layers are calculated in the *WebMO* front end to *Gaussian 09* (Gaussian, Inc., Wallingford CT, 2009).

We utilized molecular mechanics calculations at the AM1 level of theory to approximate the molecular distances needed in Fig. 2.15. Higher levels of theory would certainly yield more accurate values, but such values' accuracies likely exceed the accuracy of an overlayer model itself when considering fitting uncertainties, practical surface roughness, etc.

Figure 2.16 relays d values of interest. $Si_4O_6H_3$ clusters mimic the behavior of covalent silane surface attachment where the top silicon atom as shown in taupe represents a silane silicon atom and the lower three silicon atoms represent the surface of chemically oxidized Si(111). We define the depth of a silane layer, d_{Sil}, as the distance from the nitrogen's nucleus to the plane containing the three silicon atoms in the $Si_4O_6H_3$ cluster that serve as a proxy for silicon surface atoms. Importantly, a vector describing the nitrogen-to-silicon-center-of-mass distance is parallel to both the Si–C bond and to the C–N aniline bonds. In other words, we are considering the aniline moiety to "stand" normal to the silicon surface. The AM1 calculation determined d_{Sil} = 0.831 nm.

For the covalent incorporation of perylenes at aniline-terminated surfaces, we defined $d_{Sil+Pery}$ from the same plane containing the proxy silicon surface atoms. In defining the distance to the carbonyl oxygen atoms, $d_{Sil+Pery}$ considers only the component of the distance to the oxygen nuclei that is aligned with a vector defined by the aniline (lower imide) C–N bond orientation. In other words, we assume that the perylene stands upright on the silicon surface due to roughly 120° bond angles around the imide nitrogen and a C–N aniline or imide bond that is approximately oriented at a surface normal angle. The AM1 calculation determined $d_{Sil+Pery}$ = 1.99 nm.

For the ester surface **4a** and the imide surface **5a** (the numbering of these surfaces are specific to this study and are assigned in Figure 4.1 of §4.2), we calculated the distance of the fluorine nucleus to the proxy silicon surface atoms (again oriented parallel to the direction of the C–N bond vector). As the overlayer model considers the thickness of the fluorine atoms in the overlayer, d_F, a fluorine-to-surface distance would be defined as $d_{Sil+Pery+Ester} + \frac{1}{2}d_F$ and $d_{Sil+Pery+Imide} + \frac{1}{2}d_F$ with values given in Fig. 2.16. Importantly, we calculate d_F in the same manner as in §2.4.2. For a covalent radius r_F = 0.064 nm,[199] and $d_F = 2\sqrt[3]{\pi/6}\, r_F$ = 0.103 nm. Subtraction yields d_{Pery} = 1.16 nm, d_{Ester}= 0.45 nm, and d_{Imide} = 0.58 nm. The ester calculation assumes a carbon chain standing upright which may introduce an error in d_{Ester}.

While AM1 calculations yield height terms for the molecular species, we again derive the height or thickness of an interfacial oxide, d_{Ox}, from the

1a model   **4a** model   **5a** model
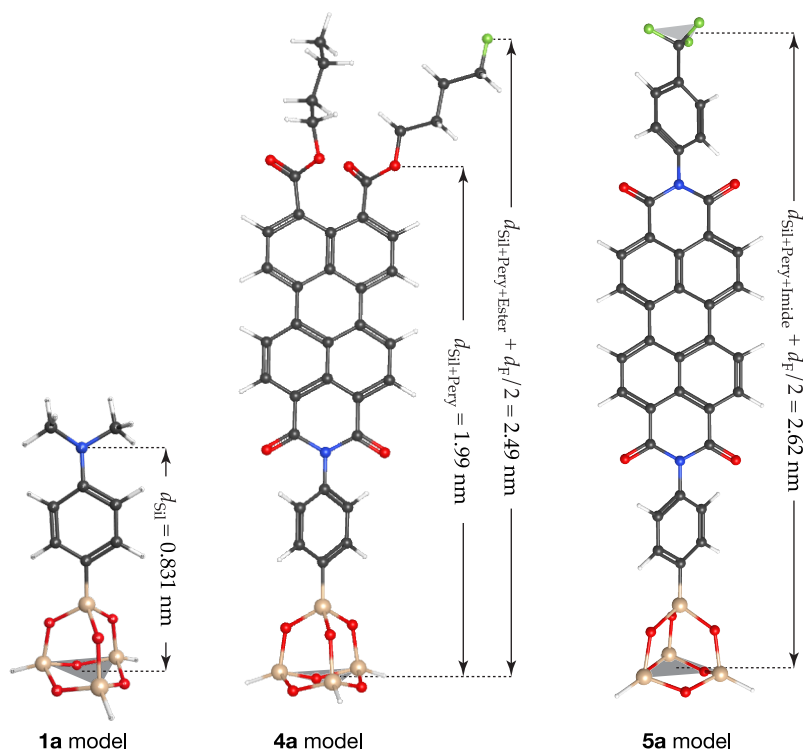
Figure 2.16   AM1 calculation results for sample molecules that elucidate distances and/or thicknesses of molecular species employed in the overlayer model.

experimental I_{Ox}/I_{Si} and eq 2.26. Before considering partial surface coverages by derivatized-perylene species, the model accounts for the coverage of the phenylaminosilane. Modeled as a monolayer of fixed height and variable coverage, we consider the intensity of the N 1s feature in the silane to result from a uniform coverage of nitrogen atoms, yielding eq 2.29 that utilizes identical SF_N, d_N, and λ_N values from the previous section.

$$I_N = \frac{4}{a_{Si}^2 \sqrt{3}\, d_N} SF_N \Phi_N \left(1 - \exp\frac{-d_N}{\lambda_N \cos\theta}\right) \qquad (2.29)$$

The intensity of the bulk silicon signal is attenuated by the uniform coverage of the oxide layer and, in a fractional coverage model, by a fractional coverage of the phenylaminosilane monolayer. The combination of these two attenuations yields eq 2.30 for I_{Si} where all silicon parameters are taken from §2.4.2.

$$I_{Si} = 8a_{Si}^{-3} SF_{Si} \exp \frac{-d_{Ox}}{\lambda_{Si,Ox} \cos \theta} \left(1 - \Phi_N + \Phi_N \exp \frac{-d_N/2 - d_{Sil}}{\lambda_{Si,Org} \cos \theta}\right) \qquad (2.30)$$

Combining eqs 2.29 and 2.30 yields eq 2.31 for the I_N/I_{Si} ratio.

$$\frac{I_N}{I_{Si}} = \frac{3^{-\frac{1}{2}}d_N^{-1}}{2a_{Si}^{-1}} \frac{SF_N}{SF_{Si}} \frac{\Phi_N \left(1 - \exp \frac{-d_N}{\lambda_N \cos \theta}\right)}{\exp \frac{-d_{Ox}}{\lambda_{Si,Ox} \cos \theta} \left(1 - \Phi_N + \Phi_N \exp \frac{\frac{-d_N}{2} - d_{Sil}}{\lambda_{Si,Org} \cos \theta}\right)} \qquad (2.31)$$

Experimental I_N/I_{Si} ratios come from the integrated area of the total N 1s feature and the area of the Si 2p feature corresponding only to the silicon substrate, Si^0. For ten aniline-functionalized samples of surface **1a**, the phenylaminosilane surface, $I_{N\,1s}/I_{Si\,2p} = 0.35 \pm 0.10$, which corresponds to $\Phi_N = 1.4 \pm 0.2$. Thus, we interpret the physical model of aniline coverage in surface **1a** as a "complete" monolayer that may in fact contain domains of multilayer coverage. We do not further interpret a physical meaning for this coverage beyond recognition that subsequent coverage models for surfaces **4a** and **5a** will assume a complete, monolayer coverage of by the phenylaminosilane.

As discussed in §4.5.1, the fractional coverage of PTCDA groups was quantified by conversion of the terminal anhydride to a fluorobutylester/butylester pair, surface **4a**. The high conversion efficiency of the reaction and bright F 1s photoelectron feature enables perylene quantification by XPS. I_F is given in eq 2.32 where d_F was described above, $SF_F = 1.00$, and $\lambda_F = 2.05$ nm, a literature value reported for fluorinated polymers.[200]

$$I_F = \frac{4}{a_{Si}\sqrt{3}\,d_F} SF_F \Phi_F \left(1 - \exp \frac{-d_F}{\lambda_F \cos \theta}\right) \qquad (2.32)$$

Regarding the silicon attenuation, we assume that the activation of a terminal anhydride on surface **2a** to form an acid-ester moiety and the subsequent reaction with 1-fluoro-4-bromobutane reacts with exposed perylenes to completion. That is to say, we assume complete conversion of perylenes on **2a** to ester species of surface **4a**. As far as the overlayer model is concerned, complete conversion means that there are no unreacted perylene anhydride surface species remaining, and $\Phi_F = \Phi_{Pery}$ for further equations utilizing prior coverages of perylene anhydrides. Thus, eq 2.33 describes the Si 2p photoelectron intensity for surface **4a**.

$$I_{Si} = 8a_{Si}^{-3} \, SF_{Si} \, \exp \frac{-d_{Ox}}{\lambda_{Si,Ox} \cos \theta} \, \exp \frac{-d_{Sil}}{\lambda_{Si,Org} \cos \theta} \times$$

$$\left(1 - \Phi_F + \Phi_F \exp \frac{\frac{-d_F}{2} - d_{Ester} - d_{Pery}}{\lambda_{Si,Org} \cos \theta} \right) \tag{2.33}$$

Combining eqs 2.32 and 2.33 yields eq 2.34 for the relationship between fluorine and bulk silicon photoelectron features for surface **4a**.

$$\frac{I_F}{I_{Si}} = \frac{3^{-\frac{1}{2}} d_F^{-1} \, SF_F}{2a_{Si}^{-1} \, SF_{Si}} \frac{\Phi_F \left(1 - \exp \frac{-d_F}{\lambda_F \cos \theta} \right)}{\exp \frac{-d_{Ox}}{\lambda_{Si,Ox} \cos \theta} \exp \frac{-d_{Sil}}{\lambda_{Si,Org} \cos \theta}} \times$$

$$\frac{1}{\left(1 - \Phi_F + \Phi_F \exp \frac{\frac{-d_F}{2} - d_{Ester} - d_{Pery}}{\lambda_{Si,Org} \cos \theta} \right)} \tag{2.34}$$

Inputting an average I_F/I_{Si} ratio of 0.13 ± 0.01, measured across four samples, and an average oxide thickness of 1.1 ± 0.1 nm, the coverage by surface **4a** was determined to be 0.15 ± 0.02. This coverage is ascribed to the coverage of total anhydride-terminated perylene groups, Φ_{Pery}, attached to the surface.

The analysis of surface **5a** bears many similarities to the quantification of surface **4a**. The chief difference is that we are now looking at a terminal $-CF_3$ group attached by way of a terminal phenylimide. If the surface coverage of **5a** were to be the same as **4a**, the F 1s signal should be 3× the signal from a single fluorine atom, barring changes in the organic layer height and the oxide depth. (Note that this 3× value is added to the numerator and effects a change to the sign of the square root.) The I_F/I_{Si} ratio for surface **5a** is given in eq 2.35.

$$\frac{I_F}{I_{Si}} = \frac{3^{+\frac{1}{2}} d_F^{-1} \, SF_F}{2a_{Si}^{-1} \, SF_{Si}} \frac{\Phi_F \left(1 - \exp \frac{-d_F}{\lambda_F \cos \theta} \right)}{\exp \frac{-d_{Ox}}{\lambda_{Si,Ox} \cos \theta} \exp \frac{-d_{Sil}}{\lambda_{Si,Org} \cos \theta}} \times$$

$$\frac{1}{\left(1 - \Phi_{Pery} + \left(\Phi_{Pery} - \Phi_F \right) \exp \frac{-d_{Pery}}{\lambda_{Si,Org} \cos \theta} + \Phi_F \exp \frac{\frac{-d_F}{2} - d_{Ester} - d_{Pery}}{\lambda_{Si,Org} \cos \theta} \right)} \tag{2.35}$$

Of four surface **5a** samples analyzed, the experimental I_F/I_{Si} ratio = 0.36 ± 0.04 with an average oxide thickness, d_{Ox} = 1.91 nm. Assuming that Φ_{Pery} is 0.15, previously calculated from eq 2.34, then Φ_F = 0.10 ± 0.02 or ~10% of Si(111) atop sites are functionalized with surface **5a**.
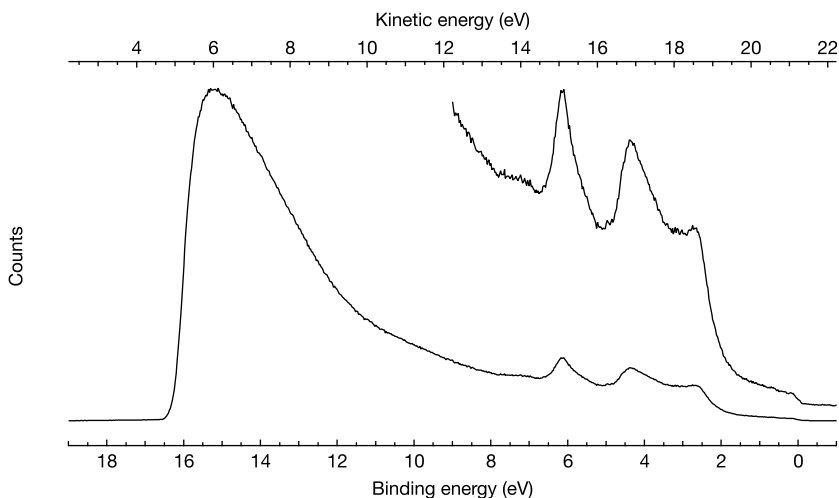
Figure 2.17   Ultraviolet photoelectron spectrum of sputter-cleaned gold foil. The high kinetic energy inset has been magnified by 5×.

2.5   Ultraviolet Photoelectron Spectroscopy

Ultraviolet photoelectron spectroscopy (UPS) experiments utilized the same photoelectron system described in the XPS section. UPS is primarily employed to probe valence electrons at the surface of samples and utilized to determine the surface work function, Φ_S, Fermi level, E_F, and the valence band maximum, E_{VBM}, of metals and semiconductors. UPS employs ultraviolet radiation which is absorbed by valence-state electrons at the surface. Provided enough energy, these electrons are emitted with a kinetic energy equal to $h\nu$ (21.22 eV) minus the binding energy, the same as eq 2.1. Compared to soft x-rays, the energy of ultraviolet light is significantly lower, thus, the kinetic energy of ejected electrons is substantially lower than core-level photoelectrons. For this reason, the attenuation lengths electrons emitted UPS experiments are almost an order of magnitude shorter than for XPS. The analysis depth for a typical UPS experiment is ~2 − 3 nm. Consequently, organic contamination on surfaces will strongly attenuate low-energy electrons and surfaces require in-situ cleaning or thorough sample rinsing before analysis. A UP spectrum for sputter-cleaned Au is presented in Fig. 2.17.

At the high-kinetic-energy side of the UP spectrum, peaks here represent photoelectrons emitted from directly from valence electrons. The sharp edge at the highest **KE** is given by electrons coming directly from the Fermi level E_F. In the case of semiconductors, this edge represents ($E_F − E_{VBM}$) or the energetic "distance" from the sample's Fermi level energy to the valence band maximum energy. Located at the low-kinetic-energy end of the spectrum is

the onset of photoemission or the secondary electron cutoff energy. These are valence band electrons that have experienced significant inelastic scattering on the way to the surface, yielding an increasing background in addition to the primary photoelectrons. The electrons right at the leading edge of the secondary electron cutoff have just enough energy overcome the local vacuum energy level. When in electrical contact, the Fermi levels of the spectrometer and sample equilibrate. Using a metal sample, such as sputter-cleaned Au, the Fermi level, $\mathbf{E_F}$, of the spectrometer is calibrated to 0 eV, in terms of binding energy. With the instrument properly calibrated, we can determine the surfaces work function, $\mathbf{\Phi_S}$, or the distance of the sample's Fermi level to the vacuum level, $\mathbf{E_{vac}}$, with eq 2.36.

$$\mathbf{\Phi_S} = \mathbf{E_{He\,I}} - \mathbf{E_{SEC}} \qquad (2.36)$$

In eq 2.36 $\mathbf{E_{He\,I}} = h\nu = 21.22$ eV, the energy of the He 1α line (or He I), and $\mathbf{E_{SEC}}$ is the secondary electron cutoff value, after fitting to the leading edge to the x-axis. $(\mathbf{E_F} - \mathbf{E_{VBM}})$ is fit by a linear-regression of high kinetic energy edge of the trace to the x-axis. $\mathbf{E_{VBM}}$, or which is the opposite sign of ionization potential, IP, the distance from $\mathbf{E_{vac}}$ to $\mathbf{E_{VBM}}$, is then calculated with eq 2.37.

$$\mathbf{E_{VBM}} = \mathbf{E_F} - (\mathbf{E_F} - \mathbf{E_{VBM}}) \qquad (2.37)$$

While eq 2.37 may read like a tautology, the value within the parentheses is determined from fitting the high kinetic energy edge and $\mathbf{E_F}$ is derived from the $\mathbf{\Phi_S}$ after changing the sign. In the absence of inverse photoelectron spectroscopy, eq 2.38 yields the location of the conduction band maximum$\mathbf{E_{CBM}}$, or the negative of electron affinity, EA, the distance from $\mathbf{E_{vac}}$ to $\mathbf{E_{CBM}}$.

$$\mathbf{E_{CBM}} = \mathbf{E_{VBM}} + \mathbf{E_g} \qquad (2.38)$$

In eq 2.38, $\mathbf{E_g}$ is the band gap energy of the sample. Figure 2.18 presents a general band-energy diagram that relates some of the previous equations and values.

2.5.1 Experimental Settings and UPS Procedures

He 1α (21.22 eV) radiation was provided by a helium-gas discharge UVS 40A2 (PREVAC, Poland) UV source and UV40A power supply. A leak-valve allowed ~15 mtorr of ultra-high purity (UHP) He gas into the UV source and the power was maintained at 80 mA to ensure a high ratio of He I to He
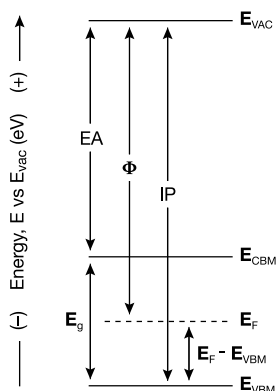
Figure 2.18 Generic band-energy diagram to illustrate the definitions and locations of the electron affinity, *EA*, work function, **Φ**, ionization potential, *IP*, band gap, E_g, conduction band minimum, CBM, valence band maximum, VBM, vacuum level, E_{vac}, conduction band minimum, E_{CBM}, Fermi level, E_F, and valence band maximum, E_{VBM}.
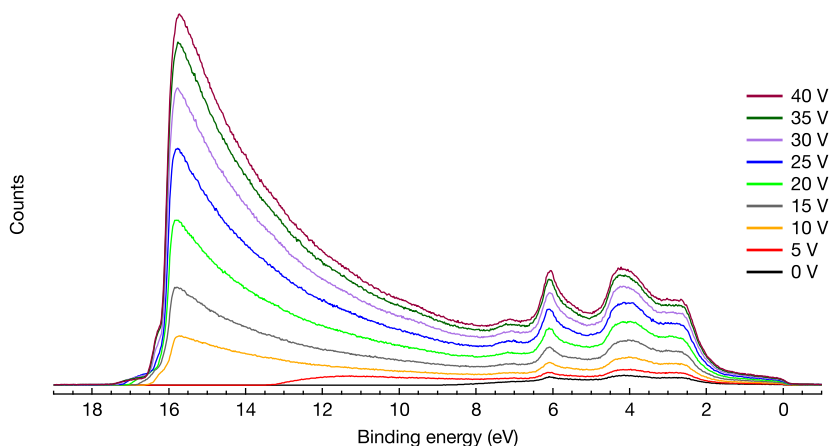
Figure 2.19 Ultraviolet photoelectron spectrum of sputter-cleaned gold foil as a function of the bias potential applied to the sample.

II radiation. Differential pumping of the UV source helped keep a majority of helium gas from the analysis chamber. During UPS measurements, the base-pressure of the chamber was maintained $<3 \times 10^{-8}$ Torr.

Samples were positioned at $0°$ with respect to the surface normal toward the analyzer during UPS measurements. This geometry ensures that with the electric field oriented toward the analyzer, the majority of low-energy photoelectrons are accelerated into the analyzer. The low-energy, secondary electrons used to determine the surface work function require additional kinetic energy to overcome the spectrometer work function. Applying a potential bias to the sample linearly increased the energy of all electrons within the sample. Figure 2.19 presents the gold UP spectra at different biases. Increasing the negative bias increased the secondary electron counts

while alignment of $\mathbf{E}_{SEC}$ yielded a consistent $\mathbf{\Phi}_{Au}$ value of 5.1 eV after –20 V. To limit the number of photoelectrons allowed into the detector during UPS, the physical aperture was set to "2" and the lens area was set to minimum in the software, which probed a physical analysis area with a diameter of 150 μm. In some cases where counts exceeded 1 million CPS, the multiplier voltage was stepped down. High-resolution UP spectra utilized a pass energy of 5.85 eV, a 0.025 eV step size, and a 50 ms dwell time.

2.6   Infrared Spectroscopy

All infrared spectroscopy experiments utilized a Bruker Vertex 70 (Bruker, Billerica MA) equipped with a DLaTGS detector and a liquid nitrogen cooled MCT detector. Blackman-Harris 3-term apodization and a zero-filling factor of value of 2 smoothed the infrared spectra. Dry nitrogen gas containing <0.5% O_2 purged the accessory, detector, and source compartments (Parker Balston model N2-45, Parker Hannifin, Lancaster, NY).

For powdered, molecular reference samples, a Golden Gate Attenuated Total Reflectance (ATR) accessory (Specac, UK) was utilized. The ATR accessory contained a diamond plate surface where a single 45° reflection probed the sample. Backgrounds were taken on the clean diamond plate surface and data was collected with a 512-scan average at 4 cm^{-1}. ATR experiments utilized the DLaTGS detector and a source aperture of 8 mm, which provided a high signal to noise ratio.

To probe the species bound to silicon surfaces after various functionalization steps, transflection infrared spectroscopy was employed. Near the Brewster angle, when only p-polarized light is utilized, the technique can be described as a "double transmission" experiment. The p-polarized light is transmitted through the sample, reflected off a mirror beneath the sample, and transmitted back through the silicon.[201–205] At high angles of incidence, infrared modes oriented perpendicular to the surface strongly interact yielding high absorption values compared to parallel modes along the surface. For example, Si–H bonds on Si(111) stand completely perpendicular to the surface and by increasing the angle of incidence of p-polarized light, the signal at 2083 cm^{-1} is concomitantly increased.

Transflection infrared spectroscopy of functionalized silicon surfaces employed an AutoSeagull Variable Angle Reflection Accessory (Harrick Scientific, Pleasantville, NY). The reduced light throughput by the accessory necessitated the use of the MCT detector for its increased sensitivity compared to the DLaGTS detector. We utilized an aperture size of 1.5 mm which yielded the maximum signal before saturating the detector. Figure 2.20 illustrates the beam path through the accessory and the sample. Briefly, light is p-polarized with a KRS-5 wire-grid polarizer prior to entering the AutoSeagull. The light is then reflected off multiple mirrors which vary the
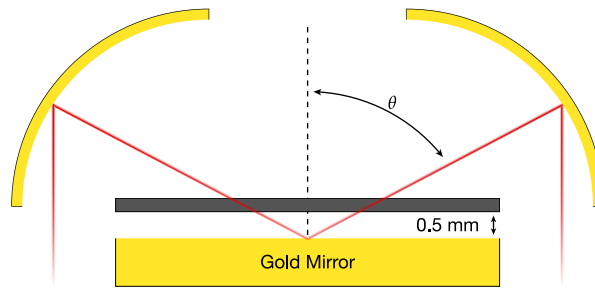
Figure 2.20   Optical geometry of the Harrick Autoseagull utilized in transflection infrared spectroscopy. The p-polarized light is reflected and focused by a gold parabolic mirror, transmitted through the silicon sample, reflected from the flat gold mirror beneath the sample, transmitted back through the silicon, reflected from the second parabolic mirror, and detected. θ is the angle of incident light and the 0.5 mm represents the spacers utilized to hold silicon above the mirror. .

light's incident angle before reaching a parabolic mirror which focuses the light onto the gold mirror beneath the sample. The p-polarized infrared light is almost entirely transmitted through the silicon at the Brewster angle of 74° with respect to the surface normal. At these shallow angles, >95% of the light is reflected before being transmitted back through the silicon and detected. Moreover, ~0.5 mm spacers were placed in between the silicon and gold mirror to further reduce interference fringes caused by constructive and deconstructive interference.[201] The gold mirror and spacers were excluded in transflection measurements on TiO_2 surfaces. Infrared light passes through the TiO_2 before being reflected by the layer of FTO beneath the TiO_2 film.[206]

2.7   Time-Resolved Microwave Photoconductivity Spectroscopy

Contactless, transient (time-resolved) microwave photoconductivity spectroscopy (TRMPS) quantified the lifetime of photogenerated charge carriers for the functionalized silicon samples. TRMPS measurements were conducted with an in-house fabricated instrument utilizing K_a-band microwave radiation. Photogenerated charge carriers in silicon were yielded by a 10 ns, 905 nm laser diode pulse. The diode power was adjusted to generate ~10^{11} photons per pulse as measured at a calibrated photodiode in its recommended, reverse-bias circuit (Thorlabs, FDS100-Cal) over a ~0.05 cm^2 area. An oscilloscope recorded changes in microwave power at a finline detector as a function of time, and a custom LabVIEW-based program fit the power signal to a single-exponential-decay function with a y-axis offset to yield the characteristic carrier recombination lifetime, τ.

Transient photoconductivity measures the change in reflected microwave power. The microwaves reflected from and incident upon the sample yield a ratio related to the dielectric function of the material. As charge-carriers are generated under illumination the dielectric function is concomitantly altered yielding a change in the microwave reflectivity of the sample.[110,128,207] By using high electronic quality, intrinsic, single crystal silicon, the majority of reflected microwaves are the result of excess free electrons in the conduction band and holes in the valence band effected by illumination. Recombination of thermally generated free-electrons are not considered as their recombination velocities happen on much shorter timescales.

Higher level injection is not considered in this model as it occurs at at much shorter time scales, roughly 1 μs. To ensure that the defect-dense edges of diced silicon samples do not contribute to the rate of recombination, all samples were diced so that the distance between the illumination spot and the edge of the silicon surface was at least $3\sqrt{D\tau} \approx 5.6$ mm, based on a carrier diffusivity, $D = 35$ cm^2 s^{-1}, and a maximum characteristic lifetime of 1 ms. For the resulting pseudo-one-dimensional system, eq 2.39 relates the experimentally derived carrier lifetime, τ, to the bulk recombination lifetime, τ_{Bulk}, the wafer thickness, d (unrelated to the term in the substrate overlayer model), and the surface recombination velocity (SRV), S, for photogenerated carriers.

$$\frac{1}{\tau} = \frac{1}{\tau_{Bulk}} + \frac{2S}{d} \tag{2.39}$$

For intrinsic silicon, where the concentrations of holes and electrons are equal, $\tau_{Bulk} \gg \tau$, which simplifies eq 2.39 to eq 2.40.

$$S = \frac{d}{2\tau} \tag{2.40}$$

The τ term is determined by fitting the experimentally acquired microwave decay to a single-exponential function with a y-axis offset. More than 100 scans were averaged for each sample before fitting the raw data to a single exponential.

CHAPTER 3

SYNTHESIS AND CHARACTERIZATION OF ALKYLAMINE-FUNCTIONALIZED SI(111) FOR PEROVSKITE ADHESION WITH MINIMAL INTERFACIAL OXIDATION OR ELECTRONIC DEFECTS

Portions adapted from:

Abstract

We investigated synthetic strategies for the functionalization of Si(111) surfaces with organic species containing amine moieties. We employed the functionalized surfaces to chemically "glue" perovskites to silicon with efficient electron transfer, and minimal oxidation leading to deleterious recombination at the silicon substrate. A two-step halogenation-alkylation reaction produced a mixed allyl-methyl monolayer on Si(111). Subsequent reactions utilized multiple methods of brominating at the allyl double bond including reaction with HBr in acetic acid, HBr in THF and molecular bromine in dichloromethane. Reaction with ammonia in methanol effected conversion of the bromide to the amine. X-ray Photoelectron Spectroscopy (XPS) quantified chemical states and coverages, transient-microwave photoconductivity ascertained photogenerated carrier lifetimes, Atomic Force Microscopy (AFM) quantified perovskite-silicon adhesion, and nonaqueous photoelectrochemistry explored solar-energy-conversion performance. The HBr bromination followed by the amination yielded a surface with ~10% amine sites on the Si(111) with minimal oxide and surface recombination velocity values below 120 cm s^{-1} following extended exposures to air. Importantly, conversion of amine sites to ammonium and deposition of methylammonium lead halide via spin coating and annealing did not degrade carrier lifetimes. AFM experiments quantified adhesion between perovskite films and alkylammonium-functionalized or native-oxide silicon surfaces. Adhesion forces/interactions between the perovskite and the alkylammonium-functionalized film was comparable to the interaction between the perovskite and native-oxide silicon surface. Photoelectrochemistry of perovskite thin films on alkylamine-functionalized n$^+$-Si showed significantly higher V_{oc} than n$^+$-Si with a native oxide when in contact with a nonaqueous ferrocene$^{+/0}$ redox couple. We discuss the present results in the context of utilizing molecular organic recognition to attach perovskites to silicon utilizing organic linkers so as to inexpensively modify silicon for future tandem-junction photovoltaics.

3.1   Introduction

Herein, we investigate the passivation and functionalization of monolayers on Si(111) to introduce terminal ammonium functionality for the purpose of chemically "gluing" perovskites to the silicon and characterize the adhesion of the perovskite film to silicon and its resulting photoelectrochemical performance. We utilize a two-step halogenation-alkylation procedure to initially functionalize the silicon surface.[104] Alternative functionalization strategies with broad functional group tolerance exist,[134,138–139,154–155,208] however the two-step halogenation-alkylation demonstrates excellent passivation properties with low surface-recombination velocities following prolonged air exposures.[209] Mixed-monolayers utilizing methyl and allyl groups en-

ables a high coverage of silicon sites for effective passivation with a chemical handle for further functionality.[151−152,165,167,169,210] We explore functionalization strategies to brominate the double bond on a mixed allyl/methyl-functionalized Si(111) surface prepared by a two-step halogenation-alkylation, and subsequently aminate the alkylbromide site for perovskite deposition. The ultimate goal involves producing an alkylammonium-functionalized silicon surface that demonstrates minimal oxidation, strong perovskite-silicon adhesion, and good electronic properties. X-ray photoelectron spectroscopy (XPS) experiments and substrate-overlayer-coverage models quantified interfacial silicon oxidation and fractional surface coverage of bromine and nitrogen species. As the morphology and arrangement of bromine and ammonium groups on the surface is not quantified by XPS, we include a sensitivity study to consider how variations in values employed in the substrate-overlayer equations may affect our interpretation of the photoelectron results. Transflection infrared spectroscopy verified the presence of allyl and of methyl groups on the mixed monolayer surfaces. Time-resolved microwave photoconductivity spectroscopy (TRMPS) measurements ascertained the carrier recombination lifetimes and surface recombination velocity (SRV) values of photogenerated carriers in the silicon. While we are not concerned with photogenerated carrier lifetimes in bulk silicon as it directly relates to tandem-junction solar cells per se, SRV values are an important proxy for the density of defect states at the silicon surface that promote deleterious recombination at the silicon/perovskite interface. Adhesion force techniques determined the adhesion force between $MAPbI_3$ films and silicon substrates. Photoelectrochemistry measured the current density–potential, J–E, curves of perovskite thin films deposited on degenerately doped n^+-Si that served as the ohmic back contact to the perovskite. Photoelectrochemical experiments contrasted the electron transfer and recombination of charge-carriers at the back contact as a function of the respective silicon surface chemistry.

3.2   Experimental

3.2.1   Materials and Chemicals

The experiments utilized single-side polished, 525 ± 25 μm thick, 1–5 Ω cm resistivity, phosphorous-doped n-Si(111) (EL-CAT Inc., Ridgefield Park, NJ) for X-ray photoelectron spectroscopy. The photoconductivity experiments used double-side polished, 525 ± 25 μm thick, >3000 Ω cm resistivity, intrinsic silicon, i-Si(111), (EL-CAT Inc.). Photoelectrochemistry and AFM experiments employed single-sided polished, 525 ± 15 μm thick, degenerately arsenic doped, ≤0.006 Ω cm resistivity wafers (Wafer Works Corp.) that are termed n^+-Si(111) below.

Reagents for etching and cleaning silicon included the RCA Standard Clean–1 (SC–1 or RCA–1) solution, the RCA Standard Clean–2 (SC–2 or RCA–

2) solution, aqueous hydrogen fluoride, and aqueous ammonium fluoride. *Warning, aqueous hydrogen fluoride is an acute poison that is toxic at even small amounts and limited exposures*. A Millipore Milli-Q system provided 18 MΩ cm resistivity water for all water requirements. A solution containing five volume-parts water, one part $H_2O_{2(aq)}$ (35 wt %, Alfa Aesar) and one part $NH_4OH_{(aq)}$ (28% NH_3, Alfa Aesar) comprised the SC–1 solution. The SC–2 solution consisted of 5 volume-parts water, one part hydrogen peroxide, and one part hydrochloric acid (12 M, ACS grade, Alfa Aesar). The $HF_{(aq)}$ was diluted to 6 M from a commercial stock solution (49%, electronic grade, Transene Company Inc., Danvers, Massachusetts). The ammonium fluoride solution (40% in water, electronic grade, Transene) was sparged with argon (ultra-high purity, Airgas) for 30 minutes prior to use. A stream of argon dried the silicon samples as needed.

Chemicals employed for the two-step halogenation-alkylation functionalization of silicon surfaces included liquid bromine (99.8%, Alfa Aesar) that was degassed via three freeze-pump-thaw cycles on a diffusion-pump-equipped, argon-purged Schlenk line with a base pressure below 1×10^{-3} torr and stored over degassed P_4O_{10} (99.9925%, Alfa Aesar). Tetrahydrofuran (THF, 99.8%, anhydrous, Alfa Aesar,) was degassed prior to experiments via three freeze-pump-thaw cycles on the Schlenk line and stored over activated 3 Å molecular sieves (Alfa Aesar). Methylmagnesium chloride (CH_3MgCl, 3 M in THF, Alfa Aesar) and allylmagnesium chloride (CH_2CHCH_2MgCl, 2 M in THF, Sigma Aldrich) were diluted to 1 M in anhydrous THF during experiments. Molecular sieves further maintained "dry" methanol (99.9% min, semiconductor grade, Alfa Aesar) and glacial acetic acid (AcOH, 99.7%, Alfa Aesar). Benzoyl Peroxide (99.7% dry mass, wet with 25% water, Alfa Aesar) was dried under vacuum.

Chemicals utilized for the functionalization of the allyl double bond included dichloromethane (DCM, 99.5%, Pharmco-Apper), hydrogen bromide (33 wt % in glacial acetic acid, Alfa Aesar), and glacial acetic acid. Dichloromethane and glacial acetic acid were dried over activated molecular sieves and the Br_2/DCM and HBr/AcOH solutions were degassed immediately preceding use via three freeze-pump-thaw cycles.

Chemicals employed for the amination of the alkylbromide included ammonia (2 M in methanol, Alfa Aesar) and sodium hydroxide (98.5%, Acros). Three freeze-pump-thaw cycles removed dissolved oxygen from the ammonia solution.

Chemicals for the deposition of methylammonium lead iodide included $HCl_{(aq)}$ (11.6 M, Alfa Aesar, as received), lead iodide (lead(II) iodide, 99.9985% metals basis, Alfa Aesar) and methylammonium iodide. Reaction of 10 mL $CH_3NH_{2(aq)}$ (21 M, Alfa Aesar, as received) with 20 mL of HI(aq) (10 M, Alfa Aesar, as received) at 25 °C with stirring for 2 h, followed by solvent removal by rotary evaporation produced methylammonium iodide. Washing

the crude methyl ammonium iodide product three times with diethyl ether (99+%, spectrophotometric grade, inhibitor free, Alfa Aesar, as received) followed by solvent removal on the Schlenk line afforded ~15 g of methylammonium iodide. Additional solvents for the spin deposition of methylammonium lead iodide included N,N-dimethylformamide (DMF, ≥99.8%, Certified ACS, Fisher Chemical).

Chemicals for the photoelectrochemistry included lithium perchlorate (battery grade, Sigma-Aldrich), ferrocene (Cp_2Fe, bis(cyclopentadienyl)iron(II), 99%, Sigma-Aldrich), ferrocenium hexafluorophosphate (Cp_2FePF_6, bis(cyclo pentadienyl)iron(III)hexafluorophosphate, 97%, Aldrich), and 1,1,2,2-tetrach loroethane (98+%, Alfa Aesar). Ferrocene was purified by vacuum sublimation while ferrocenium hexafluorophosphate was purified via recrystallization and further degassed under vacuum. Lithium perchlorate was used as received. Photoelectrochemical experiments utilized a ferrocene$^{+/0}$ solution consisting of 100 μM of ferrocene, ~5 μM ferrocenium, and 1 M $LiClO_4$ in "dry" tetrachloroethane. The ferrocene$^{+/0}$ solution was stored over activated molecular sieves for several days prior to use. A series of freeze-pump-thaw cycles on the Schlenk line and storage over activated molecular sieves prepared the tetrachloroethane at least one week prior to use.

Dicing, oxidation, and etching steps preceded wafer functionalization. The SSP n-Si(111) wafers for photoelectron spectroscopy experiments were diced into ~0.3 cm^2 pieces, while wafers for all other experiments were diced in to 2–3 cm^2 pieces. Initial cleaning consisted of a 10-min. exposure to the SC-1 solution at 77 °C, a water rinse, a 10 s submersion in 6 M $HF_{(aq)}$, copious rinsing in water, and drying under argon. Samples subsequently cleaned via a 10 min submersion in the SC–2 solution at 77 °C, rinsing in water, a 10 s submersion in 6 M $HF_{(aq)}$, a copious water rinse, and drying under argon. Following the second HF exposure, a four-minute immersion in argon-sparged $NH_4F_{(aq)}$, rinsing with H_2O, and drying under argon effected large hydrogen-terminated terraces on the Si(111) surface. Following the ammonium fluoride etch, samples were immediately transferred to an evacuated reaction vessel.

3.2.2   Wafer Preparation and Functionalization

A two-step halogenation-alkylation reaction functionalized the hydrogen-terminated Si(111) samples. An air-free reaction vessel connected to the diffusion-pumped Schlenk line contained silicon wafers in individual wells to minimize scratching from adjacent wafers. Three pump-argon-purge cycles effected atmospheric $O_{2(g)}$ removal. The halogenation step utilized gas-phase bromine delivered via the vapor headspace from liquid Br_2. Prior to $Br_{2(g)}$ exposure, the raising the pressure in the Schlenk line and the sample reaction vessel to ~500 mtorr of argon minimized bumping in the liquid bromine source flask. The sample reaction vessel was opened to the liquid bromine flask for 1 s allowing Br_2 vapor to fill the vessel. A two-minute

exposure brominated the silicon surfaces in the reaction vessel, which was subsequently evacuated and filled with an argon ambient to atmospheric pressure. Unrelated to the ongoing functionalization methods, three brominated Si(111) samples were expeditiously transferred to the XPS with nominal ambient air exposure. XP spectra quantified the Br 3d and Si 2p regions of the brominated Si(111) samples to test and validate the substrate-overlayer model that is employed below to ascribe surface coverages from XPS data. Section A.1 contains the Fig. A.1 with the photoelectron spectra and interpretation for bromine-terminated Si(111).

Grignard chemistry functionalized the bromine-terminated Si(111). Cannula transfer filled each well of the silicon reaction vessel with 3–6 mL of a THF solution of 0.2 M CH_2CHCH_2MgCl and 0.8 M CH_3MgCl under argon to keep each wafer submerged throughout the reaction period. Separately, a solution of THF containing only 3–6 mL of 0.8 M CH_3MgCl prepared methyl-terminated Si(111) surfaces for adhesion studies that were otherwise processed in a similar manner to the mixed allyl/methyl-terminated silicon samples. An oil bath maintained at 72 ± 1 °C heated the reaction vessel throughout the three-hour reaction period. Following Grignard reactions, 3–6 mL THF was added via an air-free syringe. The reaction vessel was opened to ambient atmosphere, and each silicon wafer was expeditiously removed, placed in a centrifuge tube, and submerged in THF for initial sonication. The samples were sonicated in 10 minute, sequential steps in THF, methanol, and argon-sparged water. The sparging step minimized dissolved carbon dioxide that could otherwise acidify the water and deleteriously react with the freshly prepared double bond. Bromination of the double bond was initiated directly following alkylation as reports note that exposure to the air negatively affects the reactivity of the surface toward bromination.[211]

We explored three methods to brominate the carbon-carbon double bond for ultimate amination with minimal silicon oxidation and minimal degradation of electronic properties. All bromination reactions were completed in an air-free reaction vessel connected to the Schlenk line. Method **A** involved bromination of the double bond with a 1.2 M HBr solution consisting of 9 volume parts THF to 2 parts glacial acetic acid (formed by a dilution of 1 volume part stock solution into 4 parts THF). A small amount (<5 mg) of benzoyl peroxide was added to promote bromination of the terminal carbon or anti-Markovnikov addition.[212] Following a two hour reaction, samples were removed and rinsed with THF and with water; sequentially sonicated in THF, methanol, and water; rinsed again with water; and dried under a stream of argon. Method **B** brominated the double bond with 1.8 M hydrogen bromide in glacial acetic acid (diluted from the stock solution) with <5 mg benzoyl peroxide. The samples were reacted for 2 h, followed by sequential rinsing with methanol and with water, sequential sonication in methanol and in water, and then dried under a stream of argon. Method **C** utilized a 0.16 M Br_2 solution in DCM to brominate the double bond. Samples were reacted

for 1 h then rinsed with boiling DCM, sonicated in DCM, rinsed with water and dried under a stream of argon. Brominated samples were transferred back to an air free vessel for amination or to a nitrogen-purged glovebox to await analysis.

Aliphatic substitution using with ammonia produced aminated surfaces following bromine reaction with the allyl-functionalized Si(111). Terminal alkyl-bromide samples reacted for 48 h in a 2 M solution of ammonia in methanol that was previously degassed with three freeze-pump-thaw cycles. All samples were then rinsed with methanol and with water, and sonicated sequentially in methanol, in water, and lastly in 0.1 M $NaOH_{(aq)}$ for ten minutes to remove any bromide salts that may have formed during the substitution. A stream of argon dried all samples following sonication.

A combination and X-ray Photoelectron Spectroscopy (XPS), Time-Resolved Microwave Photoconductivity Spectroscopy (TRMPS), and Transflection Infrared Spectroscopy experiments quantified the chemical composition and carrier properties of the functionalized surfaces. Detailed in the §A.3, transflection experiments confirmed the presence of allyl and of methyl groups on the functionalized silicon surfaces, however bromine and amine coverages were too low for transflection quantification. Direct, expeditious transfer to the XPS load lock followed sample drying under argon. In contrast to the direct transfer for XP spectroscopy, samples remained in a nitrogen-purged glove box for one day prior to initial TRMPS quantification. For spectroscopic investigations that targeted the oxidative stability of these samples under prolonged exposure to an air ambient, samples were stored in the dark in plastic centrifuge tubes until ready for the respective measurement. For the oxidation study, samples brominated with method **C** (Br_2 in methanol) were scanned over one month to measure the formation of oxide and its deleterious impact on carrier recombination.

3.2.3   Deposition of Methyl Ammonium Lead Iodide Thin Films

Analyses of carrier recombination both preceding and following methylammonium lead iodide deposition utilized i-Si(111) and n$^+$-Si(111) samples that were brominated via method **C** (Br_2 in DCM). TRMPS measurements necessitated intrinsic silicon to minimize deleterious bulk recombination at dopant sites while PEC experiments required degenerately doped n$^+$-Si with minimal photoactivity. Following quantification of carrier recombination lifetimes via TRMPS, a 10 min sonication in a 0.1 M $HCl_{(aq)}$ solution of alkylamine-functionalized silicon samples converted alkylamine groups to alkylammonium chlorides yielding surface that we refer below to as alkylammonium-functionalized surfaces. Acidification of the amine groups directly preceded the perovskite deposition that followed established procedures.[213] A 0.8 M PbI_2 and 1.6 M CH_3NH_3I solution in DMF was drop cast on alkylammonium-functionalized silicon surfaces that were spinning at 4000 rpm for 30 s fol-

lowed by drying under argon, and heating at 110 °C for 60 min in an air ambient. Perovskite-deposited samples were stored in the dark in plastic centrifuge tubes for two days prior to the post-deposition carrier recombination analysis via TRMPS. To compare and contrast the adhesion of perovskite thin films to alkylammonium-functionalized Si(111) surfaces, we followed the aforementioned deposition procedure on freshly HF-etched Si(111) and on CH_3-terminated Si(111) surfaces. The mixed-monolayer preparation method under the exclusion of allylmagnesium chloride yielded the CH_3-terminated Si(111) surface.

3.2.4   Adhesion measurements between MAPbI$_3$ and silicon

Four distinct silicon surfaces were prepared for the measurement of adhesion between the perovskite film and the substrate: native oxide, hydrogen-terminated, methyl-terminated, and alkylammonium-functionalized surfaces. The native oxide was prepared by similar steps leading to H-terminated surfaces with $NH_4F_{(aq)}$ as described above, after which the sample remained in a clean, covered centrifuge tube, exposed to air for one week to form a clean native oxide layer. The methyl-terminated surface was prepared as indicated above from Grignard solution composed only of CH_3MgCl.

Deposition of methylammonium lead iodide thin films was performed as described above on both the native oxide and alkylammonium-functionalized silicon surfaces. Attempts at spin deposition of the perovskite on methyl-terminated and on hydrogen-terminated silicon surfaces were unsuccessful, as the methylammonium lead iodide solution simply spun off of these surfaces during spin coating. Consequently, quantitative adhesion measurements only included perovskite thin films deposited on to alkylammonium-functionalized and on native oxide silicon substrates.

The Soboyejo research group performed the following AFM experiments. A Dimension 3100 AFM (Bruker Corporation, Billerica, MA, USA) characterized the surface morphology of the perovskite surface, and the adhesion force between the perovskite thin film silicon substrates. Adhesion experiments utilized a NanoWorld PointProbe® CONT Silicon AFM Probe tip (NanoWorld Innovative, Neuchâtel, Switzerland) to obtain the deflection, δ, in contact mode. Spring constants, k, of the individual AFM tips were determined experimentally using the thermal tune method. The adhesion force, F, was then computed from the corresponding deflection and the measured spring constant measured via Hooke's law, $F = k\delta$ for each tip. Finally, the average adhesion forces between the silicon-based tips and deposited substrates (ammonium-functionalized and native oxides) were estimated from the deflection and spring constant. Figure A.2, of §A.2, presents a schematic of the adhesion force measurements with additional experimental information in the figure caption.

3.2.5   Electrode fabrication and photoelectrochemical methods

Electrodes were fabricated from perovskite-deposited samples using degenerately doped n^+-Si(111) and additional electrodes utilized hydrogen-terminated n^+-Si(111) with no perovskite thin film ensure minimal photoactivity from the silicon substrate. Briefly, >1 cm^2 electrodes were fabricated with a gallium indium liquid alloy back contact, silver paint, and LOCTITE Hysol® 9460 epoxy. Perovskite-on-n^+-Si electrodes were transferred to the glovebox for electrochemistry directly following epoxy curing. The "plain" n^+-Si wafers were etched in 10% HF for 5 s followed by rinsing in water, drying in a stream of argon, and directly transferred to the glovebox.

Briefly, all experiments utilized a thin-film photoelectrochemical cell configuration in a nitrogen-filled dry box, and a 300 W ELH-type tungsten-halogen lamp provided illumination. A potentiostat (SP 300, Bio-Logic, Claix, France) acquired current-density–potential, J–E, scans as cyclic voltammograms at 50 mV s^{-1}. Following IUPAC convention, figures and images represent anodic current as a positive value and cathodic current as a negative value.[214]

3.3   Results

3.3.1   Bromination of Allyl/Methyl-Functionalized Si-(111)

As mentioned above, three methods explored the bromination of mixed allyl/methyl-functionalized Si(111) surfaces with the goal of efficient bromine coverage with minimal silicon surface oxidation. Method **A** utilized 1.2 M HBr solution in THF/acetic acid, method **B** employed 1.8 M HBr in acetic acid, while method **C** used 0.16 M Br$_2$ in DCM.

Figure 3.1 presents representative XP spectra of the Si 2p and Br 3d regions for mixed allyl/methyl-functionalized Si(111) surfaces directly following the respective bromination methods. For features in the Si 2p region, we ascribe the purple trace to photoelectrons ejected from bulk Si^0 species and the green trace to covalently functionalized silicon surface sites. In addition to the principal features between 99–101 eV, each Si 2p spectrum in Fig. 3.1 demonstrates a small feature at ~102.5 eV,[161,198] that we attribute to oxidized silicon, SiO$_x$. In analyses of the extent of oxidation detailed below, the integrated area of the feature at ~102.5 eV represents the intensity of the oxidized overlayer while the sum of the features between 99–101 eV represent the intensity of the silicon substrate. Notably, all three bromination methods yielded surfaces with observable oxidized silicon. For each bromination method, Fig. 3.1 displays the respective Br 3d region to which we assign two chemical features. We ascribe the doublet with a Br 3d$_{5/2}$ feature located at ~70.5 eV,[151,169,211] (blue trace) to photoelectrons from bromine atoms bound to carbon, indicative of the desired bromination of the double bond. In addition to the blue trace, the Br 3d region demonstrates a second doublet at ~1 eV lower bind-
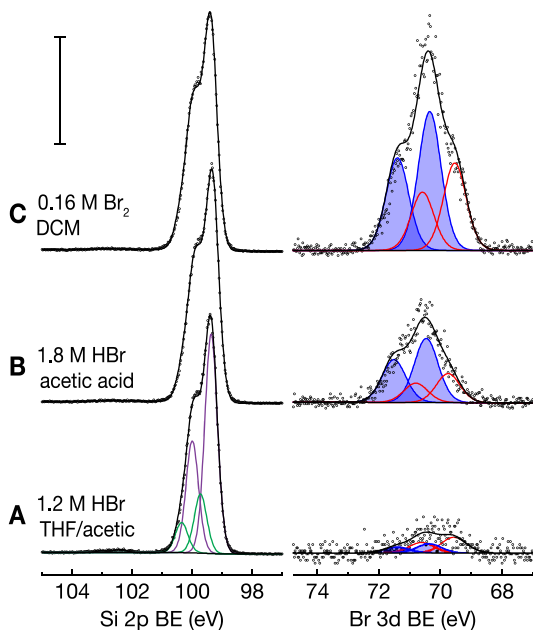
Figure 3.1   XP spectra of the Si 2p and Br 3d regions for mixed methyl/allyl-functionalized Si(111) surfaces subject to differing bromination methods. The purple and green traces in the Si spectra represent paired doublets respectively attributed to bulk Si^0 and covalently functionalized silicon surface sites. We attribute the sets of doublets in the Br 3d region as due to bromine covalently bound to carbon (blue) and to silicon (red). The scale bar represents 1000 photoelectron counts per second in the Si 2p spectra. The fits for the Si 2p spectra are only included in **A** to simplify the figure as **A**, **B**, and **C** all closely resemble one another. The Br 3d spectrum in **A** is magnified 64× with respect to its Si 2p spectrum, and the Br 3d spectra in **B** and **C** are magnified 32× with respect to their respective silicon spectra.

ing energy[151,169] (red trace) that we attribute to photoelectrons from bromine covalently attached to silicon. In determining bromine coverages for the successful bromination of the double bond, we only consider the peak area of the blue trace.

Table 3.1 summarizes the XPS-determined coverage results for the bromination of mixed allyl/methyl-terminated Si(111) utilizing the three methods under study. In Table 1, the chemical species Br(C) and Br(Si) denote bromine bonded to carbon and to silicon, and respectively correspond to the blue and the red peak assignments in Fig. 3.1. The chemical species SiO_x refers to the oxidized silicon feature at ~102.5 eV from the spectra in Fig. 3.1 All peak areas are reported as a ratio that is relative to the total fitted area of the Si 2p features between 99–101 eV (purple and green traces in Fig. 3.1), and represent an average from three separate functionalization trials. Coverage values

Table 3.1   Peak area ratios for bromine and silicon oxide species with respect to the bulk silicon peak area for the three different bromination procedures.[a]

	Species	Peak area vs Si	Coverages
Method A:	Br(C)	0.001 ± 0.001	$1 \pm 1\%$
1.2 M HBr in	Br(Si)	0.002 ± 0.001	$1 \pm 1\%$
THF/acetic acid	SiO$_x$	0.006 ± 0.002	$6 \pm 2\%$
Method B:	Br(C)	0.015 ± 0.003	$6 \pm 2\%$
1.8 M HBr in	Br(Si)	0.006 ± 0.001	$3 \pm 2\%$
neat acetic acid	SiO$_x$	0.008 ± 0.003	$8 \pm 3\%$
Method C:	Br(C)	0.022 ± 0.003	$5 \pm 1\%$
0.16 M Br$_2$	Br(Si)	0.017 ± 0.003	$7 \pm 2\%$
in DCM	SiO$_x$	0.005 ± 0.002	$8 \pm 2\%$

[a] Species Br(C), Br(Si), and SiO$_x$ represent photoelectron signals originating from alkylbromide groups, silicon bromide, and silicon oxide respectively. The overlayer model detailed in the Section 2.4.2 yielded surface coverages reported per the surface density of silicon sites for Br(C) and Br(Si), and as a percentage of a monolayer for SiO$_x$. Coverages reported for method C assume two bromine atoms per functionalized silicon site corresponding to addition of Br$_2$ across an individual double bond.

in Table 3.1 represent the results of the XPS overlayer model for each respective peak area and are reported as a percent of the Si(111) atop site density, $\sigma_{\text{Si(111)}}$, for the bromine coverage and oxidized silicon. The coverage values in Table 3.1 demonstrate significantly higher bromination of the allyl/methyl-functionalized Si(111) for methods **B** and **C** as compared to method **A**. Due to the low relative coverage of bromine, we did not investigate ongoing amination or long-term oxidation studies for surfaces that were brominated via method **A**.

3.3.2   Amination of Brominated Surfaces

A methanolic ammonia solution functionalized samples that had been previously brominated by methods **B** and **C**. Figure 3.2 presents representative XP spectra of the N 1s, Br 3d, C 1s, and Si 2p regions following a two-day amination reaction. Two features persisted in the N 1s photoelectron spectra, a weak feature centered ~400.5 eV and a stronger feature centered at ~398.0 eV that is shaded orange in Fig. 3.2A. We ascribe the higher binding energy feature in the N 1s to adsorbed molecular ammonia,[215] or amide formation by method **B**,[194] and the lower energy peak as due to an alkylamine nitrogen,[216] and NH$_2$–Si.[215] For comparison with XP spectra of methylammonium lead halide, we observe a feature at 402.2 eV that we attribute to ammonium nitrogen groups (not shown). As the shaded feature at 398.0 eV is the only spectral component ascribed to the desired amine product, we only consider the area
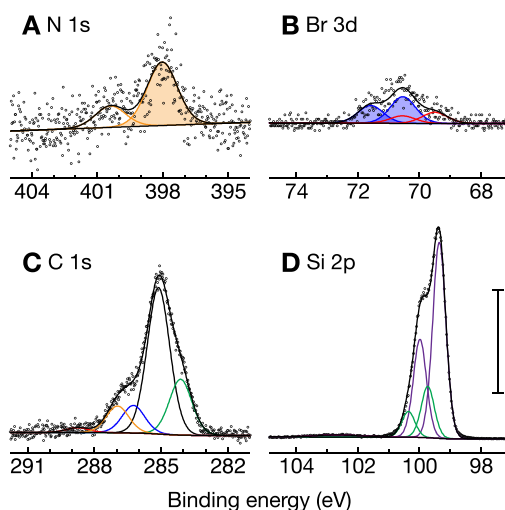
Figure 3.2   High-resolution XP spectra of **A** N 1s, **B** Br 3d, **C** C 1s, and **D** Si 2p regions following an amination reaction in order to convert interfacial alkylbromide species to alkylamines. We attribute the shaded feature at 398.1 eV in the N 1s region (frame **A**) to nitrogen atoms in amine groups bound to carbon. Notably, the observed bromine features in frame **B** indicate that the amination reaction does not remove all bromine from the functionalized Si(111) surfaces. The y-axis scale bar represents 1000 photoelectron counts per second. The C 1s is magnified 5× relative to the Si 2p region while both the N 1s and Br 3d have been magnified 32×.

of that feature in calculating alkylamine coverages. Interestingly, spectra of the Br 3d region demonstrate small but persistant bromine photoelectron signals following the amination reaction that would indicate incomplete conversion of the alkylbromide to alkylamine functionality. Spectral assignments in Fig. 3.2B follow the assignments of Br 3d features seen in Fig. 3.1B. Multiple chemical features exist in the C 1s spectral region that was fit with five peaks that were constrained to the same FWHM value. We attribute the low binding energy feature at 284.3 eV to photoelectrons from carbon atoms directly bonded to silicon, however the remainer of the C 1s features contain contributions from the amine carbon atoms, unreacted allyl groups, and adventitiously adsorbed species in undefined ratios that prohibit spectral assignments. Lastly, the Si 2p region in frame **D** demonstrates a small component at 102.5 eV attributed to oxidized silicon.

Table 3.2 provides the XPS-determined peak area ratios and calculated surface coverage for chemical species observed on Si(111) surfaces that were aminated following bromination of both methods **B** and **C**. Chemical species reported include nitrogen attached to carbon, denoted N(C), that is attributed to alkylamines related to the orange shaded feature in Fig. 3.2**A**; bromine at-

Table 3.2   Peak area ratios for nitrogen, bromine, and silicon oxide with respect to the bulk silicon peak area following amination.[a]

	Species	Peak area vs Si	Coverages
	N(C)	0.017 ± 0.003	$10 \pm 1\%$
Method B:	Br(C)	0.006 ± 0.002	$2 \pm 1\%$
1.8 M HBr in acetic acid	Br(Si)	0.003 ± 0.001	$1 \pm 1\%$
	SiO$_x$	0.021 ± 0.003	$20 \pm 5\%$
	N(C)	0.018 ± 0.003	$6 \pm 2\%$
Method C:	Br(C)	0.018 ± 0.003	$4 \pm 2\%$
0.16 M Br$_2$ in DCM	Br(Si)	0.011 ± 0.002	$5 \pm 2\%$
	SiO$_x$	0.017 ± 0.003	$17 \pm 5\%$

[a] Species Br(C), Br(Si), N(C), and SiO$_x$ represent photoelectron signals originating from alkylbromide groups, silicon bromide, alkylamine groups and silicon oxide respectively. The overlayer model yielded surface coverages for Br(C), Br(Si), and N(C) as a fraction of the silicon site density and oxide coverage as a percentage of a monolayer for SiO$_x$. Coverage of Br(C) and N(C) for samples brominated via method **C** assume functionalization of two bromine or nitrogen atoms per allyl-functionalized silicon surface site.

tached to carbon, denoted Br(C), that is attributed to unreacted alkylbromide related to the blue shaded doublet in Fig. 3.2**B**; bromine attached to silicon, denoted Br(Si); and oxidized silicon, denoted SiO$_x$. As in the case of Table 3.1, the peak ratios in Table represent average XPS peak areas of each respective chemical species relative to the total peak area of Si 2p features between 99 and 101 eV for a total of three samples. As with Table 3.1, Table 3.2 presents coverage values as a percentage of the Si(111) atop site density, $\sigma_{Si(111)}$, and oxidized silicon coverage as a percentage of a monolayer of silicon oxide, which was taken to be 0.35 nm.[161]

3.3.3   Air Stability of Alkylamine-Functionalized Silicon Surfaces

XP spectra and TRMP spectra respectively quantified the degree of oxidation and carrier recombination lifetimes for amine-functionalized samples following prolonged exposure to air. Figure 3.3 presents the Si 2p photoelectron region of one representative sample in which each trace is normalized to the height of the Si 2p$_{3/2}$ feature at 99.4 eV and the region ascribed to oxidized silicon further inset at 20× magnification. Successive traces denote data acquisition immediately after functionalization (red), following one week (green), two weeks (blue), three weeks (orange), and following four weeks in an air ambient (black). The evolution of the inset feature attributed to silicon oxide demonstrates that initial functionalization proceeds with a degree of oxidation that somewhat increases over the subsequent three weeks in air.
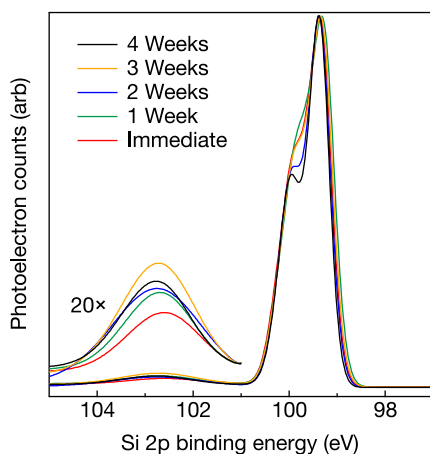
Figure 3.3   Si 2p photoelectron spectra of an alkylamine-functionalized surface immediately following functionalization (red), following one week (green), two weeks (blue), three weeks (orange), and following four weeks in an air ambient (black). When normalized to the amplitude of the Si $2p_{3/2}$ feature at 99.4 eV, the time evolution of the 102.5 eV feature attributed to oxidized silicon serves as a proxy for the atmospheric oxidation of this alkylamine-functionalized surface (inset magnified 20×).

Table 3.3   Peak area ratios and percent monolayer coverages of SiO$_x$ during an oxidative time study of alkylamine-functionalized Si surfaces.[a]

Air exposure	Peak area vs Si	Oxide Coverage (%)
Immediate	0.032 ± 0.006	$20 \pm 5\%$
1 week	0.038 ± 0.006	$30 \pm 5\%$
2 weeks	0.065 ± 0.010	$50 \pm 10\%$
3 weeks	0.066 ± 0.010	$50 \pm 10\%$
4 weeks	0.051 ± 0.010	$40 \pm 10\%$

[a] XP spectroscopy quantified oxidation weekly for three samples that were otherwise exposed to an air ambient in the absence of illumination.

Table 3.3 summarizes the results of the XPS oxidation study. In Table 3.3, the peak area data represents the ratio of the Si 2p feature at 102.5 eV attributed to oxidized silicon vs the area of the total silicon area between 99 and 101 eV. Equation 2.26 in the §2.4.2 converts the peak area ratios into an approximate coverage of silicon oxide in percentage of a monolayer of SiO$_2$. The results in Table 3.3 demonstrate that a nominal degree of oxidation accompanies the amination reaction, however the degree silicon oxidation stabilizes within the four-week duration of the oxidation study.
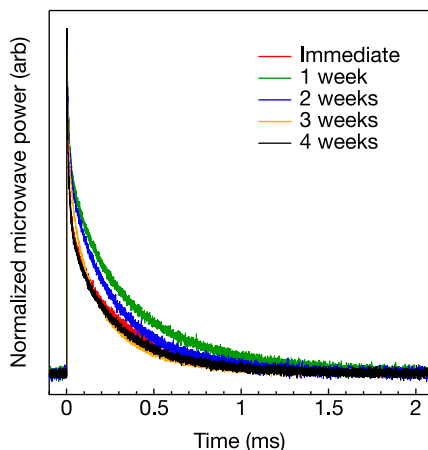
Figure 3.4   Normalized TRMP spectra of the charge-carrier lifetime in an alkylamine-functionalized i-Si(111) sample immediately following functionalization (red), and following one week (green), two weeks (red), three weeks (orange), and four weeks (black) in an air ambient. Fits to a single exponentially decaying function established the characteristic lifetime for each trace.   Lifetime values decrease somewhat throughout the initial two weeks before stabilizing between the final two measurements.

Correlating the XPS-quantified surface oxide coverage with carrier recombination properties is critical to understanding whether the oxide observed in Fig. 3.3 deleteriously affects carrier dynamics. Figure 3.4 presents TRMPS results for a single amine-functionalized surface on i-Si(111) as a function of exposure to an air ambient. Each trace in Fig. 3.4 is normalized to the microwave power value immediately following sample illumination. Successive traces correspond to sampling following direct transfer from a nitrogen-purged glove box (red), following one week (green), two weeks (blue), three weeks (orange), and following four weeks in air (black). Determination of characteristic recombination lifetime values, τ, utilized data from 0.3 ms following the illumination light pulse to ensure that recombination followed single-exponential statistics in the low-level-injection domain. The general trend in τ values in Fig. 3.4 follows a slight decrease following the first two weeks in air and stabilization in values for longer durations. Table 3.4 details the eq-2.40-derived surface recombination velocity average and standard deviation values for a total of four samples. As with the raw results in Fig. 3.4, the recombination velocity values increase initially before stabilizing.

Table 3.4   Surface-recombination velocity values for four wafers that were functionalized with the ammonia procedure and exposed to an air ambient.[a]

Air exposure	SRV (cm s^{-1})
Immediate	80 ± 50
1 week	80 ± 50
2 weeks	90 ± 50
3 weeks	110 ± 60
4 weeks	110 ± 70

[a] Recombination velocities increased somewhat before leveling off following three weeks in air.
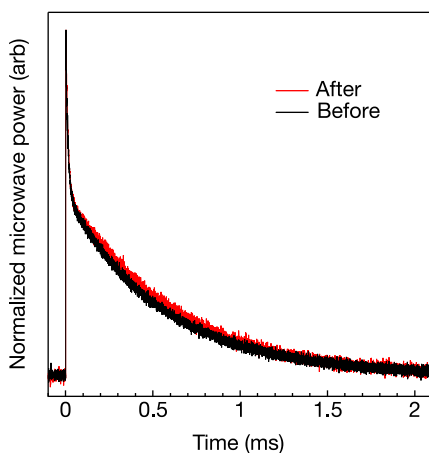
Figure 3.5   Charge-carrier lifetime decay of a single alkylamine-functionalized sample before and after the deposition of a methylammonium lead iodide perovskite thin film. The similarity in shapes and the concomitant characteristic decay lifetime values between the two traces indicates that perovskite deposition procedure does not adversely affect the carrier recombination dynamics of this alkylamine-functionalized silicon sample.

3.3.4   Silicon Carrier Dynamics before and Following Methylammonium Lead Iodide Deposition

Figure 3.5 presents the intensity-normalized TRMPS results for an alkylamm-onium-functionalized silicon wafer both immediately before (black) per-ovskite thin-film deposition, and following 4 weeks in the nitrogen-purged glovebox (red). Perovskite thin-film deposition on alkylamine-functionalized surfaces produced smooth, shiny films. Comparatively, attempts to deposit thin films on purely alkyl terminated Si(111) surfaces yielded non-uniform films characterized by delamination, and rapid coalescence of the subse-
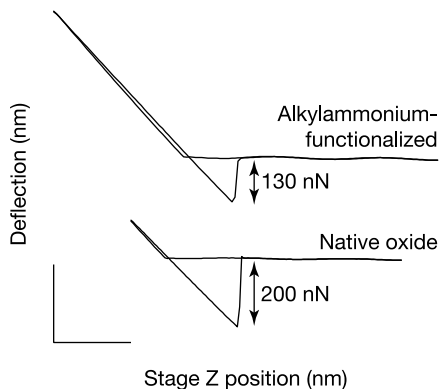
Figure 3.6 AFM force-displacement behavior for MAPbI$_3$ deposited on to alkylammonium-functionalized Si(111) (top) and on to Si(111) with a native oxide (bottom). The hysteresis in tip deflection yields an adhesion force of 130 nN for the perovskite deposited on to the alkylammonium-functionalized Si(111) and 200 nN for the perovskite deposited on to native oxide. The scale bar is 200 nm in both the x and the y axes.

quent droplets yielding poor overall surface coverage. Due to the poor coverage on the hydrogen-terminated and CH$_3$-terminated Si(111) surfaces, subsequent measurements only utilized acidified alkylamine-functionalized (alkylammonium) Si(111) samples. For the two samples studied, the surface recombination velocity was 48 cm s^{-1} immediately before the deposition procedure and 51 cm s^{-1} following the deposition and 4 weeks in the glovebox. The overall similarity between the two scans in Fig. 3.5 and the recombination velocity values indicates that neither the methylammonium lead halide deposition procedure nor subsequent exposure to air significantly alters the recombination properties for this sample.

3.3.5 Adhesion Force Measurements on Functionalized and Native Oxide Samples

Figure 3.6 presents the AFM force curves that we employ to quantify the adhesion of the perovskite thin films on silicon surfaces as a function of the silicon surface chemistry. In Fig. 3.6 the x-axis represents the physical position of the sample stage while the y-axis represents the amount of deflection the tip due to interaction with the perovskite/silicon samples. The deflection is proportional to the force require to move the tip and perovskite from the silicon substrate. Force measurements were conducted on perovskite samples deposited on alkylamine-functionalized silicon and on silicon with a native oxide. The perovskite deposition process on H-terminated or CH$_3$-terminated silicon resulted in nearly instantaneous delamination during spin
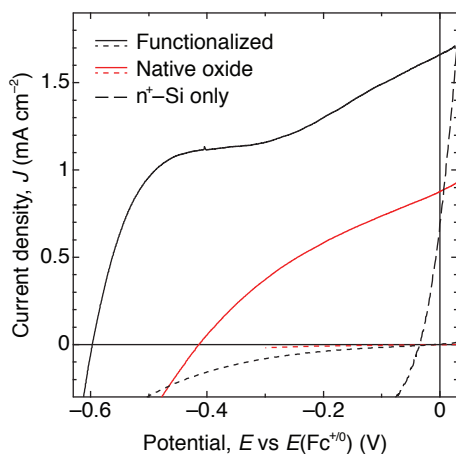
Figure 3.7   Photocurrent density–potential (J–E) performance of perovskite thin films deposited on an alkylamine-functionalized sample (black trace) and a native oxide sample (red trace). The long-dashed black trace validates minimal photoactivity from a non-functionalized, hydrogen-terminated n^+-Si electrode.   Solid traces for the alkylamine-functionalized and native oxide samples indicate scans under illumination while corresponding short-dashed traces represent scans in the dark.

deposition and were thus not considered in the AFM experiments. From the rapid deflection force quantified in Fig. 3.6, the adhesion force between the perovskite thin film and silicon with a native oxide was 200 ± 45 nN while the force in the functionalized sample was 130 ± 45 nN. These results indicate that perovskite films adhere with comparable if somewhat less strength to our alkylammonium-functionalized silicon surfaces as compared to silicon with a native oxide.

3.3.6   Photoelectrochemistry

Figure 3.7 presents representative current-density–voltage, J–E, scans for perovskite electrodes as a function of the surface chemistry at the silicon back contact. In Fig. 3.7 the solid traces correspond to J–E scans acquired under ELH-simulated 1 Sun illumination for perovskite thin films with an alkylammonium-functionalized n^+-Si back contact (black) and with n^+-Si with an interfacial native oxide (red). The black and red dotted lines represent J–E scans in the absence of illumination for thin films with back contacts of alkylammonium-functionalized and of native oxide n^+-Si, respectively. The black dashed line represents a J–E scan of hydrogen-terminated n^+-Si(111) to verify the absence of significant photoactivity so as to establish that acquired photovoltage, V_{oc}, values originated from photoactivity within the perovskite thin film. The perovskite electrode with an alkylammonium-functionalized

n$^+$-Si back contact in Fig. 3.7 demonstrates V_{oc} values of –597 mV (black solid trace), while an average of three similar electrodes demonstrated an average V_{oc} of -650 mV. The perovskite electrode with an n$^+$-Si back contact containing a native oxide shows a V_{oc} of –415 mV (red solid trace), and an average ascertained V_{oc} = –480 mV. The V_{oc} for hydrogen terminated n$^+$-Si in Fig. 3.7 is 32 mV, while the acquired three-electrode average V_{oc} was –35 mV. The absence of appreciable photovoltage from n$^+$-Si electrodes supports our assignment of V_{oc} values to photoactivity in the perovskite thin films. Thus, perovskite thin films that have an n$^+$-Si back contact demonstrated higher V_{oc} values for alkylammonium-functionalized silicon surfaces as compared to silicon with a native interfacial oxide.

3.4   Discussion

3.4.1   Coverage versus Oxidation in the Bromination of Allyl/Methyl-Terminated Si(111)

Previous reports of Si(111) surface functionalization utilizing allylmagnesium halide and methylmagnesium halide solutions achieve 50–80% coverage of allyl moieties with respect to the surface density of Si(111) atop sites.[152] In comparison with the expected coverage of allyl sites, the near 10% coverage observed in the present study implies a very limited bromination of the double bonds available on the Si(111) surface. Two principal factors likely contribute to this low coverage: the high steric crowding of species that are covalently bound to Si(111), and the lack of strenuous reaction conditions that could deleteriously oxidize the silicon surface. Unlike the ~0.5 nm sulfur-sulfur distance[217] adopted by adjacent thiol molecules occupying three-coordinate positions on the Au(111) surface, covalent attachment at Si(111) atop sites follows the 0.384 nm nearest-neighbor spacing of silicon atoms on that surface. The increased crowding yields 100% coverage for methyl groups, but reduced yields for larger organic moieties. Thus, it is reasonable to expect that the large HBr and Br$_2$ molecules would poorly penetrate an already crowded allyl-functionalized surface. Additionally, with only one tetrahedral carbon, allyl chain may have limited ability to reorient on the surface for increased "visibility" of the double bond.

Comparing and contrasting the bromine methodologies, method **A** (HBr in THF and acetic acid) yielded the lowest coverage of alkylbromide species. We attribute the low coverage when utilizing THF as the solvent to both poor solvation of transition states in the addition reaction as well as a possible side reaction involving HBr acid cleavage of the THF solvent.[218] Methods **B** (HBr in acetic acid) and **C** (Br$_2$ in DCM) yielded similar bromine coverages to each other on a per-silicon-site basis, and a significantly higher coverage relative to method **A**. In addition to bromination of the double bond, all three methods brominated the silicon substrate. We attribute the bromination of silicon to

reactions of HBr and Br_2 with Si–H bonds that reform in a hydrogenation side reaction that accompanies the allylmagnesium halide reaction with Si(111) surface sites.[151] While method **B** and method **C** react with a similar fraction of double bonds on the Si(111) surface, method **B** yields significantly lower coverage of the undesired brominated silicon as compared to method **C**. Notably, all three bromination methods resulted in very little oxidation of the silicon substrate.

3.4.2 Coverage versus Oxidation in the Amination of Allyl/Methyl-Terminated Si(111)

The formation of alkylamines yielded a concomitant reduction in both alkyl-bromide and silicon bromide species. That the quantity of silicon bromide decreased following the ammonia exposure suggests that the silicon surface may have been functionalized with $-NH_2$ groups in addition to alkylbromide sites. This silicon amination is important as it suggests that atmospheric oxygen would similarly be able to penetrate through the monolayer to the surface to oxidize the surface at silicon bromide sites. Despite the possibility for oxidation at silicon bromide sites, the air exposure results do not demonstrate a significant increase in silicon oxide over the course of four weeks. Of note, photoelectrons from amine-functionalized silicon atoms would also appear at ~102 eV, thus ascribing all Si 2p features between 102–104 eV to SiOx may overestimate oxide coverages.[215] The slight decrease in oxide signal demonstrated for the week-four (black) trace relative to the week-three trace (orange) in Fig. 3.3 for one sample is reflected in the relative change in average oxide coverage values reported for multiple samples in Table 3.3. The difference between coverage values for the two-week, three-week, and four-week exposures in Table 3.3. are similar in magnitude to their reported standard deviations and all likely represent similar values within the measurement uncertainty inherent in photoelectron spectroscopy.[194] The oxide that did form over the four weeks did not significantly contribute to an increase in a trap state density that would increase the surface-recombination velocity on the aminated surfaces. While the 110 cm s^{-1} surface-recombination velocity average following four weeks in air is higher than the ~30 cm s^{-1} value observed for methyl-terminated Si(111), this value is comparable to recombination velocities for other mixed-monolayer silicon surfaces.[151–152,173]

Interestingly, the calculated coverages for amine and remaining bromine species exceed the calculated initial bromine coverages for both methods **B** and **C**. Similarly, the peak ratios for all non-oxide species add up to a greater number following amination as compare to before (0.031 following vs 0.021 before for method **B**, and 0.047 following vs 0.039 before for method **C**). We believe that this difference exceeds the uncertainty in the XPS and its peak fitting. A more likely explanation is that the cumulative species on the

surfaces following amination serve to attenuate the bulk silicon photoelectron intensity more as compared to the attenuation prior to amination.

3.4.3   Adhesion of Methylammonium Lead Iodide and Silicon Stability

Due to the extremely hydrophobic nature of hydrogen-terminated and of CH_3-terminated Si(111) surfaces, attempts the deposit perovskite thin films often yielded rough, patched, and inconsistent perovskite layers that often delaminated during the spin deposition process. In contrast to hydrogen-terminated Si(111) and mixed allyl/methyl-functionalized Si(111), thin-film deposition on alkylammonium-functionalized Si(111) demonstrated uniform wetting and adhesion. By introducing the ammonium functionality by acid-ification of the alkylammonium-functionalized silicon, surface wettability to the perovskite precursors greatly increases. Indeed, ammonium itself may be incorporated into interfacial methylammonium lattice sites of the perovskite thin film so as to introduce intimate ionic bonding between the perovskite thin film and the silicon substrate.[219–220]

The AFM studies support the qualitative observation of strong adhesion of perovskite thin films to alkylammonium-functionalized silicon. While the native oxide required a greater force to delaminate the film from the substrate, the alkylammonium-functionalized surface showed comparable adhesion. Notably, the observed adhesion between the perovskite and the silicon resulted from a ~10% Si(111) site coverage of nitrogen groups as quantified by the XPS above. This result suggests that higher alkylammonium group coverages would afford stronger binding between perovskites and silicon surfaces. Such explorations are underway.

3.4.4   Implications for Solar Energy Conversion in Silicon-Perovskite Tandem Junction Cells

Band alignments between silicon and perovskite are such that n-type, degen-erately doped silicon could serve as the ohmic contact to n-type methylam-monium lead iodide. This ohmic contact is relevant to a tandem junction morphology that utilizes a silicon tunnel junction to electrically connect a silicon absorber to a perovskite absorber such as $MAPbI_3$. This connection further relies on both strong adhesion between the perovskite and the sili-con as well as a high electronic quality interface with a low opportunity for recombination of photogenerated charge carriers. The experiments detailed above demonstrate the viability of organic monolayers in both chemically "gluing" and electrically "wiring" perovskite thin films to silicon.

Figure 3.8A highlights the band edge positions and approximate Fermi level energies for both n-type, degenerately doped silicon (n^+-Si) and methylam-monium lead iodide perovskite (Perov.) as well as the redox potential energy $--qE(A^+/A)$ of the ferrocene$^{+/0}$ couple, $CpFe^{+/0}$. The conduction band edge,
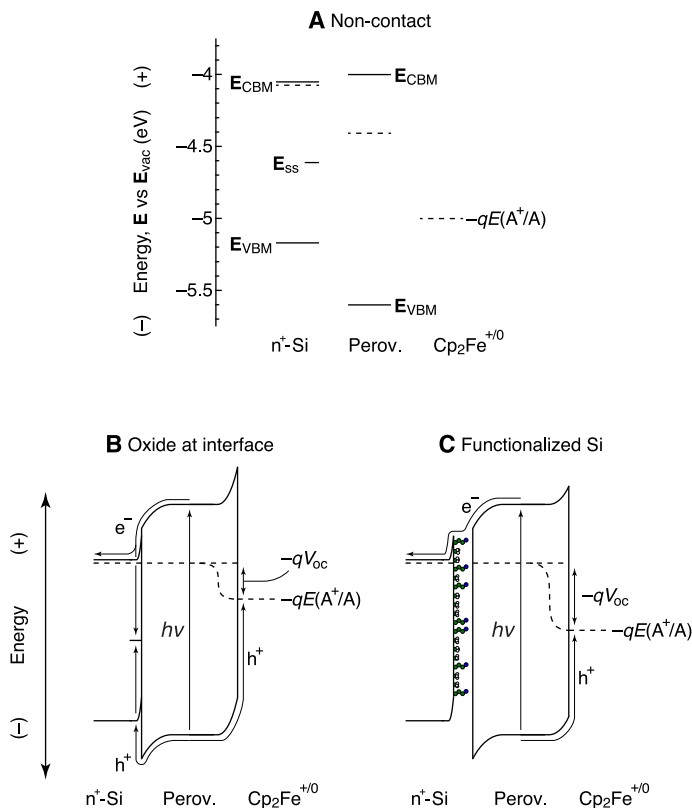
Figure 3.8   Alignment, **A**, of conduction and valence band edges, E_{CBM} and E_{VBM}, for n^+-Si, perovskite (Perov.) and the energy $-qE$ corresponding to the redox potential, $E(A^+/A)$ of a nonaqueous ferrocene$^{+/0}$ redox couple, $CpFe^{+/0}$. A model that fits the experimental data includes recombination at silicon surface states for illuminated perovskite thin films contacting the interfacial native oxide of the silicon back contact, **B**, and efficient carrier collection at the back contact for illuminated perovskite thin films in contact with alkylammonium-functionalized silicon, **C**. The implications for back-contact recombination yield open-circuit photovoltages, V_{oc}, for perovskite thin films in contact with alkylammonium-functionalized silicon that are larger as compared to perovskite thin films in contact with a silicon native oxide.

E_{CBM}, and valence band edge, E_{VBM}, energies for silicon, n^+-Si, are based on an electron affinity of 4.05 eV and a band gap energy of 1.12 eV, and mid-gap surface state energies, E_{ss}, due to silicon dangling bonds.[221] Reports vary on the position of MAPbI$_3$ band edge positions,[222] but many results converge on a valence band position between –5.4 and –5.8 eV vs the vacuum energy level, E_{vac}, and a conduction band edge lower than –3.9 eV. As drawn in Fig. 3.8A, we place the MAPbI$_3$ perovskite E_{CBM} at –3.95 eV and E_{VBM} at –5.5 eV vs E_{vac}

and note that small deviations from these values would not significantly impact the data interpretation. We place the ferrocene$^{+/0}$ redox potential energy at –5.00 eV vs E_{vac} based on the ferrocene$^{+/0}$ formal potential, $E^{0\prime}$, at +0.311 V vs the saturated calomel electrode when in nonaqueous solvent with lithium perchlorate as the supporting electrolyte,[223–224] the +0.241 V potential of the saturated calomel electrode vs the normal hydrogen electrode, and the –4.45 eV potential energy of the normal hydrogen electrode vs E_{vac}.[225]

Figure 3.8 further presents a model that fits the experimental results for perovskite/silicon interfaces with a native silicon oxide (frame **B**) and alkylammonium-functionalized silicon (frame **C**). The x-axis positions and depletion widths are not to scale.   The photoelectrochemistry results demonstrate higher V_{oc} values under illumination for perovskite/ferrocene$^{+/0}$ rectifying junctions couple when alkylammonium-functionalized n$^+$-Si forms the back contact to the perovskite layer relative to V_{oc} values when native-oxide-n$^+$-Si forms the back contact.   The photoelectron spectroscopy and transient microwave carrier lifetime measurements demonstrate that the organic-functionalized surfaces demonstrate a low density of interfacial oxide and minimal interfacial trap states, respectively.   We ascribe the performance when native-oxide silicon forms the back contact to an added recombination pathway at silicon dangling bonds at the perovskite/interface (Fig. 3.8**B**). That the mixed monolayer effectively passivates the silicon surface and successfully adheres MAPbI3 to silicon yields a larger overall V_{oc} under illumination (Fig. 3.8**C**) as compared to the native oxide interface. Assuming an interfacial barrier height, Φ_B, of 1.05 eV based on a –5.00 eV vs E_{vac} position of the ferrocene$^{+/0}$ redox couple and a conduction band edge of –3.95 eV vs E_{vac}, the –650 mV average V_{oc} for the perovskite/ferrocene$^{+/0}$ rectifying junction demonstrates efficient carrier collection and minimal deleterious recombination.[130,223,226–227] Thus, the combination of photoelectrochemical, carrier lifetime, and surface science analyses demonstrate that organic layers effectively electrically and chemically glue perovskite thin films to silicon.

Electrical connections between methylammonium lead iodide perovskites and degenerately doped as employed in the photoelectrochemical analyses are particularly relevant to the design and fabrication of scalable, inexpensive tandem-junction PV. Tandem silicon/perovskite devices have employed configurations in which a low-work-function material (electron transporting) formed the back contact,[228] or a high-work-function material (hole transporting) formed the back contact from the perovskite top absorber to the silicon lower absorber.[229] While studies to date have utilized metal oxide connecting layers between the perovskite and silicon absorbers, the present work demonstrates that near-ambient-temperature, solution-processed, organic monolayers accomplish the chemical adhesion whist maintaining the necessary low-defect-density of the silicon substrate. Future work may further optimize these the interfacial properties by increasing the density of

alkylammonium sites, and by incorporating carrier-selective organic moieties as are employed in organic photovoltaics.

3.5 Conclusions

We synthesized mixed allyl/methyl-functionalized Si(111) we subsequently brominated with HBr or Br_2, and then aminated with NH_3 to yield alkylamine-functionalized Si(111) surfaces. Amine coverage was roughly 10% of available silicon surface sites. The coverage by bromide functional groups is possibly limited by the tight packing of adjacent allyl groups Si(111) surface sites. Photoelectron spectroscopy of alkylamine-functionalized surfaces demonstrated that oxidation did not exceed one half of one monolayer of SiO_2 following four weeks of air exposure. Concomitant with stable oxide coverages over four weeks, the surfaces maintained good electronic integrity as quantified by low surface recombination velocity values. Acidification of the alkylamine produced alkylammonium functionalization that afforded uniform deposition of perovskite thin films. Importantly, the deposition and annealing steps required to deposit methylammonium lead iodide thin films did not compromise the electronic integrity of the silicon surface as quantified by similar recombination lifetimes prior to and following the thin-film deposition. Adhesion force experiments found that alkylamine-functionalized surfaces had lower, but comparable, adhesion to the perovskite film and higher coverages of ammonium functionalities would increase the force.

The above procedure yields modest functional group coverage whilst maintaining the high electronic quality of the silicon. Future studies on the surface will explore the factors that control bromination of surface-tethered double bonds, elucidate the physical structure and orientation of functionalized moieties, and investigate the ohmic/rectifying charge transfer behavior at silicon/perovskite interfaces that are "glued" with organic monolayers.

CHAPTER 4

COVALENT ATTACHMENT AND CHARACTERIZATION OF PERYLENE MONOLAYERS ON SI(111) AND TIO$_2$ FOR ELECTRON-SELECTIVE CARRIER TRANSPORT
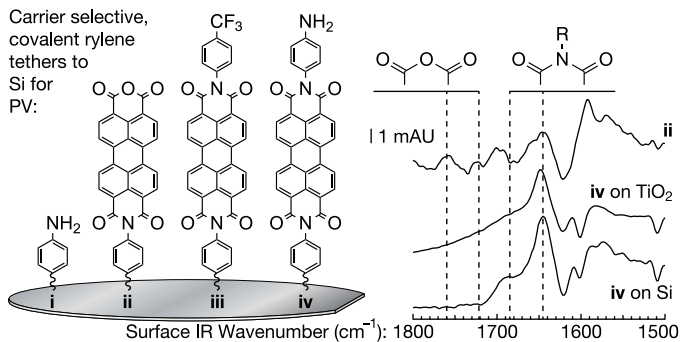
Portions adapted from:

4.1   Abstract

We functionalized chemically oxidized Si(111) and TiO$_2$ surfaces with covalently attached rylene molecules and demonstrated further chemical conversion of the attached species. Base-catalyzed activation of perylene tetracarboxylic dianhydride (PTCDA) preceded reaction with phenylaminosilane-terminated surfaces yielding surface-bound perylene via an imide linkage. Transflection infrared spectroscopy of the carbonyl vibrational region elucidated the presence of anhydride, imide, and ester species following each reaction stage. The presence of both anhydride and imide infrared features following reaction with PTCDA validate successful perylene attachment. Subsequent functionalization of the surface-attached perylenes yielded infrared spectra with little or no detectable anhydride features that indicate successful conversion to ester or imide species based on respective reactions with alkyl bromides or aryl amines. X-ray photoelectron spectroscopy (XPS) quantified fractional coverages of surface-attached perylene species following a post-deposition derivatization with fluorine-containing alkyl bromides and with anilines. Overlayer model interpretation of the photoelectron results determined perylene surface coverage of ~15% relative to the surface density of Si(111) atop sites, and a ~10% surface coverage of imide-terminated perylene species. The interpreted coverage data yields an approximate conversion efficiency for the anhydride-to-imide derivatization at surface-attached perylenes of ~66%. We discuss the present results in terms of possible coverage and packing on oxide-free silicon surfaces, the utilization of covalently attached rylene species as electron-transporting and hole-blocking connecting layers in molecular electronics and tandem-junction photovoltaics (PV).

4.2   Introduction

Carrier transport layers between light absorbers and electrodes or between semiconductors in tandem-junction solar cells are essential components of high-efficiency photovoltaics.[62,83,230–233] Research in non-traditional absorbers (e.g. perovskites) necessitates commensurate research into materials and interfaces that provide the oft-desired atmospheric isolation, and carrier selectivity with minimal light absorption and/or antireflective properties.

Among transport materials used for emerging perovskite- and antifluorite-based solar devices,[234–235] metal oxides are well investigated.[62,230–231,236–238] Oxides of titanium, zinc, and tin are typically chosen for their stability, ease of deposition, and energy levels that are well aligned with the conduction band edge of the light-absorbing semiconductor and also contain a valence band edge far lower than its contacts to effect hole blocking behavior. However, such oxides are limited by immutable energy levels, lattice defects,[239] oxygen diffusion,[67–68] and high sintering temperatures incompatible with non-traditional absorber materials of recent interest. Further, the interface

between metal-oxides and the tetrahedral (110) perovskite face, the dominant face in thin-film perovskites, is plagued with defects arising from lattice mismatches.[79] Researchers ascribe such strains to non-radiative decay of carrier lifetimes and decreased power efficiencies.[240] Rigid crystal structures, lattice constants, and energy levels for a given metal oxide drive investigations into non-oxide-based transport later materials.

An organic approach provides many strong candidates for tunable, oxide-free connecting layers.[83−84,241] The deposition of organic layers such as fullerenes or nanotubes, and planar aromatic species has recently been shown to counteract the negative effects of lattice mismatch in addition to their own electron-hole extraction attributes.[80−81] Uniform thin films of PBCM can be deposited by both spin-coating[83,242] and dip-coating methods.[243] Other organic carrier-transport materials such as Spiro-MeOTAD and PEDOT:PSS have also been utilized and applied to substrates in similar fashions.[63,244] While thin films of organics have increased carrier selectivity with concomitant increases in performances,[62−63,80,83−84,245] challenges remain in controlling nanoscale film thickness as well as conductivity. The absence of well-defined covalent attachment to a semiconductor substrate may yield poorly ordered thin films, weak adhesion, agglomeration, and concomitant electronic issues.[83,196,245−247]

Covalent attachment of organic connecting layers could improve conductivity with minimal yet well-controlled layer thicknesses, robust attachment to silicon, and decreases in defect density from the soft, flexible contact to the adjacent material. Leveraging organic, synthetic control of surfaces should enable the formation of films of well-defined thickness and chemical handles for attachment of further contacts or semiconducting absorber layers. Several organic species exist that are amenable to functionalization allowing for tunability of energy levels and addition of terminal groups to increase adhesion at the interface. Among electron-transport and hole-blocking materials, rylene-based molecules are particularly compelling.[91−93] Rylenes demonstrate HOMO–LUMO tunability based on length, absolute energy positioning via bay-position derivatization, ease of covalent attachment via catalyst-free anhydride-to-imide conversions with minimal side reactions, and robust thermal stability of the resulting rylene imides.[248−249] Further, the practical deployment of rylenes such as perylene should be inexpensive and scalable due to their broad use as pigments over the last century. Ultrathin perylene layers have been studied on surfaces such as silver,[250] silicon,[251] and copper[252] surfaces following evaporative deposition. In all cases, PTCDA was oriented planer to the surface and only covalently attached in the case of UHV-cleaned copper, yielding an opening of the anhydride moieties. Recently, derivatives of rylene diimide layers were applied to substrates for use as electron transport layers in inverted, p-i-n perovskite solar cells.[95,253−255] Yet, direct surface attachment strategies, subsequent influences on electronic properties, and implications for carrier transport in PV-relevant surface remain underexplored. Such studies motivate the present investigation.
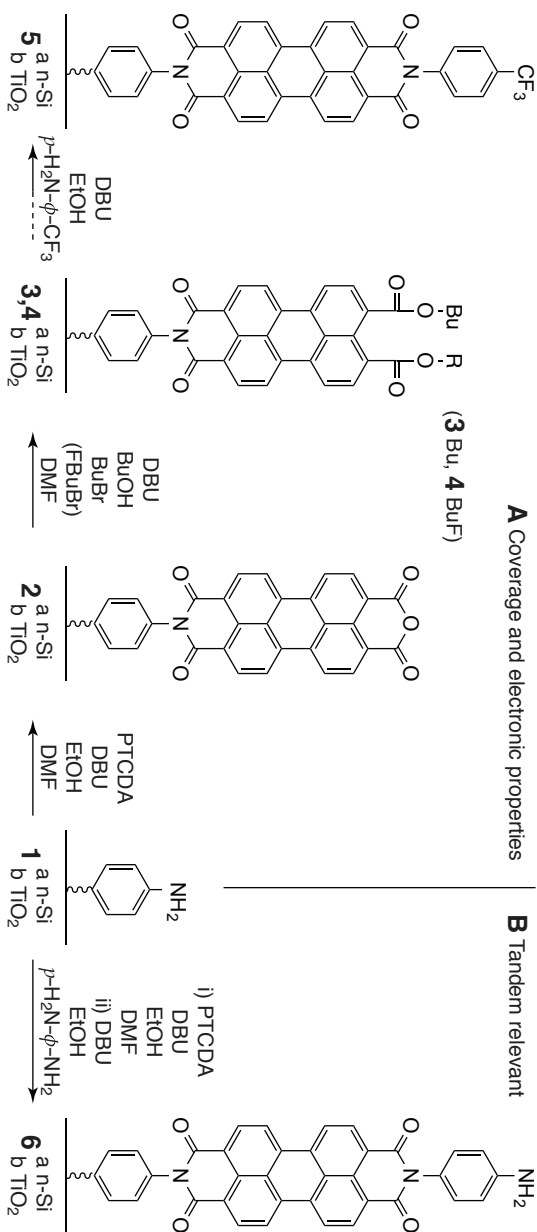
Figure 4.1   Functionalization strategies with perylene derivatives begin at aniline-derivatized surfaces, **1**. Probes of coverage products and conversion efficiencies, **A**, utilize perylene-attached surfaces **2**, that are further derivatized to yield alkyl esters **3**, fluorinated alkyl esters **4**, and fluorine-containing imides **5**. Surfaces relevant to tandem-junction photovoltaics, **B**, include a terminal aniline, **6**, for incorporation at perovskite interfaces.

In this work, we utilize perylene tetracarboxylic dianhydride (PTCDA) to study attachment and reactivity strategies that could ultimately be employed for covalently attached, carrier-selective connector layers for solar energy applications. Phenylamino silane was grafted to oxide surfaces to provide an aniline moiety with a terminal amine necessary for PTCDA attachment. We utilized substrates including chemically oxidized Si(111) and TiO_2. We chose chemically oxidized Si(111) because such surfaces maintain a high degree of surface flatness needed for coverage calculations from photoelectron spectra. Separately, we utilize titania surfaces for their relevance as substrates for possible inexpensive non-traditional photovoltaic absorbers. While titania is effective for electron-transporting and hole-blocking properties, the molecular species explored may yield soft contacts between arbitrary metal oxides and a non-traditional absorber to minimize lattice mismatches and exposed surface states. As shown in Fig. 4.1, reactions begin with covalently, surface tethered aniline **1**, to which we attached PTCDA to yield surface **2**. For all reactions and surfaces included in Fig. 4.1, **a** denotes species that are covalently tethered to oxidized Si(111) and **b** specifies species on TiO_2 substrates. Secondary functionalization of the surface-exposed anhydride species yielded surfaces **3**, **4**, and **5** for surface coverage analyses. Secondary functionalization separately utilized molecules with terminal aryl amines, **6**. Surface **6** bears relevance to incorporation into a top absorber material such as ammonium-containing perovskites that demonstrate interfacial A-type cation substitution,[84] that may be exploited for interfacial adhesion.[196] In concert, X-ray photoelectron spectroscopy (XPS) and infrared spectroscopy probed surface attachment and coverage to reveal the compatibility of synthetic chemical strategies in yielding the desired layer characteristics. The present findings provide a promising direction toward applying molecular electronics on oxide-free interfaces with layer-by-layer control of interfacial chemical and electronic properties.

4.3   Experimental

4.3.1   Materials and Chemicals

The experiments utilized single-side polished, 525 ± 25 μm thick, 1–5 Ω cm resistivity, phosphorus-doped n-Si(111) (EL-CAT Inc., Ridgefield Park, NJ) for X-ray photoelectron spectroscopy. Infrared spectroscopy experiments employed double-side polished, 525 ± 25 μm thick, 0.10–0.12 Ω cm resistivity, boron-doped p-Si(111), (EL-CAT Inc.). TiO_2 thin films were deposited on fluorine-doped tin oxide (FTO)/glass slides with a surface resistivity of ~7 Ω sq^{-1}, (Sigma-Aldrich).

Solutions for the etching and cleaning of silicon surfaces include piranha solution, aqueous hydrogen fluoride, and aqueous ammonium fluoride. ***Caution:*** *Aqueous hydrogen fluoride is an acute poison that is toxic at even small amounts*

and limited exposures, and piranha solution is a strong oxidant that reacts highly exothermically with organic matter. A Millipore Milli-Q system provided 18 MΩ cm resistivity water for all water requirements. Piranha solution consisted of a 3:1 mixture of concentrated sulfuric acid (98%, Fisher Chemical) and H$_2$O$_{2(aq)}$ (35 wt %, Alfa Aesar) that was freshly prepared as used. The HF$_{(aq)}$ was diluted to 6 M from a commercial stock solution (49%, electronic grade, Transene Company Inc., Danvers, Massachusetts). Argon (ultra-high purity, Airgas) sparged an aqueous ammonium fluoride solution (40%, electronic grade, Transene) for 30 min prior to use. A stream of argon dried the silicon samples as needed. Solvents for cleaning silicon wafers and FTO slides include acetone (99.5% min, Fisher Chemical), methanol (MeOH, 99.9% min, semiconductor grade, Alfa Aesar), and toluene (99.7% min, Alfa Aesar).

Chemicals employed for TiO$_2$ thin film deposition on FTO include titanium(di isopropoxide)-*bis*-(2,4-pentanedionate) (75% in isopropanol, Alfa Aesar), *n*-butanol (99.5%, Acros Organics) to form 0.15 M and 0.30 M solutions.

The solution utilized in the silanization of Si and TiO$_2$ surfaces consisted of 4M p-aminophenyltrimethoxy silane (90%, Gelest) in toluene that was previously dried for >24 h over freshly activated 3 Åmolecular sieves. The silane solution in toluene was freshly prepared in a nitrogen-purged flush box to minimize water-catalyzed silane polymerization.

The reagents used in the attachment of perylene to surfaces and subsequent further functionalization steps included perylene-3,4,9,10-tetracarboxylic di-anhydride (PTCDA, 97%, Sigma-Aldrich), dimethylformamide (DMF, 99.8% min, Alfa Aesar) 1,8-diazabicyclo[5.4.0]undec-7-ene (DBU, 98% min, Alfa Aesar), Ethanol (EtOH, dried over sieves, denatured, 92%, Alfa Aesar), *n*-bromobutane (99%, Acros Organics), 1-bromo-4-fluorobutane (97%, Alfa Aesar), p-trifluoromethylaniline (99%, Aldrich), and *p*-phenylenediamine (sublimed ≥99% Sigma) that were all used as received.

4.3.2   Surface Preparation and Functionalization

Dicing, cleaning, and preparation of Si wafers and TiO$_2$ samples preceded *p*-aminophenylsilane deposition and perylene functionalization. Samples for XPS were diced in to ~0.3 cm^2 pieces and wafers for IR studies were cut into 1 cm × 3 cm pieces to accommodate wide beam spots at nearly grazing angles. Si samples were rinsed with acetone, methanol, and H$_2$O before a 10-min submersion in piranha solution. Samples were subsequently rinsed and dried with argon to await surface functionalization.

TiO$_2$ thin films were deposited onto FTO-coated slides. FTO-coated glass slides were initially rinsed with water and dried before sequential sonication in acetone, IPA, and H$_2$O, drying in argon, and further drying in a 100 °C oven. Each FTO slide was initially covered with the 0.15 M titanium precursor solution, spun at 3000 RPM for 25 s, then dried on a hot plate that was set

to 120 °C under an air ambient. After a short period of cooling, the 0.30 M titanium precursor solution was spun onto the surface in the same fashion and dried under argon. The compact TiO_2 films were directly annealed in a furnace at 500 °C for a minimum of 2 h to form the anatase phase and subsequently stored in plastic centrifuge tubes until silanization. Prior to silanization, surfaces were immersed in DI water to promote the formation of terminal hydroxyl groups and to avoid "radical gettering" of ambient carbon contamination.

Preparation of Si(111)-based **1a** and TiO_2-based **1b** surfaces utilized silanization. Under an air ambient, samples were individually loaded in piranha-cleaned glass test tubes, immersed in the *p*-aminophenylsilane solution (<3 mL), sealed in parafilm, and heated to 80 °C for 4 h. Following heating, an additional 2–3 mL of toluene was added to each test tube, directly followed by decanting, and sequential sonication in fresh toluene, MeOH, and H_2O, then blown dry with argon and left overnight in a 100 °C oven.

Reaction with PTCDA converted aniline-terminated silicon surfaces **1a** to **2a**, and aniline-terminated TiO_2 surfaces **1b** to **2b**. Initially, PTCDA was activated by opening up the anhydride groups on each perylene molecule with DBU and ethanol to form reactive carboxylic ester-acid moieties.[256] Although PTCDA can react directly with terminal amines, reports note that such direct conversion with aryl amines is slow, requires high temperatures, and is hindered by the poor solubility of PTCDA itself.[91] In our hands, attempts to direct conversion to imide functionalities yielded low surface coverages and will not be discussed further in lieu of conversions with activated perylenes. For each ~0.3 cm^2 sample of **1a** and/or **1b** undergoing functionalization, activation utilized 0.029 mmol PTCDA, 0.075 mmol DBU, and 0.150 mmol EtOH in 0.075 mL DMF that was stirred for 5 h at 60 °C after which the solution was diluted to 0.5 mL with additional DMF. The ~3 cm^2 samples for infrared spectroscopy utilized solutions of 3 mL in total volume with reagent concentrations scaled accordingly. The activated PTCDA solutions submerged individual wafer samples in sealed test tubes for 72 h at 60 °C under an air ambient to yield surfaces **2a** and **2b**. Surfaces **2a** and **2b** were rinsed in acetone followed by sequential 10-min sonication steps in acetone, toluene, MeOH, and H_2O then blown dry with argon.

From surfaces **2a** and **2b**, we synthesized **3a** and **3b** to establish the presence of the relevant functional groups via infrared spectroscopy and **4a** and **4b** to quantify total functionalized perylene surface coverage via XPS. For **3a** and **3b**, we added 3 mL DMF, 3.4 mmol DBU, and 5.5 mmol BuOH to submerge each ~3 cm^2 sample of **2a** and **2b** for 3–4 h at room temperature after which we added 0.55 μmol of n-bromobutane (60 μL) followed by further heating for 16 h at RT to yield **3a** and **3b**. For **4a** and **4b**, we added 1 mL DMF, 1.1 mmol DBU, and 1.8 mmol BuOH to submerge each ~0.3 cm^2 sample of **2a** and **2b** for 3–4 h at RT after which we added 0.18 μmol of 1-bromo-4-fluoro-butane

followed by further heating for 16 h at RT to yield **4a** and **4b**. Samples **3** and **4** were then rinsed in acetone, IPA, and H$_2$O, followed by drying under argon.

From surfaces **2a** and **2b**, we respectively synthesized **5a** and **5b** to quantify the effective conversion of terminal anhydrides on perylene-derivatized surfaces to aryl imides. Such quantification utilized XPS of the ~0.3 cm^2 samples. We added 1 mL DMF, 1.1 mmol DBU, and 1.8 mmol BuOH to submerge each ~0.3 cm^2 sample of **2a** and **2b** for 3–4 h at RT after which we added 0.16 μmol of p-trifluoromethylaniline (~20 μL) followed by further heating for 72 h at 80 °C to yield **5a** and **5b**. Surfaces **5a** and **5b** were rinsed, cleaned, and dried as with **3a–4b** as above.

Lastly, from surfaces **2a** and **2b**, we respectively synthesized **6a** and **6b** to produce surfaces to yield a species with a terminal aniline functionality that may be acidified to an anilinium for incorporation into a subsequently deposited perovskite thin film.[196] For XPS samples, we added 1 mL DMF, 1.1 mmol DBU, and 1.8 mmol BuOH to submerge each ~0.3 cm^2 sample of **2a** and **2b** for 3–4 h at RT, after which we added 0.50 μmol of p-phenylenediamine followed by further heating for 72 h at 80 °C to yield surfaces **6a** and **6b**. Surfaces **6a** and **6b** were rinsed, cleaned, and dried as with **3a–5b** as above.

4.3.3   Synthesis of Comparison Molecules for Interpretation of IR Spectra

We acquired infrared spectra for perylene derivatives to assist with the interpretation of the interfacial IR spectra. For interpretation of the infrared spectrum of surface **2a**, we synthesized N,N'-*bis*-(p-trifluoromethylphenyl)-perylene-3,4:9,10-dicarboxyimide, **7**, for its two cyclic imide groups, and N-(p-trifluoromethylphenyl)-perylene-3,4-carboxyanhydride-9,10-carboxyimide, **8**, for its one anhydride and one imide functionality. To assist with the infrared spectral interpretation of surface **3a**, we synthesized tetrakis-(butyl)-perylene-3,4,9,10-tetracarboxylate, **9**, for its four ester carbonyls and perylene-3,4-dibutylester-9,10-N-p-trifluoromethylaniline imide, **10** for its cyclic imide and two carbonyl species. Perylene molecules **7–10** are presented in Fig. 4.2 and their synthesis procedures and provides the full IR spectra are presented in §B.1.

4.4   Results

We present stepwise the results of derivatization and functionalization of surfaces to ultimately elucidate the effectiveness and surface coverage at each transformation step. Importantly, each derivatization starts with aniline-terminated surfaces on either silicon or TiO$_2$ substrates. Figure B.15 presents a representative XP spectrum for surface **1a** to demonstrate the successful grafting of the aniline-containing silane. For ten samples of surface **1a**, XP
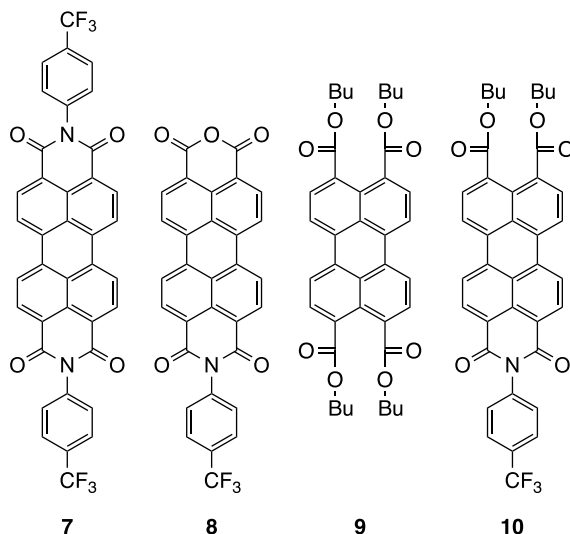
Figure 4.2   Molecular perylene derivatives to serve as spectroscopic analogs for surfaces **2**–**6** when determining the absorption modes of relevant surface IR spectra.

spectra reveal an average N 1s-to-Si 2p area ratio of 0.35 ± 0.10, that only includes Si 2p ascribed to bulk silicon species. As described in §2.4.3, one "perfect" monolayer of aniline termination would yield a N 1s-to-Si 2p peak area ratio of 0.13 based on a nitrogen atom surface density that matches the idealized 7.83×10^{14} sites cm^{-2} density of Si(111) atop sites. For the average experimental N 1s-to-Si 2p peak area ratio of 0.35 ± 0.05, the substrate overlayer model yields an effective monolayer coverage of 1.4 ± 0.2 relative to the site density of Si(111) atop sites. We interpret the overlayer model results as at least one monolayer of coverage of aniline sites on surface **1a** and on all subsequent surfaces.

4.4.1 Functionalization of Aniline-Terminated Silicon and TiO$_2$ Surfaces with PTCDA

We first present the incorporation of PTCDA into aniline-terminated surfaces through the reaction from **1a** to **2a** and **1b** to **2b** to establish the successful covalent grafting of perylene onto the surfaces. As mentioned above, these reactions utilized activated PTCDA in which the anhydride groups were opened to form carboxylic ester-acid moieties for increased reactivity relative to that of PTCDA itself. Reaction between the surface-bound aniline and the activated PTCDA should yield a perylene species with one anhydride and one imide group for which infrared spectroscopy should reveal the characteristic features of each.
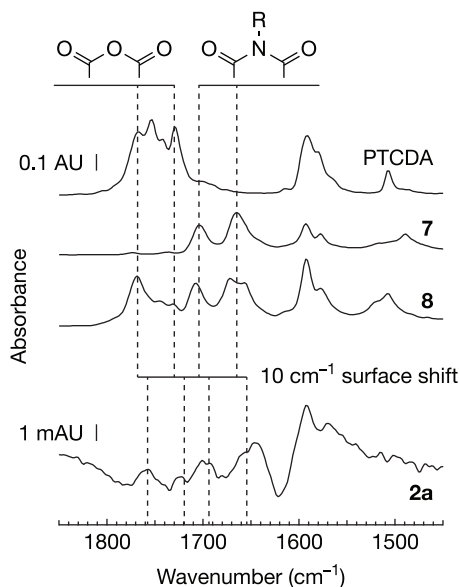
Figure 4.3   Transflection infrared spectrum of the carbonyl region for surface **2a** and comparison ATR-IR spectra of reference molecules PTCDA for its two cyclic anhydride groups, **7** for its two cyclic imide groups, and **8** with one cyclic anhydride and one cyclic imide species. Dashed guide lines align with bands arising from the carbonyl anhydride features in PTCDA and imide features in **2a** and include a 10 cm^{-1} shift for alignment with concomitant features in the **2a** surface spectrum. The qualitative alignment of spectral features in molecule **8** and surface **2a** with the dashed guide lines supports the successful covalent grafting of PTCDA onto an aniline-terminated surface. The lower scale bar represents one milliabsorbance unit (mAU) for the spectrum of surface **2a** while the upper scale bar represents 0.1 absorbance unit (AU) for the molecular ATR-IR spectra of PTCDA, **7**, and **8**.

Figure 4.3 presents a representative infrared spectrum of the carbonyl region for PTDCA-reacted aniline species on silicon, **2a**. For interpretation of the surface infrared results, Fig. 4.3 further includes representative ATR IR spectra of PTCDA for its two anhydride moieties, N,N'-bis-(p-trifluoromethylphenyl)-perylene-3,4:9,10-dicarboxyimide **7** for its two cyclic imide groups, and N-(p-trifluoromethylphenyl)-perylene-3,4-carboxyanhydride-9,10-carboxyimide **8** for its one-anhydride and one-imide functionality. The quartet of peaks in the PTCDA spectrum between 1770 and 1730 cm^{-1} demonstrates carbonyl stretching features for its two anhydride species with symmetric and asymmetric coupling within individual and across opposing anhydride groups.[257] The infrared spectrum of **7** with its two imide groups demonstrates strong features at 1703 and 1665 cm^{-1} that respectively indicate symmetric and asymmetric stretches of six-member-cyclic imides.[258] Figure 4.3 further in-

cludes dashed guide lines to the 1770 and 1730 cm^{-1} anhydride carbonyl features in PTCDA as well as the 1703 and 1665 cm^{-1} imide carbonyl features in molecule **7**. With one anhydride and one imide moiety, the IR spectrum of molecule **8** in Fig. 4.3 demonstrates features ascribable to both groups at qualitatively similar intensities. As indicated by guide lines with a 10 cm^{-1} shift, peaks at 1647 and 1657, 1698, and 1724, 1759 cm^{-1} for surface species **2a** demonstrate good agreement to spectral features in the molecular species and of molecule **8** in particular. A comparable a spectral shift exists for non-covalently bound molecular crystalline adsorbates on metal and silicon surfaces.[250–251,259] We ascribe the shift in chemical features to clustering of the adsorbed perylenes in their reaction with an aniline-terminated surface. Separately, each spectrum contains features at 1591–1595 and at 1575–1579 cm^{-1} that indicate perylene C–C ring vibrations. The combination of anhydride/imide/and perylene ring features demonstrates the successful covalent grafting of PTCDA to aniline-terminated silicon surfaces to yield surface **2a**.

4.4.2 Activation of Terminal Perylene Cyclic Anhydrides and Conversion to Esters

Quantifying perylene surface coverage of **2a** and **2b** as well as determining a respective conversion efficiency from **1a** and **1b** presents challenges. Surfaces **2a** and **2b** present few distinct chemical features in a photoelectron spectrum for quantifying surface coverages that would enable a conversion efficiency from their respective **1a** and **1b** surfaces. In contrast to XPS results, the infrared chemical features afforded by spectra **2a** and **2a** are distinct, however, interpreting absorbance values requires knowledge of oscillator strengths that may be affected by interfacial packing and orientation, as well as interactions with the chemically oxidized silicon substrates. Instead, we subsequently utilized the high conversion efficiency for esterification of cyclic anhydride species[260] to incorporate species that are more amenable to coverage analyses. From **2a** and **2b**, reaction with *n*-bromobutane respectively yielded **3a** and **3b** to establish the successful reaction of the surface-exposed anhydride group of **2a** and **2b**. Separately, reaction of **2a** and **2b** with 1-bromo-4-fluorobutane respectively yielded **4a** and **4b** for XP spectroscopic analysis of surface coverage due to the presence of fluorine.

Figure 4.4 presents a representative infrared spectrum of the carbonyl region for **3a**. As with Fig. 4.3, Fig. 4.4 includes representative ATR IR spectra for tetrakis(butyl)-perylene-3,4,9,10-tetracarboxylate, **9**, for its complete ester conversion and absence of imide or anhydride species as well as for *N*-(*p*-trifluoromethylphenyl)-bis(butyl)-perylene-3,4-carboxyimide-9,10-dicarboxylate, **10**, for its mixed ester and one imide functionality. The spectrum of **9** demonstrates features at 1720 and 1706 cm^{-1} that are characteristic of ester carbonyls.[260] The spectrum of **10** demonstrates peaks at 1705 and 1665 cm^{-1} that resemble the features ascribed to imide carbonyl modes for molecule **7**
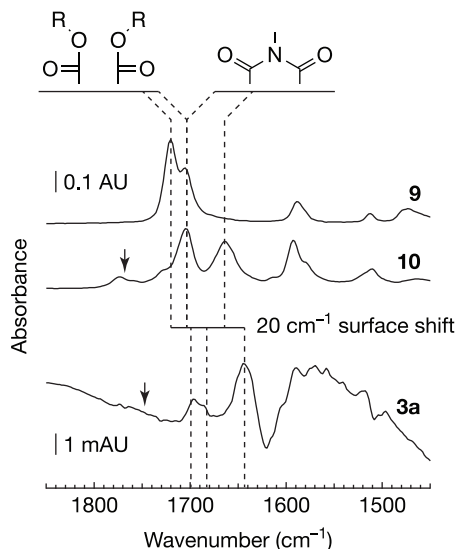
Figure 4.4   Transflection infrared spectrum of the carbonyl region for surface **3a**, and comparison ATR-IR spectra for the tetraester **9** and mixed ester-imide molecule **10**. Dashed guide lines aligned with ester carbonyl and imide carbonyl features in **9** and in **10** demonstrate alignment with features in surface **3a**, with a small shift in imide carbonyl modes towards lower wavenumbers. The qualitative alignment between reference molecule spectra and the surface spectrum **3a** with a 20 cm^{-1} shift supports the successful activation of surface **2a** to yield the mixed diester-imide surface species in **3a**. The arrow for **10** indicates the location of the symmetric anhydride carbonyl mode in PTCDA and in **8**, while the 20 cm^{-1}-shifted arrow for **3a** further supports high conversion of surface anhydrides in **2a** to esters in **3a**. The lower scale bar represents 1 miliabsorbance unit (mAU) for surface **3a** while the upper scale bar represents 0.1 absorbance unit (AU) for the ATR-IR spectra of **9** and **10**.

in Fig. 4.3. The spectrum of **10** further includes an arrow to 1770 cm^{-1}, which is the location of the strong symmetric anhydride mode observed for PTCDA and molecule **8** in Fig. 4.4. Indeed, we assign the small, arrow-adjacent feature at 1775 cm^{-1} in **10** to anhydride features due to trace quantities of a mixed imide-anhydride perylene species. Trace imide-anhydride perylene molecules may be due either to incomplete anhydride activation, or water-vapor-induced closing of a small quantity of the ester moieties to reform anhydride. The dibutyl ester features of **10** are hidden between the symmetric imide and asymmetric anhydride peaks. As with Fig. 4.3, guide lines assist with interpretation of spectral features for surface **3a** in Fig. 4.4 that are shifted by 20 cm^{-1} based on visual inspection of peak alignment. We interpret the broad feature at ~1643 cm^{-1} of 3a to the asymmetric imide carbonyl mode and the features between 1685 and 1700 cm^{-1} to a poorly resolved combination of a symmetric imide and the ester carbonyl modes. We ascribe the

larger, 20 cm^{-1} shift in carbonyl features in **3a** relative to the 10 cm^{-1} shift in features in **2a** to the addition of two ester groups per perylene molecule that would be tightly packed at clustered perylene sites on the surface. Importantly, the surface **3a** spectrum includes an arrow that is shifted by 20 cm^{-1} relative to the arrow for molecule **8**. As this arrow at 1748 cm^{-1} represents the anticipated location of a symmetric anhydride carbonyl mode, the lack of resolvable features indicates an absence of detectable quantities of anhydride sites remaining on the **3a** surface. The presence of ester and imide carbonyl features along with the absence of resolvable anhydride features indicates nearly complete conversion of the terminal anhydrides of surface **2a** to ester species. This high anhydride-to-ester conversion demonstrated for surface **3a** enables the overlayer analyses of surface **4a** photoelectron spectra that reveal the perylene coverage on surfaces **2a**, **3a**, and **4a**.

Figure 4.5 presents the F 1s, C 1s, N 1s, and Si 2p XP spectra of a representative **4a** surface that we employ to establish surface coverage of perylene species. Activation of anhydride-terminated surface **2a** and subsequent 16 h reaction with 1-bromo-4-fluorobutane at room temperature yields surface **4a**. For the F 1s region in Fig. 4.5, the feature centered at ~687 eV indicates the presence of fluorine bound to carbon. The N 1s region is well described with a trace feature at 399 eV and a principal feature centered at ~401 eV due to both the imide nitrogen atoms as well as unreacted aniline surface species. Four peaks describe features in the C 1s region that we attribute to C–F carbon species centered at ~290 eV, C=O species centered at ~288 eV, C–N at ~287 eV, and both surface aryl C–C and adventitiously adsorbed species centered at a binding energy of ~285 eV.[194] Lastly, the Si 2p spectrum contains three sets doublets for which we present the fitted binding energy values of each 2p$_{3/2}$ doublet. Si 2p peaks include red-fitted features at 103.1 eV corresponding to highly oxidized silicon in the chemical oxide, and green-fitted features at 99.8 eV ascribable to Si^{1+} in the interfacial Si/SiO$_x$ region, and purple-fitted features at 99.5 eV ascribed to bulk Si^0. For the four samples studied, the average ratio of the area of the fitted F 1s feature to the area of the Si 2p$_{3/2}$ feature ascribed to bulk Si^0 is 0.13 ± 0.01. As detailed in eq 2.34, a substrate overlayer model interprets the F-to-Si ratio as fractional coverage of fluorine-tagged diester perylene species of 0.15 ± 0.02 on surface **4a** relative to the density of silicon atop sites on an idealized Si(111) surface. The peak-area ratio of N 1s to Si^0 for surface **4a** is 0.26 ± 0.04. We attribute the decrease in peak-area ratio to increased attenuation of the N 1s photoelectrons by the perylene overlayer and dissimilar phenylaminosilane layer coverages between experiments. Figure B.17 presents analogous XP spectra for a representative surface of **4b**.
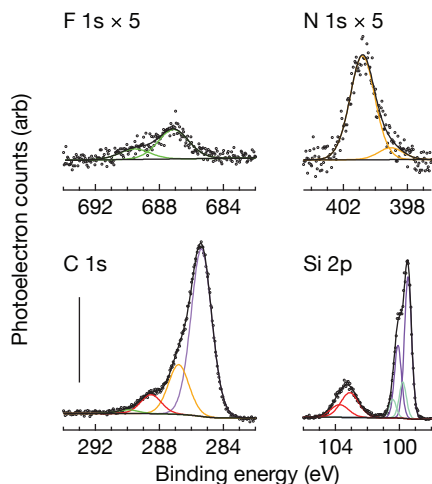
Figure 4.5   XP spectra of a representative **4a** surface, including the F 1s, C 1s, N 1s, and Si 2p regions. We attribute the peaks in the F 1s spectrum to carbon-bound fluorine atoms in the terminal perylene-attached esters. Features in the N 1s include overlapping contributions from imide nitrogen and unreacted surface aniline species. The four fitted C 1s features result from C–F, C=O, C–N, and an overlap of C–C and adventitious carbon species. Oxidized surface and bulk species contribute to the Si 2p region. The vertical scale bar in the C 1s frame represents 400 counts per second (cps) for C 1s and Si 2p, with the F 1s and N 1s regions scaled by a factor of five.

4.4.3   Incorporation of Aryl Amines at Terminal Perylene Cyclic Anhydrides

Beyond the insight afforded by the ester-containing surfaces **3a** and **4a**, we are particularly interested in imide-terminated surfaces that could ultimately present chemical handles to attach to additional photovoltaic absorbers or top contacts. Quantification of surface **5a** that was establishes the activation and reactivity of the terminal cyclic anhydride species of surface **2a** to yield terminal aryl imides.

Figure 4.6 presents F 1s, C 1s, N 1s, and Si 2p photoelectron spectra of a representative **5a** surface following reaction of a DBU-activated surface **2a** with *p*-trifluoromethylaniline at 80 °C for 72 h. Similarly to Fig. 4.5, the F 1s feature centered at ~687 eV in Fig. 4.6 indicates the presence of fluorine bound to carbon. In contrast to a strong the respective signals in Fig. 4.5, the N 1s, C 1s, and Si 2p features for the **5a** surfaces are strongly attenuated in Fig. 4.6 based on the N 1s peak area and a smaller scale bar. Variability in the coverage of the initial phenylaminosilane monolayer also may contribute to the low N 1s signal. As in Fig. 4.5, the C 1s region is described by four peaks that we attribute to a trace C–F carbon species centered at ~293 eV, an imide carbon

species centered at ~289 eV, and two features at ~287 and ~285 that represent overlapping contributions of unreacted C–N aniline sites in the phenylamino silane, aromatic carbon, and adventitious carbon species.[194] Two doublets effectively describe spectral features in the Si 2p region including a doublet in red with a Si $2p_{3/2}$ component centered ~104 eV, and a purple doublet that appears at 100.0 eV. We assign the red doublet to highly oxidized silicon, SiO_x, and the purple doublet to non-resolved contributions of interfacial Si^{1+} and bulk Si^0. All measured **5a** surfaces demonstrate larger relative SiO_x contributions compared to Si^{1+} and Si^0 that we ascribe to the long, 80 °C functionalization under an air ambient.

Photoelectron spectra for four samples of surface **5a** demonstrated an average F-to-Si^0 area ratio of 0.36 ~ 0.04. The F-to-Si ratio is higher for the **5a** surfaces as compared to the 0.13 ~ 0.01 ratio for the **4a** surfaces due to the higher density of fluorine atoms per molecular moiety and a larger silicon oxide layer that more strongly attenuates bulk Si^0 photoelectrons. The overlayer model detailed in eq 2.35 yields a fractional surface coverage 0.10 ~ 0.02 of *p*-trifluoroaniline-derivatized perylene species on the **5a** surfaces per Si(111) atop site density for the experimental F-to-Si ratio of 0.36 ~ 0.04. The N 1s to Si^0 ratio for surface **5a** is 0.08 ~ 0.02, which is notably lower than for **1a** due to attenuation by the bulky perylene overlayer and variations in phenylaminosilane coverage between experiments. Control tests with under the same conditions to form **5a**, without the aniline, confirm the N:Si ratio is unchanged. This overlayer model assumes a vertical orientation of perylene species and clustering that would not abnormally affect the attenuation of sub-surface signals.

The model-quantified coverage of species relevant to surfaces **5a** and **4a** based on the photoelectron data yield insight into conversion efficiency for secondary reactivities at perylene-derivatized surfaces. As mentioned above, we assume complete anhydride-to-ester conversions of **2a** to **3a** and of **2a** to **4a** based on literature reports of near-unity conversion of each molecular analogue. Thus the 0.15 ± 0.02% coverage of fluorinated ester species in **4a** is a proxy for the perylene coverage of **2a** that serves as a starting point for the anhydride-to-imide conversion of surface **2a** to **5a**. From the fractional Si-site coverage of 0.10 ± 0.02% for **5a** and the interpreted "initial" perylene coverage of 0.15 ± 0.02% for **2a**, we quantify an approximate conversion efficiency of **2a** to **5a** of 66%. Importantly, the reaction to yield surface **5a** demonstrated a strong temperature dependence. Reactions with *p*-trifluoromethylaniline as above but at 60 °C and at 40 °C yielded no XPS-detectable F 1s signals.

4.4.4   Incorporation of Terminal Functionality Relevant to Tandem-Junction PV

Surfaces **5a** establish the viability of terminal imide formation at covalently surface-attached perylene moieties. While the trifluoromethyl species yielded
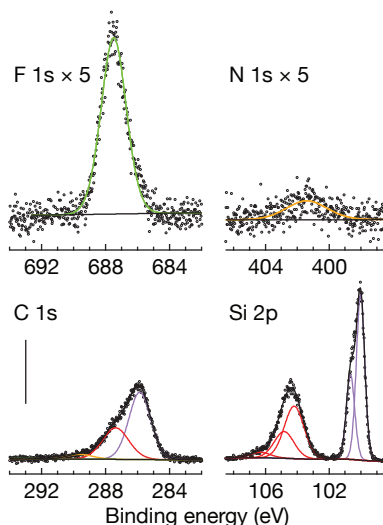
Figure 4.6   Representative XPS of surface **5a**, including the F 1s, C 1s, N 1s, and Si 2p regions. The single peak in the F 1s spectrum results from fluorine in terminal –CF$_3$ groups. Features in the N 1s, C 1s, and Si 2p regions match assignments to spectra features in Fig. 4.5. The vertical scale bar in the C 1s frame represents 200 counts per second (cps) for C 1s and Si 2p, with the F 1s and N 1s regions scaled by 5×.

a strong F 1s feature for determining surface coverage values, that particular species is not relevant for connecting semiconductor absorber layers in tandem junction morphologies. Relevant terminations include amine groups that may be acidified to ammonium halides that previous reports[196] implicate in perovskite adhesion of through substitution of the A-type cation in the perovskite lattice.[84] Introduction of a terminal amine species for perovskite adhesion motivates the synthesis of surface **6a**.

Figure 4.7 presents the representative IR spectra of the carbonyl region for both surfaces **6a** on silicon and **6b** on TiO$_2$ substrates. To aid in the identification of relevant features, we re-include a representative ATR spectrum of **7** with its symmetric and asymmetric imide modes at 1703 and 1665 cm^{-1}, respectively. The small additional features at 1774 and 1737 cm^{-1} for molecule **7** indicate the trace presence of unreacted anhydride. In contrast to the two sharp, well-defined features in molecule **7**, the surface spectra of **6a** and **6b** demonstrate one well-defined feature at 1650–1645 cm^{-1} that we assign to the asymmetric stretch, and a shoulder at 1700–1680 cm^{-1} that we assign to the symmetric stretch. The broad, low signal of the symmetric stretch for surface **6b** is may be caused by a disordered orientation inherent to the physically textured TiO$_2$ surface. The presence of unreacted anhydride and two dissimilar imide species contributes to the overall broadening of the spectrum for
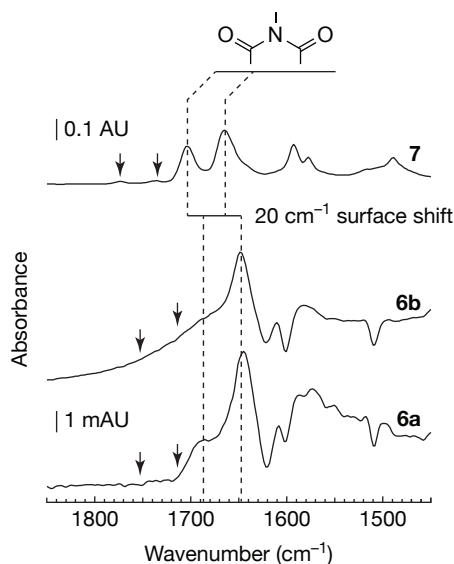
Figure 4.7   Transflection spectrum of surface **6a** and external-reflection spectrum of surface **6b** both demonstrate a small shift in carbonyl features to lower wavenumber values relative to the ATR-IR spectrum of molecule **7** with its two cyclic imide species. Arrows in the spectrum of molecule **7** represent the location of trace anhydride modes, and the absence of such surface-shifted features in the spectra of **6a** and **6b** demonstrate an absence of anhydride within the limits of detection. The presence of imide-ascribable features and no detectable anhydride-ascribable features supports the successful incorporation of phenylenediamine with high conversion yields. Aniline-terminated surfaces served as the background for each spectrum.

surface **6b**. In contrast to a possibility of anhydride features for surface **6b**, the absence of observable features between 1800 and 1720 cm^{-1} suggests a high conversion of terminal anhydride groups to the imide on surface **6a** for the silicon substrates.

4.5   Discussion

4.5.1   Attachment Strategies

Surface attachment of perylene derivatives to ITO and silicon carbide have previously been reported.[261–263] However, these functionalization strategies have either required complicated, expensive syntheses or higher temperature imide condensations which limit applications and substrates. A typical imidization reaction of an anhydride group on PTCDA requires temperatures from around 100–160 ˜, depending on the desired aliphatic R– group

and generally higher temperatures for aryl amines. Attachment of PTCDA is further hindered by its low solubility in almost all solvents and despite the low surface density of a vertically-oriented PTCDA monolayer, significantly higher solution concentrations are required. To address both complications, a PTCDA attachment strategy was adapted to utilize activated perylene "acid-ester" species rather than the less reactive and less soluble anhydride reagent.[256] In our hands, the "activated" PTCDA was more amenable to reactions and yield higher surface coverages of attached perylene groups relative to non-base-opened PTCDA anhydrides. Additionally, the imidization required cooler reaction temperatures and solubility of activated PTCDA was increased by orders of magnitude in solution. With the ultimate goal of coupling p-phenylenediamine to the perylene, we decided to attach the PTCDA first to the surface and to sequentially couple the aryl amine. A single-step alternative to the sequential reaction may have yielded unwanted AB polymers of a perylene diimide connected with phenyl units. Combined with the poor solubility of *N*-(*p*-aminophenyl)-perylene-3,4-carboxyanhydride-9,10-carboxyimide, the possibility for polymerization motivated the multi-step approach. Future efforts to tailor the terminal species for molecular or ionic recognition of non-perovskite materials may revisit this choice.

Silanization yielded the terminal amine groups necessary to surface tether the PTCDA. We chose silane surface chemistry for the ease of preparing an initial aniline-terminated surface that should make the surface transformations on Si(111) and TiO$_2$ effectively substrate agnostic. From §2.4.3, the photoelectron spectroscopy of surface **1a** and applied overlayer modes indicates coverage in excess of one monolayer that is not uncommon in silane monolayer formation.[264] Considering the high surface coverage of phenylaminosilane groups, surface attachment of PTCDA should not be limited by the availability of free amine sites.

With no unique X-ray photoelectron features, analysis of the carbonyl region of the infrared spectrum provides the strongest evidence for the successful synthesis of surface **2a**. Of note, we observed a higher signal-to-noise ratio for a transflection configuration rather than a pure RAIRS geometry. In the IR accessory employed, the nearly focused beam path did not necessitate large samples as is needed for traditional transmission IR acquired at the 74° Brewster angle of silicon. The surface IR spectra for **2a** contains both the symmetric and asymmetric stretches for the anhydride and the imide species in relatively equal amounts. We attribute presence of the imide stretching frequencies to the formation of the imide at the bottom of the PTCDA. The "upper" anhydride is reformed after contact with water and is represented by the persistence anhydride peaks in the IR spectrum. The deviations in the carbonyl frequencies between the reference molecule spectra and surface-attached PTCDA spectrum are consistent with the shifts found in previous IR studies of surface-bound carbonyl species.[265–267] Unfortunately, while IR

provides the qualitative confirmation of attachment of PTCDA, at this stage it does not provide quantifiable surface coverage information.

Conversion of surface **2a** to **3a** and to **4a** afforded an analysis of surface coverage. Solution-based studies of perylene chemistry shows that the transformation of PTCDA to tetrakis(butyl)perylene-3,4,9,10-tetracarboxylate **9** is nearly quantitative.[260] For the spectrum of **3a** in Fig. 4.4, the absence of definitive anhydride features confirms a high conversion of terminal anhydrides to ester species, although the small features between 1800–1750 cm^{-1} may be from residual anhydride species. Thus, we believe that the activation of terminal anhydrides and subsequent esterification proceeds at very high, but perhaps not quantitative, yields. As shown in Fig. B.4, the ester C=O stretches of molecular species **10** are of weaker intensity compared to the imides and in the spectra of **3a**, those vibrational modes are obscured by the symmetric imide stretch. For the XPS studies of the esterification of perylene on surfaces, we employed 1-bromo-4-fluorobutane to yield surface **4a** with a calculated overlayer coverage of 15% of the site density of atop sites on Si(111). Based on the loss of anhydride signals in the IR studies on **3a**, we surmise that the fluorinated ester coverage of surface **4a** is a reliable proxy for the coverage of perylene species in surface 2a, or ~15% of the density of atop sites on Si(111).

With an established perylene surface coverage, conversion of surface **2a** to **5a** established the efficacy of post-attachment derivatization of the perylene cyclic anhydride species. We chose to incorporate *p*-trifluoromethylaniline for its fluorine photoelectron signal as well as its similar size to the desired *p*-phenylenediamine. As an arylamine, *p*-trifluoromethylaniline should have a lower reactivity than an associated alkylamine, and thus the coverages quantified should represent a lower bound on achievable transformations at terminal surface perylene anhydrides. Importantly, our experiments revealed that a temperature of 80 °C or higher were required to form the imide, even after activation of the anhydride, possibly due to the deactivation of the aniline by the electron-withdrawing nature of the –CF$_3$ group. We determined the surface coverage of **5a** to be ~10% of the surface density of Si(111) atop sites. Considering average perylene surfaces coverages were consistently 15%, the 10% site density on surface **5a** implies a conversion yield of ~66% from the anhydride-terminated surface. We caution against overinterpretation of the calculated conversion yields due to the number of assumptions inherent in photoelectron peak fitting and application of overlayer models, but we believe that the data imply good conversion yields that validates the choice of incorporating the terminal imide to an already-surface-attached perylene anhydride. Broadly, the coverage by **5a** is comparable to yields for solution-based perylene syntheses.[91,256] The desired surface functionalization, **6a/6b**, utilized an identical procedure to the **5a/5b** transformations, but employed phenylenediamine as the arylamine. Characterization with IR indicated an absence of anhydride features that we similarly ascribe to a high conversion

yield of surface perylene anhydrides to the imide with a new terminal amine functionality.

Sections B.3 and B.4 includes analogous data for transformations on TiO_2 substrates as presented herein for silicon substrates, and includes infrared and XP spectra for surfaces **2b**, **3b**, and **5b**. While surface **2b** demonstrates PTCDA features and surfaces **4b** and **5b** demonstrate F 1s features, the inherent disorder of the TiO_2 surface represents an unconstrained surface area and roughness that limits direct applications of the overlayer analyses. The combination of observable fluorine for surfaces **4b** and **5b** as well as both the presence of imide carbonyl and the absence of anhydride carbonyl features for surface **6b** in §B.14 demonstrate the viability similar transformations for PTCDA on TiO_2 as on silicon substrates.

4.5.2 Implications for Tandem-Junction PV

As mentioned above, we chose chemical transformations on silicon and TiO_2 substrates for their relevance to connecting layers in tandem-junction photovoltaics and other electronic applications. TiO_2 substrates are particularly relevant as ohmic contacts to many n-type semiconductor materials. Covalent attachment of electron transport layers should lead to more efficient ohmic transfer of electrons while blocking hole transport into TiO_2 defect states for an overall increase in V_{oc} and concomitant photovoltaic efficiency.

We are particularly interested in the use of covalently attached, well-defined, ordered perylene monolayers as applied as connecting layers in future inexpensive tandem-junction photovoltaics. Tandem-junction solar cells consisting of hybrid organic-inorganic perovskites and silicon are an enticing prospect their low-cost, and band gap tunability to realize the favorable band gap pairing of ~1.7 and 1.1 eV with silicon to match currents and maximize efficiencies. Additionally, the conduction bands of both materials are closely matched to allow electron transfer from the perovskite to silicon in a p-i-n orientation. We hypothesize that covalent attachment of perylene diimide monolayers at the interface of tandem-junction solar cells will facilitate efficient electron transfer and hole blocking between silicon and perovskites.

Looking to oxide free interfaces, the covalent attachment of organic transport materials is necessary in minimizing oxidation under ambient conditions. Further, precise control of the organic-ETL depth is can be easily controlled by reagents and reaction conditions. The variability of the imidization chemistry allows for the attachment of longer rylene molecules or the repeated attachment of perylene molecules to form longer "chains" attached to the surface.

We also envision that the attachment of perylene monolayers to oxide surfaces will alleviate lattice strain issues associated the mismatch of differing crystal faces and lattice lengths between substrates and perovskite thin films. Soft,

flexible layers of organic molecules on metal oxide substrates have already been shown to increase of perovskite efficiency.[80−81,268] As we have previously shown, amine-terminated, oxide-free silicon surfaces are far more amenable to perovskite depositions and have shown commensurate increases in open-circuit voltage and short-circuit current values.[196]

We report perylene surface coverages as a function of the density of Si(111) atop sites particularly for consideration of how perylene derivatives may arrange on oxide free surfaces. Figure 4.8 displays top-down views of model Si(111) surfaces with a N-(p-trifluoromethylphenyl)-perylene-3,4-(aryl surface tether)-9,10-carboxyimide species similar to surface **5a**. We present the molecular orientations with the long perylene axis aligned with [111] due to the [111]-parallel alignment of Si(111) atop bonds. Aryl imides as modeled in Fig. 4.8, surfaces **2–6**, and molecules **7**, **8**, and **10** demonstrate N–aryl bond alignment with the long axis of the perylene. However, the steric crowding of phenyl hydrogens with the carbonyl oxygens force an aryl imide plane rotation of >50° relative to the plane containing the perylene carbon species.[269−270] Thus, we would expect the perylene long axis to align parallel to a Si [111] vector as depicted in Fig. 4.8. Importantly, Fig. 4.8 presents the perylene species with relevant van der Waal atomic radii to elucidate crowding and steric considerations involved in packing perylene on silicon surfaces. Frames **A–C** respectively considerer regular, idealized geometries arranged with 1-in-3, 1-in-4, and 1-in-7 atop site packing, and include an adlayer unit cell. The Si(111) (1 × 1) surface cell highlighted in frame **C** has an edge length $a_{Si(111)} = 0.384$ nm as derived from a $\frac{\sqrt{2}}{2}a_{Si(100)}$ transformation, where $a_{Si(100)}$ = 0.543 nm is the length of one side of the cubic Fd$\bar{3}$m (space group 227) silicon fcc unit cell. A regular, idealized 1-in-3 adlayer packing arrangement, or ~33% coverage would adopt a ($\sqrt{3} \times \sqrt{3}$)R30° surface unit cell, while a 1-in-4 packing arrangement of 25% coverage would adopt a (2 × 2) surface unit cell and a 1-in-7 packing arrangement of ~14% coverage would adopt a ($\sqrt{7} \times \sqrt{7}$)R(tan$^{-1} \frac{\sqrt{3}}{5}$)° cell where tan$^{-1} \frac{\sqrt{3}}{5} \approx 19.1°$. The ~14% packing in frame **C** is particularly relevant to the present work as that approximates well the ~15% coverage of perylenes in surface **2a** and the ~10% coverage functionalized perylenes in surface **5a**. While the surfaces studied herein would obviously not adopt such an ideal, regular geometry as in Fig. 4.8**C**, that picture remains relevant for visualizing an average coverage that should exist for the experimental results. Visualization of van der Walls radii further illustrates that while the adlayer molecules in frame **A** do not collide per se, achieving 33%, or 1-in-3 atop derivatization may be challenging to achieve and may not be desirable for tandem junction PV. Such dense perylene films as in Fig. 4.8**A** would demonstrate little flexibility due to steric crowding and may not demonstrate strong adhesion to idealized binding sites on a subsequently deposited such as a perovskite with a cubic or pseudo-cubic unit cell. As many solar-relevant perovskite cubic and pseudo-cubic unit cell lengths
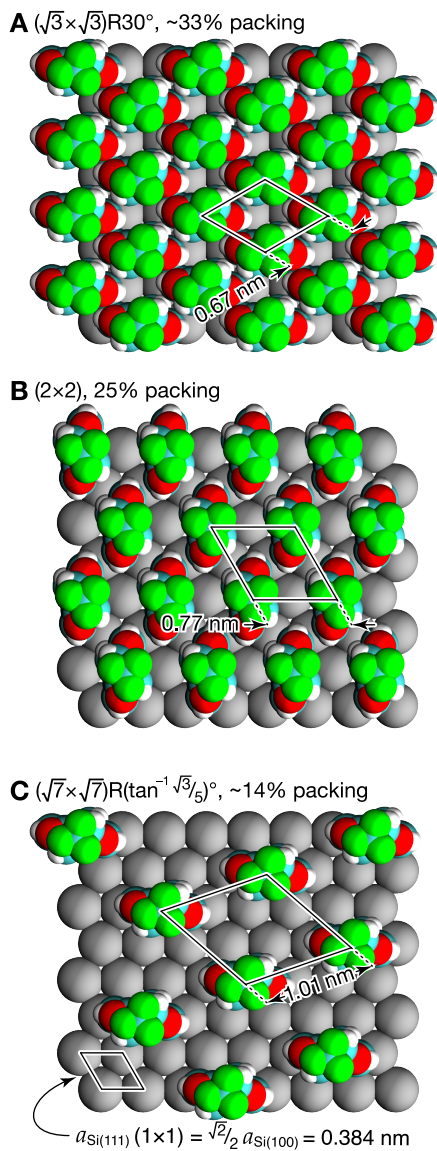
Figure 4.8 Idealized models of regular packing of vertically oriented, covalently bound perylene adlayer molecules with (**A**) 1-in-3, (**B**) 1-in-4, and (**C**) 1-in-7 packing densities on oxide-free silicon surfaces. Each frame contains a representation of the adlayer unit cell and dimensions.

are 0.5–0.6 nm, a terminal ammonium with ~14% $(\sqrt{7} \times \sqrt{7})R(\tan^{-1} \frac{\sqrt{3}}{5})°$ packing and ~1.01 nm spacing may be able to substitute at every other A-type cation site at a perovskite interface. Analyses of such packing, interactions, and adhesion merits further study.

4.6   Conclusions

We covalently functionalized silicon and TiO_2 substrates with derivatives perylene and demonstrated further derivatization of the surface attached perylene species. Coverage of perylene species was ~15% as determined by X-ray photoelectron spectroscopy and interpretations of photoelectron feature areas by a substrate overlayer model. Derivatization of perylene cyclic anhydrides by aryl amines including *p*-trifluoromethylaniline demonstrated coverages of ~10% and *p*-phenylenediamine reaction demonstrated no detectable quantity of unreacted anhydride sites.

The procedures detailed above yield perylene-functionalized surfaces with the potential to attach a variety of terminal functional groups. The successful secondary functionalization of perylene-containing surfaces with terminal amines paves the way toward chemically gluing perovskites to silicon surfaces with well-defined, covalently attached species that demonstrate controllable band-level tuning and high conductivity. Future microscopy and spectroscopy studies will address the coverage, orientation, and packing of the perylene and derivatized perylene moieties on the silicon surfaces. Additional studies will examine the interfacial electronics at surface-attached perylenes and explore the effects on charge-carrier dynamics in perovskite photovoltaic applications.

CHAPTER 5

PERYLENE-FUNCTIONALIZED TIO$_2$ INTERFACES FOR ENHANCED CARRIER SELECTIVITY IN MAPBI$_3$ PEROVSKITE DEVICES.

5.1 Introduction

High-performance organic-inorganic perovskite solar cells have finally reached point where they are competitive with traditional photovoltaic materials, including silicon, CIGS, and III–V materials.[46] Numerous companies have been started to utilize perovskite materials for commercial photovoltaics including Oxford PV, Toshiba, Panasonic, Tandem PV, and Energy Materials Corp.[271] The best single-junction perovskite efficiencies were extracted by tuning the stoichiometries[42] of the cations and anions. A (FAPbI$_3$)$_{0.92}$(MAPbBr$_3$)$_{0.08}$ perovskite recently showed near 23% efficiencies[44] and the record perovskite efficiency is 25.2%,[26] likely held by a similar material. As important as the absorbing material itself, are the materials that surround the perovskite in efficient solar cells: carrier-selective transport materials.

Electron transport layers (ETL) and hole transport layers (HTL) are integral elements of high-efficiency photovoltaic devices.[272] The quality of the ETL has a greater effect on the conversion efficiencies and V_{oc} of perovskite cells and thus receives a great deal of academic interest.[47,60,62,83,85–86,238,253,273] Metal-oxides have been widely employed as ETLs, especially TiO$_2$, which has ideal band-energy alignments for transporting electrons and blocking holes in organic-inorganic n-i-p type perovskite devices.[62] Defects at the TiO$_2$/perovskite interface, including Ti^{3+} states, have been shown to suppress electron charge-extraction, deleteriously impacting the device performance.[274] Passivation strategies have including doping the TiO$_2$ layer with metals and salts, as well as functionalization with semiconducting organic molecules.[85]

Fullerene derivatives have been recently found use as a soft, interlayer at the TiO$_2$/perovskite interface[275] which provide the aforementioned passiva-

tion effects and a soft contact to defects arising from lattice mismatch.[240] While PCBM has desirable characteristics including ideal conduction band alignment and fast charge-carrier mobilities, ultra-thin films are difficult to deposit without domain-formation or pinhole defects for shunt resistances.[88] Fullerenes are sometimes incorporated into polymers to aid in the uniform deposition of thin films, however, the insulating polymers add series resistance to the cell.[80] Further, fullerenes are difficult to functionalize, for the purposes of tuning the electronic properties and increasing their adhesion with chemical handles, and purification processes are costly to produce material at scale.

Inexpensive, tunable, perylene diimides (PDI) present an appealing alternative to the passivation of TiO_2 surfaces at the TiO_2/perovskite interface. Perylene derivatives have been studied for over a century and have been utilized industrially as dyes and pigments, resulting in inexpensive precursor materials. Perylenetetracarboxylic dianhydride (PTCDA) is particularly compelling as anhydride to imide conversion reactions present easy routes toward a wide range of chemical attachments that improve solubility and functional moieties that increase surface adhesion.[91,261−262] Further, the bay-position derivatization with electron-donating and withdrawing groups offer tunability of the HOMO-LUMO gap and sensitive alignment of the absolute energy levels.[91] PDIs have shown promise as the sole electron transport layers in perovskite cells with efficiencies exceeding 15%.[253] However, without covalent surface functionalization strategies, these PDI multilayers are typically spin-coated with variable thicknesses depending on the specific PDI solubility and deposition parameters.

In this work, we prepared $MAPbI_3$ perovskite devices utilizing the $MAPbI_3$ ETLs, which were functionalized with covalently attached PDIs, following chemical strategies we recently reported.[276] PDI-functionalized surfaces displayed ideal band-energy alignments to facilitate efficient electron transfer between $MAPbI_3$ and TiO_2. Despite the increased resistance in PDI-functionalized devices compared to bare TiO_2, perylene containing surfaces displayed enhanced charge extraction when compared to silane derivatized TiO_2.

5.2   Experimental

5.2.1   Materials and Chemicals

TiO_2 thin films were deposited on fluorine-doped tin oxide (FTO)/glass slides with a surface resistivity of ~7 Ω cm^{-1}, (Sigma-Aldrich). A Millipore Milli-Q system provided 18 MΩ cm resistivity water for all water requirements. Solvents for cleaning FTO slides and TiO_2 films include acetone (99.5% min, Fisher Chemical), methanol (MeOH, 99.9% min, semiconductor grade, Alfa

Aesar), isopropanol (IPA, 99.8% min, technical grade, Acros Organics), and toluene (99.7% min, Alfa Aesar). Kapton tape (McMaster-Carr) with an acrylic-based adhesive was used to the etching and patterning of various layers in the device. Etching of the FTO utilized hydrochloric acid (HCl, certified ACS Plus, Fisher Scientific) and zinc dust (98%, Acros Organics).

Chemicals employed in the deposition of TiO_2 thin films on FTO include titanium(diisopropoxide)-*bis*-(2,4-pentanedionate) (75% in isopropanol, Alfa Aesar), *n*-butanol (99.5%, Acros Organics) to form 0.15 M and 0.30 M solutions. Deposition of mesoporous TiO_2 layers utilized transparent titania paste (Sigma Aldrich).

The solution utilized in the silanization of TiO_2 surfaces consisted of 4 mM *p*-aminophenyltrimethoxysilane (90%, Gelest) in toluene that was previously dried for >24 h over freshly activated 3Å molecular sieves. The silane solution in toluene was freshly prepared in a nitrogen-purged flush box to minimize water-catalyzed silane polymerization.

The reagents used in the attachment of perylene to surfaces and subsequent further functionalization steps included perylene-3,4,9,10-tetracarboxylic dianhydride (PTCDA, 97%, Sigma-Aldrich), dimethylformamide (DMF, 99.8% min, Alfa Aesar) 1,8-diazabicyclo[5.4.0]undec-7-ene (DBU, 98% min, Alfa Aesar), Ethanol (EtOH, dried over sieves, denatured, 92%, Alfa Aesar), and *p*-phenylenediamine (sublimed ≥99% Sigma) that were all used as received. 4-bromoaniline (98% min, Alfa Aesar) and imidazole (99% min, Acros Organics) were utilized in the synthesis of molecular perylene surface-analogs.

The solution used in the deposition methylammonium lead iodine thin films contained DMF, dimethylsulfoxide (DMSO, 99.9%, certified ACS, Fisher Chemical), lead iodide (PbI_2, 99.999%, Alfa Aesar), and methylammonium iodide, MAI, synthesized according to a previously reported procedure. Diethyl ether (>99%, certified ACS, Fisher Chemical) was used as an antisolvent.

Copper thiocyanate (CuSCN, 96% min, Alfa Aesar) and diethyl sulfide (98%, TCI) made up the solution used to deposit the hole-blocking layer. Gold wire (Au, 99.99%, Kurt J. Lesker) was used for thermally evaporated contacts.

5.2.2   Surface Preparation and Functionalization

FTO slides were diced into ~4 cm^2 pieces then sequentially rinsed in acetone, IPA, and H_2O to remove any glass powder and organics which may prevent the etching of the FTO before drying with argon. Kapton tape masked the center and one edge of the FTO slides. The remaining edges were etched away by a mixture of powdered zinc and 1 M HCl for two minutes. After the FTO was etched, the samples were rinsed with H_2O, sonicated in dilute HCl to ensure to removal of all Zn, and rinsed once more with H_2O. The tape was removed and the samples were sonicated sequentially in acetone, IPA, and

H$_2$O to ensure any adhesive residue left from the Kapton tape was removed. The samples were then dried under a flow of argon and further dried in an oven at 100 °C.

Prior to the deposition of the compact TiO$_2$ layer, Kapton tape was a reapplied to the remaining FTO edge to maintain an uncovered, conductive contact for device measurements. The c-TiO$_2$ layer was deposited by first covering the sample with the 0.15 M titanium precursor solution and spin coating at 4000 RPM for 30 s. After drying the sample at 100 °C for 5 minutes, the process was repeated with the 0.30 M titanium precursor solution. The Kapton tape was removed and the samples were annealed for 2 h in 500 °C tube furnace. Once the samples had cooled, they were returned to the spin coater and covered with the TiO$_2$ paste before spinning at 4000 RPM for 30 s. The samples were dried and annealed for another two hours at 500 °C.

The following organic functionalizations were conducted in an air ambient. Ammonium-terminated, perylene-functionalized TiO$_2$ surfaces were prepared according to a previously published procedure.[276] Mesoporous TiO$_2$ surfaces were plasma cleaned to remove organic contamination. After plasma cleaning, surfaces were dipped in 18 MΩ cm deionized water to terminate the surface with –OH groups and prevent "radical gettering" of ambient organic species. After drying in an oven, the samples were submerged in the 4 mM *p*-aminophenyltrimethoxysilane solution in toluene for 4 h at 70 °C in sealed test tubes to prevent solvent evaporation and exclude additional ambient humidity. The samples were then rinsed with toluene, followed by sequential sonication with toluene, MeOH, and H$_2$O. The samples were then dried by under argon and completely dried in a 100 °C oven.

The attachment of PTCDA was accomplished by a reaction between surface-attached aniline groups and the reactive "acid-ester" species of PTCDA. The acid-ester solution consisted of 5 mL DMF, 0.29 mmol PTCDA, 0.75 mmol DBU, and 1.70 mmol EtOH. The solution was stirred for 1 hour at 60 °C before submerging the phenylaminosilane-terminated TiO$_2$ samples. The surfaces reacted with the PTCDA solution for 72 h at 60 °C. The samples were then rinsed with acetone and sequentially sonicated in toluene, MeOH, and H$_2$O before drying with argon.

The terminal anhydride left by the previous reaction was converted to a terminal aniline with solution consisting of 5 mL DMF, 3.35 mmol DBU, 4.00 mmol EtOH, and 0.92 mmol p-phenylenediamine. The samples were submerged in the phenylenediamine solution for 72 hours at 80 °C. They were then rinsed with acetone, IPA, and H$_2$O, followed by drying under argon. The terminal amines were then converted to positively-charge ammonium groups via submersion in a dilute, aqueous HCl solution and dried under argon.

The depositions of the MAPbI$_3$ and CuSCN thin films were performed in a nitrogen-purged glovebox. A N$_2$ gas generator (Parker Balston model N2-45, Parker Hannifin, Lancaster, NY) maintained N$_2$ purity ≥99.5%. The perovskite solution contained 7.00 mmol DMF, 1.00 mmol DMSO, 1 mmol PbI$_2$, and 1.42 mmol MAI. The solution was stirred for at least 2 hours at 60 °C before use. Prior to deposition, the solution was filtered through a 45 μm PTFE filter to remove any undissolved solids that would disrupt film uniformity. Functionalized and bare TiO$_2$ surfaces were covered with the perovskite solutions before spinning at 4000 RPM for 30 s. With 10 s left in the spin cycle, 300 μL of diethyl ether was slowly syringed onto the surface to encourage crystallization of the film. The sample was then transferred to a 60 °C hot plate for 1 minute. The sample was then further annealed on a hot plate at 100 °C for 30 minutes. The 20 mg of CuSCN was dissolved in 1 mL of diethylsulfide and stirred for at least 2 hours. While the perovskite-coated samples were spinning at 4000 RPM, 35 μL of CuSCN solution was dripped onto the surface. Spinning continued for another 30 s. Gold contacts were thermally evaporated by the Rao research group onto the CuSCN films with an area of 0.13 cm^2.

5.2.3   UV-VIs Spectroscopy

Ultraviolet-visible spectroscopy (UV-Vis) was utilized to probe the optical band gap, $\mathbf{E}_g$ of thin films and molecular perylene derivatives. A Thermo Scientific Evolution 300 UV-Vis spectrometer utilized a transmission geometry to acquire the absorption characteristics of TiO$_2$, MAPbI$_3$, and CuSCN thin films on borosilicate glass slides. A Praying Mantis diffuse reflection accessory (Harrick Scientific, Pleasantville, NY) collected reflected light from molecular perylene samples to characterize the HOMO-LUMO gap. Tauc plots were prepared in IGOR Pro to determine the optical gap of materials. Absorption data was plotted as $(\alpha h v)^2$ if the material's optical gap was direct and $(\alpha h v)^{1/2}$ if indirect. Equation 2.38 determined $\mathbf{E}_{CBM}$ by adding the $\mathbf{E}_g$ values derived from the Tauc plots to UPS-quantified $\mathbf{E}_{VBM}$ values.

5.2.4   Solid-state Device Photovoltaic Characterization

A potentiostat (SP 300, Bio-Logic, Claix, France) acquired current-density–potential, J–E, scans as cyclic voltammograms at 100 mV s^{-1} in a nitrogen-filled glovebox that maintained O$_2$ levels below 2 ppm. Following IUPAC convention, figures and images represent anodic current as a positive value and cathodic current as a negative value.[214] A 1-sun calibrated, 150 W Xenon lamp provided illumination of the samples through quartz window at the bottom of the glovebox. The light intensity was calibrated with a Si photodiode (FDS100-Cal, ThorLabs) to a AM1.5G equivalent. Two Signatone S-750 joystick micropositioners enabled electrical contact of the potentiostat working and counter electrodes to the front and back contacts, respectively.
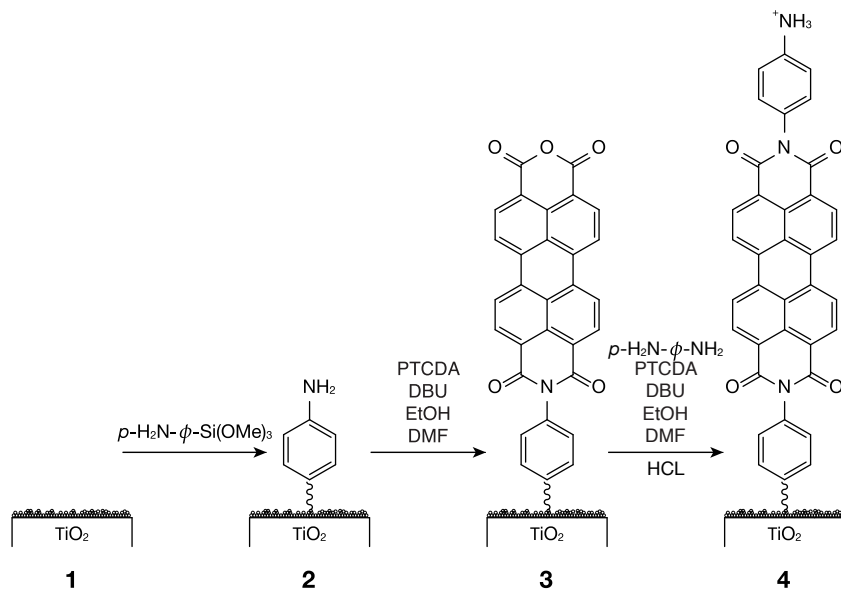
Figure 5.1   Anilinium-terminated-perylene monolayer attachment to m-TiO$_2$.

5.3   Results

Figure C.1 presents the XP spectra of the anilinium-terminated and of the perylene-functionalized TiO$_2$ surfaces. The spectra and peak-area ratios are consistent with those previously reported.[277] Figure 5.1 illustrates the functionalization steps of the mesoporous TiO$_2$ surface. Surface **1** denotes the bare m-TiO$_2$ surface, **2** represents the phenylaminosilane terminated surface, **3** is the covalently-attached, anhydride-terminated perylene surface, and **4** represents the anilinium-terminated-perylene surface.

5.3.1   Band-energy alignment of functionalized TiO$_2$ surfaces

A combination of ultraviolet photoelectron spectroscopy and UV-Visible spectroscopy determined the band-energies of semiconductor surfaces as each layer was deposited or derivatized. UP spectra were acquired during each step of the TiO$_2$ functionalization which included the bare m-TiO$_2$ surface, phenylaminosilane terminated surface, the PTCDA terminated surface, and the anilinium-terminated, perylene-functionalized surface.

Figure 5.2 presents representative UP spectra for each surface spectra presented separately with their respective **E**$_{SEC}$ and **E**$_{VBM}$ linear regressions in the §C.2. **E**$_F$ and **E**$_{VBM}$ values were calculated with eqs 2.36 and 2.37 and averaged across at least 3 samples per surface and reported in Table 5.1.
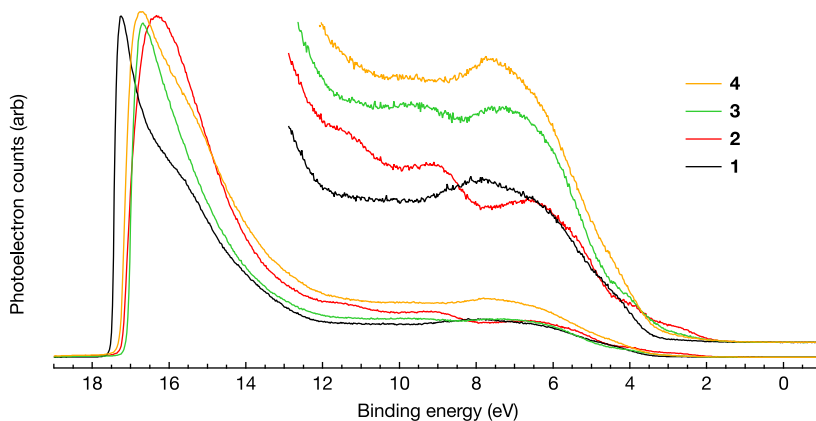
Figure 5.2 Normalized UP spectra of TiO₂ surfaces at each step of the perylene functionalization. The high-kinetic energy region is magnified by 4× with respect to the secondary electron cutoff. Surface **1** is bare m-TiO₂, **2** is the phenylaminosilane terminated TiO₂, **3** is anhydride-terminated-perylene-functionalized surface, and **4** is the anilinium-terminated perylene-functionalized surface.
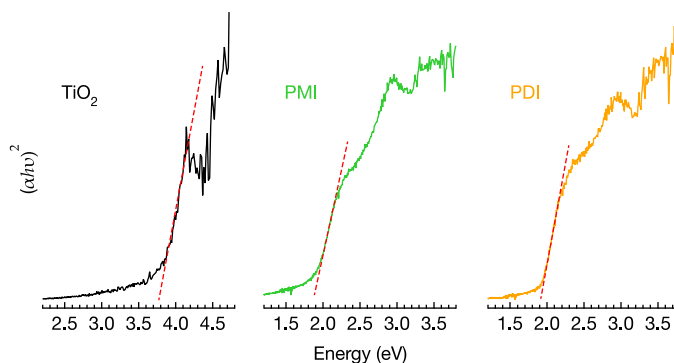
Figure 5.3 Tauc plots for m-TiO₂, perylene monoimide (an analog for surface **3**), and perylene diimide (an analog for surface **4**). The HOMO–LUMO gap of each molecule is fit and labelled with linear extrapolations to its x axis. Note: the fit for the m-TiO₂ E_g appears to intersect at 3.7 eV, yet 0 absorption falls far below the x axis in that spectrum.

The determination of the conduction band minimum, E_{CBM}, necessitated the determination of the HOMO-LUMO gap of the analogous perylene molecules on the surface being probed. *N*-(*p*-bromophenyl)-perylene-3,4-carboxyanhydride-9,10-carboxyimide and a *N,N'-bis*-(*p*-bromophenyl)-perylene-3,4:9,10-dicarboxyimide were chosen as analogs for functionalized TiO₂ surfaces **3** and **4**, respectively. Figure 5.3 presents three Tauc plots for bare TiO₂ and both perylene molecules. The TiO₂ film and both perylene molecules
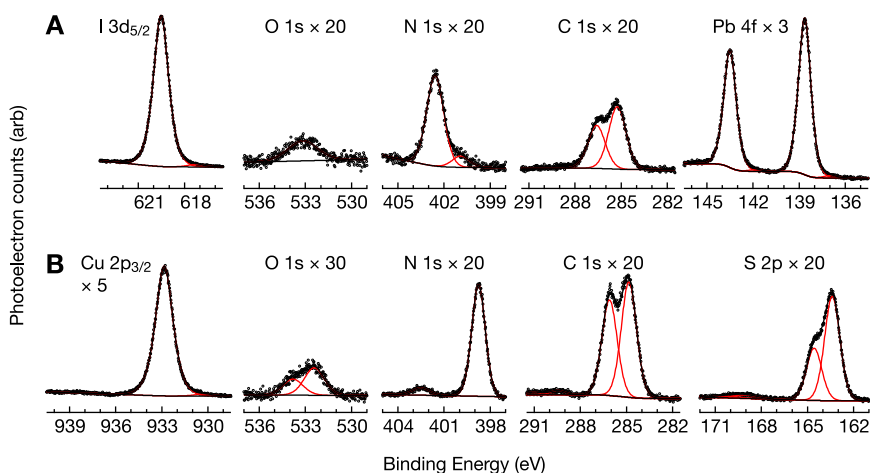
Figure 5.4   XP spectra of MAPbI$_3$ and CuSCN thin films. Frame (**A**) contains the I 3d, O 1s, N 1s, C 1s, and Pb 4f XP spectra for a MAPbI$_3$ thin film on TiO$_2$. Frame (**B**) presents the Cu 2p, O 1s, N 1s, C 1s, and Si 2p spectra of CuSCN on MAPbI$_3$.

were considered to have direct transitions.[278] Direct-transition materials contain linear edges fit to 0 absorption at the energy of the band gap when absorption is plotted as $(\alpha h\nu)^2$, where α is absorption and $h\nu$ is the radiation energy. The raw UV-Vis spectra are provided in the §C.3. Table 5.1 presents the electronic and optical data required for the determination of the band-energy alignment of the functionalized TiO$_2$ surfaces. The HOMO-LUMO gap values acquired from the Tauc plots in Fig. 5.3 plots were added to **E**$_{VBM}$ to yield **E**$_{CBM}$.

5.3.2   Deposition of MAPbI$_3$ and CuSCN thin films

Both the MAPbI$_3$ perovskite thin film and the CuSCN hole transport layers were deposited by spin coating. The chemical compositions of both the MAPbI$_3$ and CuSCN thin films were characterized by XPS and the high-resolution spectra are presented in Fig. 5.4, respectively. The I 3d, O 1s, N 1s, Pb 4f, and C 1s XP spectra for MAPbI$_3$ presented in frame **A** are similar to previously reported spectra for single crystal MAPbI$_3$.[277] The I 3d$_{5/2}$ spectrum consists of large feature at 619.5 eV at originating from the I$^-$ species in the perovskite. The small feature at 617.3 eV likely originates from a small amount PbI$_2$ near the surface. We attribute the single O 1s feature at 533 eV to adventitious organic species adsorbed prior to analysis. Metal-oxide O 1s features originating from PbO$_x$, which would be located ~530 eV, are absent from the spectra. The N 1s spectrum consists of two features located at 402.5 and 401 eV which are ascribed to –NH$_3^+$ and –NH$_2$, respectively. The Pb spectrum is dominated by the 4f$_{7/2}$ feature at 138.6 eV,

Table 5.1 Electronic properties determined by ultraviolet photoelectron and UV-Vis spectroscopies.[a]

Surface	E_g	E_{SEC}	Φ_S	E_F vs E_{vac}	(E_F−E_{VBM})	E_{VBM} vs E_{vac}	E_{CBM} vs E_{vac}
1	3.2	17.42 ± 0.07	3.81	−3.81	3.35 ± 0.03	−7.16 ± 0.10	−3.96
2	n/a	17.14 ± 0.07	4.08	−4.08	1.80 ± 0.03	−5.88 ± 0.10	n/a
3	1.9	17.12 ± 0.01	4.11	−4.11	1.70 ± 0.04	−5.81 ± 0.05	−3.91
4	1.9	17.25 ± 0.05	3.97	−3.97	1.64 ± 0.04	−5.61 ± 0.09	−3.71

[a] Band gap/HOMO-LUMO gap (E_g), secondary electron cutoff (E_{SEC}), work function of the surface (Φ_S), Fermi level (E_F), which is the opposite sign of Φ_S, ($E_{CBM} - E_{VBM}$) determined by the linear regression of the edge at high kinetic energy of the UP spectrum, valence band maximum (E_{VBM}), and conduction band minimum (E_{CBM}) energies for each step of the TiO_2 functionalization given in eV. E_g and E_{CBM} were not determined for surface **2** as the phenylaminosilane molecule is not a semiconductor. The Φ_S and E_F values share the same standard deviations as E_{SEC}, while E_{VBM} error is propagated by taking the sum of errors from E_{SEC} and ($E_{CBM} - E_{VBM}$). All values are reported in eV.
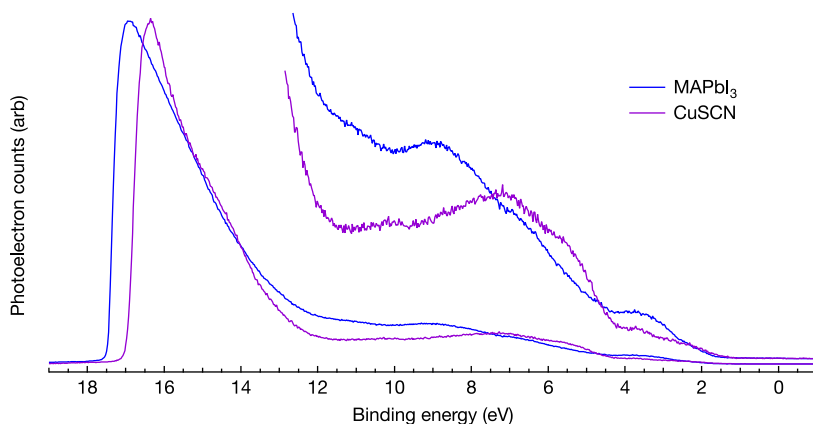
Figure 5.5   Representative UP spectra from MAPbI$_3$ and CuSCN surfaces on surface **4**. The max counts at the onset of emission have been scaled. The valence region has been magnified 6× to help view the view the Fermi edge.

attributed to Pb^{2+} in the MAPbI$_3$ crystal structure. A small shoulder is present at 137 eV which is likely attributed to PbI$_2$ or reduced Pb^0. The C 1s region consists of two features located at 286.6 and 285.2 eV which we attribute to methylammonium and adventitious carbon species, respectively. The lack Ti 2p signal, reported in the Fig. C.2, indicated that the MAPbI$_3$ thin film was relatively pinhole free within XPS detection limits.

Frame **B** of Fig. 5.4 presents the XP spectra of a CuSCN thin film deposited on the MAPbI$_3$ layer. The Cu 2p spectra consists of the two photoelectron peaks at 932.9 and 930.3 eV which are ascribed to CuSCN and Cu^0. The O 1s signal is composed of two features at 533.8 eV and 532.4 eV which we attribute SO$_4$$^{2-}$ and adventitious oxygen species. The N 1s spectrum contains two features at 402.5 and 398.8 eV that attributed to CuSCN. The C 1s spectrum contains four features at 291.1, 289.5, 285.6 and 284.5 eV. We ascribe the two higher binding energy features to oxidized O–C–N species and the remaining peaks to thiocyanate and adventitious contamination. The S 2p spectrum consists of the two doublets with the 2p$_{3/2}$ feature of each located at 169.2 and 163.4 eV. These features originate from SO$_4$$^{2-}$ and CuSCN. Figure C.3 presents the additional XP spectra for the CuSCN thin film which show small peaks I 3d and Pb 4f peaks. The presence of peaks from the underlying MAPbI$_3$ film indicate small pinhole defects within the CuSCN layer.

5.3.3   Band-energy alignment of MAPbI$_3$ and CuSCN

Figure 5.5 presents the representative UP spectra of MAPbI3 (blue) on functionalized TiO$_2$ surfaces and CuSCN (purple) deposited on those same MAPbI$_3$ thin films. Section C.2 provides each spectrum separately with their respec-
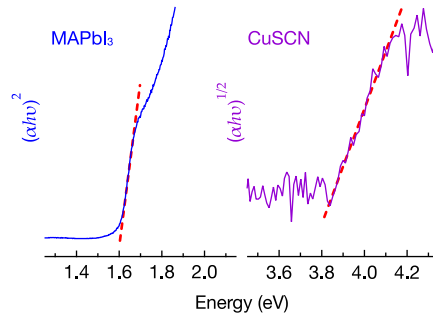
Figure 5.6   Tauc plots for MAPbI$_3$ and CuSCN thin films.
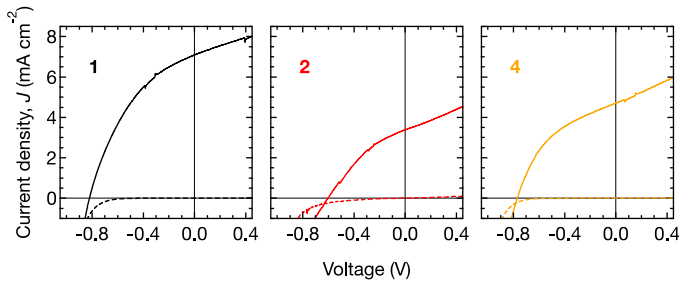
Figure 5.7   Current density-potential (J–E) curves representing performance of perovskite thin-film devices.   Three devices were tested that vary only in the functionalization of the m-TiO$_2$ surface including bare **1** m-TiO$_2$ in black, **2** a phenylaminosilane terminated surface in red, and **4** an anilinium-terminated-perylene surface in orange. Solid lines indicate forward-biased photocurrent and the dashed lines indicate scans in the dark.

tive linear regressions. For the MAPbI$_3$ surface, the location of $\mathbf{E_F}$, with respect to the $\mathbf{E_{VBM}}$, indicates the material is slightly n-type. The UP spectra for CuSCN thin films reveal the material is slightly p-type, consistent with literature values and its use as a hole-transport layer. The Tauc plots in Fig. 5.6 establish the band gaps for both MAPbI$_3$ and CuSCN utilized for the determination of the $\mathbf{E_{CBM}}$. CuSCN has been previously reported to be an indirect absorber, thus, absorption is plotted as $(\alpha h v)^{1/2}$. The energy levels for both materials are summarized in Table 5.2.

5.3.4   Current-density measurements of MAPbI$_3$ on functionalized TiO$_2$

Figure 5.7 presents representative current-density–voltage, J–E, scans for perovskite-functionalized TiO$_2$ devices. The three acquired J–E curves represented surfaces **1**, **2**, and **4** utilized as electron-transport layers in MAPbI$_3$ perovskite devices. The solid traces in Fig. 5.7 represent the scans acquired

Table 5.2   Electronic properties of MAPbI$_3$ and CuSCN layers determined by ultraviolet photoelectron and UV-Vis spectroscopies.[a]

Surface	E_g	E_{SEC}	Φ_S	E_F vs E_{vac}	(E_F–E_{VBM})	E_{VBM} vs E_{vac}	E_{CBM} vs E_{vac}
MAPbI$_3$	1.6	17.34 ± 0.07	3.88	–3.88	1.58 ± 0.02	–5.46 ± 0.09	–3.86
CuSCN	3.7	16.99 ± 0.02	4.23	–4.23	1.31 ± 0.02	–5.54 ± 0.04	–1.74

[a] All values are reported in eV.

under 1-sun calibrated, 150 W xenon lamp illumination. These devices were illuminated from the bottom up, through the glass substrate, FTO, and TiO_2 layers before reaching the perovskite active layer. The dashed lines correspond to J–E scans in the dark which verify that no photocurrent is produced. Open-circuit photovoltage and current-density values were averaged across twelve devices. Solid-state perovskite devices containing surface **1** showed an average V_{oc} of –817 mV and current-density of 7.2 mA cm^2. Interface **2** yielded a V_{oc} of –596 mV and current-density of 3.3 mA cm^2. Devices with surface **4** showed a V_{oc} of –748 mV and current-density of 3.9 mA cm^2. Bare m-TiO_2 devices, in general, showed slightly higher performance values than both **2** and **3**, however, the perylene-containing surface **4** showed higher V_{oc} and current-density values than **2**.

5.4   Discussion

5.4.1   Attachment strategies

The TiO_2 functionalization scheme from Fig. 5.1 followed a strategy we previously reported.[276] Based on the surface coverages determined for phenylaminosilane on SiO_x surfaces, it is likely that the TiO_2 surface **2** is covered by 1–2 ML of silane. Coverages for surfaces **3** and **4** should also maintain similar fractional surface coverages of ~10% which will increase the adhesion of perovskite thin films and enhance the carrier-selectivity of the interface.

5.4.2   Probing the electronic structure of functionalized TiO_2 surface

Ultraviolet photoelectron and UV-visible spectroscopies enabled the characterization of the band-energy alignment of surface energy levels. UPS determined that the surface work function Φ_S of bare, m-TiO_2 surface, **2**, was 3.81 eV and the Fermi level, E_F, would be located at –3.81 eV. Subtraction of the (E_F – E_{VBM}) value from yielded an absolute E_{VBM} position located at –7.16. With a band gap, E_g, of 3.2 eV, acquired by UV-Vis, the TiO_2 film was determined to be degenerately n-type. Adding the band gap to E_{VBM} yielded a E_{CBM} of –3.96 eV. E_F lies at a more positive energy than the E_{CBM}, though it should lie somewhere within the gap. This is due to the two distinct spectroscopies which will yield slight variations in energies, however, the Fermi level is likely pinned to the E_{CBM} between –3.8 and –3.9 eV.

Perylene derivative molecules were synthesized as analogs of the surface-attached species to enable band gap quantification by UV-Vis. The N-(p-bromophenyl)-perylene-3,4-carboxyanhydride-9,10-carboxyimide and N, N′-bis-(p-bromophenyl)-perylene-3,4:9,10-dicarboxyimide (analogs for surfaces **3** and **4**, respectively) were characterized by a diffuse reflectance with a diffuse reflectance accessory which determined the absorption of light as a function of radiation energy. TiO_2 and perylene species have previously been reported

as direct-gap absorbers, thus, light absorption was graphed as $(ahv)^2$ to determine the HOMO-LUMO gaps. Both perylene derivatives yielded HOMO-LUMO gaps of 1.9 eV, consistent with previously reported molecules. Future work will investigate opening or narrowing of the gap to tune surface energy positions by the addition of electron withdrawing and donating groups at the bay positions of the perylene. HOMO-LUMO gap values were utilized to quantify the position of E_{CBM} on perylene functionalized surfaces.

The high-resolution UP spectra of the valence band regions of functionalized TiO$_2$ surfaces, **2–4**, revealed attenuation of the sub-valence band electronic states, derived from O 2p orbitals.[279] New bands near and below the HOMO level appear upon functionalization with perylene groups. The bands centered around 11.5, 10, and 7 eV are attributed to lower-energy orbitals in the perylene aromatic systems, however, further characterization of these bands is beyond the scope of this work as contributions at these energies do not affect the carrier-transport mechanism.[280] The $(E_F - E_{VBM})$ values indicated the valence-band minimum-position referenced to the Fermi level. Analysis of the secondary electron cutoff on surfaces **3** and **4** yielded work functions near 4 eV. Absolute E_{VBM} positions were located between –5.6 and –5.8 eV, again yielding fairly n-type surfaces. The E_{CBM} of **4** was located at –3.7 eV, 0.2 eV lower than surface **3**, which was well aligned to the conduction band minimums determined for MAPbI$_3$. TiO$_2$ is already well aligned for selectively transporting electrons at the perovskite interface and blocking holes. Perylene species maintain that electron selectivity with an E_{CBM} well positioned near the bands both TiO$_2$ and MAPbI$_3$.

5.4.3   MAPbI$_3$ and CuSCN thin film morphologies

Smooth, mirror-like MAPbI$_3$ thin films were formed on all TiO$_2$ surfaces. Peak positions and stoichiometries of the MAPbI$_3$ surfaces were consistent with our previous studies.[277] XPS also corroborated the absence of pinholes in the film with lack of Ti 2p signal through the perovskite film. A small amount of S 2p photoelectrons originating from a SO$_4^{2-}$ species, attributed to CuSO$_4$, were present in the CuSCN thiocyanate surface which indicating a minute amount of oxidation of the CuSCN film.[281] Signals from both I 3d and Pb 4f were visible through the CuSCN thin film indicating the presence of holes in the layer. Future studies on high-performance devices will explore more robust hole-transport materials and deposition techniques, however, this study as this study is concerned with the electron transport layer, defects of the HTL should average across all devices.

5.4.4   Electronic structure of MAPbI$_3$ and CuSCN thin films

MAPbI$_3$ thin films demonstrated work function values of ~3.9 eV, which is consistent with other reported works.[282] The position of the E_{VBM} with respect
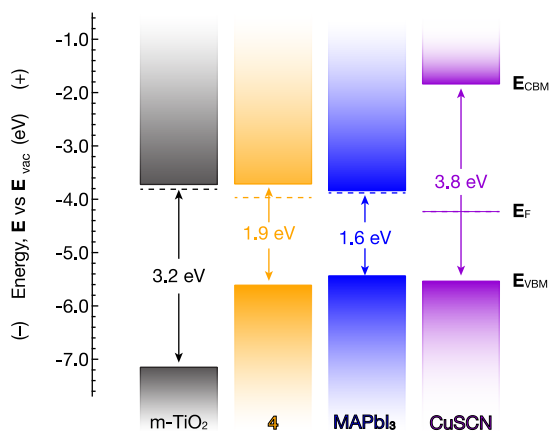
Figure 5.8 Band energy diagram that summarizes the non-contact E_g, E_{VBM}, E_{CBM}, and E_F positions of of m-TiO$_2$, surface **4**, MAPbI$_3$, and CuSCN.

to E_F indicates the film is highly n-type, possible due to iodine vacancies or reduced Pb^0 species close to the surface.[283] Ultraviolet photoelectron studies of the CuSCN layers quantified work average work function values ~4.2 eV, which put the E_{VBM} near –5.5 eV, confirming the p-type characteristics, consistent with previous reports.[272] Our bulk band gap determination of 3.7 eV puts the conduction band maximum at –1.8 eV, far above the calculated E_{CBM} of MAPbI$_3$, making the CuSCN a suitable hole transport and electron blocking layer.

5.4.5 Performance of functionalized-TiO$_2$-MAPbI$_3$ devices

The band-energy alignments of TiO$_2$/perovskite/CuSCN devices are illustrated Figure 5.8 which highlights the differences between bare and functionalized m-TiO$_2$ surfaces. Surface **4**, the anilinium-terminated, perylene-functionalized TiO$_2$ surface maintained ideal E_{CBM} alignment between the TiO$_2$ and MAPbI$_3$ layers for carrier-transfer of electrons.

In general, the bare m-TiO$_2$/perovskite-based devices display better photovoltaic performances than the other two surfaces tested. The decrease in V_{oc} and current-density is likely the result of resistant domains formed in the phenylaminosilane layer of functionalized TiO$_2$ interfaces. A better comparison of the perylene charge-transfer characteristics is made between surfaces **3** and **4**, which both contain the phenylaminosilane layer. The V_{oc} of surface **4** showed an increase of 25% compared to surface **3** and a similar increase in the current-density. Future studies on perylene-functionalized TiO$_2$ devices will utilize connecting layers which do not form resistant domains. Studies into other amine-terminated silane systems, such as APTES which is less likely

to form multilayers, and adsorbed carboxylic acid-terminated perylenes are currently underway.

5.5   Conclusions and future work

We characterized the electronic band-structure of perylene-functionalized TiO_2 surfaces. Uniform, pinhole-free $MAPbI_3$ films were formed on functionalized TiO_2 surfaces indicating the organic monolayer was compatible with the perovskite deposition procedures. We determined that perylene monolayers maintained the $\mathbf{E}_{CBM}$ values near 3.7 eV, which was well aligned to transport electrons from the conduction band of $MAPbI_3$ perovskites. The photovoltaic conversion efficacy of perylene-functionalized devices performed below those with bare m-TiO_2 surfaces. The anilinium-terminated perylene surface did, however, outperform the phenylaminosilane covered surface, indicating enhanced electron extraction at the TiO_2-perylene-$MAPbI_3$ interface.

Acknowledgements

PRESENT WORK AND FUTURE DIRECTIONS FOR PERYLENE INTERFACES ON TIO₂ AND TANDEM-JUNCTION SILICON/PEROVSKITE DEVICES

Current work on perylene-functionalized TiO_2 perovskite devices is focused on the connecting layer between the perylene and the imide. The current devices we have characterized used a phenylaminosilane to graft a monolayer of aniline groups to the TiO_2 surface. Reactions of aniline terminated surface with the reactive "acid-ester" perylene yielded covalently attached perylene which were further functionalized with terminal aminophenylimide groups. Characterization of the photovoltaic performance of these functionalized-TiO_2 devices resulted in perylene-functionalized surfaces having greater V_{oc} and current-density than the silane functionalized surface but both surfaces performed worse than the bare TiO_2 devices. The 150 mV increase from silane- to perylene-functionalized TiO_2 surfaces is a promising result for perylene diimides utilization as a soft, carrier-selective contact for perovskites.

The decrease in performance is attributed to series resistance created in the insulating silane layer. A single silane monolayer should not effect such a drastic increase in resistance, however, the phenylaminotrimethoxysilane is likely forming multilayer islands and domains across the TiO_2 surface. XPS and IR characterization of the phenylamino surface are unable to reveal the uniformity of the silane layer. High-resolution SEM or TEM experiments will help reveal the uniformity of these monolayers and guide the way toward optimizing the conditions in which monolayers are applied. APTES is an appealing alternative to aminophenyltrimethoxysilane as monolayers have been extensively studied and characterized.[134] The phenylaminosilane was chosen at first as it extended the aromatic system from the perylene down to the surface. Fortunately, short-chain alkyl groups from in APTES between the surface and perylene should not deleteriously affect the charge-transfer characteristics.[151,169,172−174] Separately, we are looking at the derivatization of perylene groups with carboxylic acid groups on one end and an ammonium

group at the other end. Carboxylic acids have previously been reported to form uniform monolayers on TiO_2 surfaces.[284] Pereylenedicarboxylic acid adsorption on TiO_2 nanoparticles has also been studied.[285] Carboxylic acids do not polymerize and functionalization methods have been optimized to exclude multilayers. Future studies involve the synthesis of dicarboxylic acid perylene species and characterization of the respective monolayers on m-TiO_2 films. Perovskite devices based on these functionalized TiO_2 surfaces will also be tested and further optimization of the $MAPbI_3$ and CuSCN layers will aid in the extraction of high conversion efficiencies.

Characterization of surface defects at the TiO_2 and $MAPbI_3$ interfaces with perylene remains underexplored. Thin-film XRD and photoluminescence (PL) will help reveal the nature of defects and their densities present at these interfaces at various steps of the device. The functionalization surfaces and presence of amine–terminated perylenes should passivate these interfacial defects, yielding lower defect densities. Cross-sectional TEM of these interfaces may also help characterize the quality of the interface, though sample preparation may prove difficult. In conjunction with these studies, charge-carrier dynamics of complete devices will be explored to corroborate the presence of or lack of defects.

Separately, we have also investigated the functionalization of oxide-free Si(111) surfaces with perylene monolayers. Perylene monolayers alone should provide the charge-carrier selectivity to transfer electrons from the perovskites while blocking wholes at the interface. Our intention is to synthesize mixed aniline/methyl monolayers and utilize the perylene attachment methods discussed in Chapter 4 to connected perylenes via an imide linkage.

For practical, oxide-free, tandem-junction silicon/perovskite devices with perylene as an electron-transport layer, an ohmic contact in the form of an n-p^{++}-n^{++} tunnel junction. Our monolayer functionalization studies utilized n$^+$-Si to simulate the tunnel-junction surface. Our first hurdle came with oxidation of H–n$^+$-Si surfaces which showed increased oxidation rates compared to the n-Si samples. N-type dopants increase the susceptibility of silicon surfaces toward oxidation due to higher free-electron densities.[286] The concentration of large dopants like arsenic near the surface act like defects, leaving the surface vulnerable to oxidation. Ammonium fluoride etch times were increased to 20 minutes and samples spent less than 30 s in air before being transferred to an argon containing reaction vessel to decrease the eliminate oxide formation prior to surface functionalization-passivation.

We first attempted to graft aniline groups to the surface through halogenation of the surface with bromine and arylation with lithiated aniline groups. The Rose group has previously reported efficient arylation of Si(111) surfaces between 20–50% coverage with lithium reagents.[170,176–177,287] We utilized 4-lithium-*N*,*N-bis*-dimethylaniline as an analog to determine the reaction conditions required to effect efficient coverage of surface-bound aniline groups.
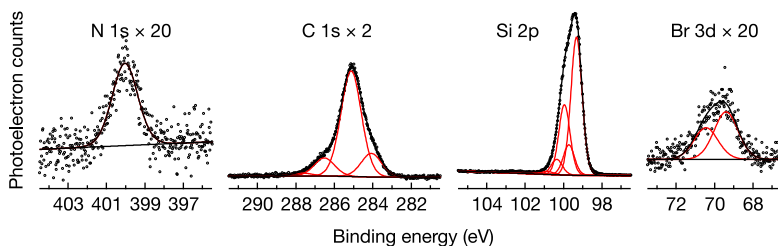
Figure 6.1 XP spectra of a mixed dimethylaniline/methyl monolayer on Si(111). Photoelectron counts of all spectra are scale to the Si 2p region.
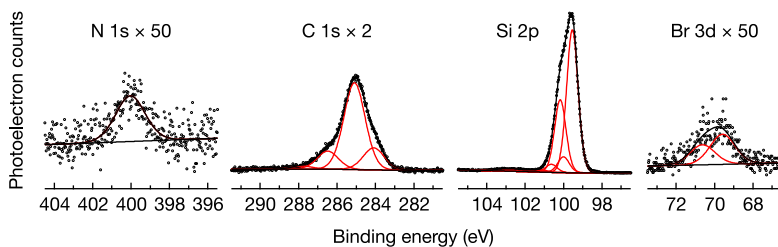
Figure 6.2 XP spectra of a mixed TMS-protected-aniline/methyl monolayer on Si(111). Photoelectron counts of all spectra are scale to the Si 2p region.

In our hands, we were unable to achieve surface coverages greater than 2–3% with lithiated dimethylaniline. We resorted to Grignard species, which necessitated longer reaction times and higher temperatures, but yielded surface coverages ~25%, evident by the N:Si ratio from a mixed methyl/dimethylaniline monolayer on Si(111) in Fig. 6.1.

We initially utilized 4-bromo-*N,N-bis*(TMS)aniline as a precursor for our Grignard reagent. The TMS groups protecting the amine group from the Grignard can easily be removed after grafting the molecule to the surface. Making our own Grignard allowed us to choose higher temperature solvents to increase the reaction temperatures enabling high surface coverages, however, the Grignard was difficult to synthesize without rigorous preparation of magnesium turnings and the commercial Grignard reagent in THF was also utilized. Surface coverages of the TMS-protected aniline were limited to ~10% (XPS shown in Fig. 6.2). We attribute this lower coverage to steric hindrance where bulky TMS groups have more trouble making it to the surface after some are initially attached. We believe this reaction can be optimized for higher surface coverages but other amine terminated alkyl groups will also be studied.

The aniline-terminated surfaces were reacted with perylene in the same manner as reported in Chapter 4. All wet-chemical reactions, including attach-
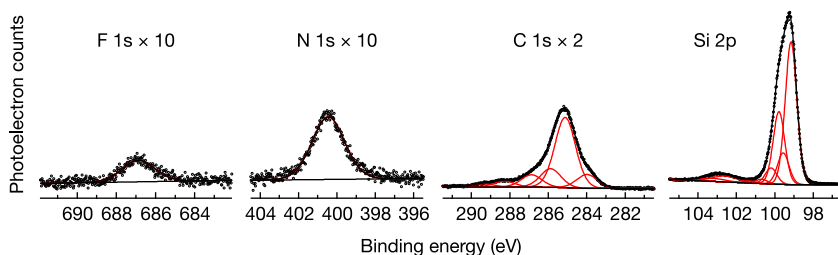
Figure 6.3   XP spectra of a fluorinated butylester perylene attached to an aniline/methyl monolayer on Si(111). Photoelectron counts of all spectra are scale to the Si 2p region.

ment of PTCDA to the surface, were performed under argon in degassed solutions to limit the rate of oxidation of the silicon. Figure 6.3 presents the fluorinated butylester perylene on "oxide-free" silicon. About 1 ML of oxide was still was still formed under these conditions, however, the coverage of PTCDA groups was ~10%, similar to coverages found in Chapter 4 on chemically oxidized Si(111) surfaces. There was also a strong increase in the N 1s signal, which still remains a mystery. Future investigations here will explore reaction conditions that yield lower oxidation of silicon.

Unlike the n-i-p TiO$_2$/perovskite devices, silicon/perovskite tandem-junction devices cannot be illuminated through Si and are typically illuminated through the perovskite layer first. Future investigations into these devices may include the deposition of ultrathin gold contacts, where light is still transmitted through the gold layer, or gold fingers to make contact with the hole transport layer. In our hands, we liquid photoelectrochemical methods as front contact/hole-collectors. THF was chosen as a solvent as both the CuSCN and MAPbI$_3$ films were relatively insoluble and ferrocene$^{+/0}$ and LiClO$_4$ were extremely soluble. Like Chapter 3, degenerately doped n$^+$-Si was used to only measure photoactivity of the perovskite and charge extraction at the perylene interface. So far, devices have shown only small V_{oc} values ~50 mV and more testing is required to utilize this technique in characterizing device performance. Once the oxidation due to perylene monolayer formation has been minimized and suitable device contact/testing method has been established, perylene monolayers should exhibit excellent charge-carrier selectivity at the Si/perylene/perovskite interface.

A

SUPPORTING INFORMATION AND FIGURES FOR CHAPTER 3

A.1 Bromination of Si(111) Surfaces

As mentioned in the Section 3.3.1, XPS quantified the Br 3d and Si 2p regions of three bromine-terminated Si(111) samples. These samples were hydrogen-terminated Si(111) that were brominated with a two-minute exposure to $Br_{2(g)}$. As previous reports demonstrate that halogenation of Si(111) yields an effectively 100%-terminated surface, photoelectron spectra of these surfaces provides a valuable validation of the substrate overlayer model.

To develop a prediction for $I_{Br\,3d}/I_{Si\,2p}$ that is relevant to a bromine-terminated surface as is relevant to the XPS data in Fig. A.1, we employed modified parameters for plugging in to eq 2.16. Firstly, we used $d_B = d_{Br}$ for the intimately contacting layers. Additionally, the silicon photoelectrons would be traveling through an overlayer consisting entirely of bromine. Because the
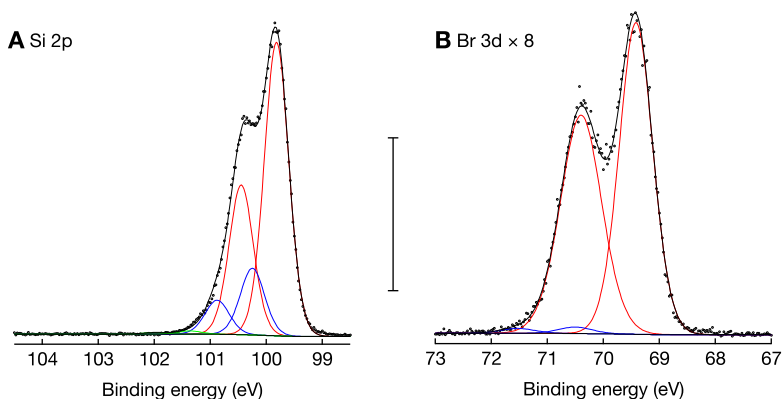
Figure A.1 XP photoelectron spectra of the (**A**) Si 2p and the (**B**) Br 3d regions for a hydrogen-terminated Si(111) wafer that was exposed to $Br_{2(g)}$ for two minutes, evacuated, and transferred expeditiously into the XPS load lock. A Shirley-type background and three p-type doublets denoted by the red, blue, and green traces fit the Si 2p region well, while a Shirley-type background and two d-type doublets denoted by the red and blue traces fit the Br 3d region well. We ascribe the red doublet in the Si 2p spectrum to bulk Si^0 and the blue doublet to interfacial Si bound to bromine atoms. For Br 3d, we ascribe the red doublet to bromine atoms that are covalently bound to Si(111) atop sites, while the trace blue doublet may represent a tail function on the otherwise Gaussian peaks. The scale bar represents 1000 cps for Si 2p in frame **A** and 125 cps for Br 3d in frame **B**.

kinetic energy of Si 2p photoelectrons is similar to the kinetic energy of Br 3d photoelectrons, we used λ_{Br} in place of $\lambda_{Si\,2p,Br}$. Finally, as we are considering 100% coverage of the Si(111) atop sites, we set N_{Br}/N_{Si} to $3^{-1/2}d_{Br}^{-1}/(2a^{-1})$. 100% Br–Si termination was confirmed with eq A.1.

$$\frac{I_{Br}}{I_N} = \frac{3^{-\frac{1}{2}}d_{Br}^{-1}}{2a^{-1}} \frac{\Phi_{Br}\left(1 - \exp\frac{-d_{Br}}{\lambda_{Br}\cos\theta}\right)}{\left(1 - \Phi_{Br} + \Phi_{Br}\exp\frac{-d_{Br}}{\lambda_{Si,Br}\cos\theta}\right)} \tag{A.1}$$

A.2   Adhesion Force Measurements

The atomic force microscopy (AFM) method involves bringing AFM tips (coated or uncoated) close enough for adhesive interactions to occur, Fig. A.2, part **A**. This is important to characterize the interfacial interaction or strength at the nanoscale. This ultimately causes the tips to jump into contact, part **B** in Fig. A.2. The tips then undergo elasticity as they are displaced further in the same direction, Fig. A.2, part **C**. Upon their retraction, the displacements are reversed, as the loads are reduced to zero, part **D** in Fig. A.2. However, the
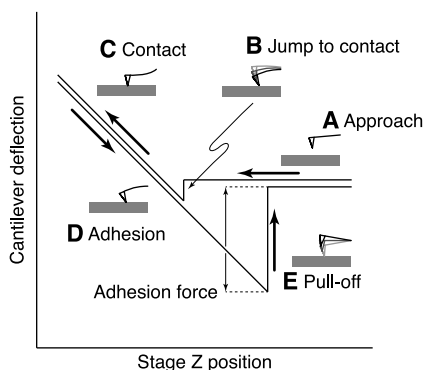
Figure A.2   Schematic of an atomic force microscope force-displacement behavior. (**A**) The AFM tip begins its approach toward the surface. (**B**) AFM tip undergoes a slight repulsive force before contact. The cantilever is deflected, represented a force between the tip and the surface. (**C**) Upon contact with the surface, the cantilever angle is further changed as the tip is pushed into the film. (**D**) as the AFM tip is pulled away, the deflection of the cantilever is representative of the force being applied to remove the tip. (**E**) The tip is pulled out and change in cantilever deflection at the pull-off point is representative of the force required to delaminate an area of perovskite film from the substrate.

tips do not detach at zero load, due to the effects of adhesion. Consequently, the retraction has to be continued until the adhesive interactions are overcome by the applied forces. This therefore results in the pull-off of the AFM tips from the substrates, Fig. A.2, part **E**. The resulting pull-off force, F, is a measure of the adhesion as quantified by Hooke's law, eq A.2, where k is the stiffness of the AFM cantilever and δ is the displacement of the AFM tip at the onset of pull-off.

$$F = k\delta \qquad\qquad (A.2)$$

A.3   Transflection infrared spectroscopy of alkylated Si(111)

The spectra for methyl, mixed methyl/allyl, and allyl terminated surfaces are provided in Fig. A.3. The negative peak at 2083 cm^{-1} indicates the negative signal of Si–H due to the background subtraction. As the surface becomes more constrained, more allyl groups, the Si–H signal becomes less negative indicating that more H–Si sites are left over after the functionalization compared to the methyl-terminated surface. The peak previously used to quantify the coverage by allyl groups is located at 1628 cm^{-1}.[152] We attribute a small feature at 1625 cm^{-1} to the allyl group. Two absorption signals can
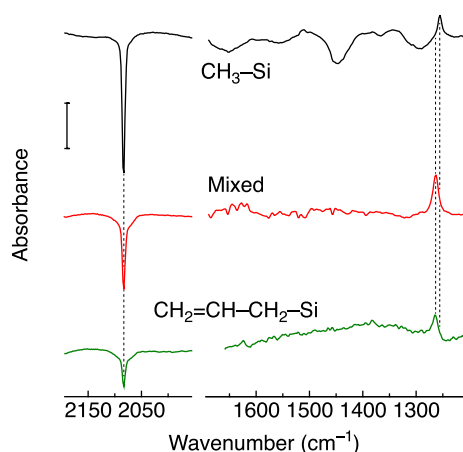
Figure A.3   Transflection infrared spectra of the methyl- (black, top), mixed allyl/methyl- (red, middle), and allyl-functionalized (green, bottom) Si(111) surfaces. Polynomial backgrounds were applied to flatten baselines, and the scale bar represents 1 milliabsorbance unit.   The strong negative feature at 2083 cm^{-1} ascribed to the Si–H stretch and positive feature at 1256 cm^{-1} ascribed to the symmetric – CH$_3$ "umbrella" bend indicates successful methylation and displacement of silicon-hydrogen bonds for the methyl-terminated Si(111) surface. For allyl-functionalized Si(111) (green), the weaker negative feature for the Si–H stretch indicates incomplete surface functionalization relative to the methylated surface as expected for the relatively larger allyl group and the commensurate increase in steric crowding. For allyl-functionalized silicon, we attribute the weak feature at 1625 cm^{-1} to the allyl C=C stretch, and the feature at 1265 cm^{-1} is ascribed to the CH$_2$ bend at Si–CH$_2$–CH=CH$_2$ and is further indicative of successful introduction of allylation of the Si(111). Mixed allyl/methyl monolayers demonstrate a larger negative Si–H feature as compared to the allylated surface and a broad feature due to both –CH$_2$– and –CH$_3$ bending modes.

be found at ~1260 cm^{-1}, the –CH$_3$ umbrella mode at ~1256 cm^{-1} and the Si–CH$_2$–R bend at ~1265 cm^{-1}. Due to their close proximity, the features cannot be differentiated in the mixed monolayer to quantify the relative ratios of each functional group in that monolayer.

Attempts to quantify further functionalized surfaces were also unsuccessful. The N–H stretches are too low in signal and are obscured by the large O–H band which persists even after long purges. C–Br stretches are either too low in signal to be detected or are beyond the range of the setup's MCT detector.

APPENDIX B

SUPPORTING INFORMATION AND FIGURES FOR CHAPTER 4

B.1   Synthesis of Functionalized Perylene-Based Comparison Molecules

The numbering scheme below represents the ordering that reflects their use as comparison molecules in the manuscript and reflects a non-linear ordering for their use as building blocks for the comparison molecules themselves. We re-include images of molecules **7–10** for ease of accessibility.

In brief, the molecular sequence starts with the activation of perylene tetracarboxylic dianhydride and stabilization/protection with butanol to form the tetraester species, **9**, that demonstrates good long-term stability in an air ambient. Controlled, stoichiometric addition of acid reactivates one side of the molecule to which the addition of a fluorine-containing aniline species yields **10**. Further addition of acid to **10** in the absence of a reacting aniline
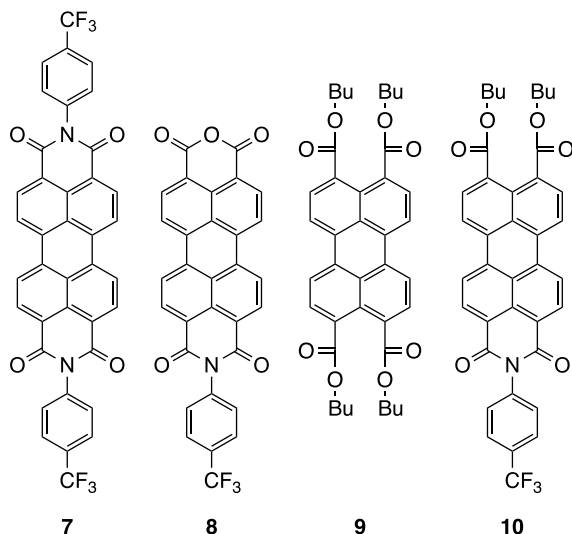
Figure B.1   Repeat of Fig. 4.2. Molecular perylene derivatives to serve as spectroscopic analogs for surfaces **2–6** when determining the absorption modes of relevant surface IR spectra.

or amine species yields **8** with its re-formed anhydride group. Lastly, we synthesized **7** from **8** by activation of the anhydride and reaction with the fluorine-containing aniline. Notably, alternative routes to **7** may have started with molecules **9** or **10**, or PTCDA itself as molecule **7** contains the same imide species. Our choice of starting material for the synthesis of **7** was one of practicality as it reserved the possibility of the formation of asymmetric imide molecules.

B.1.1   Tetrakis-(butyl)-perylene-3,4,9,10-tetracarboxylate, 9

4 g (10.2 mmol) of perylene-3,4,9,10-tetracarboxylic dianhydride (PTCDA) dissolved in 50mL of DMF in a round-bottomed flask. 5.52 mL (92.0 mmol) of n-BuOH and 4.52 mL (29.1 mmol) of DBU was added to the flask. The solution was stirred at 60 °C for 30 min. A solution of 6.52 mL (37.5 mmol) bromobutane and 60 mL of DMF was then added to the flask and stirring was continued for another 90 min at the same temperature. The precipitated solid **9** was filtered via vacuum filtration, washed with water, and dried.

B.1.2   Perylene-3,4-dibutylester-9,10-N-p-trifluoromethylaniline imide, 10

First, 3 g (4.79 mmol) of **9** was dissolved in 60 mL of heptane and 12 mL of toluene. 2.62 g (13.8 mmol) of p-TsOH $\cdot$ H$_2$O was added and the mixture was stirred at refluxing temperatures for 30 min. The flask was then

cooled and the solid filtered out with vacuum. The solid product was then washed with copious amounts of water and dried to yield perylene-3,4-dibutylester-9,10-monoanhydride. Directly following synthesis and isolation, 1.06 g (2.03 mmol) of perylene-3,4-dibutylester-9,10-monoanhydride was added to a flask with containing 25 mL of DMF, 0.420 mL (2.03 mmol) p-trifluoromethylaniline, and a catalytic amount of $ZnAc_2 \cdot H_2O$. This solution was refluxed for 20 h and solid **10** was collected and dried following vacuum filtration and sequential rinsing with water and ethanol.

B.1.3   Perylene-3,4-monoanhydride-9,10-N,N,-4-trifluoromethylaniline imide, 8

First, 0.926 g (1.39 mmol) of **10** was dissolved in 37 mL of toluene alongside 2 g (10.5 mmol) p-TsOH $\cdot$ H_2O. The solution was then refluxed for 20 h. The solid product was collected after vacuum filtration and washing with copious amounts of water. The product **8** was then dried in a 100 °C oven overnight.

B.1.4   Perylene-3, 4, 9, 10-N,N,-4-trifluoromethylaniline bisimide, 7

First, 0.200 g (0.37 mmol) of **8** was added to a round-bottomed flask containing 4 g of imidazole, 0.080 (0.44 mmol) $Zn(OAc)_2$ and 0.125 mL (1.02 mmol) p-trifluoromethylaniline. The flask was then purged was then heated to 140 °C and stirred overnight under atmosphere of argon for 24 h. After cooling, 20 mL of H_2O of was added to the flask and the solid product was collected via vacuum filtration. The crude product was then washed with H_2O and EtOH. The dark red product **7** was subsequently dried in a 100 °C oven overnight.

B.2   ATR-IR Spectra of Perylene-Based Comparison Molecules

Below are ATR-IR spectra of PTCDA and comparison molecules **7–10**.
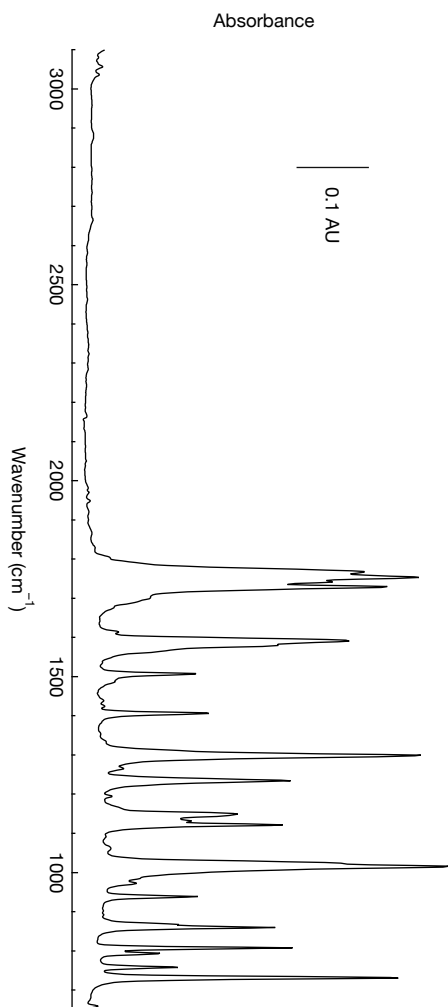
Figure B.2 ATR-IR spectrum of perylene-3,4,9,10-tetracarboxylic dianhydride, PTCDA.
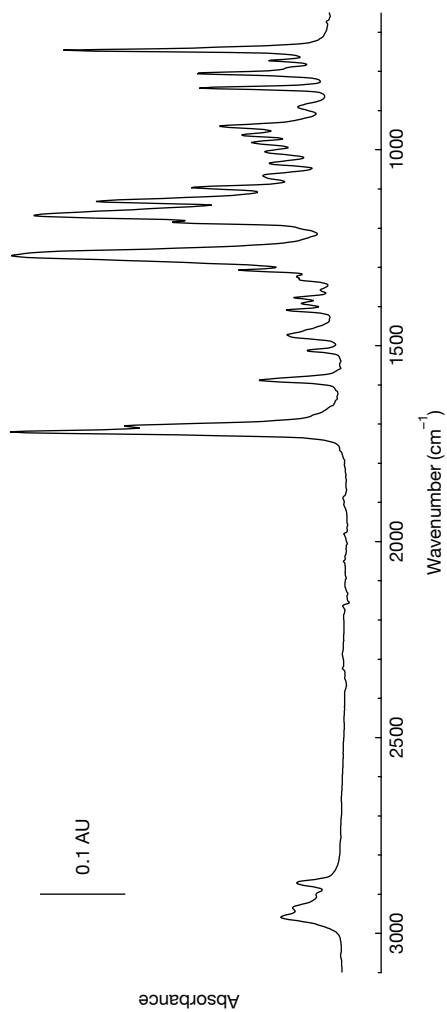
Figure B.3   ATR-IR spectrum of tetrakis(butyl) perylene-3,4,9,10-tetracarboxylate, **9**.
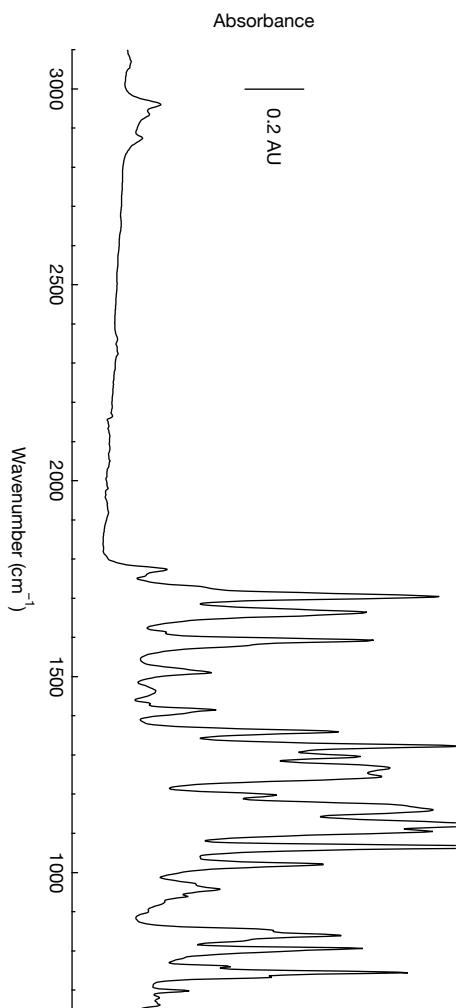
Figure B.4 ATR-IR spectrum of perylene-3,4-dibutylester-9,10-*N*-4-trifluoromethylaniline imide, **10**.
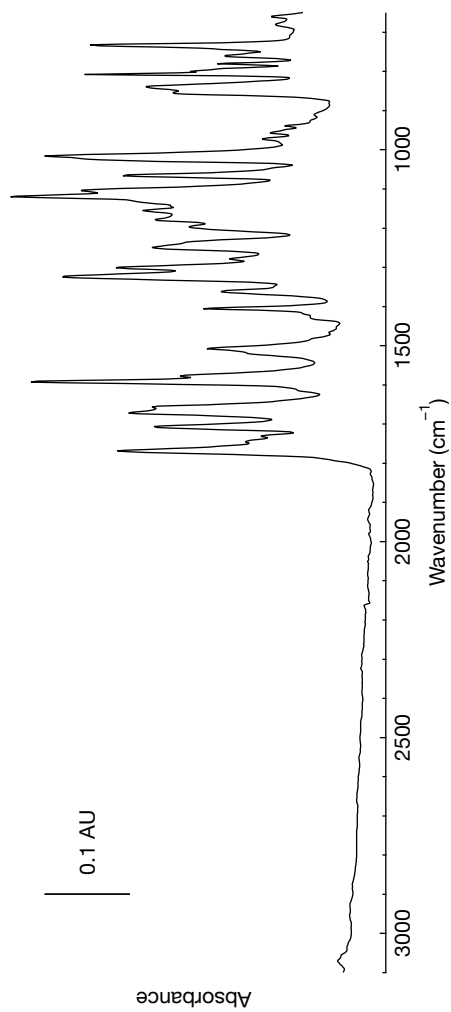
Figure B.5   ATR-IR spectrum of perylene-3,4-monoanhydride-9,10-N-4-trifluoromethylaniline imide, **8**.
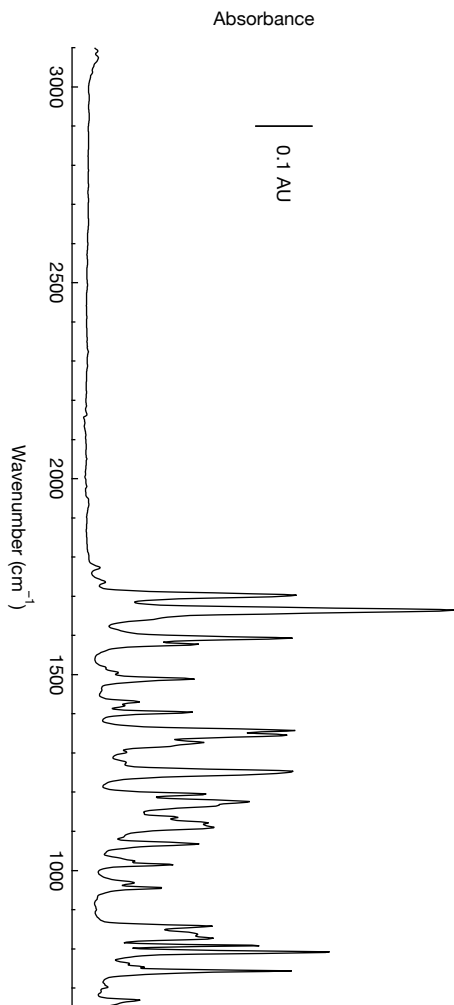
Figure B.6   ATR-IR spectrum of perylene-3, 4, 9, 10-*N*, *N*-4-trifluoromethylaniline bisimide, **7**.

B.3 Transflection Infrared Spectra of Surfaces

All spectra below were acquired at a polarization angle of 90° in OPUS. Spectra for silicon oxide substrates were collected in transflection mode at a reflection angle of 80° versus a surface normal angle unless otherwise specified. Spectra for samples that utilized TiO_2 as a substrate were acquired in reflection mode at 60° versus a surface normal angle.
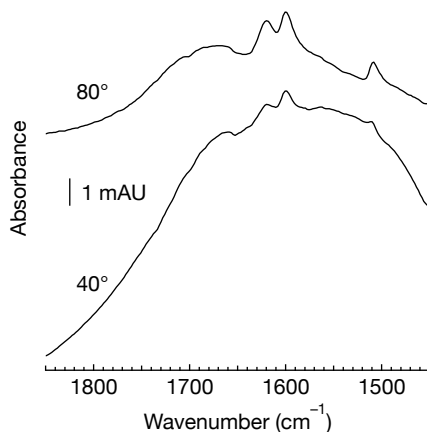
Figure B.7 Transflection infrared spectrum of surface **1a** as a function of reflection angle with respect to the surface normal as indicated. This is a carbonyl zoom-in of the image in Fig. B.8.
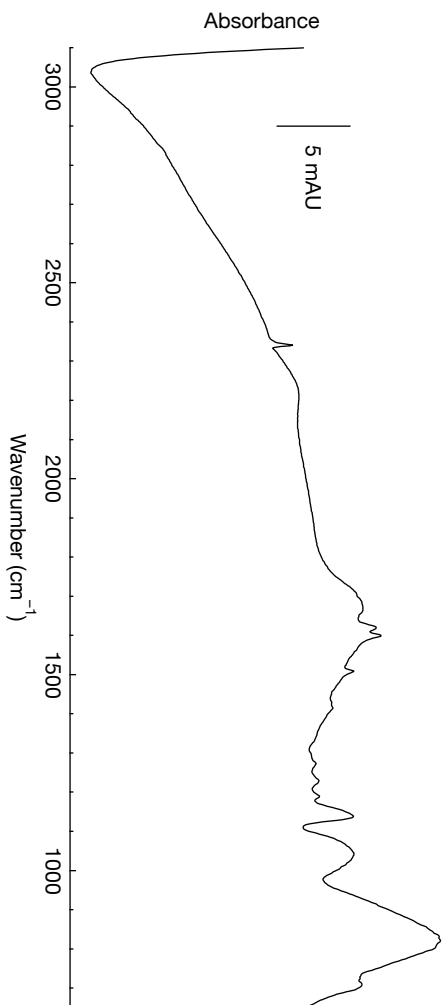
Figure B.8   Transflection infrared spectrum of surface **1a**. This is the full spectrum of the carbonyl window show in Fig. B.7.
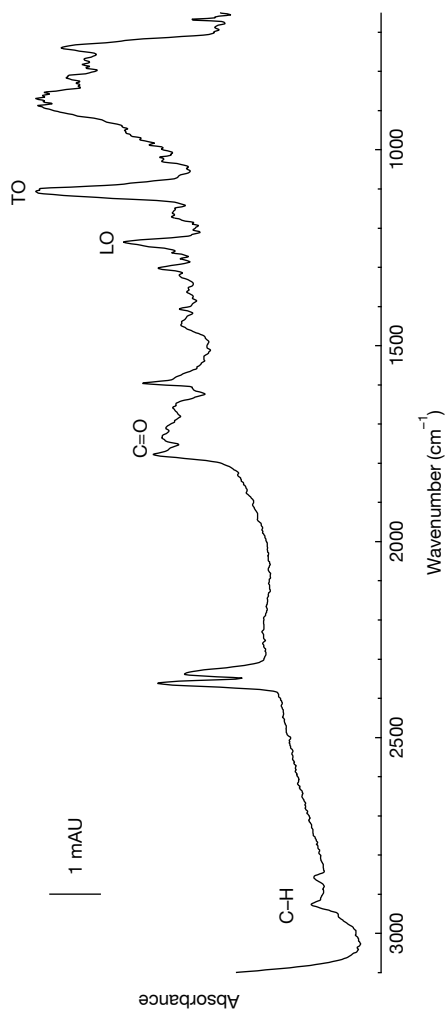
Figure B.9 Transflection infrared spectrum of surface **2a**. This represents a wide-range scan of the spectrum depicted for surface **2a** in Fig. **2** in the main text. The "LO" and "TO" tags respectively refer to features ascribed to the longitudinal optical and transverse optical modes in silicon oxide.
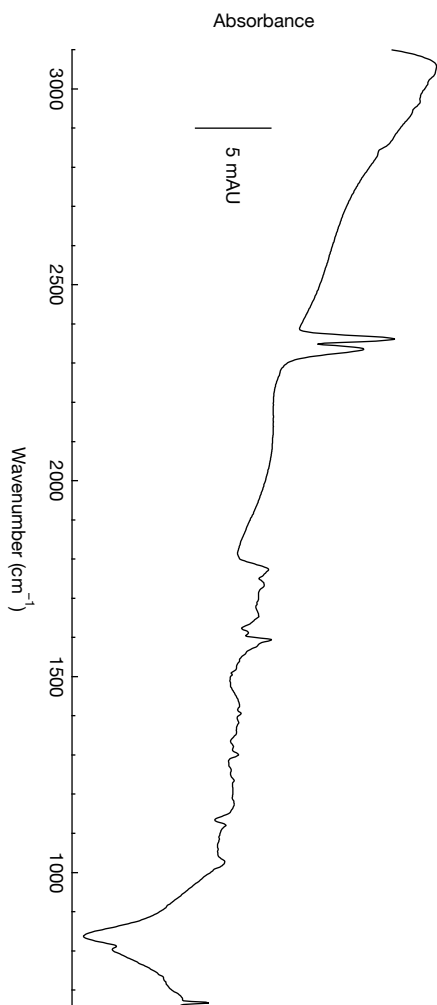
Figure B.10   Reflection infrared spectrum of surface **2b**.
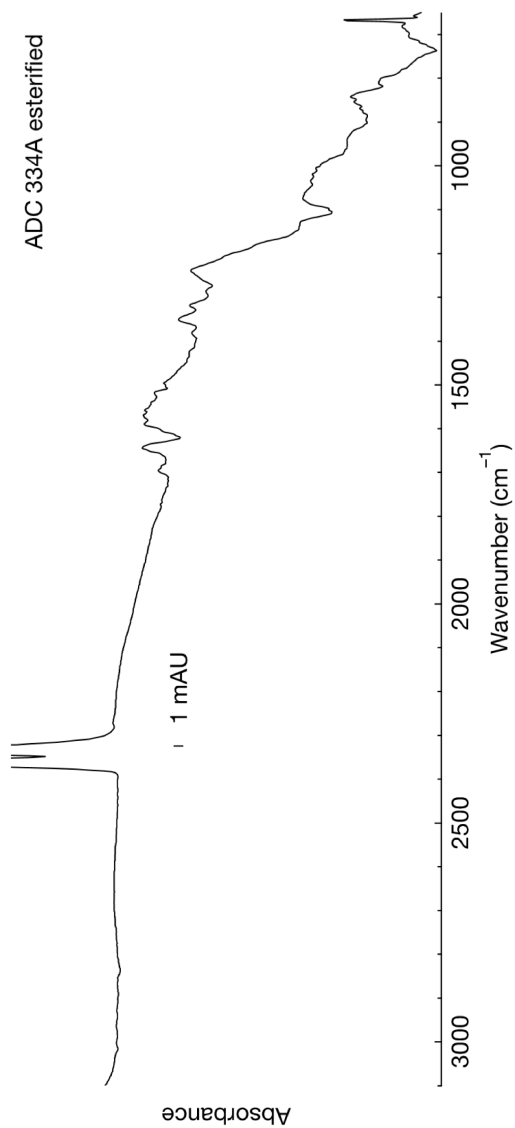
Figure B.11   Transflection infrared spectrum of surface **3a**. This represents a wide-range scan of the spectrum depicted for surface **3a** in Fig. **3** in the main text.
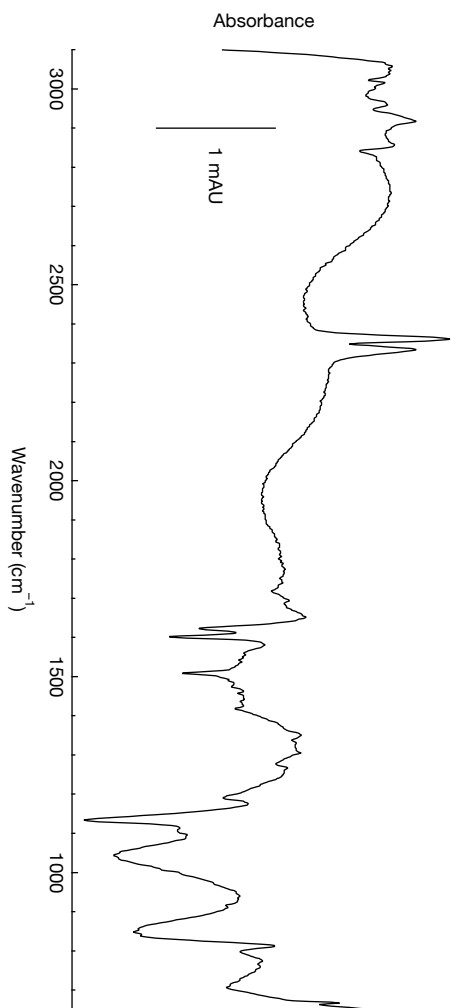
Figure B.12 Reflection infrared spectrum of surface **3b**.
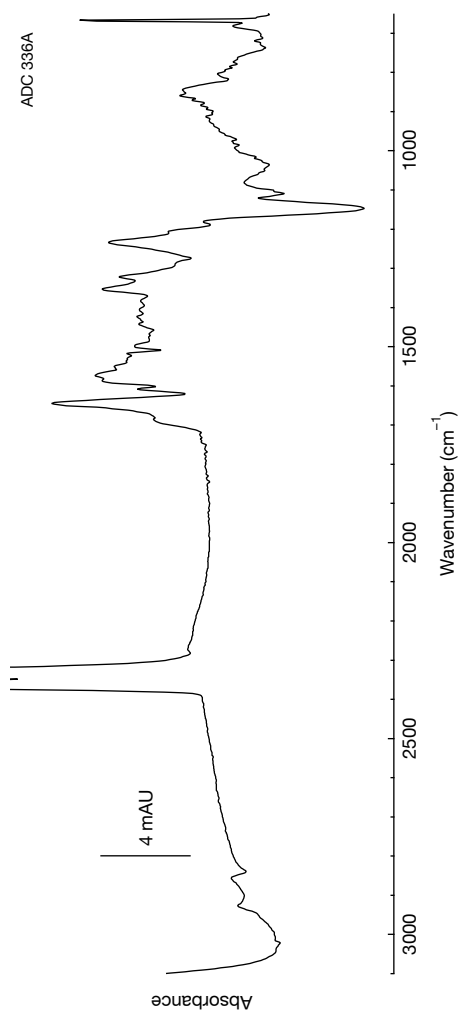
Figure B.13   Transflection infrared spectrum of surface **6a**. This represents a wide-range scan of the spectrum depicted for surface **6a** in Fig. **6** in the main text.
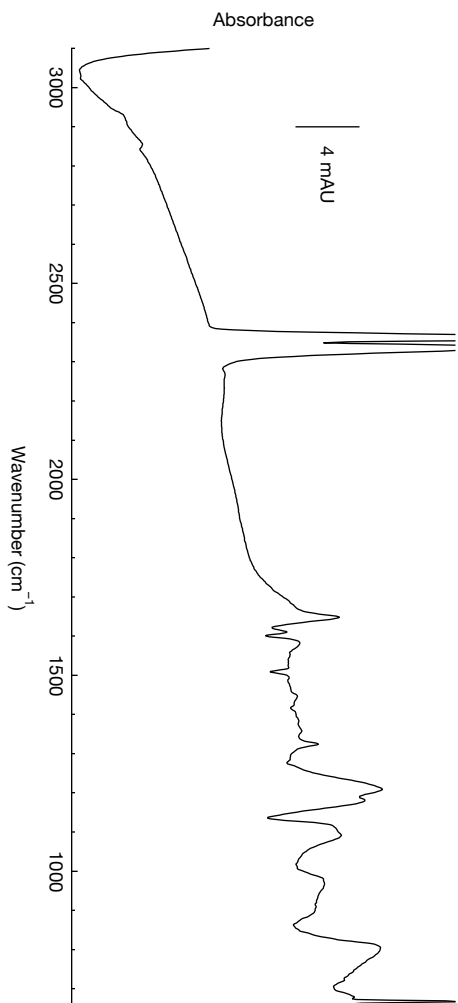
Figure B.14   Reflection infrared spectrum of surface **6b**. This represents a wide-range scan of the spectrum depicted for surface **6b** in Fig. **6** in the main text.

B.4 Photoelectron Spectra of Surfaces
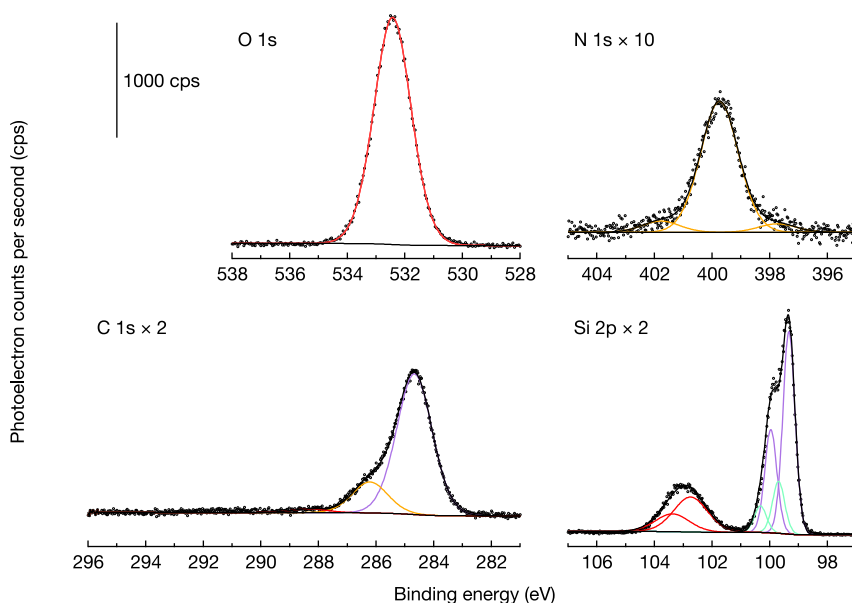
Figure B.15 Photoelectron spectra of a representative surface **1a**. The N-1s-to-Si-2p ratio for this particular sample is 0.42 when considering only the bulk contributions to the silicon region of the photoelectron spectrum. The ratio for an average of ten samples is 0.35 ± 0.10. We interpret this ratio in terms of a surface coverage of aniline silane species with an overlayer model in §2.4.3.
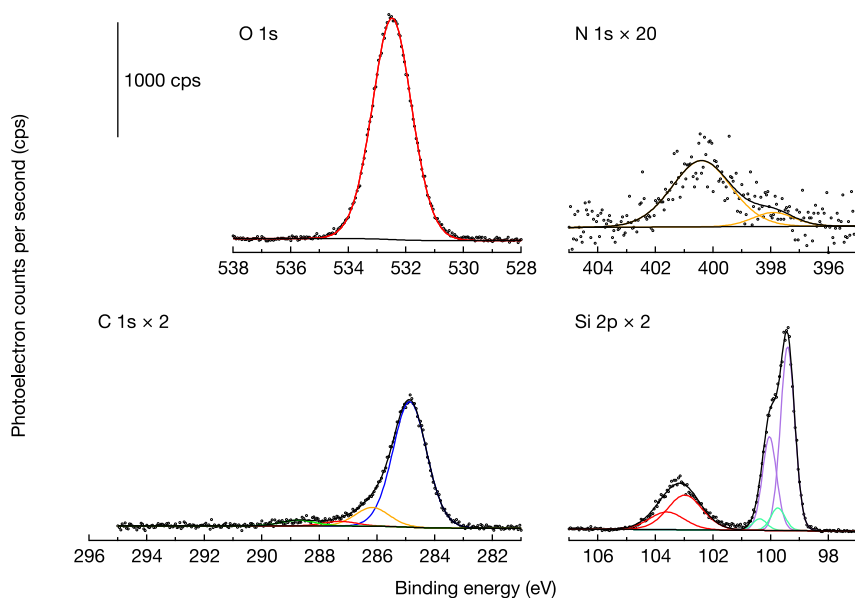
Figure B.16   Photoelectron spectra of a surface **2a**. The absence of distinct, perylene-specific chemical features in this spectrum yields challenges in application of O 1s, C 1s, or N 1s peak area values to overlayer models. Thus, we do not employ photoelectron spectra of surface **2a** for the purpose of quantifying perylene coverages or conversion yields in producing surface **2a** from surface **1a**.
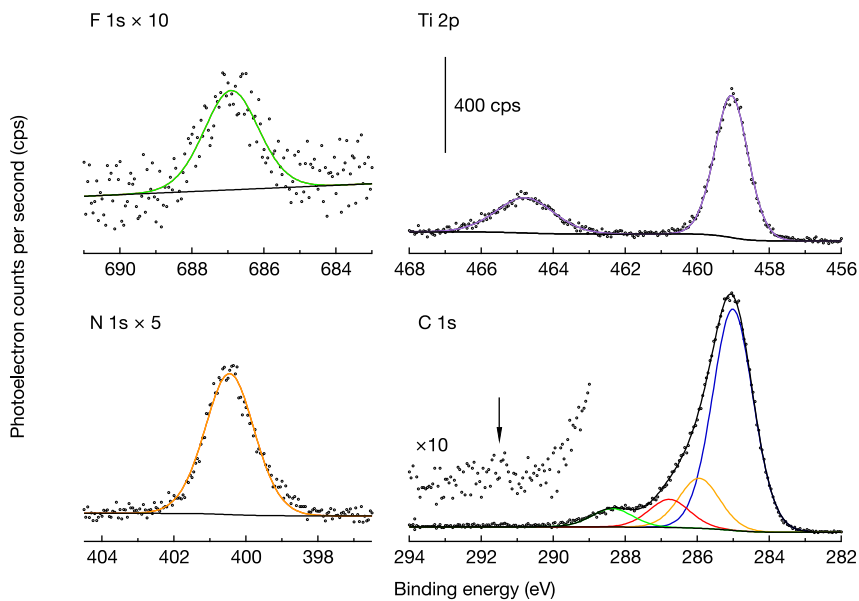
Figure B.17 Photoelectron spectra of surface **1a**. The fluorine and nitrogen frames are magnified relative to the carbon and titanium frames that both represent 1200 cps from top to bottom. The magnified inset in the C 1s frame reveals a nominal contribution of carbon bonded to fluorine. Per established methodology, the fitted Ti $2p_{3/2}$ and Ti $2p_{1/2}$ features are not mutually constrained with identical FWHM values.
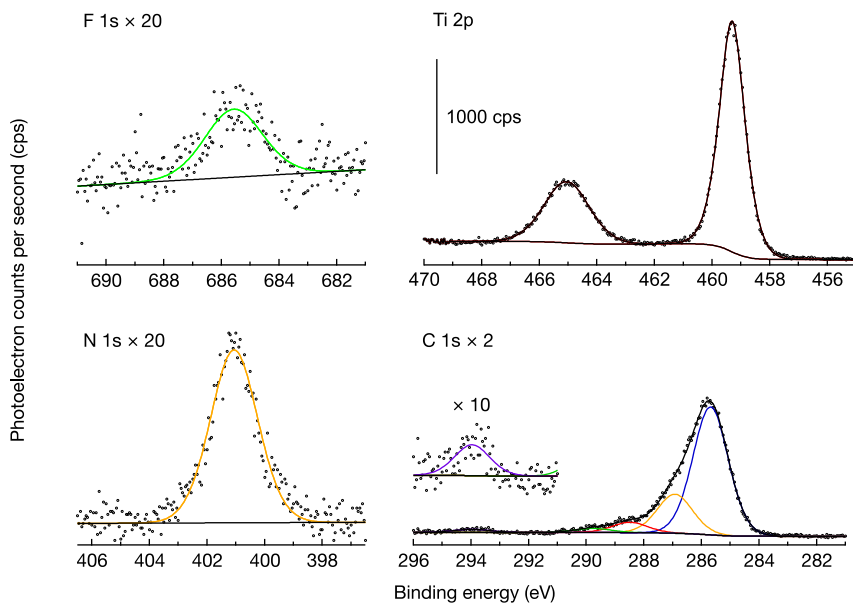
Figure B.18   Photoelectron spectra of surface **5b**.
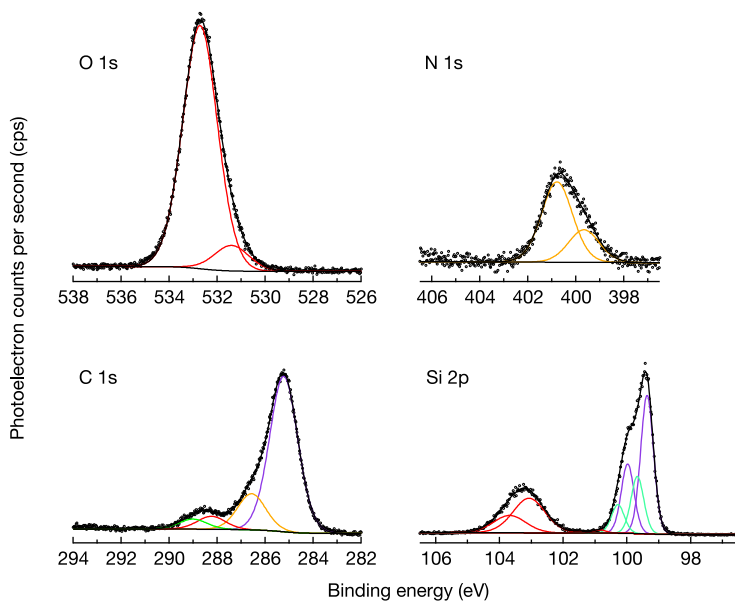
Figure B.19   Photoelectron spectra of surface **6a**.

APPENDIX C

SUPPORTING INFORMATION AND FIG-
URES FOR CHAPTER 5

C.1   X-ray Photoelectron Spectra of Surfaces
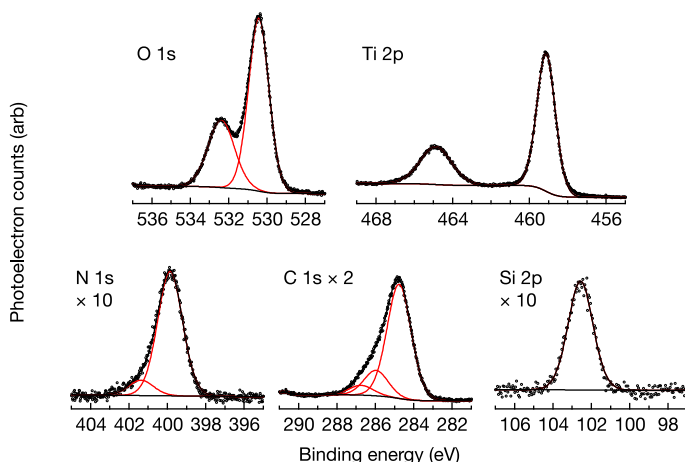
Figure C.1   XP spectra of surface **2**. Features are scaled to the O 1s peak.
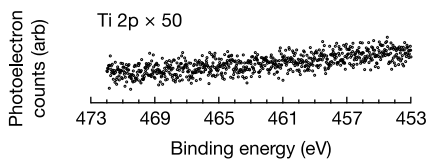
Figure C.2   Ti 2p X-ray photoelectron region acquired during scans of the MAPbI$_3$ surface. Vertical scaling is relative to I 3d in Fig. 5.4A with identical horizontal scaling.
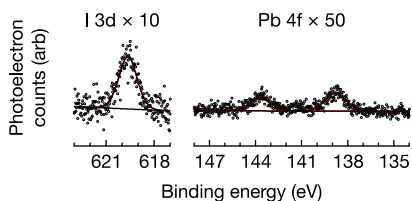
Figure C.3   I 3d and Pb 4f X-ray photoelectron regions acquired during scans of the CuSCN surface that correspond to the data in Fig. 5.4B. As with the other spectra Fig. 5.4B, these plots have vertical scaling based on the I 3d region in Fig. 5.4A.

C.2 Ultraviolet Photoelectron Spectra of Surfaces
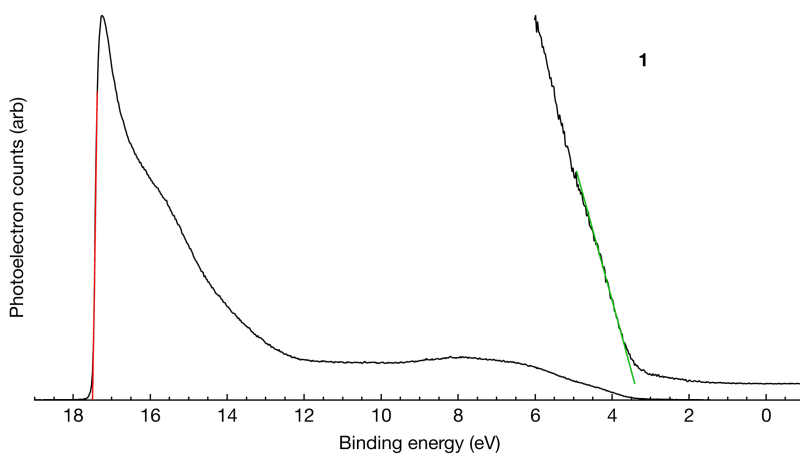
Figure C.4 UP spectra of functionalized TiO_2 surface, **1**.
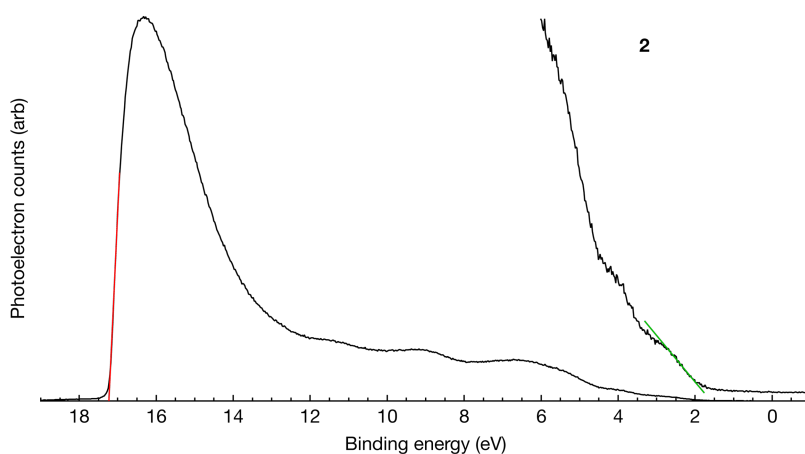
Figure C.5 UP spectra of functionalized TiO_2 surface, **2**.
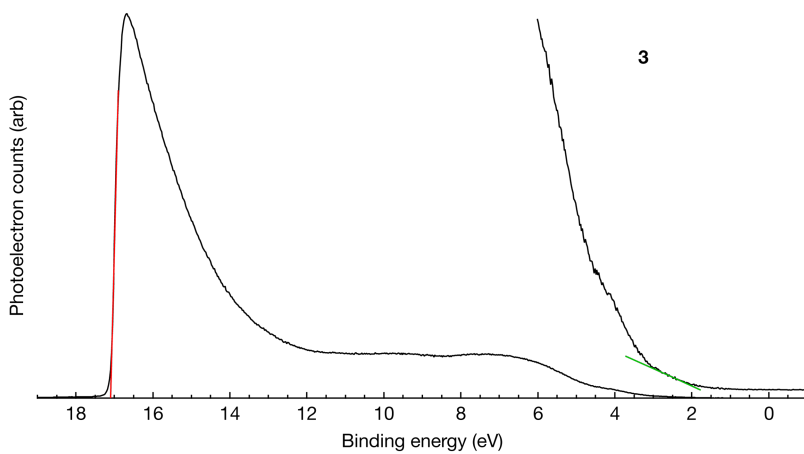
Figure C.6   UP spectra of functionalized TiO$_2$ surface, **3**.
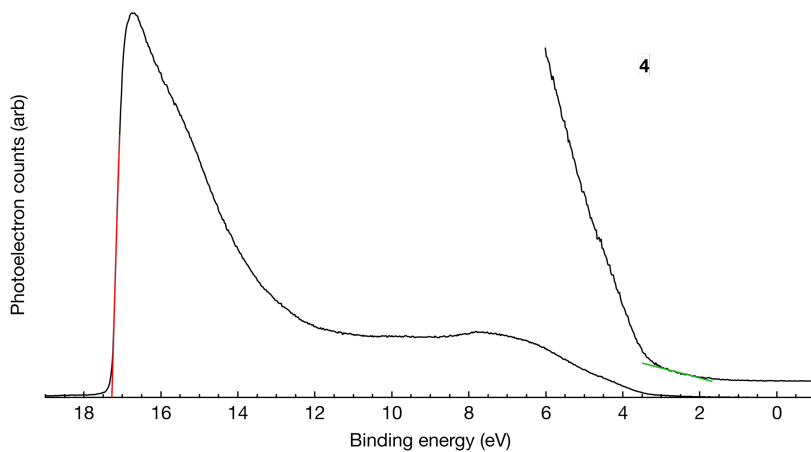
Figure C.7   UP spectra of functionalized TiO$_2$ surface, **4**.
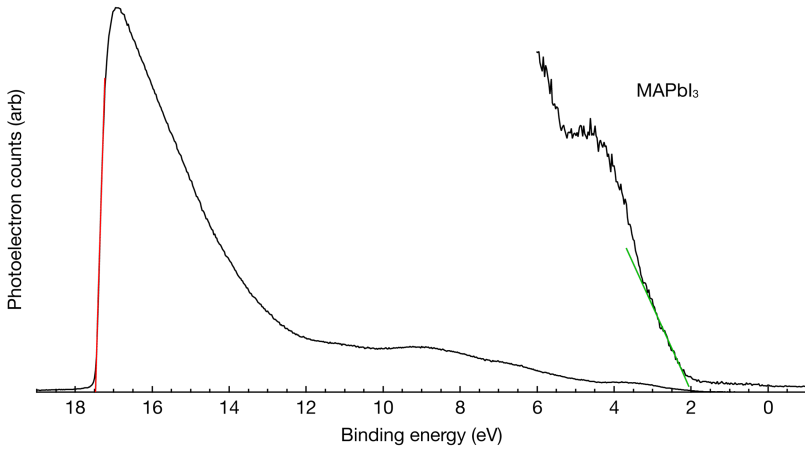
Figure C.8   UP spectra of MAPbI$_3$ thin films on TiO$_2$.
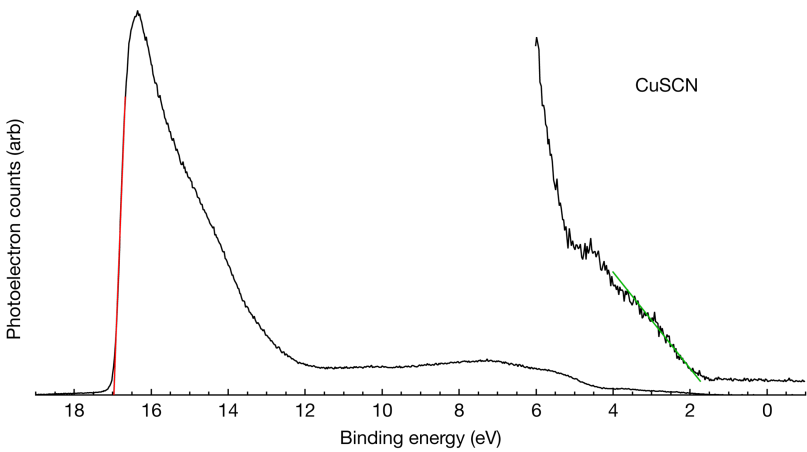
Figure C.9   UP spectra of CuSCN thin films on MAPbI$_3$.

C.3   Raw UV-Vis spectra
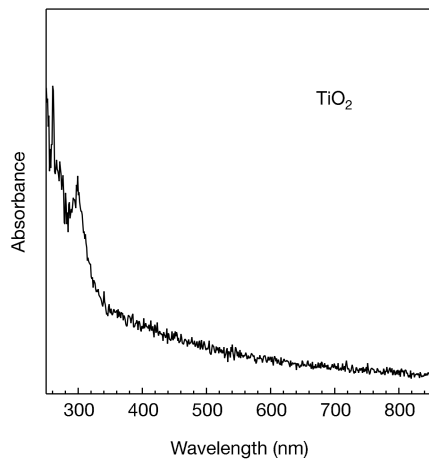
Figure C.10   UV-Vis absorption spectra of an m-TiO$_2$ thin film.
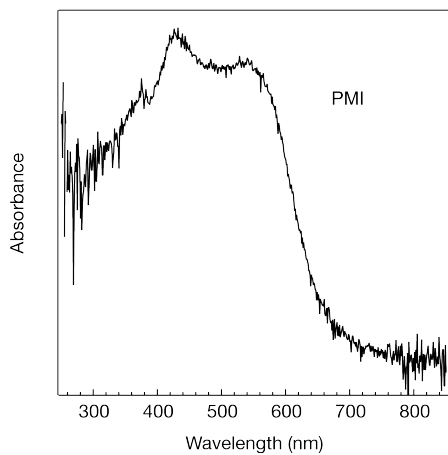
Figure C.11   UV-Vis absorption spectra of of perylene monoimide monoanhydride.
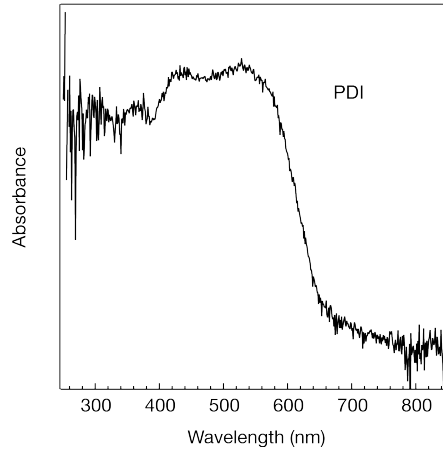
Figure C.12   UV-Vis absorption spectra of perylene diimide.
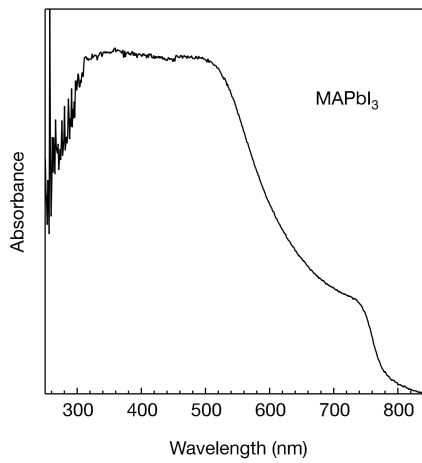
Figure C.13   UV-Vis absorption spectra of an MAPbI$_3$ thin film.
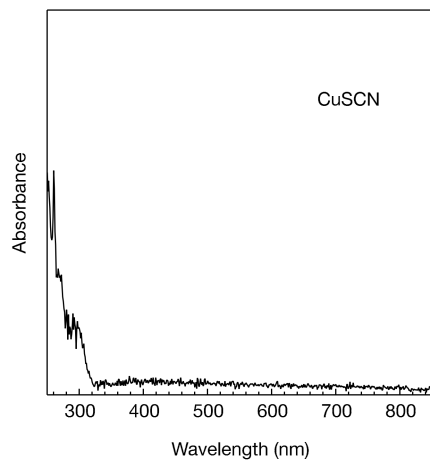
Figure C.14   UV-Vis absorption spectra of an CuSCN thin film.

APPENDIX D

ORIGINAL OVERLAYER MODEL FROM CHAPTER 3

Between the publications of Chapters 3 and 4, we redesigned our substrate-overlayer models to be more rigorous and presented them in §2.4.2 and §2.4.3. These sections reflect the updated models and equations. The original models and equations, published in the Supporting Information section of *Synthesis and Characterization of Alkylamine-Functionalized Si(111) for Perovskite Adhesion With Minimal Interfacial Oxidation or Electronic Defects*,[196] are presented here, with only minor changes. We also include the original Br sensitivity analysis which is briefly mentioned in this Thesis in Section §2.4.2.

D.1 The original overlayer model for functionalized organics on Si(111)

Utilizing photoelectron spectra to ascertain functional group coverage requires fitting the acquired data to a substrate overlayer model.[185] Figure
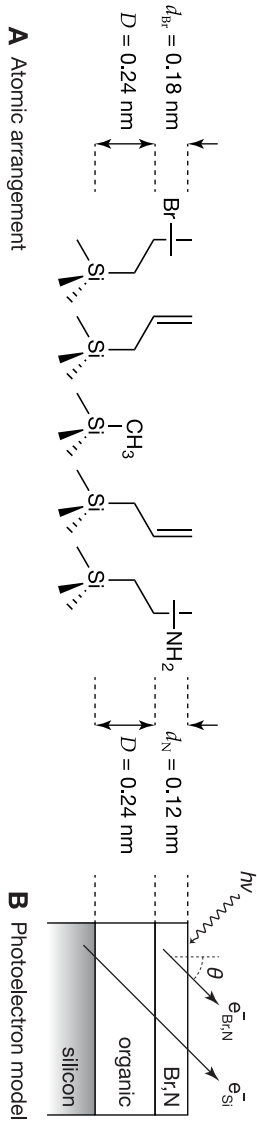
Figure D.1 Bromine and nitrogen localization on mixed allyl/methyl Si(111) surfaces (frame **A**) as related to the substrate overlayer model (**B**) that ascribes surface coverages from experimental XPS intensities.

D.1 presents a cartoon depiction of mixed allyl/methyl-functionalized Si(111) with bromine and/or amine functionalization of the double bond (frame **A**), and the substrate overlayer model employed for interpretation of the photoelectron data. The overlayer models described by Ebel,[189] and Fadley[190] serve as the basis herein and resemble one that was previously employed to model organic functionalization of InP(111)B.[192] The present model represents bromine- or amine functionalized double bonds as an organic layer of thickness D on top of the silicon, and a layer of the bromine or nitrogen atoms themselves with layer thickness d on top of the organic layer. Figure D.1 denotes the atomic arrangement (frame **A**) and photoelectron interpretation (frame **B**) of the model. As the precise orientation of the species on the surface remains unknown, we include the results of a sensitivity analysis that explores how variations in d and D affect the calculated coverages. For the model employed, the signal intensity due to Br 3d photoelectrons, $I_{Br\,3d}$, and the intensity due to Si 2p photoelectrons, $I_{Si\,2p}$, are proportional respectively to the terms in eqs D.1 and D.2. Equations D.1 and D.2 would contain additional parameters to quantitatively describe signal intensities, but such values cancel out[185,190] when considering the experimentally acquired ratio of Br 3d to Si 2p photoelectron signals, $I_{Br\,3d}/I_{Si\,2p}$ as given by eq D.3.

$$I_{Br\,3d} \propto SF_{Br\,3d}\, \rho_{Br}\, \lambda_{Br\,3d,Br} \left(1 - \exp\frac{-d_{Br}}{\lambda_{Br\,3d,\,Ov}\cos\theta}\right) \tag{D.1}$$

$$I_{Si\,2p} \propto SF_{Si\,2p}\, \rho_{Si}\, \lambda_{Si\,2p,Ov} \exp\frac{-d_{Br} - D}{\lambda_{Si\,2p,Ov}\cos\theta} \tag{D.2}$$

$$\frac{I_{Br\,3d}}{I_{Si\,2p}} = \frac{SF_{Br\,3d}}{SF_{Si\,2p}}\frac{\rho_{Br}}{\rho_{Si}}\frac{\lambda_{Br\,3d,Br}}{\lambda_{Si\,2p,Si}}\frac{1 - \exp\frac{-d_{Br}}{\lambda_{Br\,3d,Ov}\cos\theta}}{\exp\frac{-d_{Br}-D}{\lambda_{Si\,2p,Ov}\cos\theta}} \tag{D.3}$$

In eqs D.1–D.3, d_{Br} refers to the thickness of an atomic bromine monolayer, $SF_{Br\,3d}$ and $SF_{Si\,2p}$ respectively represent the instrument and angle-specific atomic sensitivity factor for the Br 3d and the Si 2p photoelectrons,[194] while ρ_{Br} and ρ_{Si} denote the volumetric number density of bromine atoms and silicon atoms in their respective layers. Bromine attenuation terms in eqs D.1–D.3 include: $\lambda_{Br\,3d,Br}$, the attenuation length of Br 3d photoelectrons through a bromine layer; and $\lambda_{Br\,3d,Ov}$, the attenuation length of Br 3d photoelectrons through an arbitrary overlayer. The attenuation length inside the exponential is itself further attenuated by $\cos\theta$ for photoelectrons collection at an angle θ away from the surface normal angle. The λ terms outside of the exponential do not carry an angle dependence for samples that are larger

than the analyzer solid-angle acceptance area for a given θ value.[190,288] When solving for nitrogen rather than bromine coverages, $I_{N\,1s}$ replaces $I_{Br\,3d}$, d_N replaces d_{Br}, $SF_{N\,1s}$ replaces $SF_{Br\,3d}$, ρ_N replaces ρ_{Br}, $\lambda_{N\,1s,N}$ replaces $\lambda_{Br\,3d,Br}$, and $\lambda_{N\,1s,Ov}$ replaces $\lambda_{Br\,3d,Ov}$, in eqs D.1 and D.3.

In practice, we utilized *Mathematica* to solve for ρ_{Br} or ρ_N by setting eq D.3 to experimentally determined intensity ratios. Dividing the acquired volumetric number density values, ρ_{Br} or ρ_N, by their respective d_{Br} and d_N values yields a surface density, $\rho_{Br} = \rho_{Br}/d_{Br}$ and $\rho_N = \rho_N/d_N$, while for Br$_2$ functionalization we further divide the surface density value by 2 so as to account for the expected double bromination across a single double bond. Lastly, we divide the surface number density, ρ_{Br} or ρ_N, by the surface number density of Si(111) atop sites, ρSi(111). Notably, this yields the fractional coverage of Br or N species as a function of available silicon sites, not the conversion efficiency from the allyl-functionalized surface. We represent these fractional coverages as a percent of the surface density of Si(111) atop sites.

Notably, this overlayer model and implementation does not consider the attenuating effect of adventitiously adsorbed species on the functionalized silicon surfaces. Ignoring the contributions of adventitious species is valid for experimental ratios of Br 3d and Si 2p photoelectrons because those photoelectrons have similar kinetic energy values and would be similarly attenuated by adventitious adlayers, thus $I_{Br\,3d}/I_{Si\,2p}$ would remain unchanged. In contrast to Br 3d, the N 1s photoelectrons are roughly 25% lower in energy as compared to Si 2p photoelectrons. Thus, N 1s photoelectrons would be attenuated more by adventitious adlayers vs Si 2p photoelectrons, and this would somewhat underestimate nitrogen coverage values for an experimentally determined $I_{N\,1s}/I_{Si\,2p}$ ratio.

D.1.1   The original silicon oxide on Si(111) Model

Equation D.3 may be modified to describe the coverage of silicon oxide directly atop a silicon substrate. In modeling oxide coverage, I_{Si^0} replaces $I_{Si\,2p}$ and specifically refers to the Si 2p photoelectrons attributed to bulk Si^0 while I_{Ox} replaces $I_{Br\,3d}$ and specifically refers to the Si 2p photoelectrons attributed to highly oxidized silicon. Further: $SF_{Si\,2p}$ replaces $SF_{Br\,3d}$ and cancels out with the existing $SF_{Si\,2p}$ in the denominator; ρ_{Ox} replaces ρ_{Br}; ρ_{Si^0} replaces ρ_{Si}; d_{Ox} replaces d_{Br}; $D = 0$ for the intimately contacting oxide; λ_{Ox} replaces $\lambda_{Br\,3d,Br}$, $\lambda_{Br\,3d,Ov}$, and $\lambda_{Si\,2p,\,Ov}$; and λ_{Si^0} replaces $\lambda_{Si\,2p,Si}$ to yield eq D.4.

$$\frac{I_{Ox}}{I_{Si^0}} = \frac{\rho_{Ox}}{\rho_{Si^0}} \frac{\lambda_{Ox}}{\lambda_{Si^0}} \frac{1 - \exp\frac{-d_{Ox}}{\lambda_{Ox}\cos\theta}}{\exp\frac{-d_{Ox}-D}{\lambda_{Ox}\cos\theta}} \tag{D.4}$$

Unlike the organic coverages that derive from ρ via eq D.3 as above, known density values for silicon and its oxide enable solving for d_{Ox}, via the rearrangement in eq D.5.

$$d_{Ox} = \lambda_{Ox} \cos \theta \, \ln \left(\frac{I_{Ox}}{I_{Si^0}} \frac{\rho_{Si^0}}{\rho_{Ox}} \frac{\lambda_{Si^0}}{\lambda_{Ox}} + 1 \right) \qquad (D.5)$$

In eq D.5, the ρ and λ ratio terms may be derived from the ratio of absolute intensity values of samples that are infinitely deep, or at least $\gg \lambda$ such that $I_{Ox}^{\infty} \propto \rho_{Ox} \lambda_{Ox}$ and $I_{Si^0}^{\infty} \propto \rho_{Si^0} \lambda_{Si^0}$. Employing $I_{Si^0}^{\infty} / I_{Ox}^{\infty}$ rather than the ρ and λ terms enables an experimental determination of each absolute intensity value in a more accurate, side-by-side experiment for the particular instrument employed. Substituting the absolute intensity terms into eq D.5 yields eq D.6 that researchers commonly employ for quantifying thin oxide coverages on silicon.[161,197−198]

$$d_{Ox} = \lambda_{Ox} \cos \theta \, \ln \left(\frac{I_{Ox} I_{Si^0}^{\infty}}{I_{Si^0} I_{Ox}^{\infty}} + 1 \right) \qquad (D.6)$$

D.1.2   Parameterizing the original overlayer model

Between eqs D.3 and D.6, several terms require numerical values including the sensitivity factors, attenuation lengths, and density values.

We utilized published instrumental sensitivity factors for the Phi5600 instrument employed for the experimentally utilized 90° angle between the incoming x-ray radiation and the center of the analyzer collection axis. Table 8.1 relays values for Si 2p, Br 3d, and N 1s.[194]

Attenuation length values came from both experimental results and model calculations. For Si 2p photoelectrons travelling through bulk silicon ($\lambda_{Si\,2p,Si}$ in eq D.3 and λ_{Si^0} in eq D.7) we utilized 2.8(23) nm from Seah and Spencer,[198] and for Si 2p photoelectrons travelling through silicon oxide overlayers that are less than 8 nm thick, $\lambda_{Ox} = 3.4(85)$ nm.[197]

Equation D.7 determined the attenuation length of Br 3d and N 1s photoelectrons through their respective pure materials, $\lambda_{Br\,3d,Br}$ and $\lambda_{N\,1s,N}$.[184] Equation D.7 relies upon the kinetic energy of the particular photoelectron, **E**, in eV; Z, the atomic number; and a, the average lattice parameter in nanometers. Equation D.8 defines a for a particular element as a function of: atomic molar mass A in g mol−1, the mass density ρ of the element in kg m−3, and Avogadro's number N.

$$\lambda = 0.316\,\text{nm}\ a^{1.5} \left[\frac{\mathbf{E}}{Z^{0.45}\left(3 + \ln\frac{\mathbf{E}}{27}\right)} + 4 \right] \tag{D.7}$$

$$a = 10^8 \left(\frac{A}{\rho N}\right)^{1/3} \tag{D.8}$$

For bromine, $Z = 35$, $A = 79.9$ g mol^{-1}, $\rho = 4050$ kg m^{-3} for solid bromine at 123 K[289], and $\mathbf{E} = 1414$ eV for Al Kα excitation, (based on a Br 3d binding energy of 69 eV and an instrumental work function of 3 eV) yielding $\lambda_{\text{Br 3d,Br}}$ = 2.9(45) nm. For nitrogen, $Z = 7$, $A = 14.0$ g mol^{-1}, $\rho = 817$ kg $^{-3}$ for solid ammonia at 80 K[290], and $E = 1085$ eV for Al Kα excitation, (based on the N 1s binding energy of 398 eV) yielding $\lambda_{\text{N 1s,N}}{}^{184}$ = 3.8(3) nm.

Equation D.3 further relies on attenuation lengths for Si 2p, Br 3d, and N 1s photoelectrons travelling through the functionalized organic mono-layer. We utilize eq D.9, which was parameterized for photoelectrons emitted from a gold substrate through self-assembled thiol monolayers of controlled thicknesses.[193]

$$\lambda = 0.90\,\text{nm} + 0.0022\,\text{nm} \times \mathbf{E} \tag{D.9}$$

As above, $\mathbf{E}_{\text{Br 3d}} = 1414$ eV yields $\lambda_{\text{Br 3d,Ov}}$ = 3.2(0) nm, $\mathbf{E}_{\text{N1s}} = 1085$ eV yields $\lambda_{\text{N 1s,Ov}}$ = 3.2(87) nm, and $\mathbf{E}_{\text{Si2p}} = 1384$ eV (for a 99 eV binding energy) yields $\lambda_{\text{Si 2p,Ov}}$ = 3.9(45) nm.

Equation D.3 also requires density values. We utilize $\rho_{\text{Si}} = 5.00 \times 10^{22}$ atoms cm^{-3} from a bulk silicon density of 2.33 g cm^{-3}, and ultimately solve for ρ_{Br} as detailed below. Because we report the bromine and nitrogen coverage values as a percentage of the Si(111) site density, eq D.3 also requires $\sigma_{\text{Si(111)}}$ = 7.83×10^{14} sites cm^{-2}. The $\sigma_{\text{Si(111)}}$ value is based on the 0.384 nm nearest-neighbor spacing of hexagonally packed Si atoms on the (111) surface, which is in turn based on the diamond-like unit cell length of 0.543 nm.[77]

Lastly, D.3 requires values for d and for D. As shown in Fig. D.1, we utilize $d_{\text{Br}} = 0.18$ nm, $d_{\text{N}} = 0.12$ nm and $D = 0.24$ nm for both bromine and nitrogen coverage models. We determined d values from the length of a cubic volume that is equal to the spherical atomic volume for a given covalent atomic radius, i.e. $4\pi r_{Br}^3/3 \equiv d_{Br}^3$, therefore $d_{\text{Br}} = 2\sqrt[3]{\pi/6}r_{\text{Br}}$. The mathematical overlayer model treats photoelectrons as travelling through layers that are uniform throughout their depth. Thus we believe that using the spherical-to-equivalent-cubic-volume calculation for d is preferable to simply doubling a

radius as would be a model for a layer of close-packed hard spheres with void space. From r_{Br} = 0.114 nm and r_N = 0.075 nm,[291] the volumetric conversion yields d_{Br} = 0.18 nm and d_N = 0.12 nm, which are the values reported in Fig. D.1. We utilized D = 0.24 nm based on positioning the Br or N atom in the middle of the double bond and a C–C bond length of 0.154 nm and an angle of 109.5°. This position reflects the unknown addition mechanism of the Br atom across the double bond due to competing issues of increased 2° C stability vs the high packing density of allyl groups on the surface. Further, the distribution of double bond orientations and subsequent adatom positions are unknown a priori. Thus, we include a sensitivity study below to explore how differences in the chosen d and D values ultimately affect calculated coverages for a fixed, experimentally determined photoelectron intensity ratio.

Equation D.6 requires an experimental determination of $I^{\infty}_{Si^0}$ and I^{∞}_{Ox}. Sequential Si 2p acquisitions of directly abutting samples of a freshly HF-etched Si(111) wafer and a piranha-etched glass microscope slide respectively yielded each absolute intensity. Careful mounting ensured that the sampling surfaces of the silicon wafer sample and the glass side were at the same physical height on the sample puck. Our determined $I^{\infty}_{Si^0}/I^{\infty}_{Ox}$ = 1.41 agrees with other studies of functionalized silicon surfaces,[161] as well as Seah and Spencer who report the inverse number, $I^{\infty}_{Ox}/I^{\infty}_{Si^0}$, that they term R_0 for a number of previous studies as having a mean value of 0.76 ± 0.08.[198] We report oxide coverages as percentages of a monolayer of oxide as a function of SiO_2 units per Si(111) surface atom assuming the thickness of a monolayer of SiO_2 is 0.35 nm.[161] Surface coverage as a percentage was determined by first inputting peak areas of oxidized and bulk silicon in eq D.5 to determine a "depth" of silicon oxide. For example: a sample has a SiO_x:Si area ratio of 0.021. After plugging this ratio into eq D.5, we calculate an oxide depth of 0.054 nm. Dividing this by an ideal SiO_2 monolayer depth, 0.35 nm, we calculate it to be 0.15 monolayers deep. To convert this value to a percent coverage of surface Si(111) sites, we first calculate the number of atoms of oxidized silicon in a volume of SiO_2. By molecular weight, there is 1.239 g of Si in one cm^3 of SiO_2, meaning there are 2.66×10^{22} Si atoms cm^{-3}. Dividing the volume by the single monolayer of SiO_2 yields, 0.35 nm, yields 9.30×10^{14} oxidized silicon atoms cm^{-2}. The ratio of oxidized silicon atoms in one monolayer of SiO_2 to Si(111) atoms is 1.19. This is the factor used to convert monolayers of oxide calculated by eq D.5 to percent coverage report in the main paper. The reported and literature values above were summarized in Table D.1.

D.1.3   Sensitivity Analysis and the Implications for Coverage Uncertainties

D.1.3.1   *How changes in the d and D values affect calculated coverages*   As the exact morphology of the functionalized monolayer remains unclear, it is

Table D.1   Values employed for analysis of XP spectra of the xth element.[a]

$x \equiv$	SF_x	a_x (nm)	$\lambda_{x,x}$ (nm)	$\lambda_{x,Ov}$ (nm)
Si 2p	0.283	n/a	2.8(23)	3.9(45)
Br 3d	0.895	0.31(99)	2.5(75)	4.0(11)
N 1s	0.477	0.30(52)	3.8(12)	3.2(87)

[a] Values include the SF_x sensitivity factors, $\lambda_{x,x}$ attenuation lengths for photoelectrons of a particular material traveling through that material, a_x lattice parameter, and $\lambda_{x,Ov}$ attenuation length values for photoelectrons travelling through an organic overlayer. Moulder et al. supplied all sensitivity factor values.[194] Equation D.8 determined the lattice parameter values for Br 3d and N 1s. Previous reports provided $\lambda_{x,x}$ for silicon ($\lambda_{\text{Si 2p,Si}}$), while eq D.7 yielded $\lambda_{x,x}$ for Br 3d and for N 1s. Equation D.9 determined attenuation length values for photoelectrons travelling through organic overlayers, $\lambda_{x,Ov}$.

critically important to understand how changes in the D and d values show in Fig. D.1 impact the calculated coverage values for specific, XPS-determined peak ratios. Thus we performed a sensitivity analysis in which the value of D was varied for a fixed d, and an analysis in which the value of d was varied for a fixed D. We accomplished this by setting eq D.3 equal to three experimentally relevant peak ratios and solving for the percent coverage surface density as a function of the surface density of Si(111) atop sites, σSi(111). We chose $I_{\text{Br 3d}}/I_{\text{Si 2p}} = 0.016, 0.018$, and 0.020 to resemble the experimental data reported in the manuscript, which respectively correspond to the dotted, solid, and dash-dotted traces in Fig. D.2.

In Fig. D.2, the black traces correspond to the lower, black axis and denote varying values of the organic spacer length, D, when r_{Br} is fixed to 0.114 nm (corresponding to $d_{\text{Br}} = 0.184$ nm). For the "default" D value of 0.24 nm, $I_{\text{Br 3d}} / I_{\text{Si 2p}} = 0.016$ corresponds to a fractional bromine coverage of 8.9%, while Br 3d to Si 2p ratios of 0.018 and 0.020 respectively correspond to fractional bromine coverages of 10(.0)% and 11(.1)%. Figure D.2 varies D from 0.09 nm through 0.39 nm, or in other words the "default" D value plus or minus a distance corresponding to one carbon-carbon single-bond length. As demonstrated by Fig. D.2, varying D by 0.30 nm has very little effect on the resulting bromine coverage for a given experimentally determined ratio of Br 3d to Si 2p intensities. Importantly, changes in D only affect the Si 2p intensity, and this range of D values remains significantly smaller than the attenuation length of silicon electrons through this organic layer, (i.e. $D << \lambda_{\text{Si 2p, Ov}}$) leading to the overall "sluggish" response of the calculated bromine coverage to changes in D. Considering only the $I_{\text{Br 3d}} / I_{\text{Si 2p}} = 0.018$ line, varying D from 0.09 through 0.39 changes the calculated fractional bromine coverage from 10.(57)% to 9.4(90)%.

In addition to changes in D for a fixed d, Fig. D.2 presents the results of a study of changes in d for a fixed $D = 0.24$ nm in the red traces versus the red axes at the top of the graph. The abscissae align the spherical radius of
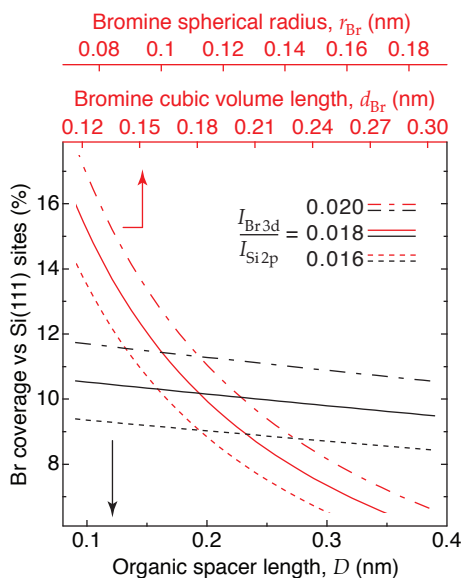
Figure D.2   A sensitivity analysis explores how changes in the value of the organic spacer length, D (black traces, bottom axis) for a fixed value of bromine size, and how changes in the bromine size (red traces, top axes) for a fixed value of D change the calculated bromine coverage in the XPS overlayer model. The bromine size is represented two axes of the spherical radius of a bromine atom, r_{Br}, as well as the length d_{Br} of a cubic volume equal to the sphere for a given r_{Br} value. The dotted, solid, and dash-dotted traces represent experimentally relevant photoelectron intensity ratios, $I_{Br 3d}$ / $I_{Si 2p}$ of 0.016, 0.018, and 0.020. This analysis demonstrates that the calculated coverage has a very weak dependence on the organic spacer length, D, but a more direct dependence on the choice of the atomic radius value that determines d.

a bromine atom r_{Br} with the converted length of one side of a cubic volume, d_{Br}, that is equal to spherical volume ($d_{Br} \equiv r_{Br}$ from above). Recall that the "default" value d_{Br} = 0.18 nm results from a bromine radius of 0.114 nm, which in turn is a covalent radius for a bromine atom that could approach 0.20 nm for an ionic bromide radius.[291] Thus, values r_{Br} in Fig. D.2 vary from 0.07 to 0.19 nm. In contrast to calculated bromine coverages showing a weak dependence on changes in D, Fig. D.2 demonstrates a much more significant dependence on changes to r and to d. Considering only the $I_{Br 3d}$ / $I_{Si 2p}$ = 0.018 line, varying r_{Br} from 0.069 nm (d_{Br} = 0.11 nm) through r_{Br} = 0.19 nm (d_{Br} = 0.31 nm) results in a change in the calculated fractional bromine coverage from 16.(86)% to 5.7(88)%. Importantly, within the vicinity of r_{Br} = 0.114 nm (d_{Br} = 0.184 nm), a 10% variation in d yields a roughly 10% variation in the calculated coverage.

The existence of D in the model represents the spacing of a bromine atom or a nitrogen atom away from the silicon surface and changes in organic chain length, bond orientation, and whether chains are standing up or laying down on the surface would all ultimate impact the final value of D. Indeed, a "real" surface likely would have a distribution of D values reflecting a distribution of atomic orientations, bond angles, and torsions of the covalently attached alkyl chains. However, the relative invariance of the calculated bromine coverages to large changes in D implies that a lack of specific knowledge of bromine or nitrogen orientations on the real, XPS-measured surfaces does not introduce a significant error in to our coverage calculations.

Versus D, the comparatively larger sensitivity to changes in d results from the model solving for σ_{Br} and σ_N from their respective ρ_{Br} and ρ_N values. Since σ values are inversely proportional to d, calculated coverages demonstrate a direct dependence on changes in d.

D.1.3.2   Implications for uncertainties in calculated coverage values   In contrast to the relative insensitivity to changes in D, the overlayer model calculates bromine coverages that vary directly with changes in d in the vicinity of the chosen value for d_{Br}. Of note, our interpretation of the sensitivity analysis is that the unknown orientation of alkylbromide and alkylamine species on the functionalized silicon surface does not deleteriously affect the calculated coverage values due to their relative insensitivity to changes in D. However, uncertainties in d do lead to uncertainties in the calculated coverage values. Considering the unknown "true" size of the bromine and the spherical-to-cubic conversion employed, we conservatively ascribe a 10% uncertainty to the values of d_{Br} and to d_N, which results in a 10% uncertainty in the calculated coverage values.

While not discussed in the present analysis but analyzed in detail elsewhere,[197] uncertainties in attenuation length values yield direct uncertainties in calculated coverage values for self-attenuation values (i.e. $\lambda_{x,\,Ov}$ in Table D.1) in bulk materials. However, coverage calculations demonstrate greater tolerance to uncertainties for attenuation lengths through thin overlayers when d $\lambda_{x,\,Ov}$.

Due to uncertainties in d and λ values we convolve a 10% uncertainty in the resulting coverage calculation with the standard deviations resulting from multiple measurements of a particular bromine, nitrogen, or silicon oxide coverage on the bulk silicon wafer.

APPENDIX E

MATHEMATICA CODES FOR VARIOUS OVERLAYER MODELS

E.1 Silicon oxide thickness or determining d_{Ox}

Below, lies the *Wolfram Mathematica* code for determining oxide depths on Si(111) surfaces. Experimental I_{Ox} / I_{Si} values are plugged in for the "experimentalratio". The equations are described in §2.4.2.

```
In[ ]:= (* A Mathematica notebook for calculating surface coverage on Si surfaces.
        If used in any way, please cite the manuscript associated with this file.
        Updated 16 January 2019 -- adc and rlgii *)

In[ ]:= (* OmniFocus III analyzer angle vs surf normal *)
        θ = π/4;

In[ ]:= SiUnitCellLength = 0.543090;(* Units are nanometers *)

In[ ]:= Si111Spacing = SiUnitCellLength × √2/2;

In[ ]:= σSi111Sites = .5 ((Si111Spacing/2)² × √3)(* Surface density of Si atoms in mono per nm²*)

Out[ ]= 7.82989

In[ ]:= (* Sensitivity factors for Phi 5600 instrument with OmniFocus III analyzer and mono illumination *)

        SFSi = 0.283;

In[ ]:= (* Thickness of nitrogen layer. Refer to Alex's amination manuscript SI or respective mathematica model *)

In[ ]:= ρSi = 8/SiUnitCellLength³ (* This is the density of silicon atoms in count per nm³*) ;
        ρSiOx = 22.8(* This is the density of silicon atoms in silicon oxide in count per nm³*)

Out[ ]= 22.8

In[ ]:= ρSiOx = 2.65× 1/(28.085+2* 15.9994) * 6.02×10²³/10²¹
        (* This is the density of silicon atoms in silicon oxide in count per nm³ based on bulk density *)

Out[ ]= 26.5513

In[ ]:= λSiOx = 3.485;(* Attenuation length of Si2p through silicon oxide *)

In[ ]:= SiliconIntensity[ d_ , D_] := SFSi × ρSi × Exp[-(d+D)/(λSiOx × Cos[θ])] ;

        OxideIntensity[ d_] := SFSi × ρSiOx × (1- Exp[-d/(λSiOx × Cos[θ])] );

In[ ]:= OxideThickness[ experimentalratio   _] := λSiOx × Cos[θ]× Log[ experimentalratio   ×1.41 + 1] ;

In[ ]:= OxideIntensity[ 1.434]/SiliconIntensity[ 1.434, 0]   (* Determines the ratio SiOx/ Si ratio for 1 monolayer of silicon oxide*)

Out[ ]= 0.419705

In[ ]:= OxideThickness[ 0.1] (* Determines oxide thickness from experimental SiOx/ Si ratio*)

Out[ ]= 0.325049
```

E.2   Revised alkylamine/alkylbromide Si(111) coverage calculations for Chapter 3

The following three pages of code contain the updated *Mathematica* code for determining alkylbromide and alkylamine coverages on Si(111) surfaces. These equations are described in §2.4.2.

```
In[*]:= (* An updated  Mathematica notebook for calculating alkylbromide and alkylamine surface coverage on Si surfaces.
        If used in any way, please cite the manuscript associated with this file.
        Updated 28 Septemeber 2020 -  adc *)

In[*]:= (* OmniFocus III analyzer angle vs surf normal *)
        Θ = π/4 ;

In[*]:= SiUnitCellLength = 0.543090;(* Units are nanometers *)

In[*]:= Si111Spacing = SiUnitCellLength × √2/2

Out[*]= 0.384023

In[*]:= SiUnitCellLength/√2

Out[*]= 0.384023

In[*]:= σSi111Sites = .5 / ( (Si111Spacing/2)² × √3 )(* Surface density of Si atoms in mono per nm²*)

Out[*]= 7.82989

In[*]:= σSi111Sites = .5 / ( (Si111Spacing/2)² × √3 )(* Surface density of Si atoms in mono per nm²*)

Out[*]= 7.82989

In[*]:= (* Sensitivity factors for Phi 5600 instrument with OmniFocus III analyzer and mono illumination *)
        SFBr = 0.895;
        SFN = 0.477;
        SFSi = 0.283;

In[*]:= (* Thickness of nitrogen layer. Refer to Alex's amination manuscript SI or respective mathematica model *)
        NThick = ∛(π/6) × 2 × 0.075 ;

        NThick

Out[*]= 0.120899

In[*]:= (* Thickness of fluorine layer based on covalent F atomic radius via H.B. Gray, ISBN 978-0935702354 *)
        BrThick = ∛(π/6) × 2 × 0.114;

        BrThick

Out[*]= 0.183767

In[*]:= (* Spacer lengths in nm, from Si to center of atom of interest *)

        (* Organic spacer connected to Br or NH2*)
        surfacetoFuncspace = 0.24;

        (* Allyl Depth on Si(111)*)
        surfacetoAllylspace = 0.17;

        (* Methyl Depth on Si(111)*)
        surfacetoMethylspace = 0.11;

In[*]:= σBr[δ_] := σSi111Sites × δ/100 (* Surf density of Br atoms in one mono / nm²*) ;
```

$$\rho Br[\,\mathcal{S}\_] := \frac{\sigma Br[\,\mathcal{S}]}{BrThick} \quad (* \text{ Vol density of Br from } \sigma Br \text{ and Br thickness in } \#/nm^3 *) \ ;$$

In[∘]:= $\sigma N[\,\mathcal{S}\_] := \sigma Si111Sites \times \frac{\mathcal{S}}{100} (* \text{ Surf density of N atoms in one mono } / nm^2 *) \ ;$

$$\rho N[\,\mathcal{S}\_] := \frac{\sigma N[\,\mathcal{S}]}{NThick} (* \text{ Vol density of N from } \sigma N \text{ and N thickness in } \#/nm^3 *) \ ;$$

In[∘]:= $\rho Si = \frac{8}{SiUnitCellLength^3} (* \text{ This is the density of silicon atoms in count per } nm^3 *) \ ;$

In[∘]:=

(* Attenuation lengths in nm *)

$\lambda SiOrg = 3.945;$

$\lambda BrBr = 2.945;$

$\lambda NN = 3.812;$

$\lambda SiSi = 2.823;$

In[∘]:=

$$BromideIntensity[\,\phi\_] := SFBr \times \frac{4}{SiUnitCellLength^2 \times \sqrt{3} \times BrThick} \times \frac{\phi}{100} \times \left(1 - Exp\left[\frac{- BrThick}{\lambda BrBr \times Cos[\,\theta]}\right]\right);$$

$$DiBromideIntensity[\,\phi\_] := SFBr \times \frac{8}{SiUnitCellLength^2 \times \sqrt{3} \times BrThick} \times \frac{\phi}{100} \times \left(1 - Exp\left[\frac{- BrThick}{\lambda BrBr \times Cos[\,\theta]}\right]\right);$$

In[∘]:= $AmineIntensity[\,\mathcal{Z}\_] := SFN \times \frac{4}{SiUnitCellLength^2 \times \sqrt{3} \times NThick} \times \frac{\mathcal{Z}}{100} \times \left(1 - Exp\left[\frac{- NThick}{\lambda NN \times Cos[\,\theta]}\right]\right);$

In[∘]:=

$$SiliconBromideIntensity[\,\phi\_] := \frac{8}{SiUnitCellLength^3} \times SFSi \times \left(1 - \frac{\phi}{100} + \frac{\phi}{100} \times Exp\left[\frac{- BrThick}{\lambda SiSi \times Cos[\,\theta]}\right]\right);$$

In[∘]:=

$SiliconAlkylBromideIntensity[\,Ox\_, \phi\_] :=$
$$\frac{8}{SiUnitCellLength^3} \times SFSi \times Exp\left[\frac{- Ox}{\lambda SiOx \times Cos[\,\theta]}\right] \times$$
$$\left(\left(\left(0.60 - \frac{\phi}{100}\right) \times Exp\left[\frac{- surfacetoAllylspace}{\lambda SiOrg \times Cos[\,\theta]}\right]\right) + \left(0.40 \times Exp\left[\frac{- surfacetoMethylspace}{\lambda SiOrg \times Cos[\,\theta]}\right]\right) + \left(\frac{\phi}{100} \times Exp\left[\frac{- BrThick/2 - surfacetoFuncspace}{\lambda SiOrg \times Cos[\,\theta]}\right]\right)\right);$$

In[∘]:=

$SiliconAlkylAmineIntensity[\,Ox\_, \phi\_, \mathcal{Z}\_] :=$
$$\frac{8}{SiUnitCellLength^3} \times SFSi \times Exp\left[\frac{- Ox}{\lambda SiOx \times Cos[\,\theta]}\right] \times \left(0.60 - \frac{\phi}{100}\right) \times Exp\left[\frac{- surfacetoAllylspace}{\lambda SiOrg \times Cos[\,\theta]}\right] +$$
$$\left(0.40 \times Exp\left[\frac{- surfacetoMethylspace}{\lambda SiOrg \times Cos[\,\theta]}\right]\right) + \left(\left(\frac{\phi}{100} - \frac{\mathcal{Z}}{100}\right) \times Exp\left[\frac{- BrThick/2 - surfacetoFuncspace}{\lambda SiOrg \times Cos[\,\theta]}\right]\right) +$$
$$\frac{\mathcal{Z}}{100} Exp\left[\frac{- NThick/2 - surfacetoFuncspace}{\lambda SiOrg \times Cos[\,\theta]}\right]$$

In[ ]:=

In[ ]:=
```
BromideIntensity[ 60]
─────────────────────────
SiliconBromideIntensity[ 60]
```
Out[ ]= 0.144352

In[ ]:=
```
BromideIntensity[ 100]
──────────────────────────────
SiliconAlkylBromideIntensity[ 0, 100]
(*  Singley brominated. Br/Si ratio for a 100% alkylbromide surface. i.e. every Si adatom has an
 alkylbromide *)
```
Out[ ]= 0.254338

In[ ]:=
```
DiBromideIntensity[ 100]
──────────────────────────────
SiliconAlkylBromideIntensity[ 0, 100]
(*  Doubly brominated. Br/Si ratio for a 100% alkylbromide surface. i.e. every Si adatom has an
 alkylbromide *)
```
Out[ ]= 0.508676

In[ ]:=
```
AmineIntensity[ 100]
──────────────────────────────
SiliconAlkylAmineIntensity[ 0, 0, 100]
(*  N/Si ratio of a 100% alkylamine surface *)
```
Out[ ]= 0.161817

In[ ]:=
```
Solve [BromideIntensity[ Coverage] / SiliconBromideIntensity[ Coverage]  == .011,  Coverage]
```
⋯ Solve: Solve was unable to solve the system with inexact coefficients. The answer was obtained by solving a corresponding exact system and numericizing the result.
Out[ ]= {{ Coverage → 4.80648}}

In[ ]:=
```
Solve [BromideIntensity[ Coverage] / SiliconAlkylBromideIntensity[ 0.072, Coverage]  == .006,  Coverage]
```
⋯ Solve: Solve was unable to solve the system with inexact coefficients. The answer was obtained by solving a corresponding exact system and numericizing the result.
Out[ ]= {{ Coverage → 2.42349}}

In[ ]:=

In[ ]:=
```
Solve [DiBromideIntensity[ Coverage] / SiliconAlkylBromideIntensity[ 0.058, Coverage]  == .018,  Coverage]
```
⋯ Solve: Solve was unable to solve the system with inexact coefficients. The answer was obtained by solving a corresponding exact system and numericizing the result.
Out[ ]= {{ Coverage → 3.65343}}

In[ ]:=
```
Solve [AmineIntensity[ Coverage] / SiliconAlkylAmineIntensity[ 0.058, 0.05, Coverage] == .018,  Coverage]
```
⋯ Solve: Solve was unable to solve the system with inexact coefficients. The answer was obtained by solving a corresponding exact system and numericizing the result.
Out[ ]= {{ Coverage → 10.8572}}

E.3   Perylene on chemically oxidized Si coverage calculations

The following two pages of code contain the *Mathematica* code for determining various surface coverages on Si(111) surfaces including phenylaminosilane (**1a**), fluorinated butylester perylenes(**4a**), and CF$_3$-aniline-terminated perylenes.(**5a**) This code is based equations discussed in §2.4.2

```
In[ ]:= (*  A Mathematica notebook for calculating surface coverage on Si surfaces.
         If used in any way, please cite the manuscript associated with this file.
         Updated 16 January 2019 —  adc and rlgii *)
In[ ]:= (*  OmniFocus III analyzer angle vs surf normal *)
         θ = π/4 ;
In[ ]:= SiUnitCellLength = 0.543090;(*  Units are nanometers *)
In[ ]:= Si111Spacing = SiUnitCellLength × (√2)/2

Out[ ]= 0.384023

In[ ]:= SiUnitCellLength/√2

Out[ ]= 0.384023

In[ ]:= σSi111Sites = .5/ ((Si111Spacing/2)² × √3) (*  Surface density of Si atoms in mono per nm²*)

Out[ ]= 7.82989

In[ ]:= 4/(SiUnitCellLength² * √3)

Out[ ]= 7.82989

In[ ]:= (*  Sensitivity factors for Phi 5600 instrument with OmniFocus III analyzer and mono illumination *)
         SFF = 1.000; SFN = 0.477; SFSi = 0.283;
         SFTi = 1.798;
In[ ]:= (*  Thickness of nitrogen layer. Refer to Alex's amination manuscript SI or respective mathematica model *)
         NThick = √(π/6) × 2 × 0.075 ;
         NThick

Out[ ]= 0.120899

In[ ]:=
In[ ]:= (*  Thickness of fluorine layer based on covalent F atomic radius via H.B. Gray, ISBN 978-0935702354 *)
         FThick = √(π/6) × 2 × 0.064;
         FThick

Out[ ]= 0.103167

In[ ]:= (*  Spacers... computed with WebMO. Distance from center of atom ( or plane in the case of -CF3) to the Si surface. Add WebMO theory level here etc etc....*)
In[ ]:= (*  This is the lengh of various spacers in nm *)

         (*  Phenylaminosilane on SiOx *)
         surfacetoNspace = 0.831; (*  From WebMO at the AM1 semi-empirical level of theory *)
         (*  PTCDA on SiOx *)
         surfacetoPTCDAspace = 1.99;(*  From WebMO at the AM1 semi-empirical level of theory *)
         (*  F-Butylester perylene on SiOx *)
         surfacetoFbutylesterspace = 2.49; (*  From WebMO at the AM1 semi-empirical level of theory *)
         (*  CF3-aniline perylene on SiOx*)
         surfacetoCF3anilinespace = 2.62; (*  From WebMO at the AM1 semi-empirical level of theory *)

In[ ]:= σF3[ φ_] := σSi111Sites × 3 × φ/100 (*  Surf density of CF3 groups in one mono / nm²) ;

         ρF3[ φ_] := σF3[φ]/FThick (*  Vol density of CF3 groups from σCF3 and F thickness in #/nm³*) ;
In[ ]:= σF[ φ_] := σSi111Sites × φ/100 (*  Surf density of F groups in one mono / nm²) ;

         ρF[ φ_] := σF[φ]/FThick (*  Vol density of F from σF and F thickness in #/nm³*) ;
In[ ]:= σN[ δ_] := σSi111Sites × δ/100 (*  Surf density of N atoms in one mono / nm²) ;

         ρN[ δ_] := σN[δ]/NThick (*  Vol density of N from σN and N thickness in #/nm³*) ;
In[ ]:= ρSi = 8/SiUnitCellLength³ (*  This is the density of silicon atoms in count per nm³*) ;

In[ ]:= ρSiOx = 22.8(*  This is the density of silicon atoms in silicon oxide in count per nm³*)
Out[ ]= 22.8

In[ ]:= ρSiOx = 2.65 × 1/(28.085+2* 15.9994) + (6.02×10²³)/10²¹(*  This is the density of silicon atoms in silicon oxide in count per nm³ based on bulk density *)
Out[ ]= 26.5513

In[ ]:= λSiOx = 3.485; (*  Attenuation length of Si2p through silicon oxide *)
```

λSiOrg = 3.945; (* Attenuation length of Si2p through the organic layer *)
λNC = 3.287; (* Attenuation length of N 1s through the organic layer *)

λNself = 0.316 * 10^{12} $\left(\dfrac{14}{817 * 6.02 * 10^{23}}\right)^{1/2}$ $\left(\dfrac{1486 - 400}{7^{0.45} * \left(3 + \text{Log}\left[\frac{1486 - 400}{27}\right]\right)} + 4\right)$; (* Attenuation length of N 1s through the organic layer *)

λFC = 2.05; (* Attenuation length of F 1s through the organic layer *)

λFself = 0.316 * 10^{12} $\left(\dfrac{19}{1505 * 6.02 * 10^{23}}\right)^{1/2}$ $\left(\dfrac{1486 - 687}{9^{0.45} * \left(3 + \text{Log}\left[\frac{1486 - 687}{27}\right]\right)} + 4\right)$ (* Attenuation length of N 1s through the organic layer *)

Out[ ]= 2.31267

In[ ]:= λFself = λFC

Out[ ]= 2.05

In[ ]:= TriFluoroIntensity[ϕ_] := SFF $\times$ ρF3[ϕ] $\times$ $\left(1 - \text{Exp}\left[\dfrac{-\text{FThick}}{\lambda\text{FC} \times \text{Cos}[\theta]}\right]\right)$;

In[ ]:= FluoroIntensity[ϕ_] := SFF $\times$ ρF[ϕ] $\times$ $\left(1 - \text{Exp}\left[\dfrac{-\text{FThick}}{\lambda\text{FC} \times \text{Cos}[\theta]}\right]\right)$;

In[ ]:= FluoroIntensity[ϕ_] := SFF $\times$ $3^{-1/2}$ $\times$ FThick^{-1} $\times$ $\dfrac{\phi}{100}$ $\times$ $\left(1 - \text{Exp}\left[\dfrac{-\text{FThick}}{\lambda\text{Fself} \times \text{Cos}[\theta]}\right]\right)$;

In[ ]:= TriFluoroIntensity[ϕ_] := SFF $\times$ $3^{1/2}$ $\times$ FThick^{-1} $\times$ $\dfrac{\phi}{100}$ $\times$ $\left(1 - \text{Exp}\left[\dfrac{-\text{FThick}}{\lambda\text{Fself} \times \text{Cos}[\theta]}\right]\right)$;

In[ ]:= AminoSilaneIntensity[ϕ_] := SFN $\times$ $\dfrac{4}{\text{SiUnitCellLength}^2 \times \sqrt{3} \times \text{NThick}}$ $\times$ $\dfrac{\phi}{100}$ $\times$ $\left(1 - \text{Exp}\left[\dfrac{-\text{NThick}}{\lambda\text{Nself} \times \text{Cos}[\theta]}\right]\right)$;

In[ ]:= SiliconSilaneIntensity[Ox_, D_, ϕ_] := SFSi $\times$ $\dfrac{8}{\text{SiUnitCellLength}^3}$ $\times$ $\text{Exp}\left[\dfrac{-\text{Ox}}{\lambda\text{SiOx} \times \text{Cos}[\theta]}\right]$ $\left(1 - \dfrac{\phi}{100} + \dfrac{\phi}{100} \times \text{Exp}\left[\dfrac{-D}{\lambda\text{SiOrg} \times \text{Cos}[\theta]}\right]\right)$

In[ ]:= $\left(\text{SFN} \times 3^{(-1/2)} \times \text{NThick}^{-1} \times \dfrac{100}{100} \times \left(1 - \text{Exp}\left[\dfrac{-\text{NThick}}{\lambda\text{Nself} \times \text{Cos}[\theta]}\right]\right)\right) \Big/ \left(\text{SFSi} \times 2 \times \text{SiUnitCellLength}^{-1} \times \text{Exp}\left[\dfrac{-0}{\lambda\text{SiOx} \times \text{Cos}[\theta]}\right] \left(1 - \dfrac{100}{100} + \dfrac{100}{100} \times \text{Exp}\left[\dfrac{-\text{surfacetoNspace} - \text{NThick}/2}{\lambda\text{SiOrg} \times \text{Cos}[\theta]}\right]\right)\right)$

Out[ ]= 0.131821

In[ ]:= $\dfrac{\text{AminoSilaneIntensity}[100]}{\text{SiliconSilaneIntensity}[0, \text{surfacetoNspace} + \text{NThick}/2, 100]}$ (* N/Si ratio for Phenylaminosilane monolayer on Si(111) *)

Out[ ]= 0.131821

In[ ]:= SiliconIntensity[Ox_, D_, d_, δ_, ϕ_] :=
SFSi $\times$ ρSi $\times$ $\left(\left(1 - \dfrac{\delta}{100}\right) \times \text{Exp}\left[\dfrac{-\text{Ox}}{\lambda\text{SiOx} \times \text{Cos}[\theta]}\right] + \dfrac{\delta}{100} - \dfrac{\phi}{100}\right) \times \text{Exp}\left[\dfrac{-\text{Ox}}{\lambda\text{SiOx} \times \text{Cos}[\theta]} + \dfrac{-D}{\lambda\text{SiOrg} \times \text{Cos}[\theta]}\right] + \dfrac{\phi}{100} \times \text{Exp}\left[\dfrac{-\text{Ox}}{\lambda\text{SiOx} \times \text{Cos}[\theta]} + \dfrac{-D}{\lambda\text{SiOrg} \times \text{Cos}[\theta]} + \dfrac{-d + \text{FThick}}{\lambda\text{SiOrg} \times \text{Cos}[\theta]}\right]$;

In[ ]:= SiliconIntensity[Ox_, D_, d_, δ_, ϕ_] := SFSi $\times$ $\dfrac{8}{\text{SiUnitCellLength}^3}$ $\times$ $\text{Exp}\left[\dfrac{-\text{Ox}}{\lambda\text{SiOx} \times \text{Cos}[\theta]} + \dfrac{-D}{\lambda\text{SiOrg} \times \text{Cos}[\theta]}\right]$ $\times$
$\left(1 - \dfrac{\delta}{100} + \left(\dfrac{\delta}{100} - \dfrac{\phi}{100}\right) \times \text{Exp}\left[\dfrac{-d}{\lambda\text{SiOrg} \times \text{Cos}[\theta]}\right] + \dfrac{\phi}{100} \times \text{Exp}\left[\dfrac{-d - \text{FThick}}{\lambda\text{SiOrg} \times \text{Cos}[\theta]}\right]\right)$;

In[ ]:= SiliconEsterIntensity[dOx_, daniline_, dFull_, ϕ_] := SFSi $\times$ $\dfrac{2}{\text{SiUnitCellLength}}$ $\times$ $\text{Exp}\left[\dfrac{-\text{dOx}}{\lambda\text{SiOx} \times \text{Cos}[\theta]} + \dfrac{-\text{daniline}}{\lambda\text{SiOrg} \times \text{Cos}[\theta]}\right]$ $\times$ $\left(1 - \dfrac{\phi}{100} + \dfrac{\phi}{100} \times \text{Exp}\left[\dfrac{-\text{dFull}}{\lambda\text{SiOrg} \times \text{Cos}[\theta]}\right]\right)$;

In[ ]:= SiliconImideIntensity[dOx_, daniline_, dPery_, dFull_, δ_, ϕ_] :=
SFSi $\times$ $\dfrac{2}{\text{SiUnitCellLength}}$ $\times$ $\text{Exp}\left[\dfrac{-\text{dOx}}{\lambda\text{SiOx} \times \text{Cos}[\theta]} + \dfrac{-\text{daniline}}{\lambda\text{SiOrg} \times \text{Cos}[\theta]}\right]$ $\times$ $\left(1 - \dfrac{\delta}{100} + \left(\dfrac{\delta}{100} - \dfrac{\phi}{100}\right) \times \text{Exp}\left[\dfrac{-\text{dPery}}{\lambda\text{SiOrg} \times \text{Cos}[\theta]}\right] + \dfrac{\phi}{100} \times \text{Exp}\left[\dfrac{-\text{dFull}}{\lambda\text{SiOrg} \times \text{Cos}[\theta]}\right]\right)$;

In[ ]:= $\dfrac{\text{FluoroIntensity}[100]}{\text{SiliconEsterIntensity}[1.0, 0.831, 2.49 - 0.831 + 0.103/2, 100]}$ (* F/Si ratio for Fbutylester Perylene monolayer*)

Out[ ]= 1.3766

In[ ]:= Solve[FluoroIntensity[coverage]/ SiliconEsterIntensity[0.32, 0.831, 2.49 - 0.831 + 0.103/2, coverage] == .022, coverage]
⋯ Solve: Solve was unable to solve the system with inexact coefficients. The answer was obtained by solving a corresponding exact system and numericizing the result.
Out[ ]= {{ coverage → 3.8202}}

In[ ]:= Solve[FluoroIntensity[coverage]/ SiliconEsterIntensity[1.07, 0.831, 2.49 - 0.831 + 0.103/2, coverage] == .126 + 0.012, coverage]
⋯ Solve: Solve was unable to solve the system with inexact coefficients. The answer was obtained by solving a corresponding exact system and numericizing the result.
Out[ ]= {{ coverage → 16.6197}}

In[ ]:= $\dfrac{\text{TriFluoroIntensity}[100]}{\text{SiliconIntensity}[0, \text{surfacetoNspace}, \text{surfacetoCF3anilinespace}, 0, 100]}$ (* F/Si ratio for CF3 aniline/ Perylene monolayer*)

Out[ ]= 0.111502

In[ ]:= $\dfrac{\text{TriFluoroIntensity}[100]}{\text{SiliconImideIntensity}[1.9, 0.831, 1.16, 2.62 - 0.831 + 0.103/2, 100, 100]}$ (* F/Si ratio for CF3 aniline/ Perylene monolayer*)

Out[ ]= 6.23422

In[ ]:= Solve[TriFluoroIntensity[coverage]/ SiliconImideIntensity[1.91, 0.831, 1.16, 2.62 - 0.831 + 0.103/2, 15, coverage] == .36, coverage]
⋯ Solve: Solve was unable to solve the system with inexact coefficients. The answer was obtained by solving a corresponding exact system and numericizing the result.
Out[ ]= {{ coverage → 10.3921}}

In[ ]:= Solve[TriFluoroIntensity[coverage]/ SiliconImideIntensity[1.56, 0.831, 1.16, 2.62 - 0.831 + 0.103/2, 15, coverage] == .23 + 0.04, coverage]
⋯ Solve: Solve was unable to solve the system with inexact coefficients. The answer was obtained by solving a corresponding exact system and numericizing the result.
Out[ ]= {{ coverage → 9.00267}}

In[ ]:= Solve[TriFluoroIntensity[coverage]/ SiliconIntensity[1.91, surfacetoCF3anilinespace * .66, surfacetoCF3anilinespace * .2, 25, coverage] == .36, coverage]
⋯ Solve: Solve was unable to solve the system with inexact coefficients. The answer was obtained by solving a corresponding exact system and numericizing the result.
Out[ ]= {{ coverage → 101.325}}

In[ ]:= Solve[AminoSilaneIntensity[coverage]/ SiliconSilaneIntensity[1.242, surfacetoNspace + NThick/2, coverage] == 0.352, coverage]
⋯ Solve: Solve was unable to solve the system with inexact coefficients. The answer was obtained by solving a corresponding exact system and numericizing the result.
Out[ ]= {{ coverage → 138.145}}

In[ ]:= Solve[AminoSilaneIntensity[coverage]/ SiliconSilaneIntensity[1.242, surfacetoNspace + NThick/2, coverage] == 0.352 + 0.10, coverage]
⋯ Solve: Solve was unable to solve the system with inexact coefficients. The answer was obtained by solving a corresponding exact system and numericizing the result.
Out[ ]= {{ coverage → 160.193}}

E.4 Original models for alkylamine/alkylbromide coverages

The following eight pages of code contain the original *Mathematica* code for determining alkyl bromide and alkylamine functionalized Si(111) surfaces. It also includes the Br sensitivity analysis. This code is based equations discussed in §2.4.2.

```
θ = π/4 ;(* Analyzer angle vs surf normal *)

SFBr = 0.895; SFSi = 0.283; SFN = 0.477; SFC = 0.296;

SiUnitCellLength = 0.543090;(* Units are nanometers *)

Si111Spacing = SiUnitCellLength × √2/2 ;

σSi111Sites = .5 / ((Si111Spacing/2)² × √3)

  (*  Surface density of Si atoms in mono per nm²*)

7.82989
```

```
In[ ]:= BrThick = ∛(π/6) × 2 × 0.114;

(*  This is how thick a layer of bromine atoms would be *)
BrThick

Out[ ]= 0.183767
```

```
NThick = ∛(π/6) × 2 × 0.075 ;

(*  This is how thick a layer of Nitrogen atoms would be *)


CThick = ∛(π/6) × 2 × 0.077 ;

(*  This is how thick a layer of Carbon atoms would be *)

space = 0.0; (*  This is the space between the silicon and our thing
 of interest *) ;
dispace = 0.32 ; (*  This is the space between the silicon and two
 terminal carbons *) ;

σBr[ percent _] := σSi111Sites × percent/100
  (*  Surf density of Br atoms in one mono / nm²*) ;

ρBr[ percent _] := σBr[ percent ]/BrThick
  (*  Vol density of Br from σBr and Br thickness in #/nm³*) ;

σN[ percent _] := σSi111Sites × percent/100
  (*  Surf density of N atoms in one mono / nm²*) ;
```

$\rho N[\ percent\ \_] := \dfrac{\sigma N[\ percent\ ]}{\text{NThick}}$

(* Vol density of N from σN and N thickness in $\#/nm^{3}$*) ;

$\sigma C[\ percent\ \_] := \sigma \text{Si111Sites} \times \dfrac{percent}{100}$

(* Surf density of C atoms in one mono $/\ nm^{2}$*) ;

$\rho C[\ percent\ \_] := \dfrac{\sigma C[\ percent\ ]}{\text{CThick}}$

(* Vol density of C from σC and C thickness in $\#/nm^{3}$*) ;

$\rho \text{Si} = \dfrac{8}{\text{SiUnitCellLength}^{3}}$ (* This is the density of silicon atoms in

count per nm^{3}*) ;

$\rho \text{SiOx} = \mathbf{22.8}$ (* This is the density of silicon atoms in silicon oxide

in count per nm^{3}*)

22.8

$\lambda \text{SiSi} = \mathbf{2.823};$ (* Attenuation length of Si2p through silicon itself *)

$\lambda \text{SiOx} = \mathbf{3.485};$ (* Attenuation length of Si2p through silicon oxide *)

$\lambda \text{SiBr} = \mathbf{3.945};$ (* Attenuation length of Si2p through the organic

layer with bromine *)

$\lambda \text{SiN} = \mathbf{3.945};$ (* Attenuation length of Si2p through the organic layer

with nitrogen *)

$\lambda \text{BrBr} = \mathbf{2.6};$ (* Attenuation length of bromine at kinetic energy of Br3d *)

$\lambda \text{NN} = \mathbf{3.812};$ (* Attenuation length of Nitrogen at kinetic energy of N1s *)

$\lambda \text{BrC} = \mathbf{4.0108};$

$\lambda \text{NC} = \mathbf{3.287};$

$\lambda \text{C} = \mathbf{2.4152};$

$\lambda \text{CC} = \mathbf{3.5422};$

BromineIntensity[d_ , percent _] :=

$\quad \mathbf{SFBr} \times \lambda \mathbf{BrBr} \times \rho \mathbf{Br}[\ percent\ ] \times \left(\mathbf{1} - \mathbf{Exp}\left[\dfrac{-d}{\lambda \mathbf{BrC}\ \mathbf{Cos}[\ \theta]}\right]\right);$

NitrogenIntensity[d_ , percent _] := $\mathbf{SFN} \times \lambda \mathbf{NN} \times \rho \mathbf{N}[\ percent\ ] \times \left(\mathbf{1} - \mathbf{Exp}\left[\dfrac{-d}{\lambda \mathbf{NC}\ \mathbf{Cos}[\ \theta]}\right]\right);$

SiliconIntensity[d_ , D_ , λSiover _] := $\mathbf{SFSi} \times \rho \mathbf{Si} \times \lambda \mathbf{SiSi} \times \mathbf{Exp}\left[\dfrac{-(d + D)}{\lambda \text{Siover}\ \times \mathbf{Cos}[\ \theta]}\right];$

CarbonIntensity[d_ , percent _] := $\mathbf{SFC} \times \lambda \mathbf{C} \times \rho \mathbf{C}[\ percent\ ] \times \left(\mathbf{1} - \mathbf{Exp}\left[\dfrac{-d}{\lambda \mathbf{CC}\ \mathbf{Cos}[\ \theta]}\right]\right);$

OxideIntensity[d_] := $\mathbf{SFSi} \times \rho \mathbf{SiOx} \times \lambda \mathbf{SiOx} \times \left(\mathbf{1} - \mathbf{Exp}\left[\dfrac{-d}{\lambda \mathbf{SiOx} \times \mathbf{Cos}[\ \theta]}\right]\right);$

```
OxideThickness[ experimentalratio    _] :=
   λSiOx × Cos[ θ] × Log[ experimentalratio    × 1.41 + 1] ;
```

```
    CarbonIntensity[ CThick, 100]
──────────────────────────────────────
SiliconIntensity[ CThick, space, λSiBr]
(* C/ Si ratio for singly brominated allyl monolayers*)

0.0571319
```

```
    BromineIntensity[ BrThick, 100]
──────────────────────────────────────
SiliconIntensity[ BrThick, space, λSiBr]

(* Br/ Si ratio for singly brominated allyl monolayers*)

0.0108244
```

```
    2 * BromineIntensity[ BrThick, 100]
──────────────────────────────────────
SiliconIntensity[ BrThick, dispace, λSiBr]
(* Br/ Si ratio for doubly brominated allyl monolayers*)

0.373534
```

```
  BromineIntensity[ BrThick, 100]
──────────────────────────────────────
SiliconIntensity[ BrThick, 0, λSiOx]
(* Br/ Si ratio for brominated silicon *)

0.16798
```

```
    NitrogenIntensity[ NThick, 100]
──────────────────────────────────────
SiliconIntensity[ NThick, space, λSiN]
(* N/ Si ratio for singly aminated allyl monolayers*)


0.17026
```

```
    2 NitrogenIntensity[ NThick, 100]
──────────────────────────────────────
SiliconIntensity[ NThick, dispace, λSiN]
(* N/ Si ratio for doubly aminated allyl monolayers*)

0.350426
```

```
    OxideIntensity[ 1.434]
──────────────────────────────────────
SiliconIntensity[ 1.434, 0, λSiOx]
(* should be the ratio of oxide to silicon for one oxide mono*)
```

```
0.444924
```

OxideThickness[**0.56**]

```
1.43418
```

$$\textbf{Solve}\left[\frac{\textbf{BromineIntensity}[\textbf{ BrThick, coverage}]}{\textbf{SiliconIntensity}[\textbf{ BrThick, space, }\lambda\textbf{SiBr}]}\ ==\textbf{0.018, coverage}\right]$$

```
{{ coverage → 9.91808}}
```

```
(*  now look at a range of space values for bromine... consider 0.2
 to 0.6 nm to bookend 0.4 by 0.2 nm *)
```

ExportString[**Range**[**space** - **0.15, space** + **0.15, 0.01**] , **"List"**]

```
0.09
0.09999999999999999
0.11
0.12
0.13
0.14
0.15
0.16
0.16999999999999998
0.18
0.19
0.2
0.21
0.22
0.23
0.24
0.25
0.26
0.27
0.28
0.29000000000000004
0.3
0.31
0.32
0.32999999999999996
0.33999999999999997
0.35
0.36
0.37
0.38
0.39
```

```
ExportString[
 Flatten[
  Table[
   {s = Solve[ BromineIntensity[ BrThick, coverage] / SiliconIntensity[ BrThick, spacing, λSiBr] == 0.018, coverage];
    s[[ All, 1, 2]][[  1]] }, { spacing, space - 0.15, space + 0.15, 0.01} ]],
  "List"]
```

```
10.465999338235363
10.428547728353955
10.391230135591925
10.354046080381417
10.316995084870662
10.280076672917836
10.243290370084953
10.20663570363176
10.170112202509646
10.133719397355627
10.097456820486267
10.061324005891711
10.025320489229669
9.989445807819456
9.953699500636048
9.918081108304158
9.882590173092328
9.847226238907055
9.81198885128692
9.776877557396748
9.741891906021804
9.707031447561977
9.672295734026001
9.63768431902572
9.603196757770327
9.568832607060662
9.534591425283503
9.500472772405915
9.466476209969567
9.432601301085121
9.398847610426602
```

```
(*  now look at a range of radius values for bromine... consider 0.05
 to 0.2 nm to bookend 0.114 nm *)
```

$$\text{ExportString}\left[\text{Range}\left[\sqrt[3]{\frac{\pi}{6}} \times 2 \times 0.05, \sqrt[3]{\frac{\pi}{6}} \times 2 \times 0.2, 0.005\right], \text{"List"}\right]$$

```
0.08059959770082348
0.08559959770082348
0.09059959770082347
0.09559959770082348
0.10059959770082348
0.10559959770082347
0.11059959770082348
0.11559959770082348
0.12059959770082349
0.12559959770082346
0.13059959770082347
0.13559959770082347
0.14059959770082348
0.14559959770082348
0.15059959770082348
0.1555995977008235
0.1605995977008235
0.1655995977008235
0.17059959770082347
0.17559959770082348
0.18059959770082348
0.18559959770082346
0.19059959770082346
0.19559959770082347
0.20059959770082347
0.20559959770082348
0.21059959770082348
0.2155995977008235
0.2205995977008235
0.22559959770082347
0.23059959770082347
0.23559959770082348
0.24059959770082348
0.24559959770082349
0.2505995977008235
0.2555995977008235
0.26059959770082347
0.2655995977008235
0.2705995977008235
```

```
0.2755995977008235
0.2805995977008235
0.2855995977008235
0.29059959770082344
0.29559959770082345
0.30059959770082345
0.30559959770082346
0.31059959770082346
0.31559959770082346
0.32059959770082347
```

```
ExportString[
 Flatten[
  Table[
   {s = Solve[
      BromineIntensity[BrThickness, coverage]
      ─────────────────────────────────────── == 0.020, coverage];
      SiliconIntensity[BrThickness, space, λSiBr]

    s[[All, 1, 2]][[1]] }, {BrThickness, ∛(π/6) × 2 × 0.05, ∛(π/6) × 2 × 0.2, 0.005}]],
  "List"]
```

```
25.606134442369633
24.088385871081865
22.738173135052357
21.529209119045934
20.440432795367073
19.454771982513023
18.55824170396619
17.739276537733964
16.988229048646026
16.296988022238917
15.65868439403622
15.067462238915875
14.518298624905785
14.006860585118718
13.52939058140955
13.082614050932369
12.663664222997474
12.270020556096501
11.899458000798289
11.550004930734994
11.219908061811902
10.907603041815944
10.611689669161784
```

```
10.330910912451323
10.064135067692927
9.810340519043988
9.568602670392332
9.338082695366436
9.11801781726549
8.907712881554286
8.706533024739656
8.513897276753244
8.329272961043431
8.152170778696329
7.982140481050728
7.818767050222952
7.661667319326358
7.510486974443706
7.364897888975665
7.224595748154903
7.08929792753273
6.95874159431409
6.832682004700902
6.7108909740356575
6.59315549962561
6.479276518760984
6.369067786693023
6.26235486126825
6.158974182575168
```

APPENDIX F

INSTRUMENT STANDARD OPERATING PROCEDURES

F.1 Glovebox

F.1.1 Catalyst Regeneration Procedure

A regeneration procedure is recommended once the base O_2 concentration exceeds 5 ppm. It's preferrable to start a regen early in the day. It takes 3 hours too heat the catalyst bed and another 3 hours of H_2 flow and it's ideal for the regen process to be monitored during the active flow of H_2 gas.

A regeneration requires:

- >2,000 PSI of UHP N_2
- >1,200 PSI of 5% H_2 / 95% N_2
- 16 hours of idle time and empty antechambers.

1. Check H_2 gas flow.

2. Open the H_2 tank and Swagelok valve.

3. Fill a bin with water and submerged a 2 L flask (for verifying flow rate).

4. Find the catalyst exhaust hose (it's connected to the vacuum pump vent).

5. Check the glovebox settings and make sure that it is set to NOT automatically start recirculation after the Regen.

6. Turn off glovebox circulation and select regeneration. You should be prompted to confirm H_2 gas flow. If you hear gas flowing from the exhaust line, use the gas to fill the submerged flask. Count the time it takes to fill 2 L.

7. Flow rate should be between 10–20 L min^{-1}.

8. If gas is flowing slowly, check to make sure the tank is completely opened.

9. Maintenance section details steps to check if gas flow is low/non-existent.

10. If gas is flowing, select confirm gas flow. Gas flow will stop and won't flow again until the catalyst has heated.

11. Take the exhaust line and connect it to a large side arm flask, submerged in ice, to collect water generated during the regen. Connect the outlet to the vacuum exhaust again to avoid H_2 build up in the glovebox room.

12. At this point, the regen process is completely automated.

13. Close the vacuum valves to both chambers as the regen process uses the vacuum to evacuate the catalyst beds.

14. Monitor the temperature of the catalyst, it should be heating up.

15. This link provides a more in-depth overview of the regen program, compared to the MBraun manual.
http://web.uvic.ca/~mcindoe/LabmasterManual.pdf

16. Monitor gas flow of both gases to ensure one doesn't run out.

17. After 16 hours, the regen program will complete.

18. Close the H_2 tank valves.

19. Enable the O_2 sensor and do a quick purge to get the O_2 level >10 ppm.

20. Fill the box with excess N_2 pressure and begin circulation. There will be a slight negative pressure in the catalyst that will pull some pressure away from the mainbox.

21. Empy the water receiver and reconnect the exhaust line.

22. At this point, the regeneration is finished.

F.1.2   Glovebox Maintenance

F.1.2.1   Leaks

1. Generally, leaks occur in small holes made in the gloves.

2. Electrical tape patches on the inside and outside will help prevent gas leakage.

3. When the gloves leak, the box will refill itself more often to maintain a positive -pressure. It should not have to refill itself more often than every 15 minutes or so.

4. Leaks, in the gloves or at flanges, can generally be found by feeling for a small flow of air.

F.1.2.2   Low or no H_2 Flow

1. Previously, corrosive gases generated during the regen have caused the catalyst exhaust valve to stick. Follow the exhaust line to find the valve in the aluminum manifold. Generally, this valve will need replacing. See glovebox maintenance folder in CBC42 for PO info.

2. Sometimes the check valve in the exhaust line will also stick. This can usually remedied with by cleaning off any residue. Make sure the check valve is oriented in the correct direction before reattaching, otherwise gas will not flow whether the valve works or not.

F.1.2.3   Filter Replacements

1. The charcoal filter and the HEPA dust filter inside the glovebox should be changed periodically.

2. Fill the charcoal filter with activated charcoal pellets outside the glovebox. Pump in over a weekend.

F.2   Phi5600

F.2.1   Regular Maintenance Procedures

F.2.1.1   Running the Titanium Sublimation Pumps (TSP)   Run the TSP filaments at least once a week. Also useful for reducing chamber pressure after scanning particularly gaseous samples.

1. Make sure X-rays have been off for at least 5 minutes.

2. Close the monochromator shutter

3. Make sure current is set all the way to 0, CCW.

4. Set the Boostivac to Continuous mode and hit the red reset button.

5. Now increase the filament current. The pressure should spike and settle down to a stable pressure with the filament running.

6. Increase current to 50 A (division between green and yellow) and let sit.

7. Once the pressure starts to uptick again, bring the current down to 0 and set the controller to off.

8. Switch the filament selector to the next CW position.

F.2.1.2   Cleaning Console Filters   These filters should be cleaned once a year. They are located against the back wall. One under the X-ray source rack, one under the Card Rack, and one under the ion pump controller.

F.2.1.3   Check Chiller Water Level   The water level of the chiller should be checked every couple months, especially after bakeouts and procedures that require disconnecting the water lines. Fill the reservoir to an inch below the metal top with distilled water.

F.2.2   Troubleshooting

F.2.2.1   Air bubbles in the waterline

1. Low water level in chiller.

2. Leak in the waterlines between the chiller in the XPS.

   (a) Water has previously leaked at the connection of the back of the chiller to the braided hoses. Tightening the hose-clamps fixed the issue.

F.2.2.2   Air bubbles in the waterline   At 15 kV, the leakage current should only be 1–2 mA. If it is higher, it is always due to contaminants in the chiller water or somewhere along the water circuit.

1. Deionizer or particle filters expended. The deionizer in the water chiller will eventually be used up, every 2 years or so. Order a new one from RBD. Similarly, small metal particles from the pipes and x-ray sources increase the conductivity of the water leading the current-leakage and will eventually clog the particle filter. RBD sources replaces as well.

2. Both X-ray sources will slowly be coated with some of the aforementioned metal particles and will need periodic cleaning. Refer to the specific manuals for disassembly instructions. Clean the Teflon tubing of the twin anode with pipe cleaners, acetic acid, and the sonicator. Dilute acetic acid blow through the source itself will also help clean it. Remember to rinse thoroughly with DI water after. The Teflon block for the monochromated source also gets contaminated with metal. Remove the compression fittings from the Teflon block, clean the block and compression fittings with dilute acetic acid and the sonicator. Rinse thoroughly before reattaching to the source.

F.2.3   Bakeout

F.2.3.1   Chamber Pump-Down   Whether the chamber was vented intentionally for maintenance or unintentionally, a system bakeout is required to bring the chamber pressure back to UHV. The bakeout procedure is also used to reduce chamber pressure after the baser pressure slowly raises over time.

1. With both the analysis chamber and loadlock at atmospheric pressure, manually open **V1**.

2. Turn on the Edwards RV3 rough pump and open the Swagelok valve connected to the loadlock to begin pumping out the entire system.

3. Monitor the pressure on the thermocouple gauge at the loadlock over the next hour. The pressure will eventually drop into the mtorr range. (If not, there's probably a leak wherever the system was worked on).

4. To help pump the chamber down, turn on the WooSung Automna pump connected to the UV Source. When the pressure at the pump is under 100 mtorr, open the valve to the UV source.

5. Once the chamber pressure (at the loadlock TC gauge) is in the mtorr range and steadily going down, turn on the loadlock turbo pump.

6. Note the state of the plumbing between **V4** and the butterfly valves of the UV source and ion gun. Generally, it's left under passive vacuum while vented and is safe to open **V4** with the turbo at full speed. If suspected to be at a higher pressure, open **V4** shortly after turning the loadlock turbo on. (We don't want excess pressure hitting the turbines but we also don't want rough pump oil vapor to travel up into that region.)

7. When the turbo controller has 4 LEDs lit, manually open **V3** to the loadlock and the turbo will start pumping out the analysis chamber.

8. If not already running, the turbo pump for the TPD chamber can also be turned on. Once at 1500 hz and stable ~0.90 A of current, open the gate valve between the analysis and TPD chamber.

9. Pump the chamber with the turbos for at least a couple hours before turning the ion gauge controller on. Switch the ion gauge controller from **Off** to **UH**V. Press **1** to select the ion gauge. The controller will scan then settle on the chamber pressure. If it beeps, try ion gauge **2**.

   (a) (Sometimes need to press the **I/T** button then **1** or **2**.)

   (b) If the controller won't read **1** or **2**, check the connection at the analysis chamber. The bakeout temperatures oxidize the pins at the filament feed through and may need gentle sanding.

10. The pressure should be in the low 10^{-5} to 10^{-6} torr. At these pressures, it's safe to turn on the ion pump.

11. Set the switch from **OFF** to **RUN**. (In **START** mode the ion pump will not turn off in the event of a pressure spike. <mark>This is bad.</mark> Use **RUN** in 99% of situations)

12. Close **V1**. (Gate valve to the TPD chamber may remain open)

13. Let the ion-pump pump the chamber for a day or at least overnight.

F.2.3.2 *Prepping Chamber for Bakeout*   All cables and materials incompatible with bakeout temperatures (200 °C) will be removed and all glass windows and feedthroughs covered with foil to prevent thermal shock. The only cables left running to the chamber should be the one to the Ion Gauge and the thermocouple cable on the monochromator that measures bakeout temperatures.

1. Disconnect the video and power cable from the microscope camera.

2. Unscrew the collar and carefully remove the microscope.

3. Note the micrometer position before removing the motors. Remove the 4 motors from the Sample Stage Manipulator Axes. Depress the button that holds motor in place and slowly pully the motor in the direction of the axis.

   (a) Disconnect motor cables from the motors. The motors are marked but remember that the Z-axis motor uses the 4″ intermediary reverse cable.

4. Remove the **Ion** and **Target** BNC connections (and the elbows) from Stage Manipulator.

5. Remove the Amphenol connection to the stage manipulator.

6. Disconnect the cable to the neutralizer.

7. Disconnect the two connections to the Ion gun.

8. Disconnect the filament power cable to the Mono source.

9. Remove the three screws to the Mono source cover and remove the cover.

10. Remove the three hex-head screws in the Teflon block. Keep a hand on the metal part of the source body to prevent any excess stretching/compression of the metal bellows and with the other hand pull the Teflon block off while twisting only a few degrees. Keep a beaker handy to collect the water that will spill out.

11. Carefully remove the two compression hose fittings. Don't pull or push the source too far or the alignment of the source will be thrown off.

12. Remove the HV connection.

13. Remove the two screws in the metal body of the next piece. Inside the soft rubber gromet, the high-voltage spring that makes contact to the anode can be compressed with a spatula and the hole body can be pulled off. Compressing the spring ensures it won't eventually get ripped off.

14. With a small, rounded spatula carefully remove the three o-rings at the end of the anode. Add a little Apiezon vacuum grease to the O-rings to prevent from drying out.

15. Remove the water lines from the twin-anode source. Like the mono source, be careful not to torque it and damage the bellows. Unscrew the cylindrical aluminum cover screws on the side with the yellow label and pull the cover off.

16. Remove the Teflon liner from the source. It shouldn't be hard to remove but make sure it hasn't caught any of the wires inside.

17. Remove the high voltage connection in the source.

18. Disconnect the filament power cable to the twin anode.

19. Remove the water connections to the UV Source. Keep a beaker handy to catch the water that drips out.

20. Remove the red BNC cable from the back of the UV source and the one from the between the water line connections and pull the aluminum block off.

21. Disconnect the 6-pin cable to the SCA Terminator box. Loosen the two hex had bolts by hand, only finger tight, and carefully pull the SCA Terminator out.

22. Disconnect the ground Amphenol connection from the lens system, near the **CTL** and **FCL** connectors..

23. Remove the **CTL** and **FCL** cables from the lens system between the hemisphere and chamber.

24. Disconnect the two multiplier high voltage supplies from the hemisphere, **J1** and **J4**.

25. Unscrew the color from the 16-Channel amplifier from under the hemisphere. Gently pull the amplifier straight from the hemisphere. Critically important not to bend any of the pins! Place the box somewhere safe where it won't fall.

26. Remove any other cables, components, and lights from the chamber.

27. Cover all ports and electrical feed-throughs with foil to prevent thermal shock.

F.2.3.3 Bakeout

1. Remove the three wooden tabletops touching the chamber. Pull up the two bakeout interlock switches at the front and back.

2. Wipe down all the surfaces with IPA and kimwipes to remove finger-prints and oils.

3. Spread the bakeout blanket on the floor and determine the location of the ports.

4. With another person, raise the blanket over the chamber and lower into place.

   (a) Wear gloves, mask, goggles, and lab coat. The insulation is itchy and the metal Velcro will scratch through skin.

   (b) Be careful not to torque the twin-anode source or any sensitive appendages on the chamber.

5. Button the corners and attach the Velcro pieces.

6. The blanket covers the window-port at the top of the monochromator but stops there.

7. Add the patch that covers the square hole at the monosource and the long patch cover the UV source.

8. Attach the compression-fitted water line vents to the twin anode source and blow out the excess water. Leave the vents on during bake out so water left behind is allowed to vent out of the source.

9. There is a piece of blanket that helps insulate **V1** from the heat that wraps around the tubing between the chamber and **V1**.

10. Add foil to the gaps around the twin anode, the monochromator, and other obvious gaps.

11. Press the **Bakeout Power** button on the electronics console. Turn the dial for 24 hours. A relay should click to indicate current flow.

12. If the space doesn't begin to heat:

    (a) Check the interlock switches.

    (b) Check the bakeout pressure set point.

13. Depending on the state of the system before starting the bakeout, the bakeout time can range between 24 and 72 hours. If vacuum wasn't broken before the bake, or only partially vented, 24 hours will suffice. From atmospheric pressure, 48 hours minimum is required.

14. It helps to keep the gate valve to the TPD chamber open during the first 24 hours of the bakeout in case of ion pump "burps". Once the pressure

is steadily going down, the gate valve can be closed with a gloved hand through the patch near the UV source.

15. The pressure should bottom out at some point during the bakeout. The bakeout of **2020-06-05** bottomed out at 2.5×10^{-7} torr and the heat was turned off.

16. Let the system cool at least 2 hours with the blanket on.

17. To help drop the pressure, after two hours, begin running the TSP filaments every 20 minutes or so. They will outgas quite a bit, slowly ramp up the current and keep the pressure below 5×10^{-6} torr. Run each filament once and then another time, ideally hitting the 50 A.

18. While the chamber is still warm, degas the ion gauge by pressing the **Degas** button on the **DIGIII**. This will take around 5 minutes.

19. Remove the compression fitting water line vents.

20. With another person, carefully remove the bakeout blanket.

F.2.3.4   Post Bakeout Assembly

1. After 4 hours or so, or once the chamber has cooled down enough, begin reconnecting components. Start with the water monochromator source.

   (a) Attach the three O-rings to the mono source.

   (b) Compress the spring within the rubber grommeted metal body and attach to the source with the three hex-head screws.

   (c) Attach the high-voltage cable.

   (d) Attach the Teflon block, carefully, as done while removing it and insert the two screws that hold it on.

   (e) Put the cover back on using the three screws. Remember to attach the grounding wire to the screw on the left.

   (f) Insert the water lines to the monosource while keeping a strong hand on the source to not damage the bellows or alignment.

   (g) Reattach the filament power cable to the monosource.

2. Insert the high-voltage cable and the Teflon lining to the twin-anode source.

   (a) Screw the metal cover back and reattach the water lines to the source.

   (b) Attach the filament power cable to the twin anode.

3. Check the water lines are attached correctly.

4. Turn on the X-ray source control **32-096**. Water should begin to flow. It may bubble at first from air pockets but should subside after 10 seconds.

   (a) If not, the water level may be low or there may be a leak.

   (b) Check for leaks and refill the reservoir with distilled water.

5. Connect the **Target** and **Ion** BNC cables to the stage manipulator.

6. Connect the Amphenol connection to the Stage manipulator.

   (a) Reconnect the X, Y, Z, and Tilt-axis motors. Check notes or pictures to make sure the micrometer positions are the same as when the motors were removed.

   (b) Reconnect the motor cables to the main cable. First loop the main cable through the handle on the hemispheres to remove tension from the motor connections.

7. Reattach the two cables to the ion gun.

8. Attach the water lines and HV cable to the UV source.

9. Insert the SCA Terminator box back to the hemisphere. Finger-tighten the hex-head bolts underneath and attach the 6-pin cable.

10. Attach the **CTL** and **FCL** cables back to the lens system.

11. Attach the grounding Amphenol connection to lens system.

   (a) If this forgotten, charge can build in the analyzer and the binding energies will be thrown off.

12. Attach the two high-voltage multiplier connections to the hemisphere.

   (a) Remember **J1** to **J1** and **J4** to **J4**.

13. Carefully insert the 16-channel amplifier back into the SCA.

   (a) Push the box over the cylindrical bar first, line up the key-notch and carefully push in. Remember to not bend any pins! Tighten the collar.

   (b) This process can be finicky but a gently and steady hand will be fine.

14. Reconnect the neutralizer cable.

15. Insert the microscope with the locator pin. Tighten the collar until snug.

   (a) Reconnect the video and power cables.

16. Check for any cables that still aren't attached.

F.2.4   Optics Degassing and Conditioning

F.2.4.1   Ion Gun

1. Open **V4** and the butterfly valve to the ion gun.

2. Turn on the **11-065** Ion Source Controller.

3. Check that the meter is switched to read **Emission**.

4. Slowly turn the emission knob clockwise.

5. You should see a small pressure spike once current begins to flow. Once the pressure drops again, bring the current to 5 mA.

6. Raise the current by 5 mA every two minutes until it sits at 25 mA. Leave for at least ten minutes.

7. Turn down the current and turn off the **11-065**.

F.2.4.2   X-ray Filaments

1. Turn on the **32-096**.

2. Select the Mono Source.

3. Select Internal Control.

4. Press the blue **Out/Act**. button.

    (a) This will enable control the filament current.

    (b) It should stay pressed in and turn blue.

5. Select the **Both** button under filament energize.

6. Select Mono Source 1 and slowly raise the current to 0.5 A.

7. Select Mono Source 2 and slowly raise the current to 0.5 A.

8. While alternating between 0.5 A each, slowly raise the current to 3.0 A.

    (a) At 3 A, there should be a small pressure spike depending on how dirty the filament is.

9. 0.1 A at a time, raise the current of each filament to 4.0 A.

10. Let both filaments run at 4.0 A for at least 12 hours.

    (a) The PHI manual will say overnight for the diffuse filament and only a few minutes for the focused filament. It can't hurt to have the focused filaments run overnight the same way.

11. The next day, lower the filament current of the mono source to 0 and switch to the Twin-anode source.

12. Raise the filament current of both the **Mg** and **Al** anodes to 3.5 A in the same manner as for the mono source.

13. Slowly raise the current of each until you reach 4.5 A. Leave running for at least 6 hours.

14. Raise to 5.0 A and let run for 30 minutes.

15. Turn off the current.

F.2.4.3 Anode Outgassing

1. Start with the twin-anode.

2. Select the Mg anode under Filament Energize.

   (a) Only one anode at a time during this process! Running multiple anodes, especially on the mono source may damage or even melt the anode.

3. Again, set the **32-096** to **Outgas** mode.

4. Select **HV** under the Parameter Display/Control section.

5. Press the red **High Voltage** button. It should start flashing red.

6. Flip the **AC POWER** and **HV ON** switches and the green bulb should light.

7. Turn the Variac until **0.5** kV is displayed.

8. Switch the display to show the filament current of the **Mg** filament.

9. Raise the current to **3.5** A. Then slowly raise the current while keeping an eye on the emission current. Do not increase passed 5.0 A filament current or 2 mA emission current.

   (a) Usually 5.0 A of filament current is reached before the emission current reaches 1 mA.

10. Slowly increase the anode voltage to **1** KV. There should be a small pressure spike. Keep increasing the voltage by **0.5** KV increments every two minutes or so until **5.0** KV. There may be small pressure spikes after increase so allow the pressure to fall back down before increasing. Use **1** KV increments until **10** kV is reached

    (a) Go slow and watch for pressure spikes.

    (b) Remember to maintain an emission current below 2.0 mA. If it starts to go higher, decrease filament current.

11. Let sit for five minutes before lowering the high-voltage and then the filament current.

12. Switch to the **Al** anode and repeat the process.

13. Repeat the anode outgassing steps on the mono source. One filament at a time!

14. Pressure spikes and noticeable increases the emission current are much more prevalent on the mono source.

15. Differences to the Twin-anode:

    (a) At **10.0** KV, the emission current should be **5** mA. Not **2** mA.

      i. During the last bakeout, to reach **5** mA of emission current; the filament current was ~ **4.5** A at **10** kV.

16. After the **5** mA of emission current is reached, let run for about 20 minutes.

   (a) Because only 2 focused filaments are being used here, not a diffuse filament, the area being cleaned in this process is much smaller. Longer anode-outgassing times here will help clean the anode before high-voltage conditioning.

17. Turn down the voltage and then the filament current.

18. Depress the **Outgas** button to turn off.

F.2.4.4   High Voltage Conditioning

1. Make sure there is no filament current or power trying to be achieved before raising the high voltage.

2. Begin by increasing the voltage to **10** kV.

3. After 2-3 minutes, raise the voltage to **10.5** kV.

4. While watching for outgassing, raise the voltage **0.5** kV every few minutes. At **13** kV, wait closer to 5–10 minutes between each increase.

   (a) If there is an arc or you see the emission current begin to creep up, lower the voltage or turn off completely and restart **2** kV lower than where the arc occurred.

      i. Sometimes an arc may confuse some of the electronics in the system like the **AVC** controller **RBD 147** box, or the computer itself. Restarting the component usually takes care of it.

   (b) Because of the smaller filaments in the mono source, it can take extra time to clean the anode.

   (c) If there is an arc, it may require additional outgassing of the mono source anode. (Repeat of the steps above)

   (d) **The last two bakeouts, after installing two focused filaments, have required fairly long high voltage conditioning (1–2 hours). Arcs occurred when going to fast and a couple times after 15 kV. Extra time helped and sitting at the anode outgas conditions helped clean the system.**

5. Once **16.5** kV is reached, let sit for at least 20 minutes then decrease the voltage to 0 kV.

F.2.4.5 Final X-ray source conditioning

1. Start with the Mono source.

2. Select Mono Source **1**.

3. Set the anode voltage to **10** kV.

4. Raise the power to **3** W. There should be a small pressure spike.

5. Increase the power to **25** W and the voltage to **10.5** KV and wait a few minutes for the pressure to decrease.

6. Increase the power to **50** W and voltage to **11** kV and wait.

7. Iteratively increase the power and voltage until **300** W and **13.5** KV is reached. Let sit for at least **20** minutes.

8. Decrease the power to 0 W and the voltage to **10** kV. Switch to filament **2** and repeat.

9. Repeat this process for the twin-anode, one at a time.

10. The ending power and voltage for the twin-anode should be **300** W and **15.0** kV.

F.2.4.6 Neutralizer Outgassing

1. Turn on the **Card Rack power** and the **RBD 147** box.

2. Open the AugerScan software and open the Neutralizer Control.

3. Set the emission control to **15.0** mA and the electron energy to **0**%.

4. Set the controller to On and run for 30s.

5. Raise the current to **16.0** mA and press enter.

6. Repeat until **21.0** mA of current is achieved.

7. Turn off the neutralizer.

F.2.4.7 Stage Heater Outgassing

1. Make sure the X-rays and other filaments have had time to cool. Outgassing of the stage may raise the chamber pressure above 5×10^{-7} torr. Running a TSP filament before-hand helps maintain pressures.

2. Turn on the **20-028A** Specimen Heater Controller. Also flip on the switch to the right.

3. Increase the temperature on the Eurotherm control to **50** °C. Watch the pressure, it will raise significantly as the filament heats up. Wait 10 minutes. If pressures raises to high, turn the temperature down.

4. Raise to **100** °C and repeat.

5. Repeat process until **250** °C is reached and heat for a half hour.

6. Turn off the heat.

7. Run the TSP again to help recover chamber pressures.

F.2.4.8 Multiplier Outgassing

1. Load the slotted silver specimen. Probably already in the chamber any-way if you're planning to align the optics.

2. Make sure the X-rays are off for the first part of this procedure.

3. Open AugerScan and open the Multiplier Properties dialogue and go to the XPS tab.

    (a) Note the current multiplier voltage (**2100** V after the **2020-06-05** Bake-out)

4. Adjust the multiplier voltage to **500** V.

    (a) Always double check that you have set the correct multiplier voltage and that it's never above 2300 V.

5. Not sure if there's a software safety value but I'm sure that voltages above **2300** V are not good for the Channeltron multiplier. . . .

6. Setup an alignment scan. The Ag 3d region will suffice. Use Survey setting pass energies and resolution. Something that will be able to run a few scans in about 10 s.

7. Run the scan and allow to go through the spectrum for 3 or 4 times.

8. There should be no signal and counts should be 0 at these low multiplier voltages.

    (a) If there is noise or signal, there may be a misconnection and it should be identified before continuing.

9. Increase the multiplier voltage by **100** V and repeat the scan. Repeat this process until **1500** V is reached.

10. Now increase by **50** V increments until **2300** V is reached.

    (a) You may see signal at the higher voltages related to noise, this is normal. Counts generally hit 40 or 80 CPS. Not actual photoelectrons since the X-rays are off, just noise from the multiplier.

11. Now, with a silver alignment specimen in the chamber, repeat this pro-cess with the X-rays on.

    (a) Use the twin anode at full power (**250** W and **15** kV)

Multiplier Properties   ✕

AES	XPS	SIMS

Multiplier: **2100** V   Acquire Gain Curve

Gain Curve Settings

Starting V: 500   V

Max V: 2300   V

V/Step: 10   V

Time/Step: 25   mS.

Analyzer: 368   eV

Pass Energy: 100   eV

Multiplier Offset   80   V

OK   Cancel   Apply   Help
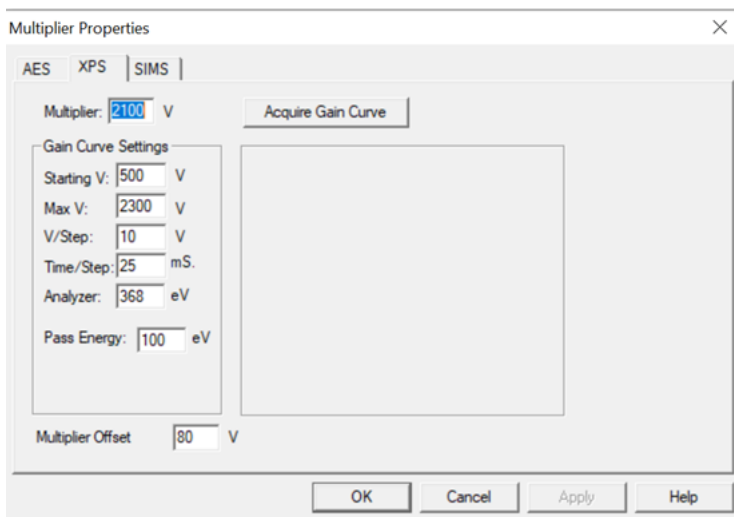
12. Sometimes I'll do this step during the final conditioning of the twin-anode at full power.

    (a) Optics aren't aligned at this point but the camera probably isn't too far off. After the **2020-06-05** bakeout, the silver specimen was in focus with the detector ~7.6 mm in the Z axis.

13. Around **1500** V, Ag peaks should begin to show up.

14. After scanning at **2300** V, run the Acquire Gain curve with the following settings. (Use the exact position of the Ag $3d_{5/2}$ peak from your alignment scans for your Analyzer value)

    (a) The Acquire gain curve may look like it's not running, give it a few seconds. Augerscan may also become unresponsive for a second but eventually it'll come back and you'll see the curve being generated.

15. Find the inflection point and use this for the multiplier voltage.

16. Multiplier conditioning is complete.
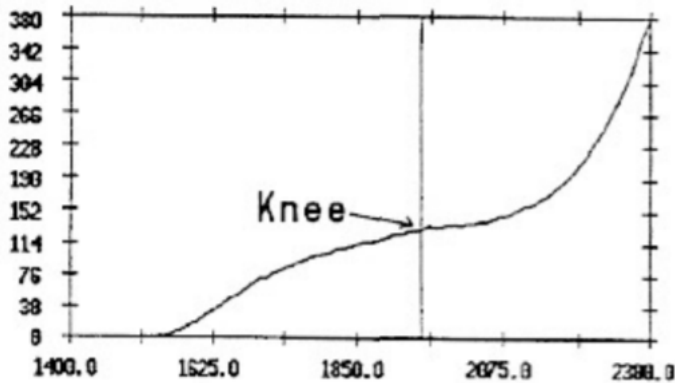
F.2.5   Optics Alignment

F.2.5.1   Finding the Focal Point of the System   The first step in aligning the optical elements within the chamber is to align the focal point of the camera to the focal point of the detector.

1. Load the silver-slotted specimen. The slits should be running in the Y-axis or from the monochromator to the hemisphere.

2. Sputter the surface with the ion gun to remove any carbon contamination from the surface.

   (a) Refer to the Ion Gun SOP in §F.2.6.3

   (b) Set the raster size to 10 mm × 10 mm. Sputter each spot for about a minute.

       i. Remember, the ion-gun port is at an angle, not pointed straight down, so at this raster size, the sputtered area is probably 20 mm × 10 mm.

   (c) Sputter the areas you think you'll be scanning most:

       i. Open area in the center for total counts, around the slits and holes, etc.

   (d) Do a quick alignment scan from 290–280 eV to check for any carbon signal.

3. From this point, we're following the Techspot Post from Randy at RBD.

   (a) https://www.rbdinstruments.com/blog/xps-analyzer-focal-point/

4. Set the physical aperture to 3 and area in minimum. Set the following hardware settings in under the System/Hardware Properties/XPS tab

Aperture:

3

Area
- ◌ Micro
- ◉ Minimum
- ◌ Small
- ◌ Large

Alignment Settings   ✕

Binding Energy

Upper Limit: 374.00 eV

Lower Limit: 362.00 eV

EV/Step: 0.800 ▼ eV

Pass Energy

187.85 ▼ eV

Acquisistion Time

Time/Step: 50.0 mS

☐ Neutralizer On

Acquire

Apply

Cancel

Help

Edit Gun Settings...
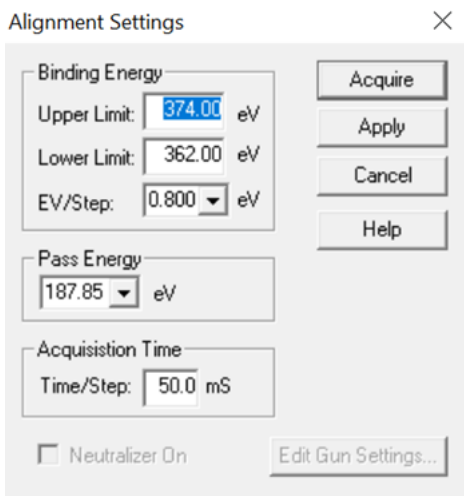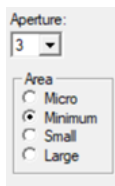
X and Y Values for the Omni Focus III Lens:

Aperture Number	Software Setting		
	Minimum-Area Mode	Small-Area Mode	Large-Area Mode
1	75 µm	—	—
2	150 µm	200 µm	500 µm
3	400 µm	600 µm	2 mm
4	800 µm	1.1 mm	4 mm
5	0.8 x 2 mm	1 x 3.5 mm	3 x 10 mm

5. Setup an alignment scan with the settings from the next page.

6. Open the Camera Software if not already open.

7. Set the Mg or Al twin-anode source to **300** W at **15** kV.

   (a) The twin-anode source illuminates the entire puck surface, making it easier to first align the camera before aligning the more focused monochromated source.

8. Lower the twin-anode source until it just starts to obscure the camera picture when complete zoomed out. ~0.75 in from the top of the puck.

9. Start the alignment scan. You should see counts for silver unless you're off the puck or in one of the large slits.

   (a) When you get counts, confirm that the lens voltages are being properly supplied and that you're actually using the minimum area. If the counts aren't changing between min, small, large, or something seems off, restart the computer, turn off the **RBD 147** box and the **Card Rack power**. Restarting everything usually fixes this. I think the an arc during high voltage conditioning can confuse some of the communications between everything.

10. Move the crosshairs to the largest slit (1000 μm). Move around this slit until you feel like you're in the center. Counts are higher close to the edges.

11. Once you feel like the detector is looking at the center of the slit, use needle nose pliers to adjust the alignment screws on the microscope collar to center the crosshairs.

12. Move the stage until the crosshairs are looking at the edge of the slit and note the counts. Move to the other side and note the counts.

    (a) These values will probably differ. Adjust the alignment screws until the edges generate roughly the same counts.

13. Move to the 800 μm slit and repeat the alignment there.

14. Next, move the the 400 μm slit.

15. Adjust the Z-axis until you achieve the lowest counts. Within reason, obviously horrible misalignment will result in low counts too. . .

16. Counts in this slit won't go to 0 but should decrease by ~70% of the middle of the silver once Z is aligned.

17. With the camera completely zoomed in, focus the camera on this slit.

18. Adjusting the focus will probably effect the X of the camera and the alignment screws will probably need slight adjust to get back to the center. Repeat the above steps if needed to center the crosshairs within a slit.

19. Now move to the 400 μm hole. Continue adjust the X and Y of the crosshairs here to find the center of the whole and keep the Z in focus.

    (a) Again, counts should be lowest within the hole at a certain Z height.

    (b) The process is iterative and steps will be repeated.

20. Set the aperture to 1 minimum and repeated alignment in the 150 μm hole.

21. Counts are very low at these settings but you should see the signal decrease within the 150 μm hole when it's centered.

    (a) Run a 5 scan multiplex or longer dwell times to help average the data if needed.

22. Refer to the PHI 5600 Installation manual or RBD Techspot for more details on finding the Focal point of the system.

F.2.5.2 *Monochromator Alignment*   Read the alignment procedures from the **10-410** Moncochromator calibration manual and the RBD Monochromator post for the Kratos, which is functionally the same design and adjustments. https://www.rbdinstruments.com/blog/kratos-monochromator-adjustment/. The **10-410** PDF is actually a bundle with one of the PDF's containing some useful notes. Use Adobe Reader to see them all. Monochromator shouldn't need much realigning after each bakeout. Bumping the source on the billows or movement when connecting and disconnecting the compression water fittings can sometimes move the beam spot however. Since we're using two focused filaments, there will need to be realignment of the source each time we want to switch between the filaments.

1. Load the silver alignment specimen along with a small piece of phosphor secured to the surface. Keep the phosphor to one side of the puck and leave a wide, clear area of silver for fine tuning the focus.

2. Sputter a spot on the silver where you plan to align the mono beam spot to the camera's crosshairs.

    (a) Remember that you'll sputter a wider area in the X-axis than you set the raster size to. Try not to sputter the phosphor.

3. Set the Aperture to **3** and the area minimum. Start an alignment with a pass energy of 117 eV, 50 ms dwell time, 1 eV/step.

    (a) Settings aren't super important here but a small aperture is desirable and quick scans at this resolution help speed up the process.

4. Unless the source is horribly misaligned, you should see counts coming from the silver. If not, move to the center of the phosphor and center the crosshairs there.

5. Turn off any light source (not the X-rays. . . .) from entering the chamber and turn the room lights off to help with the contrast. You should see a green glow coming from the phosphor about 1 mm x 2 mm, however, the beam may not be completely centered with the crosshairs.

6. Here are the adjustments to be made on source and monochromator housing:

7. Use the X-tilt of the monochromator crystal to center the beam on the phosphor to the crosshair in the X-axis.
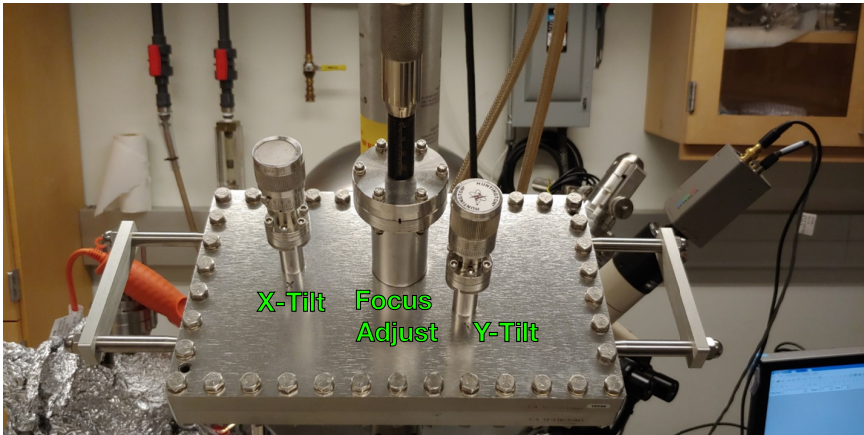
Monochromator Crystal Adjustments
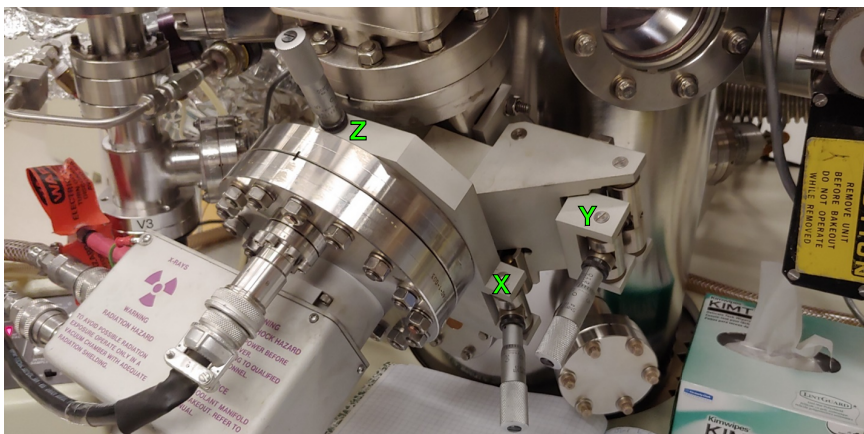
Monochromator Source Adjustments

8. The Y-axis is more tricky because the movement of the source-Y is also tied to the Y-tilt of the crystal.

   (a) For example: If you were to align the beam spot in the Y-axis by only adjusting the micrometer of the Y-source, the beam would not be properly focused, and counts would be lost. The same goes for using only Y-tilt to align the beam.

9. To align in the beam in the Y-axis, adjust the Y-Source and Y-Tilt in small steps. While the beam is in the phosphor, you'll be able to see in the camera what your small adjustments do.

10. Use the Y-Tilt to move the beam closer to the center and use the Y-Source to focus the beam and maximize brightness of the phosphor spot. Eventually you'll get it centered.

    (a) Zoom out with the microscope to help see changes in brightness of the spot, but remember to zoom back in to check that the center of the spot is in the crosshairs.

11. Use the focus adjust to help increase the brightness.

    (a) This should only be adjusted when switching between the two focused filaments. Otherwise, this should not have to be adjusted.

12. Move back to the silver spot and connect to picoammeter if not already connected. Disconnect the banana clips to the stage-bias power supply otherwise it will steal the current.

13. Turn the picoammeter on and set the range to 20 nA.

    (a) Remember to turn the picoammeter off when finished. Not sure if any current from the bias power supply would damage it or not.

14. You should start to see a photocurrent from the X-rays hitting the silver surface.

15. At the same time, start an alignment scan of the silver region.

16. Write down the counts and photocurrent at the present micrometer position of the Y-source.

17. Adjust the Y-source CW by 5 "micrometer units" and use the Y-tilt to maximize the counts or current.

18. Repeat the previous step a few times in the CW direction.

19. Go back to the first Y-source micrometer position and repeat those steps in the CCW direction.

20. At some position, the counts and current will be maximized. Carefully move around 1 micrometer adjustments to pinpoint the best alignment.

21. Use the X-tilt to roughly maximize the counts and current and use the X-source for fine tuning the counts and current.

22. The photocurrent should now be about **1–2** nA. (I have around 0.930 nA aligning to filament **2**. The counts were about half of the counts we saw with filament **1**.)

23. The **10-410** manual now says to adjust the focus knob one revolution and repeat the previous steps for the silver alignment.

    (a) Basically, adjustments to the focus will tune the FWHM of the silver peaks.

24. Lock all of the positions and write down the micrometer postions in the Maintenance Log.

F.2.5.3   Pass Energy Linearity

1. Load an Au foil and Cu foil into the chamber.

   (a) Dilute acetic acid sonication helps remove the copper oxide from the surface.

2. Acquire a 5-scan multiplex of the 4f$_{7/2}$ at 5.85 eV and 0.025 eV/step. Fit the peaks.

3. Acquire another 5-scan multiplex at 23.5 eV and 0.025 eV/step and fit the peaks.

4. The peaks should be in the same spot within 10s of millivolts. Don't worry about the exact position, we'll get to that next.

5. If the peaks are off, adjust the pass energy tracking potentiometer(picture below).

   (a) First turn of the RBD Box and Card rack power. There be high voltage here.

   (b) Adjust the Potentiometer within the SCA Terminator box under the hemisphere in one direction by a quarter turn with a flathead screwdriver.

      i. Be very careful

6. Multiplex at both pass energies again and compare the peaks. Turn the potentiometer in the other direction of the difference became greater.

7. Smaller turns to fine tune the peaks to within tens of millivolts.

F.2.5.4   Scale Factor Adjustment   The scale factor of the detector is set so that photoelectron energies are collected linearly across the spectrum. Do this step before adjusting the analyzer work function, as the peaks will shift with changes to the scale factor. The literature values for the Au 4f$_{7/2}$ peak and Cu 2$p_{3/2}$ are located at 84.00 eV and 932.67 eV, respectively, with a ΔeV of 848.67 eV.

1. Take 5-scan multiplexes of sputter cleaned Cu and Au foil samples.

2. Fit the peaks and determine the ΔeV.

3. Increase the scale factor if the ΔeV is too small or vice versa.

4. Aim for within a few millivolts of the tabulated value.

F.2.5.5   Analyzer Work Function

1. Note the current Analyzer work function in Augerscan under Hardware Properties/XPS tab.

2. 5-scan multiplex of Au $4f_{7/2}$ at 23.5 eV pass energy. Fit the peak to determine location.

3. Raise the analyzer work function to lower the binding energy.

4. Multiplex again and repeat until within a few millivolts of 84.00 eV for Au $4f_{7/2}$.

5. Optionally, take the UPS of the sputtered Au, Cu, or Ag samples at 90° toward the detector, **2** minimum aperture, with a lowered multiplier value.

   (a) The location of the Fermi-Edge should be right at 0 eV, that is the center of the slope should cross 0 eV.

The XPS should now be aligned and calibrated.

F.2.6   Phi5600 Standard Operating Procedures

F.2.6.1   XPS: Standard Operating Procedure

1. All samples must be completely dry before mounting.

2. Powders and other atypical samples must be given the okay by XPS super users before analysis. (i.e. organic powders with high vapor pressures. . .)

3. Porous samples (zeolites, MOFs. . .) which tend to hold onto gas and water

Sample Mounting (Large crystals, wafers, metals, etc.)

Use only the white UHV gloves provided in the XPS lab

Properties
Anode/Type: Al
Photon   1486.6 eV
Work Function: 3.123 eV
Gain Offset: 0
Power: 300 W
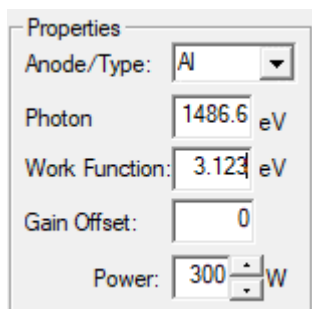
1. Crystalline samples; silicon wafers, single crystals, electrodes, etc... may be attached to the sample pucks with the CuBe prongs.

2. Prior to attaching the sample, wipe the puck, prongs, screw driver, and tweezers with IPA and a Kimwipe to remove any contamination.

   (a) To ensure the least amount of carbon contamination, suitable samples should be rinsed with acetone, IPA, and water (in that order) to remove adventitious carbon.

3. Once the sample is attached, pick up the mount and lightly shake to ensure the sample won't fall to the bottom of the chamber during introduction

Sample Mounting (Powders)

1. Powders and other small samples that can't be attached using the CuBe must use the UHV carbon tape supplied in the XPS lab.

2. Using clean UHV tweezers take one of the double-sided carbon tape circles and stick it to the puck. Using the clean, straight-edge, push down on the tape to ensure it is properly affixed and air pockets do not remain. A razor blade can help push air pockets out.

3. Remove the paper from the tape and add a uniform layer of sample. It is important to have equal coverage on the tape to maintain strong XP signal. Use the tweezers to push the samples into the tape.

4. Shake the sample mount to make sure the powder is properly affixed and will not come off during vacuum. Wife the edges with IPA as needed.

Pump-down Procedure

1. Once a samples is mounted to the puck, press the **Backfill Intro** button on the Autovalve controller. The chamber should always be actively pumped on when not loading samples or introducing them to the analysis chamber.

2. After a few seconds the chamber will reach atmospheric pressure and the cover can be removed.

3. Using the tongs sitting next to the loadlock chamber, grab the sample mount by the upper ring and bring the sample to the loadloack chamber.

4. Press the puck onto the transfer fork. The forks must hold the sample by the lower ring.

5. Once sample is attached, check that the area where the cover goes is clean from any dust and debris. Use a Kimwipe and IPA to remove any contamination from the cover's oring or loadlock.

6. Put the cover back into position and switch valve control (located on electronics console) from **AUTO** to **MANUAL**.

7. Press the valve **2** to close valve **2**.

    (a) Pay close attention to which button is being pressed here

8. Switch valve control back to **AUTO**.

9. Open the Swagelok valve, located underneath the load-lock port, to pump the load-lock with the rough pump.

    (a) If using a powdered sample, open very slowly over the course of 5 minutes.

10. Monitor the pressure with the mtorr under the computer screens gauge until it reads <1 torr.

11. Close the Swagelok valve and press **PUMP INTRO** on the auto-valve controller.

12. Samples must pump in the load lock for a minimum of 1 hour.

13. Gassy samples and ones mounted with tape typically require overnight pumping.

Sample Mounting (Air free or gassy samples)

1. Porous, hygroscopic samples and samples requiring an oxygen/water free environment must be loaded into the glovebox along with a sample puck and tools required to affix the sample.

    (a) Prior to loading into the glovebox, porous samples should be pumped on by vacuum and kept in a vacuum sealed container or inert gas to help maintain a O_2-free atmosphere within our glovebox.

2. Once the sample is mounted to the puck, the transfer suitcase can be used to hold the puck and seal it under a nitrogen atmosphere.

3. Once sealed, the transfer suitcase can be removed from the glovebox through the large antechamber. **Make sure large antechamber is purged before opening**.

4. Using the glass flange and appropriate O-rings, the transfer suitcase can be mounted to load-lock chamber of the XPS.

5. Ensure that the glass flange is aligned with the chamber so that the transfer arm will land in the appropriate spot.

6. Once attached, the chamber can be pumped on with the roughing pump. After a minute, open the valve on the transfer suitcase to pump out the nitrogen atmosphere.

7. Once the pressures reaches <1 torr, follow the same steps as above in the

8. For a majority of the samples using the transfer case, it is necessary to allow the samples to pump down overnight. Check with XPS super-user beforehand.

Introduction to the Analysis Chamber

1. Check that the pressure of the loadlock is at high vacuum and that the sample has pumped for at least 1 hour or more depending on the sample. All five bars on the **AVC** should have lit up 5 minutes into the pumping procedure.

2. Before pressing the intro sample button, check the position of the sample manipulator in the analysis chamber is in the correct position. Turn on the **Card Rack Power** and **RBD 147 Interface**.

3. Open Augerscan, then Stage Control and set the stage to unload, if not already in position.

4. Press the **Intro Sample button**. **Wait for the 2 sounds**. The first hiss is the **V3** closing the loadlock chamber to the turbo pump. The second is **V1** opening to the analysis chamber.

5. Slowly move the arm into the analysis chamber. Push all the way to the stop which is aligned with the sample manipulator.

6. Set the stage position to home. Once the stage makes contact with the puck, stop the stage movement Tilt to 50°, 40°, and back to 45°. Continue raising Z. Repeat the process in steps so as not to put stress on the arm or stage.

7. If the manipulator begins to stick while trying the raise it, don't continue trying to raise it.

8. While watching the puck, slowly pull the transfer arm back out from the analysis chamber. Once it's pulled all the way out, **V1** will automatically shut.

9. Press **Pump Intro** to actively pump the loadlock chamber.

Focusing the sample

1. On the desktop open the **MFC** program (looks like a Q*bert pyramid) to view the chamber through the microscope camera. Turn on the large LED flashlight to illuminate the chamber.

2. Use the black ring in the middle of the microscope to zoom in and out on the sample.

3. Use the X, Y, and Z-axis sample stage manipulators to view the part of the sample of interest.

4. The goal is to bring the surface of the sample into the cameras focus. Where the camera is in focus, the instruments optics and X-ray source are also in focus.

Turning on the X-ray source

1. Pressure should read $5E^{-9}$ before powering on the X-rays.

2. Flick on the power switch on the **32-096** X-ray source control.

3. Check the waterflow. Should be ~0.95 gpm. If low or not flowing at all, do not turn the X-ray source on. Contact a super-user.

4. Select your Xray source. Mono or Twin. Probably mono. Check with super-user if desiring to use the twin anode.

5. Select **Int** for internal control. **Ext** control for overnight automated scans.

6. Select Mono **2** under filament energize. (The MONO source currently has two small filaments and the crystal is currently aligned to the 2nd filament.) This selects the filament were are going to energize to produce electrons.

7. Under parameter control, select the **HV** button. This will display the voltage supplied to the anode. It should say **0** kV.

8. Press the square, red button labelled **High Voltage**. It should start to flash.

9. On the bottom left of the console, flick the two switches on for **AC** powder and **HV** on.

10. Using the variac knob, labelled **Raise Voltage**, begin to turn clockwise. The needle of the analog voltage dial on the left should also start to go up. Lately, it does not work at all. Use the **HV** in the parameter display to monitor anode voltage. Slowly turn until 10 kV is reached.

    (a) Monitor the Emisson current with the gauge located beneath the red high voltage button. At 10 kV, there should be 0-1 mA of leakage current. If current is higher, turn the voltage off and ask for help.

11. Under parameter control, press the Mono **2** button. This will display the power of the filament we plan to energize. It should display **0** watts.

12. Using the arrows underneath the Parameter Display, raise the power to **3** W. At 3–5 W a pressure spike will be seen. The pressure should drop back down quickly.

13. Once pressures returns to normal increase the power to **50** W.

14. Next increase the voltage to **11.5** kV

15. Increase the power another **50** W and voltage another **0.5** kV.

16. Repeat the process until **250** W and **13.5** kV are reached.

   (a) The goal here is too slowly bring the X-rays up to power. <mark>Never increase the power without first increasing the voltage</mark>.

17. The emission current should now display ~**18** mA. If not, ask for help.

Acquiring Data

1. In AugerScan, open System, then hardware properties. Settings should look like this, Scale factor and work function values will vary depending on the bakeout cycle. **4** minimum is the preferred aperture and area. Press OK.

   (a) <mark>In general, do not change these settings unless advised.</mark>
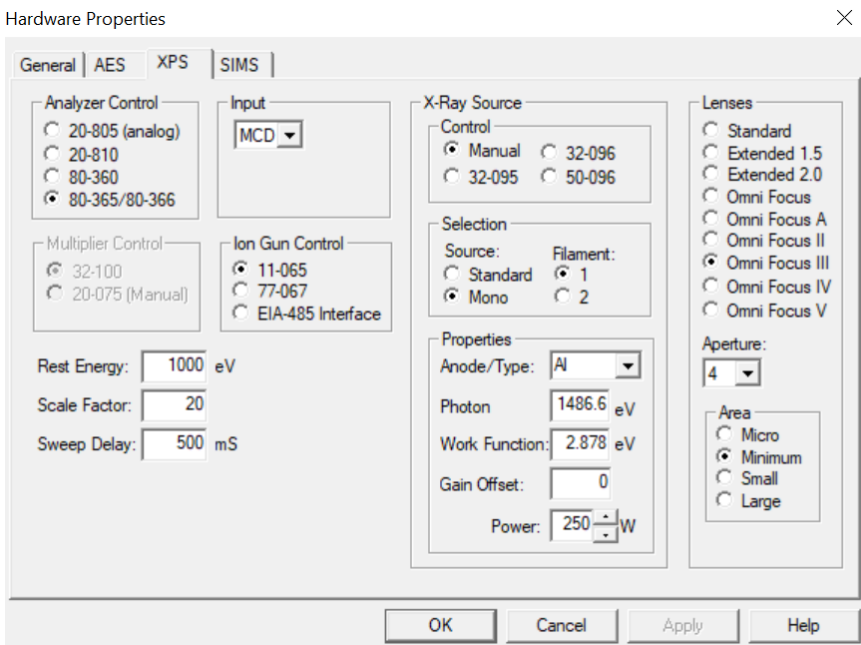
2. Now select File/New/Survey. Right click the survey window and open its settings:

3. Hit apply then in the top left, press **Acquire**. The scan should take around 12 minutes after which you will be prompted to save the data.

4. Now open File/New/Multiplex. Under the multiplex settings:

5. Choose the elements you'd like to scan for. Tighten up the upper and lower limits in order to save time. Select a number of sweeps for each sample. Repeat for each.

Survey Settings

Binding Energy
Upper Limit: 1400.00 eV
Lower Limit: 0.00 eV
EV/Step: 0.500 ▼ eV

Pass Energy
117.40 ▼ eV

Acquisistion Time
Sweeps: 5   Time: 11.7 mins.
Time/Step: 50.0 mS   ☐ Continuous

☐ Neutralizer On   Edit Gun Settings...

Acquire
Apply
Cancel
Help

Multiplex Settings

Regions
C 1s
N 1s
O 1s
Sn 3d5
Ti 2p3
F 1s

Add...
Remove
Remove All

Acquire
Apply
Cancel
Help

C 1s
Binding Energy
Upper Limit: 294.00 eV
Lower Limit: 280.00 eV
EV/Step: 0.025 ▼ eV

Acquisition Time
Sweeps: 50
Time/Step: 50 mS

Pass Energy
23.50 ▼ eV

Total Acquisition Time
Cycles: 1   Time: 134. mins.

☐ Neutralizer On   Edit Gun Settings...

6. Once you have set the parameters for each element, apply and acquire.

7. Scans can take 1-4 hours or more depending on the number of elements and scans, and resolution.

8. Once the multiplex is saved, exit the software.

Powering down the X-Ray

1. Work in the reverse that the X-rays were started. First bring the power down to **200** W, then the voltage to **13** kV. Repeat until the power is **0** W and the voltage is **10** kV

2. Then turn the voltage to zero.

3. Flick off the **AC** power and **HV** on switches.

4. Press the flashing red **HV** button to stop it from flashing.

5. Let the water run for at least 15 minutes before turning off the x-ray source control water. This allows the X-ray source to properly cool off.

Retrieving the sample

1. Set the sample stage to **home** with Stage Control.

2. Press the **Intro Sample** button and retrieve the sample in the same manner you loaded the sample. Set Stage to unload position with the fork holding the puck.

3. The sample sometimes sticks to the stage, use tilt to help move it off. Don't force it with the Z-axis.

4. With the sample in the loadlock chamber wait 30s before pressing the **Backfill intro** button. Retrieve sample.

5. Pump the empty loadlock chamber back down the using the same steps as when pumping a sample down.

6. Turn off the **Card Rack Power** and **RBD Box**.

F.2.6.2   UPS Stand Operating Procedure   This procedure assumes that there is a sample already in the chamber and that the **Card Rack** and **RBD 147 box** are already on. Do not leave X-rays on while doing UPS experiments.

1. Check the water level before turning on UV source chiller. The UV source will overheat if the water levels are too low to actively cool it during operation. Check connections for leaks etc.

2. Once the sample is in the analysis chamber, select **Diff pump ion gun** on the Auto Valve controller. This will shut **V3** (if open) and open **V4**. The line should be at high vacuum already but give it a minute to pump before the next step.

   (a) Alternatively, manually open **V4** if you trust the atmosphere of the loadlock. This way the loadlock chamber is actively pumped on.

3. Next open the butterfly valve on the vacuum line located under the UV gun. (turn counterclockwise 90°)

4. Now open (counter-clockwise) the helium leak valve located directly beneath the UV gun. At $1^{3/4}$ turns, look for the pressure to start climbing in the analysis chamber. **Check the DIG III gauge**.

5. Immediately after pressure starts to rise in the chamber, open the vacuum valve on the vacuum line connected to the Woo Sung Automa rough

pump (located behind the helium leak valve). Pressure should start to go back down on the ion gauge controller.

6. Next, watch the mtorr vacuum gauge in the cabinet next to the rough pump and slowly continue opening the helium leak valve. Don't turn turn it too fast or you'll release too much helium. Give the vacuum gauge time to equilibrate.

7. You should be aiming for around ~27 mtorr of at the thermocouple guage.

8. Now go the UPS power supply and turn it on.

9. Select the voltage number and turn the knob until it reads **1.00** kV.

10. Select **HV**, wait for the voltage to reach **1.00** kV, and press ignite.

11. If there is ignition, a purple cloud appears under the standby button and the running voltage should sit at ~0.58kV, depending on the helium pressure.

12. If there was no ignition, try to ignite again. If there still isn't, try increasing the helium pressure by about 2 mtorr. Do not increase past 35 mtorr on the mtorr guage. If there is still no ignition, seek super-user.

13. Open the TPD chamber gate valve, if clean, to help pump out additional helium.

14. Set Sample angle to 90°. Focus sample.

15. Under Hardware properties, in the XPS tab, select He I as the source. This sets the energy of incoming light to 21.2eV.

16. Set the multipler voltage to **1600** V, raise as necessary but stay below 10^6 cps.

17. Set the aperture and area to **2 minimum**.

18. With the power supply, bias the stage at **-35** V.

19. Open a survey and change the settings to scan from -13 – -37 eV. Set the pass energy to 5.85eV and set the energy per step to 0.025eV. Sweeps can be set as desired.

20. Acquire data

Turning off the UPS

1. Turn off the sample bias power supply.

2. Select **STNDBY** on the UPS power supply to turn off.

3. Close the He leak vale. DO NOT OVERTIGHTEN.

4. After 30 s, close the rough pump valve to the UV source.

5. Remove sample from chamber as usual.

6. After 5 minutes, close the TPD chamber if opened.

7. After 10 minutes, turn off UPS chiller.

8. Return sample back to home position and XPS or remove from chamber.

F.2.6.3   Operation of the 11-065/04-303A Ion Gun

1. Assuming sample is in the analysis chamber and aligned as described in the XPS procedure, and that the turbo pump has not been exposed to atmosphere for <30 min, press the **DIFF PUMP ION GUN** button on the Auto Valve Controller. **V3** will shut (turn red on AVC) and **V4** will open (turn green on AVC). Wait 2 minutes.

   (a) Optionally, switch the **AVC** to manual control and open **V4**, so that both **V3** and **V4** are open at the same time.

      i. This is useful if expecting to have **V4** open for a long time where having **V3** closed for a while may raise the pressure in the loadlock.

2. Open the butterfly valve attached to the **04-303A** Ion Gun. Wait 2 minutes.

3. Locate the **11-065** Ion Gun Source Control located in the console underneath the UPS power supply, across from the XPS main console.

4. Check that the control switch (under the Beam Voltage label) is set to **Off**.

   (a) Sometimes if the controller is turned on when this is set to the **Remote**, the beam voltage will automatically turn on. Not a huge problem but you might accidently sputter the wrong sample or a sample more than desired.

5. Turn on the **11-065** Ion Gun Source Control.

6. Switch the control back to Remote. If Beam Voltage indicator light turns on, go to Augerscan, start the sputtering, and stop it. This should turn the beam voltage off and sputtering will only start when we properly start it later.

7. <mark>NEVER</mark> touch the switches/Dials for

   (a) Beam Voltage,

   (b) Cond. Lens,

   (c) Obj. Lens,

   (d) Deflection Positions

(e) Emission Scale

(f) Getter Pump

(g) Raster Drive

8. If desired change the raster beam size to sputter a smaller spot on the sample.

(a) Remember, smaller spot sizes will sputter faster/deeper.

(b) Because the ion gun is angle toward the surface normal, the raster area is not a perfect square. More like a rectangle with the length in the X-direction.

9. The switch under the meter on the right of the controller should be set to emission.

10. Using the **Emission** knob, slowly turn clockwise and watch the meter until it reads **25** mA.

(a) Keep an eye on chamber pressure, but it should not increase unless the butterfly valve was left closed.

11. Select **Pressure** with the switch under the meter. The meter will fall back to read 0 mPa.

12. On the **04-303A** Ion Gun begin to slowly turn the leak valve counter-clockwise.

(a) Do not turn the green valve attached to the Ar bottle. This remains open.

13. After about 1 $^{1/2}$ turns, monitor the chamber pressure. Once you see an increase in pressure, watch the pressure gauge on the **11-065** Ion Gun control.

14. Slowly turn until the pressure reads **12–14** mPa. Avoid overshooting the pressure.

(a) Chamber pressure should be around $2E^{-8}$ Torr before starting sputtering.

15. In Augerscan, select the **Sputtering** tab on the right of the tool bar (circled in red).

16. Set a Sputter time in minutes. The minimum time is 0.1 m or 6 s.

17. Press **Start**.

18. The pressure will increase in the analysis chamber because of Ar ions entering the chamber and atoms being remove from the sample surface.
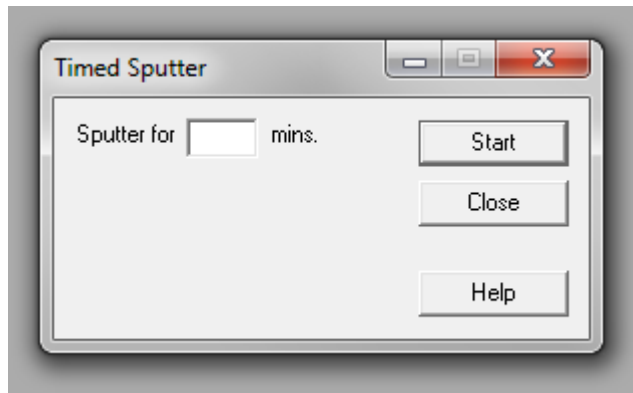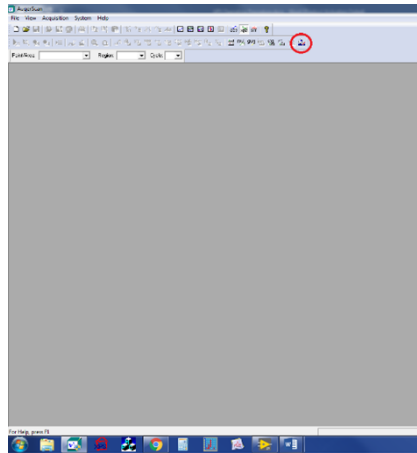
(a) Pressures might briefly enter the 10^{-7} Torr tange but quickly drop, depending on the type of sample.

19. When the sputtering is finished, pressure should return to the low 10^{-8} Torr.

Turning off the Ion Source

1. Close the leak valve located on the Ion Gun.

   (a) Do NOT overtighten!

2. Change back to **Emission** on the switch located underneath the meter on the 11-065 control.

3. Turn the Emission knob counter-clockwise until emission current reaches **0** mA.

4. Turn off the **11-065** Source after a few minutes once the power supply has had a chance to cool.

5. Wait at least five minutes before closing the Ion Gun butterfly valve to allow most of the Ar atoms to be pumped away by the turbo pump.

6. Switch back to **Pump Intro** on the Auto Valve Controller or manually close **V4**.

APPENDIX G

CUSTOM IGOR PROCEDURE FILES

G.1 Custom Igor Procedure Files

G.1.1 Loading Bruker IR Data–RLG_LoadbrukerDPT.ipf

The following code is our Igor Procedure file used load IR data from the Bruker Vertex 70 FT-IR. The IR, acquired with Bruker's OPUS software, saves the data as `0.#` or for example `IRdata.0`. These files can only be opened in OPUS and must be converted to Data Point Table files or `IRdata.dpt` within the OPUS application on the FT-IR computer.

```
0 #pragma TextEncoding = "MacRoman"
1 #pragma rtGlobals=1      // Use modern global access method and strict
      wave access.
2 #pragma version = 8.0      // we're using long file names and folder
    names in Data Browser
3
4 // RLG_loadBrukerDPT.ipf
5 // this file the function for loading a *.dpt data file
```

```
6  // this is a DPT tab-delimited text from OPUS that has been exported
      as *.dpt
7  // last edited 13 June 2018
8  // Alex Carl
9
10
11 Function TestLoadBrukerDPT(fullPath, called_automatically, myDFR)
12    String fullPath
13    Variable called_automatically
14    DFREF myDFR
15
16    // standard variables
17    String cmd="",scanType="",tempstring="", filename="", tablenamestr
      ="", graphnamestr="",regioninfo=""
18    Variable returnValue = 0, num_columns = 0, num_fit_peaks = 0,
       refNum = 100, i = 0, num_lines = 0
19
20    WAVE Wavenumber, Absorbance
21    String wnstr="_cm-1"
22    String Wavenumberwave=filename+wnstr
23    String Abstr="_A"
24    String Absorbancewave=filename+Abstr
25
26    // main block
27    Printf "Loading the DPT data file \"%s\"...\r", ParseFilePath(0,
       fullPath,":",1,0)
28
29    String extension = ParseFilePath(4, fileName, ":", 0, 0)
30    if (CmpStr(extension,"dpt") == 0)
31       Print "This is a .dpt file"   // For debugging only
32    else
33       Print "This is not a .dpt file"  // For debugging only
34    endif
35
36    // if fullPath is specified, use that, othewise use the path
       Symbolic Path to open the electrochemistry data file
37    Open /R/Z=1 refNum as fullPath
38
39    if (V_flag == 0)  // data found
40
41    // First column is wavenumber, second is absorbance
42       num_columns = ItemsInList(cmd,"\t")
43
44       // append to the topmost table or make a new table if there
      aren't any
45       tablenamestr = WinList("*",";","WIN:2")
46       if (ItemsInList(tablenamestr) > 0)
47          tablenamestr = StringFromList(0,tablenamestr)
48       else
49          tablenamestr = "Table0"
50             Edit /N=$tablenamestr
51             // we might not have gotten the requested table name.
      lets's see what the topmost table is just in case...
52             tablenamestr = WinName(0,2)
53       endif
54       AppendToTable /W=$tablenamestr Wavenumber, Absorbance
```

```
55      endif
56
57      return returnValue;
58  End
59
60
61  Function LoadBrukerDPT(fullPath, called_automatically, myDFR)
62      String fullPath
63      Variable called_automatically
64      DFREF myDFR
65
66      // standard variables
67      String cmd="",scanType="",tempstring="", filename="", tablenamestr
         ="", graphnamestr="",regioninfo=""
68      Variable returnValue = 0, num_columns = 0, num_fit_peaks = 0,
         refNum = 100, i = 0, num_lines = 0
69
70      // load the DPT file
71      Printf "Loading the Bruker DPT data file \"%s\"...\r",
         ParseFilePath(0,fullPath,":",1,0)
72      LoadWave /A/J/N fullPath
73
74      if (V_flag)
75        // change the names from wave0 and wave1 to something more
         readable both here and in the file
76        Rename myDFR:wave0, Wavenumber
77        Rename myDFR:wave1, Absorbance
78        WAVE Wavenumber=myDFR:Wavenumber
79        WAVE Absorbance=myDFR:Absorbance
80
81        // make a table with wavenumber and absorbance
82        tablenamestr = "Table_" + ParseFilePath(3, fullPath, ":", 0, 0)
83        tablenamestr = tablenamestr[0,250]
84        tablenamestr = ReplaceString(" ", tablenamestr, "_")
85        tablenamestr = ReplaceString("!", tablenamestr, "_")
86        tablenamestr = ReplaceString("$", tablenamestr, "_")
87        tablenamestr = ReplaceString(",", tablenamestr, "_")
88        tablenamestr = ReplaceString("-", tablenamestr, "_")
89        Edit /N=$tablenamestr Wavenumber, Absorbance
90
91        returnValue = 1
92      else
93        returnValue = 0
94      endif
95
96
97        // Make a graph of the data
98        graphnamestr = "Graph_" + ParseFilePath(3, fullPath, ":", 0, 0)
99        graphnamestr = graphnamestr[0,250]
100       graphnamestr = ReplaceString(" ", graphnamestr, "_")
101       graphnamestr = ReplaceString("!", graphnamestr, "_")
102       graphnamestr = ReplaceString("$", graphnamestr, "_")
103       graphnamestr = ReplaceString(",", graphnamestr, "_")
104       graphnamestr = ReplaceString("-", graphnamestr, "_")
105       Display /N=$graphnamestr Absorbance vs Wavenumber
```

```
106      ModifyGraph mode(Absorbance)=0,lsize(Absorbance)=0.5,rgb(
      Absorbance)=(0,0,0)
107      graphnamestr = WinName(0,1)
108
109      // add the filename and an annotation with region information
110      Print("Look at me, I'm in the filename block of the code...\n")
111      tempstring = "\\Z06" + ParseFilePath(3, fullPath, ":", 0, 0)
112      TextBox /W=$graphnamestr/C/N=file_annotation/F=0/Z=1/B=1/A=RT/X
      =2.00/Y=2.00 tempstring
113      Print tempstring + "\n"
114
115
116      for (i = 0; i < num_fit_peaks; i+=1)
117          tempstring = "Peak" + num2str(i)
118          Wave temppeakwave = $tempstring
119          AppendToGraph /W=$graphnamestr Absorbance vs Wavenumber
120          ModifyGraph mode($tempstring)=0,lsize($tempstring)=0.5,rgb(
      $tempstring)=(65535,0,0)
121      endfor
122
123      // window properties
124      ModifyGraph /W=$graphnamestr width=216,height=144,gfSize=8,
      expand=4
125      ModifyGraph /W=$graphnamestr gFont="Arial"
                              // default win
126      ModifyGraph /W=$graphnamestr gFont="Helvetica Neue"
                              // if mac, change it!!!
127      ModifyGraph /W=$graphnamestr margin(left)=24,margin(bottom)=30,
      margin(top)=12,margin(right)=12     // units are pt (72 pt = 1
      inch)
128      ModifyGraph /W=$graphnamestr mirror=1,axThick=0.5,standoff=0
129
130      // format y axis
131      SetAxis /W=$graphnamestr /A left
132      ModifyGraph /W=$graphnamestr tick(left)=2,btLen(left)=3,btThick
      (left)=0.5,stLen(left)=1;DelayUpdate
133      ModifyGraph /W=$graphnamestr stThick(left)=0.5
134      ModifyGraph /W=$graphnamestr noLabel(left)=1,lblPos(left)=15
135      ModifyGraph /W=$graphnamestr tick(left)=3
136      Label /W=$graphnamestr left "Absorbance"
137
138      //format x axis
139      SetAxis /W=$graphnamestr /A/R bottom
140      Label /W=$graphnamestr bottom "Wavenumber (cm\\S-1\\M)"
141      ModifyGraph /W=$graphnamestr tick(bottom)=2,btLen(bottom)=2,
      btThick=0.5,stLen=1
142      ModifyGraph mirror(bottom)=2
143      ModifyGraph /W=$graphnamestr stThick(bottom)=0.5
144      ModifyGraph /W=$graphnamestr lblPosMode=3
145      ModifyGraph /W=$graphnamestr lblPos(bottom)=24
146
147   return returnValue
148 End
```

G.1.2   Loading Bruker NMR Data–RLG_loadNMR.ipf

The following code is our Igor Procedure file used to load NMR data from the Bruker NMR. The files must be exported as `.txt` files from TopSpin then the file extension is changed to `.nmr`. For example: `NMRData.nmr`. At the present, the graph is set to display the data from 14 to 0 ppm (a typical proton NMR spectrum), however, carbon NMR data can also be imported and the *x* axis rescaled accordingly.

```
0 #pragma TextEncoding = "UTF-8"
1 #pragma rtGlobals=3       // Use modern global access method and strict
       wave access.
2 #pragma version = 8.0       // this calls some more modern functions,
     make sure a modern version is used
3
4 // RLG_loadNMR.ipf
5 // this file contains functions to load and plot NMR data that was
       exported from TopSpin
6 // last edited 7 August 2019
7 // adc rlgii
8
9 Function LoadNMR(fullPath, called_automatically, myDFR)
10    String fullPath
11    Variable called_automatically
12    DFREF myDFR
13
14    Variable returnValue = 0, refNum = 100, i = -1
15    String dataline, tablenamestr="", graphnamestr="", ,tempstring=""
16    Variable left_x = 0, right_x = 0
17
18    Open /R/Z=1 refNum as fullPath
19
20    if (V_flag == 0)                                             //
       data found
21       returnValue = 1
22
23       // skip initial header header
24       FReadLine refNum, dataline
25       FReadLine refNum, dataline
26       FReadLine refNum, dataline
27       FReadLine refNum, dataline
28       Print dataline // this now holds the ppm boundaries saved in
       file
29       left_x = str2num(StringFromList(3, dataline, " "))
30       right_x = str2num(StringFromList(7, dataline, " "))
31
32       printf "Left value is %.15f, and", left_x
33       printf " the right value is %.15f.\n", right_x
34
35       // skip more header
36       FReadLine refNum, dataline
37
38       FReadLine refNum, dataline // this now holds the number of
39       Variable /G myDFR:numpoints = 1
40       NVAR /Z numpoints = myDFR:numpoints
```

```
41      numpoints = str2num(StringFromList(3, dataline, " "))

42
43      FReadLine refNum, dataline
44      FReadLine refNum, dataline
45      FReadLine refNum, dataline
46      FReadLine refNum, dataline

47
48      // make waves to hold the data
49      WAVE /Z ppm = myDFR:ppm, amplitude = myDFR:amplitude
50      Make /O/N=(numpoints) ppm, amplitude

51
52      for (i=0; i < numpoints; i++)
53          FReadLine refNum, dataline
54          ppm[i] = left_x - i*(left_x - right_x)/(numpoints-1)
55          amplitude[i] = str2num(dataline)
56      endfor
57    endif
58    Close refNum

59
60    // data is loaded.  now for some manipulation.

61
62    // duplicate amplitude to keep original, unmanipulated data.
63    Wave/Z amplitude_orig = myDFR:amplitude_orig
64    Duplicate amplitude amplitude_orig

65
66    // kind of normalize the amplitude data
67    Wavestats/Q/Z amplitude
68    amplitude /= V_max

69
70    // integrate the amplitude wave, and normalize that integrated
        wave
71    Wave/Z amplitude_INT = myDFR:amplitude_INT
72    Integrate /METH=1 amplitude /X=ppm /D=amplitude_INT
73    Wavestats/Q/Z amplitude_INT
74    amplitude_INT -= V_min
75    amplitude_INT /= (V_max - V_min)
76    amplitude_INT = 1 - amplitude_INT

77
78    // now it's all in.  now for the table, graph, and the formatting
        ...

79
80    // make a table with ppm and amplitude
81    tablenamestr = "Table_" + ParseFilePath(3, fullPath, ":", 0, 0)
82    tablenamestr = tablenamestr[0,250]
83    tablenamestr = ReplaceString(" ", tablenamestr, "_")
84    tablenamestr = ReplaceString("!", tablenamestr, "_")
85    tablenamestr = ReplaceString("$", tablenamestr, "_")
86    tablenamestr = ReplaceString(",", tablenamestr, "_")
87    tablenamestr = ReplaceString("-", tablenamestr, "_")
88    Edit /N=$tablenamestr ppm, amplitude, amplitude_INT  // notably,
        do not add amplitude_orig... keep that hidden :)

89
90    // Make a graph of the data
91    graphnamestr = "Graph_" + ParseFilePath(3, fullPath, ":", 0, 0)
92    graphnamestr = graphnamestr[0,250]
93    graphnamestr = ReplaceString(" ", graphnamestr, "_")
```

```
94     graphnamestr = ReplaceString("!", graphnamestr, "_")
95     graphnamestr = ReplaceString("$", graphnamestr, "_")
96     graphnamestr = ReplaceString(",", graphnamestr, "_")
97     graphnamestr = ReplaceString("-", graphnamestr, "_")
98     Display /N=$graphnamestr amplitude vs ppm;DelayUpdate
99     AppendToGraph/R amplitude_INT vs ppm
100    ModifyGraph mode=0,lsize=0.5,rgb(amplitude)=(0,0,0),rgb(
       amplitude_INT)=(65535,0,0)
101    graphnamestr = WinName(0,1)
102
103    // add the filename and an annotation with region information
104    tempstring = "\\Z06" + ParseFilePath(3, fullPath, ":", 0, 0)
105    TextBox /W=$graphnamestr/C/N=file_annotation/F=0/Z=1/B=1/A=RT/X
       =60.00/Y=2.00 tempstring
106    Print tempstring + "\n"
107
108    // window properties
109    ModifyGraph /W=$graphnamestr width=360,height=144,gfSize=8,expand
       =2
110    ModifyGraph /W=$graphnamestr gFont="Arial"
                               // default win
111    ModifyGraph /W=$graphnamestr gFont="Helvetica Neue"
                                 // if mac, change it!!!
112    ModifyGraph /W=$graphnamestr margin(left)=24,margin(bottom)=30,
       margin(top)=12,margin(right)=12     // units are pt (72 pt = 1
       inch)
113    ModifyGraph /W=$graphnamestr mirror=0,axThick=0.5,standoff=0
114    ModifyGraph /W=$graphnamestr axThick(left)=0,axThick(right)=0
115
116
117    // format y axis
118    SetAxis /W=$graphnamestr left -0.025,1.025  // it's normalized-ish
       , so data is _almost_ between 0 and 1
119    SetAxis /W=$graphnamestr right -0.025,1.025  // it's normalized,
       so data is between 0 and 1
120    ModifyGraph /W=$graphnamestr tick=2,btLen=2,btThick=0.5,stLen=1;
       DelayUpdate
121    ModifyGraph /W=$graphnamestr stThick=0.5
122    ModifyGraph /W=$graphnamestr noLabel(left)=1,lblPos(left)=15,
       noLabel(right)=1
123    ModifyGraph /W=$graphnamestr tick(left)=3,tick(right)=3
124    Label /W=$graphnamestr left "Amplitude"
125
126    //format x axis
127    SetAxis /W=$graphnamestr /A/R bottom
128    SetAxis/R bottom 14.1,-2.1
129    ModifyGraph manTick(bottom)={0,1,0,0},manMinor(bottom)={5,0}
130    Label /W=$graphnamestr bottom "Chemical Shift (ppm)"
131    ModifyGraph /W=$graphnamestr tick(bottom)=2,btLen(bottom)=2,
       btThick=0.5,stLen=1
132    ModifyGraph mirror(bottom)=2
133    ModifyGraph /W=$graphnamestr stThick(bottom)=0.5
134    ModifyGraph /W=$graphnamestr lblPosMode=3
135    ModifyGraph /W=$graphnamestr lblPos(bottom)=24
136    ModifyGraph /W=$graphnamestr mirror=0
137
```

```
138    return returnValue
139 End
140
141
142 Function NMR_zero_between_csr()
143    DFREF originalDFR, blockDFR
144    Variable data_found=0, graphtracenum, waves_in_a_table = 0,
        cols_in_a_table, i, j
145    String graphname = "", tablename = "", table_list = "",
        temp_string
146    Wave amplitude, ppm, amplitude_ORIG, trace_wave, x_trace_wave
147    Variable pcsr1, pcsr2
148
149    // do this no matter what
150    originalDFR = GetDataFolderDFR()
151
152    // make sure that cursor A and cursor B are on a trace called "
        amplitude*" something
153    // get name of trace that cursor A is on
154    temp_string = StringFromList(1,StringFromList(0,CsrInfo(A,WinName
        (0,1))),":")
155    // see if it's "amplitude*"
156    if (GrepString(temp_string,"amplitude"))
157       // now check cursor B
158       temp_string = StringFromList(1,StringFromList(0,CsrInfo(B,
        WinName(0,1))),":")
159       // see if it's "amplitude*"
160       if (GrepString(temp_string,"amplitude"))
161          data_found = 1
162       else
163          data_found = 0
164       endif
165    else
166       data_found = 0
167    endif
168
169    if (data_found)
170       // find out what waves correspond to the traces that cursor A
        is on.
171       Wave x_trace_wave = CsrXWaveRef(A, WinName(0,1))
172       Wave trace_wave = CsrWaveRef(A, WinName(0,1))
173       // what data folder is the trace wave in?  use that to figure
        out where amplitude and amplitude_INT are at
174       blockDFR = GetWavesDataFolderDFR(trace_wave)
175       // and make wave assignments
176       Wave/Z amplitude = blockDFR:amplitude
177       Wave/Z ppm = blockDFR:ppm
178       Wave/Z amplitude_INT = blockDFR:amplitude_INT
179
180       // zero out the amplitude wave between the two cursors... start
        by doing it in the right order...
181       if (pcsr(A) > pcsr(B))
182          pcsr2 = pcsr(A)
183          pcsr1 = pcsr(B)
184       else
185          pcsr1 = pcsr(A)
```

```
186          pcsr2 = pcsr(B)
187      endif
188
189      for (i = 0; i < pcsr2-pcsr1+1; i++)
190          amplitude[(pcsr1+i)] = 0
191      endfor
192
193      // now normalize the amplitude wave
194      Wavestats/Q/Z amplitude
195      amplitude /= V_max
196
197      // integrate the normalize amplitude wave, and normalize that
     integrated wave
198      Integrate /METH=1 amplitude /X=ppm /D=amplitude_INT
199      Wavestats/Q/Z amplitude_INT
200      amplitude_INT -= V_min
201      amplitude_INT /= (V_max - V_min)
202      amplitude_INT = 1 - amplitude_INT
203
204      // now normalize the amplitude_INT wave
205      Wavestats/Q/Z amplitude_INT
206      amplitude_INT -= V_min
207      amplitude_INT /= (V_max - V_min)
208
209   else
210      Print "I'm sorry but I can't find NMR amplitude data.  I quit."
211   endif
212
213   SetDataFolder originalDFR
214
215   return data_found
216 End
217
218 Function NMR_reset_amplitude()
219   DFREF originalDFR, blockDFR
220   Variable data_found=0, graphtracenum, waves_in_a_table = 0,
       cols_in_a_table, i, j
221   String graphname = "", tablename = "", table_list = "",
       temp_wave_path_string, amplitude_trace_name = ""
222   Wave amplitude, ppm, amplitude_ORIG
223
224   // do this no matter what
225   originalDFR = GetDataFolderDFR()
226
227   graphname = WinName(0,1)
228   String fulltracelist = TraceNameList(graphname,";",1)
229   String amplitudeonlytracelist = ListMatch(ListMatch(fulltracelist,
     "amplitude*"),"!*INT")
230
231   if (ItemsInList(amplitudeonlytracelist) > 1)
232      Prompt graphtracenum, "Choose a trace:", popup
     amplitudeonlytracelist
233      DoPrompt "Which trace should I work on?", graphtracenum
234      if (V_Flag)
235          data_found = 0 // user cancelled
236      else
```

```
237          data_found = 1
238          // save the trace name for data
239          amplitude_trace_name = StringFromList(graphtracenum-1,
      amplitudeonlytracelist)
240          // assign the wave references for that y counts trace, the x
       BE trace, and the data folder
241          Wave/Z amplitude = TraceNameToWaveRef(graphname,
      StringFromList(graphtracenum-1, amplitudeonlytracelist))
242          Wave/Z ppm = XWaveRefFromTrace(graphname,StringFromList(
      graphtracenum-1, amplitudeonlytracelist))
243          blockDFR = GetWavesDataFolderDFR(amplitude)
244       endif
245     elseif (ItemsInList(amplitudeonlytracelist) < 1)
246       Print "I am sorry, but I can not find a trace named \"Amplitude
      \".  No soup for you."
247       data_found = 0
248     else
249       // there is only one "Amplitude" trace (integrations don't
      count) on the graph.  this is easy
250       data_found = 1
251       amplitude_trace_name = "amplitude"
252       Wave/Z amplitude = TraceNameToWaveRef(graphname,"amplitude")
253       Wave/Z ppm = XWaveRefFromTrace(graphname,"amplitude")
254       blockDFR = GetWavesDataFolderDFR(amplitude)
255     endif
256
257     // now we have references to the waves being operated on, and what
       data folder they're in
258
259
260     if (data_found)
261       // Move into the folder with the amplitude and ppm and
      amplitude_orig waves
262       SetDataFolder blockDFR
263       // reset the amplitude data
264       amplitude = amplitude_orig
265
266       // kind of normalize the amplitude data
267       Wavestats/Q/Z amplitude
268       amplitude /= V_max
269
270       // integrate the amplitude wave, and normalize that integrated
      wave
271       Wave/Z amplitude_INT = blockDFR:amplitude_INT
272       Integrate /METH=1 amplitude /X=ppm /D=amplitude_INT
273       Wavestats/Q/Z amplitude_INT
274       amplitude_INT -= V_min
275       amplitude_INT /= (V_max - V_min)
276       amplitude_INT = 1 - amplitude_INT
277
278       // reset the axis scales
279       SetAxis /W=$graphname left -0.025,1.025
280       SetAxis /W=$graphname right -0.025,1.025
281
282       SetDataFolder originalDFR
283     endif
```

```
284
285
286     return 1
287 End
```

G.1.3   Loading SRV Data–RLG_LoadSRV.ipf

```
0  #pragma rtGlobals=1  // Use modern global access method and strict
       wave access.
1  #pragma version = 8.0       // we're using long file names and folder
       names in Data Browser
2
3  // RLG_loadSRV.ipf
4  // this file the function for loading a *.srv data file
5  // this is a DPT tab-delimited text from Microwave instrument LABVIEW
       VI that has been exported as *.srv
6  // last edited 13 December 2019
7  // Alex Carl
8
9
10 Function LoadSRV(fullPath, called_automatically, myDFR)
11     String fullPath
12     Variable called_automatically
13     DFREF myDFR
14
15     // standard variables
16     String dataline, cmd="",scanType="",tempstring="", filename="",
        tablenamestr="", graphnamestr="",regioninfo=""
17     Variable returnValue = 0, num_columns = 0, num_fit_peaks = 0,
        refNum = 100, i = 0, num_lines = 0, Scans = 0
18
19     // loads the SRV data
20     Printf "Loading the Grimm SRV data file \"%s\"...\r",
        ParseFilePath(0,fullPath,":",1,0)
21     LoadWave /A/J/N fullPath
22
23     if (V_flag)
24        // creates waves and changes the names of those waves for the
        time, voltage, and last tau data if a fit was being performed in
        LabVIEW at the time of saving.
25        Rename myDFR:wave0, tim
26        Rename myDFR:wave1, voltage
27        Rename myDFR:wave2, last_raw_tau_capture
28        WAVE tim=myDFR:tim
29        WAVE voltage=myDFR:voltage
30        Wave last_raw_tau_capture=myDFR:last_raw_tau_capture
31
32        // make a table with time and voltage
33        tablenamestr = "Table_" + ParseFilePath(3, fullPath, ":", 0, 0)
34        tablenamestr = tablenamestr[0,250]
35        tablenamestr = ReplaceString(" ", tablenamestr, "_")
36        tablenamestr = ReplaceString("!", tablenamestr, "_")
37        tablenamestr = ReplaceString("$", tablenamestr, "_")
38        tablenamestr = ReplaceString(",", tablenamestr, "_")
39        tablenamestr = ReplaceString("-", tablenamestr, "_")
40        Edit /N=tablenamestr tim, voltage
41
42        returnValue = 1
43     else
44        returnValue = 0
45
46     endif
```

```
47
48
49     //Make a graph of the data
50     graphnamestr = "Graph_" + ParseFilePath(3, fullPath, ":", 0, 0)
51     graphnamestr = graphnamestr[0,250]
52     graphnamestr = ReplaceString(" ", graphnamestr, "_")
53     graphnamestr = ReplaceString("!", graphnamestr, "_")
54     graphnamestr = ReplaceString("$", graphnamestr, "_")
55     graphnamestr = ReplaceString(",", graphnamestr, "_")
56     graphnamestr = ReplaceString("-", graphnamestr, "_")
57     Display /N=graphnamestr Voltage vs tim
58     ModifyGraph mode(Voltage)=0,lsize(Voltage)=0.5,rgb(Voltage)
       =(0,0,0)
59     graphnamestr = WinName(0,1)
60
61     // add the filename and an annotation with region information
62     Print("Look at me, I'm in the filename block of the code...\n")
63     tempstring = "\\Z06" + ParseFilePath(3, fullPath, ":", 0, 0)
64     TextBox /W=graphnamestr/C/N=file_annotation/F=0/Z=1/B=1/A=RT/X
       =2.00/Y=2.00 tempstring
65     Print tempstring + "\n"
66
67     for (i = 0; i < num_fit_peaks; i+=1)
68        tempstring = "Peak" + num2str(i)
69        Wave temppeakwave = $tempstring
70        AppendToGraph /W=graphnamestr voltage vs tim
71        ModifyGraph mode($tempstring)=0,lsize($tempstring)=0.5,rgb(
       $tempstring)=(65535,0,0)
72     endfor
73
74     //Window Properties
75     ModifyGraph /W=$graphnamestr width=216,height=144,gfSize=8,expand
       =2
76     ModifyGraph /W=$graphnamestr gFont="Helvetica Neue"
                                    // if mac, change it!!!
77     ModifyGraph /W=$graphnamestr margin(left)=24,margin(bottom)=30,
       margin(top)=12,margin(right)=12     // units are pt (72 pt = 1
       inch)
78     ModifyGraph /W=$graphnamestr mirror=1,axThick=0.5,standoff=0
79
80     // format y axis
81     SetAxis /W=$graphnamestr /A left
82     ModifyGraph /W=$graphnamestr tick(left)=2,btLen(left)=3,btThick(
       left)=0.5,stLen(left)=1;DelayUpdate
83     ModifyGraph /W=$graphnamestr stThick(left)=0.5
84     ModifyGraph /W=$graphnamestr noLabel(left)=1,lblPos(left)=15
85     ModifyGraph /W=$graphnamestr tick(left)=3
86     Label /W=$graphnamestr left "Microwave power (arb)"
87
88
89     //format x axis
90     Label /W=$graphnamestr bottom "Time (ms)"
91     ModifyGraph prescaleExp(bottom)=3
92     ModifyGraph /W=$graphnamestr tick(bottom)=2,btLen(bottom)=2,
       btThick=0.5,stLen=1
93     ModifyGraph mirror(bottom)=2
```

```
94     ModifyGraph /W=$graphnamestr stThick(bottom)=0.5
95     ModifyGraph /W=$graphnamestr lblPosMode=3
96     ModifyGraph /W=$graphnamestr lblPos(bottom)=24
97
98     return returnValue
99  End
```

G.2   OPUS macros for controlling the Harick AutoSeagull

Macros were written for experiments utilizing multiple angles of measurement and polarization with the AutoSeagull. The macros would set the angle of incident light, the polarization, and take backgrounds. Macros could also be adapted to acquire data as well, however, the variability of water vapor in the atmosphere necessitated the active monitoring of data acquisition. An important note with the software for controlling the AutoSeagull in Opus is that the p-polarization, or 90°, is actually what we refer to as s-polarized. For example, the highest signal from H-Si(111) services is acquired when the polarizer is set to 0°.

G.2.1   Multi angle/polarization background macro

This macro is designed to take eight background measurements at 20°, 40°, 60°, and 80°, each at 0° and 90° polarizations. First, the polarization is set to 0° and the incident angle of light is set to 20°. With the command `SendCommand(0,{UNI = MOT37=6800});` the motor is first set to its maximum angle of 88° to calibrate and then steps down to 20°. The `REM SendCommand` function will adjust the motors based only on its last known position. This is useful if shorter times between angle changes are desired.

Importantly, you must create your own experiment file for the macro to use. Replace `ADC autoseagull MCT.xpm` with the appropriate experiment file.

```
0 SendCommand(0,{UNI = MOT36=0});
1 SendCommand(0,{UNI = MOT37=6800});
2 MeasureReference (0, {EXP='ADC autoseagull MCT.xpm', XPP='C:\OPUS_7
     .0.123.1158\XPM'});
3 <$ResultFile 2> = SaveReference (0, {EXP='ADC autoseagull MCT.xpm',
     XPP='C:\OPUS_7.0.123.1158\XPM', BSF='C:\OPUS_7.0.123.1158'});
4 SendCommand(0,{UNI = MOT37=4800});
5 MeasureReference (0, {EXP='ADC autoseagull MCT.xpm', XPP='C:\OPUS_7
     .0.123.1158\XPM'});
6 <$ResultFile 2> = SaveReference (0, {EXP='ADC autoseagull MCT.xpm',
     XPP='C:\OPUS_7.0.123.1158\XPM', BSF='C:\OPUS_7.0.123.1158'});
7 SendCommand(0,{UNI = MOT37=2800});
8 MeasureReference (0, {EXP='ADC autoseagull MCT.xpm', XPP='C:\OPUS_7
     .0.123.1158\XPM'});
9 <$ResultFile 2> = SaveReference (0, {EXP='ADC autoseagull MCT.xpm',
     XPP='C:\OPUS_7.0.123.1158\XPM', BSF='C:\OPUS_7.0.123.1158'});
10 SendCommand(0,{UNI = MOT37=800});
11 MeasureReference (0, {EXP='ADC autoseagull MCT.xpm', XPP='C:\OPUS_7
     .0.123.1158\XPM'});
12 <$ResultFile 2> = SaveReference (0, {EXP='ADC autoseagull MCT.xpm',
     XPP='C:\OPUS_7.0.123.1158\XPM', BSF='C:\OPUS_7.0.123.1158'});
13 SendCommand(0,{UNI = MOT36=100});
14 SendCommand(0,{UNI = MOT37=6800});
15 MeasureReference (0, {EXP='ADC autoseagull MCT.xpm', XPP='C:\OPUS_7
     .0.123.1158\XPM'});
```

```
16 <$ResultFile 2> = SaveReference (0, {EXP='ADC autoseagull MCT.xpm',
      XPP='C:\OPUS_7.0.123.1158\XPM', BSF='C:\OPUS_7.0.123.1158'});
17 SendCommand(0,{UNI = MOT37=4800});
18 MeasureReference (0, {EXP='ADC autoseagull MCT.xpm', XPP='C:\OPUS_7
      .0.123.1158\XPM'});
19 <$ResultFile 2> = SaveReference (0, {EXP='ADC autoseagull MCT.xpm',
      XPP='C:\OPUS_7.0.123.1158\XPM', BSF='C:\OPUS_7.0.123.1158'});
20 SendCommand(0,{UNI = MOT37=2800});
21 MeasureReference (0, {EXP='ADC autoseagull MCT.xpm', XPP='C:\OPUS_7
      .0.123.1158\XPM'});
22 <$ResultFile 2> = SaveReference (0, {EXP='ADC autoseagull MCT.xpm',
      XPP='C:\OPUS_7.0.123.1158\XPM', BSF='C:\OPUS_7.0.123.1158'});
23 SendCommand(0,{UNI = MOT37=800});
24 MeasureReference (0, {EXP='ADC autoseagull MCT.xpm', XPP='C:\OPUS_7
      .0.123.1158\XPM'});
25 <$ResultFile 2> = SaveReference (0, {EXP='ADC autoseagull MCT.xpm',
      XPP='C:\OPUS_7.0.123.1158\XPM', BSF='C:\OPUS_7.0.123.1158'});
```

CHAPTER 8

REFERENCES

1. IEA. Key World Energy Statistics 2020. https://doi.org/10.1787/71b3ce84-en (accessed Sepember 10, 2020).

2. Armstrong, R. C.; Wolfram, C.; de Jong, K. P.; Gross, R.; Lewis, N. S.; Boardman, B.; Ragauskas, A. J.; Ehrhardt-Martinez, K.; Crabtree, G.; Ramana, M. V. The Frontiers of Energy. *Nat. Energy.* **2016**, *1*, 15020. https://doi.org/10.1038/nenergy.2015.20

3. Tsao, J. Y. L., Nathan S.; Crabtree, George W; . Solar Faqs. https://www.sandia.gov/ jytsao/Solar%20FAQs.pdf.

4. Basic Research Needs for Solar Energy Utilization. Report on the Basic Energy Sciences Workshop. *Argonne National Laboratory.* **2005**.

5. Lewis, N. S. A Prospective on Energy and Environmental Science. *Energy Environ. Sci.* **2019**, *12*, 16-18. https://doi.org/10.1039/C8EE90070A

6. Hou, Y.; Vidu, R.; Stroeve, P. Solar Energy Storage Methods. *Ind. Eng. Chem. Res.* **2011**, *50*, 8954-8964. https://doi.org/10.1021/ie2003413

7. Rady, A. C.; Giddey, S.; Badwal, S. P. S.; Ladewig, B. P.; Bhattacharya, S. Review of Fuels for Direct Carbon Fuel Cells. *Energy Fuels.* **2012**, *26*, 1471-1488. https://doi.org/10.1021/ef201694y

8. Nayak, P. K.; Mahesh, S.; Snaith, H. J.; Cahen, D. Photovoltaic Solar Cell Technologies: Analysing the State of the Art. *Nat. Rev. Mater.* **2019**, *4*, 269-285. https://doi.org/10.1038/s41578-019-0097-0

9. Tian, Y.; Zhao, C. Y. A Review of Solar Collectors and Thermal Energy Storage in Solar Thermal Applications. *Appl. Energy.* **2013**, *104*, 538-553. https://doi.org/10.1016/j.apenergy.2012.11.051

10. Dincer, I. Evaluation and Selection of Energy Storage Systems for Solar Thermal Applications. *Int. J. Energy Res.* **1999**, *23*, 1017-1028.

11. Sarbu, I.; Sebarchievici, C. A Comprehensive Review of Thermal Energy Storage. *Sustainability.* **2018**, *10*. https://doi.org/10.3390/su10010191

12. Johnson, Matthew P. Photosynthesis. *Essays Biochem*. **2016**, *60*, 255-273. https://doi.org/10.1042/ebc20160016

13. Montoya, J. H.; Seitz, L. C.; Chakthranont, P.; Vojvodic, A.; Jaramillo, T. F.; Nørskov, J. K. Materials for Solar Fuels and Chemicals. *Nat. Mater*. **2017**, *16*, 70-81. https://doi.org/10.1038/nmat4778

14. Lewis, N. S. Introduction: Solar Energy Conversion. *Chem. Rev*. **2015**, *115*, 12631-12632. https://doi.org/10.1021/acs.chemrev.5b00654

15. Lewis, N. S. Research Opportunities to Advance Solar Energy Utilization. Science. **2016**, *351*, aad1920. https://doi.org/10.1126/science.aad1920

16. Hadar, I.; Song, T.-B.; Ke, W.; Kanatzidis, M. G. Modern Processing and Insights on Selenium Solar Cells: The World's First Photovoltaic Device. *Adv. Energy Mater*. **2019**, *9*, 1802766. https://doi.org/10.1002/aenm.201802766

17. Perlin, J. The Silicon Solar Cell Turns 50. https://www.nrel.gov/docs/fy04osti/33947.pdf (accessed September 12, 2020).

18. Wong, T. K. S.; Zhuk, S.; Masudy-Panah, S.; Dalapati, G. K. Current Status and Future Prospects of Copper Oxide Heterojunction Solar Cells. *Materials*. **2016**, *9*. https://doi.org/10.3390/ma9040271

19. Reynolds, D. C.; Leies, G.; Antes, L. L.; Marburger, R. E. Photovoltaic Effect in Cadmium Sulfide. *Phys. Rev*. **1954**, *96*, 533-534. https://doi.org/10.1103/PhysRev.96.533

20. Chapin, D. M.; Fuller, C. S.; Pearson, G. L. A New Silicon P-N Junction Photocell for Converting Solar Radiation into Electrical Power. *J. Appl. Phys*. **1954**, *25*, 676-677. https://doi.org/10.1063/1.1721711

21. IRENA. Renewable Power Generation Costs in 2017. https://www.irena.org/-/media/Files/IRENA/Agency/Publication/2018/Jan/IRENA_2017_Power_Costs_2018.pdfr

22. Haase, F.; Hollemann, C.; Sch"afer, S.; Merkle, A.; Rien"acker, M.; Kr"ugener, J.; Brendel, R.; Peibst, R. Laser Contact Openings for Local Poly-Si-Metal Contacts Enabling 26.1%-Efficient POLO-IBC Solar Cells. *Sol. Energy Mater. Sol. Cells*. **2018**, *186*, 184-193. https://doi.org/10.1016/j.solmat.2018.06.020

23. Lane, C. Solar Panel Efficiency: Most Efficient Solar Panels in 2020. https://www.solarreviews.com/blog/what-are-the-most-efficient-solar-panels (accessed September 10).

24. Andreani, L. C.; Bozzola, A.; Kowalczewski, P.; Liscidini, M.; Redorici, L. Silicon Solar Cells: Toward the Efficiency Limits. *Adv. Phys.: X*. **2019**, *4*, 1548305. https://doi.org/10.1080/23746149.2018.1548305

25. Woodhouse, M. S., B; Ramdas. A; Margolis, R. Crystalline Silicon Photovoltaic Module Manufacturing Costs and Sustainable Pricing: 1h 2018 Benchmark and Cost Reduction Road Map. https://www.nrel.gov/docs/fy19osti/72134.pdf (accessed September 12).

26. NREL. Best Research Cell Efficiencies. https://www.nrel.gov/pv/assets/pdfs/best-research-cell-efficiencies.20200803.pdf.

27. Tanabe, K. A Review of Ultrahigh Efficiency III-V Semiconductor Compound Solar Cells: Multijunction Tandem, Lower Dimensional, Photonic up/Down Conversion and Plasmonic Nanometallic Structures. *Energies*. **2009**, *2*, 504-530. https://doi.org/10.3390/en20300504

28. Lee, T. D.; Ebong, A. U. A Review of Thin Film Solar Cell Technologies and Challenges. *Renewable Sustainable Energy Rev*. **2017**, *70*, 1286-1297. https://doi.org/10.1016/j.rser.2016.12.028

29. Cui, Y., et al. Organic Photovoltaic Cell with 17% Efficiency and Superior Processability. *Natl. Sci. Rev*. **2019**, *7*, 1239-1246. https://doi.org/10.1093/nsr/nwz200

30. Zheng, B.; Huo, L.; Li, Y. Benzodithiophenedione-Based Polymers: Recent Advances in Organic Photovoltaics. *NPG Asia Mater*. **2020**, *12*, 3. https://doi.org/10.1038/s41427-019-0163-5

31. Duan, L.; Uddin, A. Progress in Stability of Organic Solar Cells. *Adv. Sci*. **2020**, *7*, 1903259. https://doi.org/10.1002/advs.201903259

32. Kojima, A.; Teshima, K.; Shirai, Y.; Miyasaka, T. Organometal Halide Perovskites as Visible-Light Sensitizers for Photovoltaic Cells. *J. Am. Chem. Soc*. **2009**, *131*, 6050-6051. https://doi.org/10.1021/ja809598r

33. Park, N.-G. Perovskite Solar Cells: An Emerging Photovoltaic Technology. *Mater. Today*. **2015**, *18*, 65-72. https://doi.org/10.1016/j.mattod.2014.07.007

34. Mora-Seró, I.; Saliba, M.; Zhou, Y. Towards the Next Decade for Perovskite Solar Cells. *Solar RRL*. **2020**, *4*, 1900563. https://doi.org/10.1002/solr.201900563

35. Jena, A. K.; Kulkarni, A.; Miyasaka, T. Halide Perovskite Photovoltaics: Background, Status, and Future Prospects. *Chem. Rev*. **2019**, *119*, 3036-3103. https://doi.org/10.1021/acs.chemrev.8b00539

36. Swartwout, R.; Hoerantner, M. T.; Bulović, V. Scalable Deposition Methods for Large-Area Production of Perovskite Thin Films. *Energy Environ. Mater*. **2019**, *2*, 119-145. https://doi.org/10.1002/eem2.12043

37. Yang, Z.; Zhang, S.; Li, L.; Chen, W. Research Progress on Large-Area Perovskite Thin Films and Solar Modules. *J. Materiomics*. **2017**, *3*, 231-244. https://doi.org/10.1016/j.jmat.2017.09.002

38. Wang, D.; Wright, M.; Elumalai, N. K.; Uddin, A. Stability of Perovskite Solar Cells. *Sol. Energy Mater. Sol. Cells*. **2016**, *147*, 255-275. https://doi.org/10.1016/j.solmat.2015.12.025

39. Leijtens, T.; Bush, K.; Cheacharoen, R.; Beal, R.; Bowring, A.; McGehee, M. D. Towards Enabling Stable Lead Halide Perovskite Solar Cells; Interplay between Structural, Environmental, and Thermal Stability. *J. Mater. Chem. A*. **2017**, *5*, 11483-11500. https://doi.org/10.1039/c7ta00434f

40. Niu, G. D.; Li, W. Z.; Li, J. W.; Liang, X. Y.; Wang, L. D. Enhancement of Thermal Stability for Perovskite Solar Cells through Cesium Doping. *RSC Adv*. **2017**, *7*, 17473-17479. https://doi.org/10.1039/c6ra28501e

41. Noh, J. H.; Im, S. H.; Heo, J. H.; Mandal, T. N.; Seok, S. I. Chemical Management for Colorful, Efficient, and Stable Inorganic-Organic Hybrid Nanostructured Solar Cells. *Nano Lett*. **2013**, *13*, 1764-1769. https://doi.org/10.1021/nl400349b

42. Gholipour, S.; Saliba, M., Chapter 1 - Bandgap Tuning and Compositional Exchange for Lead Halide Perovskite Materials. In *Characterization Techniques for Perovskite Solar Cell Materials*, Pazoki, M.; Hagfeldt, A.; Edvinsson, T., Eds. Elsevier: **2020**; pp 1-22.

43. Ou, Q.; Bao, X.; Zhang, Y.; Shao, H.; Xing, G.; Li, X.; Shao, L.; Bao, Q. Band Structure Engineering in Metal Halide Perovskite Nanostructures for Optoelectronic Applications. *Nanomaterials*. **2019**, *1*, 268-287.
https://doi.org/10.1016/j.nanoms.2019.10.004

44. Yoo, J. J., et al. An Interface Stabilized Perovskite Solar Cell with High Stabilized Efficiency and Low Voltage Loss. *Energy Environ. Sci*. **2019**, *12*, 2192-2199.
https://doi.org/10.1039/C9EE00751B

45. Green, M. A.; Ho-Baillie, A.; Snaith, H. J. The Emergence of Perovskite Solar Cells. *Nat. Photonics*. **2014**, *8*, 506-514. https://doi.org/10.1038/nphoton.2014.134

46. Zuo, C.; Bolink, H. J.; Han, H.; Huang, J.; Cahen, D.; Ding, L. Advances in Perovskite Solar Cells. *Adv. Sci*. **2016**, *3*, 1500324. https://doi.org/10.1002/advs.201500324

47. Mhamad, S. A.; Mohammed, A. M.; Aziz, M.; Aziz, F., Impact of Electron Transport Layers (ETLs) and Hole Transport Layer (HTLs) on Perovskite Solar Cells Performance. In *Nanostructured Materials for Next-Generation Energy Storage and Conversion: Photovoltaic and Solar Energy*, Atesin, T. A.; Bashir, S.; Liu, J. L., Eds. Springer Berlin Heidelberg: Berlin, Heidelberg, **2019**; pp 227-246.

48. Cao, F.; Wang, M.; Li, L. Graded Energy Band Engineering for Efficient Perovskite Solar Cells. *Nano Select*. **2020**, *1*, 152-168. https://doi.org/10.1002/nano.202000005

49. Shockley, W.; Queisser, H. J. Detailed Balance Limit of Efficiency of p-n Junction Solar Cells. *J. Appl. Phys*. **1961**, *32*, 510-519. https://doi.org/10.1063/1.1736034

50. Rühle, S. Tabulated Values of the Shockley–Queisser Limit for Single Junction Solar Cells. *Sol. Energy*. **2016**, *130*, 139-147.
https://doi.org/10.1016/j.solener.2016.02.015

51. Solanki, C. S.; Beaucarne, G. Advanced Solar Cell Concepts. *Energy Sustainable Dev*. **2007**, *11*, 17-23. https://doi.org/10.1016/S0973-0826(08)60573-6

52. De Vos, A. Detailed Balance Limit of the Efficiency of Tandem Solar Cells. *J. Phys. D: Appl. Phys*. **1980**, *13*, 839-846. https://doi.org/10.1088/0022-3727/13/5/018

53. Yousefi, A.; Kabutov, Q. High Efficiency Multijunction Solar Cells: Overview of Important Developments. 2012 International Symposium on Computer Applications and Industrial Electronics (ISCAIE). 3–4 Dec. 2012; **2012**; pp 14-19.

54. Garrison, R.; Kleiman, R. Higher Efficiency Tandem Solar Cells through Composite-Cell Current Matching. *Opt. Express*. **2019**, *27*, A543-A571.
https://doi.org/10.1364/Oe.27.00a543

55. Albrecht, S., et al. Monolithic Perovskite/Silicon-Heterojunction Tandem Solar Cells Processed at Low Temperature. *Energy Environ. Sci*. **2016**, *9*, 81-88.
https://doi.org/10.1039/C5EE02965A

56. Hossain, M. I.; Qarony, W.; Ma, S.; Zeng, L.; Knipp, D.; Tsang, Y. H. Perovskite/Silicon Tandem Solar Cells: From Detailed Balance Limit Calculations to Photon Management. *Nano-Micro Lett*. **2019**, *11*, 58. https://doi.org/10.1007/s40820-019-0287-8

57. Yan, L. L.; Han, C.; Shi, B.; Zhao, Y.; Zhang, X. D. A Review on the Crystalline Silicon Bottom Cell for Monolithic Perovskite/Silicon Tandem Solar Cells. *Materials Today. Nano*. **2019**, *7*, 100045. https://doi.org/10.1016/j.mtnano.2019.100045

58. Elshorbagy, M. H.; López-Fraguas, E.; Chaudhry, F. A.; Sánchez-Pena, J. M.; Vergaz, R.; García-Cámara, B. A Monolithic Nanostructured-Perovskite/Silicon Tandem Solar Cell: Feasibility of Light Management through Geometry and Materials Selection. *Sci. Rep*. **2020**, *10*, 2271. https://doi.org/10.1038/s41598-020-58978-5

59. Lal, N. N.; Dkhissi, Y.; Li, W.; Hou, Q.; Cheng, Y.-B.; Bach, U. Perovskite Tandem Solar Cells. *Adv. Energy Mater*. **2017**, *7*, 1602761. https://doi.org/10.1002/aenm.201602761

60. Pitchaiya, S.; Natarajan, M.; Santhanam, A.; Asokan, V.; Yuvapragasam, A.; Madurai Ramakrishnan, V.; Palanisamy, S. E.; Sundaram, S.; Velauthapillai, D. A Review on the Classification of Organic/Inorganic/Carbonaceous Hole Transporting Materials for Perovskite Solar Cell Application. *Arabian J. Chem*. **2020**, *13*, 2526-2557. https://doi.org/10.1016/j.arabjc.2018.06.006

61. Mohamad Noh, M. F.; Teh, C. H.; Daik, R.; Lim, E. L.; Yap, C. C.; Ibrahim, M. A.; Ahmad Ludin, N.; Mohd Yusoff, A. R. b.; Jang, J.; Mat Teridi, M. A. The Architecture of the Electron Transport Layer for a Perovskite Solar Cell. *J. Mat. Chem. C*. **2018**, *6*, 682-712. https://doi.org/10.1039/C7TC04649A

62. Lian, J.; Lu, B.; Niu, F.; Zeng, P.; Zhan, X. Electron-Transport Materials in Perovskite Solar Cells. *Small Methods*. **2018**, *2*, 1800082. https://doi.org/doi:10.1002/smtd.201800082

63. Hawash, Z.; Ono, L. K.; Qi, Y. Recent Advances in Spiro-Meotad Hole Transport Material and Its Applications in Organic–Inorganic Halide Perovskite Solar Cells. *Adv. Mater. Interfaces*. **2018**, *5*, 1700623. https://doi.org/doi:10.1002/admi.201700623

64. Schroder, D. K. Carrier Lifetimes in Silicon. *IEEE Transactions on Electron Devices*. **1997**, *44*, 160-170. https://doi.org/10.1109/16.554806

65. Hermle, M.; Feldmann, F.; Bivour, M.; Goldschmidt, J. C.; Glunz, S. W. Passivating Contacts and Tandem Concepts: Approaches for the Highest Silicon-Based Solar Cell Efficiencies. *Appl. Phys. Rev*. **2020**, *7*, 021305. https://doi.org/10.1063/1.5139202

66. Ko, C.-K.; Lee, W. G. Silicon Oxidation by Aerial Diffusion of Active Oxygen Species from UV-Irradiated TiO_2. Korean *J. Chem. Eng*. **2008**, *25*, 881-884. https://doi.org/10.1007/s11814-008-0145-8

67. Marmitt, G. G.; Nandi, S. K.; Venkatachalam, D. K.; Elliman, R. G.; Vos, M.; Grande, P. L. Oxygen Diffusion in TiO_2 Films Studied by Electron and Ion Rutherford Backscattering. *Thin Solid Films*. **2017**, *629*, 97-102. https://doi.org/10.1016/j.tsf.2017.03.024

68. Herman, G. S.; Zehr, R. T.; Henderson, M. A. Characterization of Oxygen and Titanium Diffusion at the Anatase TiO_2(001) *Surface. Surf. Sci*. **2013**, *612*, L5-L8. https://doi.org/10.1016/j.susc.2013.02.006

69. Aho, A.; Isoaho, R.; Hytönen, L.; Aho, T.; Raappana, M.; Polojärvi, V.; Tukiainen, A.; Reuna, J.; Mäkelä, S.; Guina, M. Lattice-Matched Four-Junction Tandem Solar Cell Including Two Dilute Nitride Bottom Junctions. *Prog. Photovoltaics*. **2019**, *27*, 299-305. https://doi.org/10.1002/pip.3094

70. Geisz, J. F.; Olson, J. M.; Friedman, D. J.; Jones, K. M.; Reedy, R. C.; Romero, M. J. Lattice-Matched GaNPAs-on-Silicon Tandem Solar Cells. Conference Record of the 31st IEEE Photovoltaic Specialists Conference. **2005**; pp 695-698.

71. Warmann, E. C.; Leite, M. S.; Atwater, H. A. Photovoltaic Efficiencies in Lattice-Matched III–V Multijunction Solar Cells with Unconventional Lattice Parameters. 37th IEEE Photovoltaic Specialists Conference. **2011**; pp 000570-000574.

72. Heo, H.; Sung, J. H.; Ahn, J.-H.; Ghahari, F.; Taniguchi, T.; Watanabe, K.; Kim, P.; Jo, M.-H. Frank–Van Der Merwe Growth Versus Volmer–Weber Growth in Successive Stacking of a Few-Layer Bi_2Te_3/Sb_2te_3 by Van Der Waals Heteroepitaxy: The Critical Roles of Finite Lattice-Mismatch with Seed Substrates. *Advanced Electronic Materials*. **2017**, *3*, 1600375. https://doi.org/10.1002/aelm.201600375

73. Yamaguchi, M.; Yamamoto, A.; Itoh, Y. Effect of Dislocations on the Efficiency of Thin-Film GaAs Solar Cells on Si Substrates. *J. Appl. Phys*. **1986**, *59*, 1751-1753. https://doi.org/10.1063/1.336439

74. Yang, L. Lattice Mismatched Compound Semiconductors and Devices on Silicon. Massachusetts Institute of Technology, Cambridge, MA, **2011**.

75. Long, J.; Xiao, M.; Huang, X.; Xing, Z.; Li, X.; Dai, P.; Tan, M.; Wu, Y.; Song, M.; Lu, S. High Efficiency Thin Film GaInP/GaAs/InGaAs Inverted Metamorphic (IMM) Solar Cells Based on Electroplating Process. *J. Cryst. Growth*. **2019**, *513*, 38-42. https://doi.org/10.1016/j.jcrysgro.2019.02.057

76. Targhi, F. F.; Jalili, Y. S.; Kanjouri, F. $MapbiI_3$ and $FapbI_3$ Perovskites as Solar Cells: Case Study on Structural, Electrical and Optical Properties. *Results Phys*. **2018**, *10*, 616-627. https://doi.org/10.1016/j.rinp.2018.07.007

77. Hom, T.; Kiszenik, W.; Post, B. Accurate Lattice Constants from Multiple Reflection Measurements. II. Lattice Constants of Germanium Silicon, and Diamond. *J. Appl. Crystallogr*. **1975**, *8*, 457-458. https://doi.org/10.1107/s0021889875010965

78. Treacy, J. P. W., et al. Geometric Structure of Anatase TiO_2 (101). *Phys. Rev. B*. **2017**, *95*, 075416. https://doi.org/10.1103/PhysRevB.95.075416

79. Kepenekian, M., *et al*. Concept of Lattice Mismatch and Emergence of Surface States in Two-Dimensional Hybrid Perovskite Quantum Wells. *Nano Lett*. **2018**, *18*, 5603-5609. https://doi.org/10.1021/acs.nanolett.8b02078

80. Lee, K.; Ryu, J.; Yu, H.; Yun, J.; Lee, J.; Jang, J. Enhanced Efficiency and Air-Stability of NiO_x-Based Perovskite Solar Cells Via PCBM Electron Transport Layer Modification with Triton X-100. *Nanoscale*. **2017**, *9*, 16249-16255. https://doi.org/10.1039/C7NR05235A

81. Li, H.; Xue, Y.; Zheng, B.; Tian, J.; Wang, H.; Gao, C.; Liu, X. Interface Modification with PCBM Intermediate Layers for Planar Formamidinium Perovskite Solar Cells. *RSC Adv*. **2017**, *7*, 30422-30427. https://doi.org/10.1039/C7RA04311B

82. Okada, W.; Suga, T.; Oyaizu, K.; Segawa, H.; Nishide, H. Perovskite/ceTiO2 Interface Passivation Using Poly(Vinylcarbazole) and Fullerene for the Photovoltaic Conversion Efficiency of 21%. *ACS Appl. Energy Mater*. **2019**, *2*, 2848-2853. https://doi.org/10.1021/acsaem.9b00162

83. Song, S.; Hill, R.; Choi, K.; Wojciechowski, K.; Barlow, S.; Leisen, J.; Snaith, H. J.; Marder, S. R.; Park, T. Surface Modified Fullerene Electron Transport Layers for Stable and Reproducible Flexible Perovskite Solar Cells. *Nano Energy*. **2018**, *49*, 324-332. https://doi.org/10.1016/j.nanoen.2018.04.068

84. Angmo, D., et al. Beyond Fullerenes: Indacenodithiophene-Based Organic Charge-Transport Layer toward Upscaling of Low-Cost Perovskite Solar Cells. *ACS Appl. Mater. Interfaces*. **2018**, *10*, 22143-22155. https://doi.org/10.1021/acsami.8b04861

85. Tsarev, S.; Luchkin, S. Y.; Stevenson, K. J.; Troshin, P. A. Perylenetetracarboxylic Dianhydride as Organic Electron Transport Layer for N-I-P Perovskite Solar Cells. *Synth. Met*. **2020**, *268*, 116497. https://doi.org/10.1016/j.synthmet.2020.116497

86. Said, A. A.; Xie, J.; Zhang, Q. Recent Progress in Organic Electron Transport Materials in Inverted Perovskite Solar Cells. *Small*. **2019**, *15*, 1900854. https://doi.org/10.1002/smll.201900854

87. Hamada, K., *et al*. Enhanced Device Performance with Passivation of the ceTiO2 Surface Using a Carboxylic Acid Fullerene Monolayer for a SnPb Perovskite Solar Cell with a Normal Planar Structure. *ACS Appl. Mater. Interfaces*. **2020**, *12*, 17776-17782. https://doi.org/10.1021/acsami.0c01411

88. Tsvetkov, N.; Nikolskaia, A.; Shevaleevskiy, O.; Kozlov, S.; Vildanova, M.; Moon, B. C.; Kang, J. K.; Larina, L. ceTiO2/Halide Perovskite Interface: The Impact of Surface State Passivation on Energy Alignment and Photovoltaic Performance of Perovskite Solar Cells. *Appl. Surf. Sci*. **2020**, *512*, 145666. https://doi.org/10.1016/j.apsusc.2020.145666

89. Kadem, B. Y.; Hassan, A. K.; Cranton, W. The Effects of Organic Solvents and Their Co-Solvents on the Optical, Structural, Morphological of P3HT:PCBM Organic Solar Cells. *AIP Conference Proceedings*. **2016**, *1758*, 020006. https://doi.org/10.1063/1.4959382

90. Kim, J. Y. Effect of Solvents on the Electrical and Morphological Characteristics of Polymer Solar Cells. *Polymers*. **2019**, *11*. https://doi.org/10.3390/polym11020228

91. Huang, C.; Barlow, S.; Marder, S. R. Perylene-3,4,9,10-Tetracarboxylic Acid Diimides: Synthesis, Physical Properties, and Use in Organic Electronics. *J. Org. Chem*. **2011**, *76*, 2386-2407. https://doi.org/10.1021/jo2001963

92. Zhao, X.; Xiong, Y.; Ma, J.; Yuan, Z. Rylene and Rylene Diimides: Comparison of Theoretical and Experimental Results and Prediction for High-Rylene Derivatives. *J. Phys. Chem. A*. **2016**, *120*, 7554-7560. https://doi.org/10.1021/acs.jpca.6b07552

93. Chen, L.; Li, C.; Müllen, K. Beyond Perylene Diimides: Synthesis, Assembly and Function of Higher Rylene Chromophores. *J. Mat. Chem. C.* **2014**, *2*, 1938-1956. https://doi.org/10.1039/C3TC32315C

94. Acikbas, Y.; Capan, R.; Yukruk, F.; Erdogan, M. Spun Films of Perylene Diimide Derivative for the Detection of Organic Vapors with Host–Guest Principle. *J. Inclusion Phenom. Macrocyclic Chem.* **2018**, *92*, 137-146. https://doi.org/10.1007/s10847-018-0823-z

95. Guo, Q.; Xu, Y.; Xiao, B.; Zhang, B.; Zhou, E.; Wang, F.; Bai, Y.; Hayat, T.; Alsaedi, A.; Tan, Z. a. Effect of Energy Alignment, Electron Mobility, and Film Morphology of Perylene Diimide Based Polymers as Electron Transport Layer on the Performance of Perovskite Solar Cells. *ACS Appl. Mater. Interfaces.* **2017**, *9*, 10983-10991. https://doi.org/10.1021/acsami.7b00902

96. Ahrens, M. J.; Fuller, M. J.; Wasielewski, M. Cyanated Perylene-3,4-Dicarboximides and Perylene-3,4:9,10-Bis(Dicarboximide): Facile Chromophoric Oxidants for Organic Photonics and Electronics. *Chem. Mater.* **2003**, *15*, 2684-2686. https://doi.org/10.1021/cm034140u

97. Würthner, F. Perylene Bisimide Dyes as Versatile Building Blocks for Functional Supramolecular Architectures. *Chem. Commun.* **2004**, 1564-1579. https://doi.org/10.1039/B401630K

98. Lee, S. K.; Zu, Y.; Herrmann, A.; Geerts, Y.; Müllen, K.; Bard, A. J. Electrochemistry, Spectroscopy and Electrogenerated Chemiluminescence of Perylene, Terrylene, and Quaterrylene Diimides in Aprotic Solution. *J. Am. Chem. Soc.* **1999**, *121*, 3513-3520. https://doi.org/10.1021/ja984188m

99. Vajiravelu, S.; Ramunas, L.; Juozas Vidas, G.; Valentas, G.; Vygintas, J.; Valiyaveettil, S. Effect of Substituents on the Electron Transport Properties of Bay Substituted Perylene Diimide Derivatives. *J. Mat. Chem.* **2009**, *19*, 4268-4275. https://doi.org/10.1039/B901847F

100. Sze, S. M.; Ng, K. K., Physics of Semiconductor Devices; John Wiley & Sons, Inc.: Hoboken, NJ, **2006**.

101. Zong, L.; Zhu, B.; Lu, Z.; Tan, Y.; Jin, Y.; Liu, N.; Hu, Y.; Gu, S.; Zhu, J.; Cui, Y. Nanopurification of Silicon from 84% to 99.999% Purity with a Simple and Scalable Process. Proceedings of the National Academy of Sciences. **2015**, 201513012. https://doi.org/10.1073/pnas.1513012112

102. Manchester, K. E.; Sibley, C. B.; Alton, G. Doping of Silicon by Ion Implantation. *Nuclear Instruments and Methods.* **1965**, *38*, 169-174. https://doi.org/10.1016/0029-554X(65)90127-8

103. Ghandhi, S. K., VLSI Fabrication Principles: Silicon and Gallium Arsenide; John Wiley & Sons, Inc.: New York, NY, **1994**.

104. Royea, W. J.; Juang, A.; Lewis, N. S. Preparation of Air-Stable, Low Recombination Velocity Si(111) Surfaces through Alkyl Termination. *Appl. Phys. Lett.* **2000**, *77*, 1988-1990. https://doi.org/10.1063/1.1312203

105. Cartier, E.; Stathis, J. H.; Buchanan, D. A. Passivation and Depassivation of Silicon Dangling Bonds at the Si/SiO$_2$ Interface by Atomic Hydrogen. *Appl. Phys. Lett.* **1993**, *63*, 1510-1512. https://doi.org/10.1063/1.110758

106. Kluth, G. J.; Maboudian, R. Oxidation Mechanism of the Ammonium-Fluoride-Treated Si(100) Surface. *J. Appl. Phys*. **1996**, *80*, 5408-5414. https://doi.org/10.1063/1.362727

107. Niwano, M.; Kageyama, J. i.; Kurita, K.; Kinashi, K.; Takahashi, I.; Miyamoto, N. Infrared Spectroscopy Study of Initial Stages of Oxidation of Hydrogen-Terminated Si Surfaces Stored in Air. *J. Appl. Phys*. **1994**, *76*, 2157-2163. https://doi.org/10.1063/1.357627

108. The Physics and Chemistry of SiO_2 and the Si–SiO_2 Interface 2; Springer US: New York, **1993**.

109. Eades, W. D.; Swanson, R. M. Calculation of Surface Generation and Recombination Velocities at the Si-SiO_2 Interface. *J. Appl. Phys*. **1985**, *58*, 4267-4276. https://doi.org/10.1063/1.335562

110. Yablonovitch, E.; Gmitter, T. J. A Contactless Minority Lifetime Probe of Heterostructures, Surfaces, Interfaces and Bulk Wafers. *Solid-State Electron*. **1992**, *35*, 261-267. https://doi.org/10.1016/0038-1101(92)90230-A

111. Wan, Y. M.; McIntosh, K. R.; Thomson, A. F.; Cuevas, A. Low Surface Recombination Velocity by Low-Absorption Silicon Nitride on c-Si. 2012 IEEE 38th Photovoltaic Specialists Conference, Vol 2. **2013**.

112. Rangan, S.; Bersch, E.; Bartynski, R. A.; Garfunkel, E.; Vescovo, E. Electron Spectroscopic Measurements of Band Alignment in Metal/Oxide/Semiconductor Stacks. *Physics and Technology of High-K Materials 8*. **2010**, *33*, 267-279. https://doi.org/10.1149/1.3481614

113. Hiller, D.; Julin, J.; Chnani, A.; Strehle, S. Silicon Surface Passivation by ALD-Ga_2O_3: Thermal Vs. Plasma-Enhanced Atomic Layer Deposition. *IEEE J. Photovoltaics*. **2020**, *10*, 959-968. https://doi.org/10.1109/Jphotov.2020.2989201

114. Wan, Y.; Bullock, J.; Cuevas, A. Tantalum Oxide/Silicon Nitride: A Negatively Charged Surface Passivation Stack for Silicon Solar Cells. *Appl. Phys. Lett*. **2015**, *106*, 201601. https://doi.org/10.1063/1.4921416

115. Binnig, G.; Rohrer, H.; Gerber, C.; Weibel, E. 7×7 Reconstruction on Si(111) Resolved in Real Space. *Phys. Rev. Lett*. **1983**, *50*, 120-123. https://doi.org/10.1103/PhysRevLett.50.120

116. Wang, Y.-L.; Guo, H.-M.; Qin, Z.-H.; Ma, H.-F.; Gao, H.-J. Toward a Detailed Understanding of Si(111)-7×7 Surface and Adsorbed Ge Nanostructures: Fabrications, Structures, and Calculations. *J. Nanomater*. **2008**, 874213. https://doi.org/10.1155/2008/874213

117. Avouris, P.; In-Whan, L. Probing and Inducing Surface Chemistry with the STM: The Reactions of Si(111)-7×7 with H_2O and O_2. *Surf. Sci*. **1991**, *242*, 1-11. https://doi.org/10.1016/0039-6028(91)90233-I

118. Higashi, G. S.; Chabal, Y. J.; Trucks, G. W.; Raghavachari, K. Ideal Hydrogen Termination of the Si(111) Surface. *Appl. Phys. Lett*. **1990**, *56*, 656-658. https://doi.org/10.1063/1.102728

119. Niwano, M.; Takeda, Y.; Ishibashi, Y.; Kurita, K.; Miyamoto, N. Morphology of Hydrofluoric Acid and Ammonium Fluoride-Treated Silicon Surfaces Studied by Surface Infrared Spectroscopy. *J. Appl. Phys.* **1992**, *71*, 5646-5649. https://doi.org/10.1063/1.350497

120. Kern, W. The Evolution of Silicon-Wafer Cleaning Technology. *J. Electrochem. Soc.* **1990**, *137*, 1887-1892. https://doi.org/Doi 10.1149/1.2086825

121. Kolasinski, K. W. Etching of Silicon in Fluoride Solutions. *Surf. Sci.* **2009**, *603*, 1904-1911. https://doi.org/10.1016/j.susc.2008.08.031

122. Chabal, Y. J.; Higashi, G. S.; Raghavachari, K.; Burrows, V. A. Infrared Spectroscopy of Si(111) and Si(100) Surfaces after HF Treatment: Hydrogen Termination and Surface Morphology. *J. Vac. Sci. Technol.*, A. **1989**, *7*, 2104-2109. https://doi.org/10.1116/1.575980

123. Allongue, P.; Kieling, V.; Gerischer, H. Etching Mechanism and Atomic Structure of H-Si(111) Surfaces Prepared in NH_4F. *Electrochim. Acta*. **1995**, *40*, 1353-1360. https://doi.org/10.1016/0013-4686(95)00071-L

124. Munford, M. L.; Cortes, R.; Allongue, P. The Preparation of Ideally Ordered Flat H-Si(111) *Surfaces. Sens. Mater.* **2001**, *13*, 259-269.

125. Lublow, M.; Stempel, T.; Skorupska, K.; Muñoz, A. G.; Kanis, M.; Lewerenz, H. J. Morphological and Chemical Optimization of Ex Situ NH_4F (40%) Conditioned Si(111)-(1×1):H. *Appl. Phys. Lett.* **2008**, *93*, 062112. https://doi.org/10.1063/1.2972142

126. Dumas, P.; Chabal, Y. J.; Jakob, P. Morphology of Hydrogen-Terminated Si(111) and Si(100) Surfaces Upon Etching in HF and Buffered-HF Solutions. *Surf. Sci.* **1992**, *269-270*, 867-878. https://doi.org/10.1016/0039-6028(92)91363-G

127. Jakob, P.; Chabal, Y. J. Chemical Etching of Vicinal Si(111): Dependence of the Surface Structure and the Hydrogen Termination on the pH of the Etching Solutions. *J. Chem. Phys.* **1991**, *95*, 2897-2909. https://doi.org/10.1063/1.460892

128. Yablonovitch, E.; Allara, D. L.; Chang, C. C.; Gmitter, T.; Bright, T. B. Unusually Low Surface-Recombination Velocity on Silicon and Germanium Surfaces. *Phys. Rev. Lett.* **1986**, *57*, 249-252. https://doi.org/10.1103/PhysRevLett.57.249

129. Michalak, D. J.; Gstrein, F.; Lewis, N. S. The Role of Band Bending in Affecting the Surface Recombination Velocities for Si(111) in Contact with Aqueous Acidic Electrolytes. *J. Phys. Chem. C*. **2008**, *112*, 5911-5921. https://doi.org/10.1021/jp075354s

130. Laibinis, P. E.; Stanton, C. E.; Lewis, N. S. Measurement of Barrier Heights of Semiconductor/Liquid Junctions Using a Transconductance Method: Evidence for Inversion at N-Si/CH_3OH-1,1'-Dimethylferrocene+/0 Junctions. *J. Phys. Chem*. **1994**, *98*, 8765-8774. https://doi.org/10.1021/j100086a029

131. Michalak, D. J.; Lewis, N. S. Use of near-Surface Channel Conductance and Differential Capacitance Versus Potential Measurements to Correlate Inversion Layer Formation with Low Effective Surface Recombination Velocities at N-Si/Liquid Contacts. *Appl. Phys. Lett*. **2002**, *80*, 4458-4460. https://doi.org/10.1063/1.1479456

132. Hirata, T. Orientation Dependence of Infrared Spectra on Thermal Oxidation and Subsequent Etching of Single Crystal Si. *Solid State Commun*. **1999**, *111*, 421-426. https://doi.org/10.1016/S0038-1098(99)00236-7

133. Nemanick, E. J.; Hurley, P. T.; Brunschwig, B. S.; Lewis, N. S. Chemical and Electrical Passivation of Silicon (111) Surfaces through Functionalization with Sterically Hindered Alkyl Groups. *J. Phys. Chem. B*. **2006**, *110*, 14800-14808. https://doi.org/10.1021/jp057070i

134. Pasternack, R. M.; Rivillon Amy, S.; Chabal, Y. J. Attachment of 3-(Aminopropyl) Triethoxysilane on Silicon Oxide Surfaces: Dependence on Solution Temperature. *Langmuir*. **2008**, *24*, 12963-12971. https://doi.org/10.1021/la8024827

135. Haller, I. Covalently Attached Organic Monolayers on Semiconductor Surfaces. *J. Am. Chem. Soc*. **1978**, *100*, 8050-8055. https://doi.org/10.1021/ja00494a003

136. Michalak, D. J.; Rivillon, S.; Chabal, Y. J.; Estève, A.; Lewis, N. S. Infrared Spectroscopic Investigation of the Reaction of Hydrogen-Terminated, (111)-Oriented, Silicon Surfaces with Liquid Methanol. *J. Phys. Chem. B*. **2006**, *110*, 20426-20434. https://doi.org/10.1021/jp0624303

137. Michalak, D. J.; Amy, S. R.; Aureau, D.; Dai, M.; Estève, A.; Chabal, Y. J. Nanopatterning Si(111) Surfaces as a Selective Surface-Chemistry Route. *Nat. Mater*. **2010**, *9*, 266-271. https://doi.org/10.1038/nmat2611

138. Thissen, P.; Seitz, O.; Chabal, Y. J. Wet Chemical Surface Functionalization of Oxide-Free Silicon. *Prog. Surf. Sci*. **2012**, *87*, 272-290. https://doi.org/10.1016/j.progsurf.2012.10.003

139. Buriak, J. M. Illuminating Silicon Surface Hydrosilylation: An Unexpected Plurality of Mechanisms. *Chem. Mater*. **2014**, *26*, 763-772. https://doi.org/10.1021/cm402120f

140. Pandey, D.; Zemlyanov, D. Y.; Bevan, K.; Reifenberger, R. G.; Dirk, S. M.; Howell, S. W.; Wheeler, D. R. UHV STM I(V) and XPS Studies of Aryl Diazonium Molecules Assembled on Si(111). *Langmuir*. **2007**, *23*, 4700-4708. https://doi.org/10.1021/la063235i

141. Hunger, R.; Jaegermann, W.; Merson, A.; Shapira, Y.; Pettenkofer, C.; Rappich, J. Electronic Structure of Methoxy-, Bromo-, and Nitrobenzene Grafted onto Si(111). *J. Phys. Chem. B*. **2006**, *110*, 15432-15441. https://doi.org/10.1021/jp055702v

142. Allongue, P.; Henry de Villeneuve, C.; Cherouvrier, G.; Cortès, R.; Bernard, M. C. Phenyl Layers on H–Si(111) by Electrochemical Reduction of Diazonium Salts: Monolayer Versus Multilayer Formation. *J. Electroanal. Chem*. **2003**, *550-551*, 161-174. https://doi.org/10.1016/S0022-0728(03)00076-7

143. Yang, F.; Roodenko, K.; Hunger, R.; Hinrichs, K.; Rademann, K.; Rappich, J. Near-Ideal Complete Coverage of CD_3 onto Si(111) Surfaces Using One-Step Electrochemical Grafting: An Ir Ellipsometry, Synchrotron XPS, and Photoluminescence Study. *J. Phys. Chem. C*. **2012**, *116*, 18684-18690. https://doi.org/10.1021/jp301013t

144. *Pits and Pores: Formation, Properties, and Significance for Advanced Luminescent Materials*; The Electrochemical Society, Inc.: Pennington, NJ, **1997**.

145. Teyssot, A.; Fidélis, A.; Fellah, S.; Ozanam, F.; Chazalviel, J. N. Anodic Grafting of Organic Groups on the Silicon Surface. *Electrochim. Acta*. **2002**, *47*, 2565-2571. https://doi.org/10.1016/S0013-4686(02)00116-0

146. Bansal, A.; Lewis, N. S. Stabilization of Si Photoanodes in Aqueous Electrolytes through Surface Alkylation. *J. Phys. Chem. B*. **1998**, *102*, 4058-4060. https://doi.org/10.1021/jp980679h

147. Bansal, A.; Li, X.; Lauermann, I.; Lewis, N. S.; Yi, S. I.; Weinberg, W. H. Alkylation of Si Surfaces Using a Two-Step Halogenation/Grignard Route. *J. Am. Chem. Soc*. **1996**, *118*, 7225-7226. https://doi.org/10.1021/ja960348n

148. Bansal, A.; Li, X.; Yi, S. I.; Weinberg, W. H.; Lewis, N. S. Spectroscopic Studies of the Modification of Crystalline Si(111) Surfaces with Covalently-Attached Alkyl Chains Using a Chlorination/Alkylation Method. *J. Phys. Chem. B*. **2001**, *105*, 10266-10277. https://doi.org/10.1021/jp010284p

149. Hunger, R.; Fritsche, R.; Jaeckel, B.; Jaegermann, W.; Webb, L. J.; Lewis, N. S. Chemical and Electronic Characterization of Methyl-Terminated Si(111) Surfaces by High-Resolution Synchrotron Photoelectron Spectroscopy. *Phys. Rev. B*. **2005**, *72*, 045317. https://doi.org/10.1103/PhysRevB.72.045317

150. Webb, L. J.; Nemanick, E. J.; Biteen, J. S.; Knapp, D. W.; Michalak, D. J.; Traub, M. C.; Chan, A. S. Y.; Brunschwig, B. S.; Lewis, N. S. High-Resolution X-Ray Photoelectron Spectroscopic Studies of Alkylated Silicon(111) Surfaces. *J. Phys. Chem. B*. **2005**, *109*, 3930-3937. https://doi.org/10.1021/jp047199c

151. O'Leary, L. E.; Rose, M. J.; Ding, T. X.; Johansson, E.; Brunschwig, B. S.; Lewis, N. S. Heck Coupling of Olefins to Mixed Methyl/Thienyl Monolayers on Si(111) Surfaces. *J. Am. Chem. Soc*. **2013**, *135*, 10081-10090. https://doi.org/10.1021/ja402495e

152. O'Leary, L. E.; Johansson, E.; Brunschwig, B. S.; Lewis, N. S. Synthesis and Characterization of Mixed Methyl/Allyl Monolayers on Si(111). *J. Phys. Chem. B*. **2010**, *114*, 14298-14302. https://doi.org/10.1021/jp911379c

153. Gurrentz, J. M.; Rose, M. J. Non-Catalytic Benefits of Ni(II) Binding to an Si(111)-Pnp Construct for Photoelectrochemical Hydrogen Evolution Reaction: Metal Ion Induced Flat Band Potential Modulation. *J. Am. Chem. Soc*. **2020**, *142*, 5657-5667. https://doi.org/10.1021/jacs.9b12824

154. Linford, M. R.; Fenter, P.; Eisenberger, P. M.; Chidsey, C. E. D. Alkyl Monolayers on Silicon Prepared from 1-Alkenes and Hydrogen-Terminated Silicon. *J. Am. Chem. Soc*. **1995**, *117*, 3145-3155. https://doi.org/10.1021/ja00116a019

155. Linford, M. R.; Chidsey, C. E. D. Alkyl Monolayers Covalently Bonded to Silicon Surfaces. *J. Am. Chem. Soc*. **1993**, *115*, 12631-12632. https://doi.org/10.1021/ja00079a071

156. Hartig, P. Engineering of Si(111) Surfaces by Electrochemical Deposition of Organic Layers from Dazonium Salt Solutions. Technical University of Munich, Munich, Germany, **2002**.

157. Henry de Villeneuve, C.; Pinson, J.; Ozanam, F.; Chazalviel, J. N.; Allongue, P. Molecular Grafting on Si(111) Surfaces: An Electrochemical Approach. *MRS Proceedings*. **1996**, *451*, 185. https://doi.org/10.1557/PROC-451-185

158. Rivillon Amy, S.; Michalak, D. J.; Chabal, Y. J.; Wielunski, L.; Hurley, P. T.; Lewis, N. S. Investigation of the Reactions During Alkylation of Chlorine-Terminated Silicon (111) Surfaces. *J. Phys. Chem. C*. **2007**, *111*, 13053-13061. https://doi.org/10.1021/jp071793f

159. Rivillon, S.; Chabal, Y. J.; Webb, L. J.; Michalak, D. J.; Lewis, N. S.; Halls, M. D.; Raghavachari, K. Chlorination of Hydrogen-Terminated Silicon (111) Surfaces. *J. Vac. Sci. Technol., A*. **2005**, 23, 1100-1106. https://doi.org/10.1116/1.1861941

160. Gleason-Rohrer, D. C.; Brunschwig, B. S.; Lewis, N. S. Measurement of the Band Bending and Surface Dipole at Chemically Functionalized Si(111)/Vacuum Interfaces. *J. Phys. Chem. C*. **2013**, *117*, 18031-18042. https://doi.org/10.1021/jp401585s

161. Haber, J. A.; Lewis, N. S. Infrared and X-Ray Photoelectron Spectroscopic Studies of the Reactions of Hydrogen-Terminated Crystalline Si(111) and Si(100) Surfaces with Br_2, I_2, and Ferrocenium in Alcohol Solvents. *J. Phys. Chem. B*. **2002**, *106*, 3639-3656. https://doi.org/10.1021/jp0102872

162. Haber, J. A.; Lauermann, I.; Michalak, D.; Vaid, T. P.; Lewis, N. S. Electrochemical and Electrical Behavior of (111)-Oriented Si Surfaces Alkoxylated through Oxidative Activation of Si–H Bonds. *J. Phys. Chem. B*. **2000**, *104*, 9947-9950. https://doi.org/10.1021/jp001791u

163. Boland, J. J.; Villarrubia, J. S. Identification of the Products from the Reaction of Chlorine with the Silicon(111)-(7×7) *Surface. Science*. **1990**, *248*, 838-840. https://doi.org/10.1126/science.248.4957.838

164. Li, Y.; O'Leary, L. E.; Lewis, N. S.; Galli, G. Combined Theoretical and Experimental Study of Band-Edge Control of Si through Surface Functionalization. *J. Phys. Chem. C*. **2013**, *117*, 5188-5194. https://doi.org/10.1021/jp3124583

165. Wong, K. T.; Lewis, N. S. What a Difference a Bond Makes: The Structural, Chemical, and Physical Properties of Methyl-Terminated Si(111) Surfaces. *Acc. Chem. Res*. **2014**, *47*, 3037-3044. https://doi.org/10.1021/ar500207y

166. Webb, L. J.; Lewis, N. S. Comparison of the Electrical Properties and Chemical Stability of Crystalline Silicon(111) Surfaces Alkylated Using Grignard Reagents or Olefins with Lewis Acid Catalysts. *J. Phys. Chem. B*. **2003**, *107*, 5404-5412. https://doi.org/10.1021/jp0222752

167. Plass, K. E.; Liu, X.; Brunschwig, B. S.; Lewis, N. S. Passivation and Secondary Functionalization of Allyl-Terminated Si(111) Surfaces. *Chem. Mater*. **2008**, *20*, 2228-2233. https://doi.org/10.1021/cm7024679

168. Johansson, E.; Boettcher, S. W.; O'Leary, L. E.; Poletayev, A. D.; Maldonado, S.; Brunschwig, B. S.; Lewis, N. S. Control of the pH-Dependence of the Band Edges of Si(111) Surfaces Using Mixed Methyl/Allyl Monolayers. *J. Phys. Chem. C*. **2011**, *115*, 8594-8601. https://doi.org/10.1021/jp109799e

169. Lattimer, J. R. C. Functionalization of Si(111) Surfaces and the Formation of Mixed Monolayers for the Covalent Attachment of Molecular Catalysts in Photoelectrochemical Devices. Ph.D. Thesis, California Institute of Technology, Pasadena, California, **2014**.

170. Seo, J.; Kim, H. J.; Pekarek, R. T.; Rose, M. J. Hybrid Organic/Inorganic Band-Edge Modulation of P-Si(111) Photoelectrodes: Effects of R, Metal Oxide, and Pt on H_2 Generation. *J. Am. Chem. Soc*. **2015**, *137*, 3173-3176. https://doi.org/10.1021/ja5126287

171. Cabán-Acevedo, M.; Papadantonakis, K. M.; Brunschwig, B. S.; Lewis, N. S. Surface Passivation and Positive Band-Edge Shift of P-Si(111) Surfaces Functionalized with Mixed Methyl/Trifluoromethylphenylacetylene Overlayers. *J. Phys. Chem. C*. **2020**, *124*, 16338-16349. https://doi.org/10.1021/acs.jpcc.0c02017

172. O'Leary, L. E. Mixed Functionality Semiconductor Surfaces: Formation, Characterization, Interfacial Dynamics, and Applications. California Institute of Technology, Pasadena, California, **2012**.

173. Lattimer, J. R. C.; Brunschwig, B. S.; Lewis, N. S.; Gray, H. B. Redox Properties of Mixed Methyl/Vinylferrocenyl Monolayers on Si(111) Surfaces. *J. Phys. Chem. C*. **2013**, *117*, 27012-27022. https://doi.org/10.1021/jp409958c

174. Lattimer, J. R. C.; Blakemore, J. D.; Sattler, W.; Gul, S.; Chatterjee, R.; Yachandra, V. K.; Yano, J.; Brunschwig, B. S.; Lewis, N. S.; Gray, H. B. Assembly, Characterization, and Electrochemical Properties of Immobilized Metal Bipyridyl Complexes on Silicon(111) Surfaces. *Dalton Trans*. **2014**, *43*, 15004-15012. https://doi.org/10.1039/C4DT01149J

175. Plymale, N. T.; Kim, Y.-G.; Soriaga, M. P.; Brunschwig, B. S.; Lewis, N. S. Synthesis, Characterization, and Reactivity of Ethynyl- and Propynyl-Terminated Si(111) Surfaces. *J. Phys. Chem. C*. **2015**, *119*, 19847-19862. https://doi.org/10.1021/acs.jpcc.5b05028

176. Pekarek, R. T.; Boucher, D. G.; Neale, N. R.; Rose, M. J. Energetic Tug-of-War between Pt and Leaky TiO_2: Positive and Negative Effects on the Function of Molecularly-Modified P-Si(111)—TiO_2—Pt Photocathodes. *ChemElectroChem*. **2020**, *7*, 1048-1056. https://doi.org/10.1002/celc.201901758

177. Boucher, D. G.; Speller, J. R.; Han, R.; Osterloh, F. E.; Rose, M. J. Decoupling Effects of Surface Recombination and Barrier Height on P-Si(111) Photovoltage in Semiconductor—Liquid Junctions Via Molecular Dipoles and Metal Oxides. *ACS Appl. Energy Mater*. **2019**, *2*, 66-79. https://doi.org/10.1021/acsaem.8b01563

178. O'Leary, L. E.; Strandwitz, N. C.; Roske, C. W.; Pyo, S.; Brunschwig, B. S.; Lewis, N. S. Use of Mixed CH_3–/$HC(O)CH_2CH_2$–Si(111) Functionality to Control Interfacial Chemical and Electronic Properties During the Atomic-Layer Deposition of Ultrathin Oxides on Si(111). *J. Phys. Chem. Lett*. **2015**, *6*, 722-726. https://doi.org/10.1021/jz502542a

179. Plymale, N. T.; Ramachandran, A. A.; Lim, A.; Brunschwig, B. S.; Lewis, N. S. Control of the Band-Edge Positions of Crystalline Si(111) by Surface Functionalization with 3,4,5-Trifluorophenylacetylenyl Moieties. *J. Phys. Chem. C*. **2016**, *120*, 14157-14169. https://doi.org/10.1021/acs.jpcc.6b03824

180. Einstein, A. Über Einen Die Erzeugung Und Verwandlung Des Lichtes Betreffenden Heuristischen Gesichtspunkt. *Annalen der Physik*. **1905**, *322*, 132-148. https://doi.org/10.1002/andp.19053220607

181. Smither, R. K. New Method for Focusing X Rays and Gamma Rays. *Review of Scientific Instruments*. **1982**, *53*, 131-141. https://doi.org/10.1063/1.1136941

182. Siegbahn, K.; Hammond, D.; Fellner-Feldegg, H.; Barnett, E. F. Electron Spectroscopy with Monochromatized X-Rays. *Science*. **1972**, *176*, 245-252. https://doi.org/10.1126/science.176.4032.245

183. Seah, M. P.; Dench, W. A. Quantitative Electron Spectroscopy of Surfaces: A Standard Data Base for Electron Inelastic Mean Free Paths in Solids. *Surf. Interface Anal*. **1979**, *1*, 2-11. https://doi.org/10.1002/sia.740010103

184. Cumpson, P. J.; Seah, M. P. Elastic Scattering Corrections in AES and XPS. II. Estimating Attenuation Lengths and Conditions Required for Their Valid Use in Overlayer/Substrate Experiments. **1997**, *25*, 430-446. https://doi.org/10.1002/(SICI)1096-9918(199706)25:6<430::AID-SIA254>3.0.CO;2-7

185. Seah, M. P., Quantification of AES and XPS. In Practical Surface Analysis 2nd ed.; Briggs, D.; Seah, M. P., Eds. John Wiley & Sons: **1990**; pp 201-255.

186. Jablonski, A.; Powell, C. J. The Electron Attenuation Length Revisited. *Surf. Sci. Rep*. **2002**, *47*, 33-91. https://doi.org/10.1016/S0167-5729(02)00031-6

187. Fairley, N. Peak Fitting in XPS http://www.casaxps.com/help_manual/manual_updates/peak_fitting_in_xps.pdf

188. Jansson, C.; Hansen, H. S.; Yubero, F.; Tougaard, S. Accuracy of the Tougaard Method for Quantitative Surface Analysis. Comparison of the Universal and Reels Inelastic Cross Sections. *J. Electron Spectrosc. Relat. Phenom*. **1992**, *60*, 301-319. https://doi.org/10.1016/0368-2048(92)80025-4

189. Ebel, M. F. Zur Bestimmung Der Reduzierten Dicke D/λ Dünner Schichten Mittels XPS. J. Electron *Spectrosc. Relat. Phenom*. **1978**, *14*, 287-322. https://doi.org/10.1016/0368-2048(78)80005-X

190. Fadley, C. S. Solid State and Surface Analysis by Means of Angular-Dependent X-Ray Photoelectron Spectroscopy. *Prog. Solid State Chem*. **1976**, *11*, 265-343. https://doi.org/10.1016/0079-6786(76)90013-3

191. Fadley, C. S., Basic Concepts of X-Ray Photoelectron Spectroscopy. *In Electron Spectroscopy: Theory, Techniques and Applications*, Academic Press: **1978**.

192. Sturzenegger, M.; Prokopuk, N.; Kenyon, C. N.; Royea, W. J.; Lewis, N. S. Reactions of Etched, Single Crystal (111)B-Oriented InP to Produce Functionalized Surfaces with Low Electrical Defect Densities. *J. Phys. Chem. B*. **1999**, *103*, 10838-10849. https://doi.org/10.1021/jp992290f

193. Laibinis, P. E.; Bain, C. D.; Whitesides, G. M. Attenuation of Photoelectrons in Monolayers of N-Alkanethiols Adsorbed on Copper, Silver, and Gold. *J. Phys. Chem*. **1991**, *95*, 7017-7021. https://doi.org/10.1021/j100171a054

194. Moulder, J. F.; Stickle, W. F.; Sobol, P. E.; Bomben, K. D., *Handbook of X-Ray Photoelectron Spectroscopy*; Physical Electronics Division: Perkin-Elmer Corporation, **1993**.

195. Wagner, C. D. Sensitivity Factors for XPS Analysis of Surface Atoms. *J. Electron Spectrosc. Relat. Phenom*. **1983**, *32*, 99-102. https://doi.org/Doi 10.1016/0368-2048(83)85087-7

196. Carl, A. D.; Kalan, R. E.; Obayemi, J. D.; Zebaze Kana, M. G.; Soboyejo, W. O.; Grimm, R. L. Synthesis and Characterization of Alkylamine-Functionalized Si(111) for Perovskite Adhesion with Minimal Interfacial Oxidation or Electronic Defects. *ACS Appl. Mater. Interfaces*. **2017**, *9*, 34377-34388. https://doi.org/10.1021/acsami.7b07117

197. Seah, M. P.; Spencer, S. J. Ultrathin SiO$_2$ on Si. VII. Angular Accuracy in XPS and an Accurate Attenuation Length. *Surf. Interface Anal*. **2005**, *37*, 731-736. https://doi.org/doi:10.1002/sia.2070

198. Seah, M. P.; Spencer, S. J. Ultrathin SiO$_2$ on Si II. Issues in Quantification of the Oxide Thickness. *Surf. Interface Anal*. **2002**, *33*, 640-652. https://doi.org/doi:10.1002/sia.1433

199. Gray, H. B., *Chemical Bonds : An Introduction to Atomic and Molecular Structure*, 2nd ed.; University Science Books, **1994**.

200. Ferraria, A. M.; Lopes da Silva, J. D.; Botelho do Rego, A. M. XPS Studies of Directly Fluorinated HDPE: Problems and Solutions. *Polymer*. **2003**, *44*, 7241-7249. https://doi.org/10.1016/j.polymer.2003.08.038

201. Gamsky, C. J.; Howes, G. R.; Taylor, J. W. Infrared Reflection Absorption Spectroscopy of Photoresist Films on Silicon Wafers: Measuring Film Thickness and Removing Interference Fringes. *Anal. Chem.* **1994**, *66*, 1015-1020. https://doi.org/10.1021/ac00079a015

202. Liu, H.-B.; Venkataraman, N. V.; Bauert, T. E.; Textor, M.; Xiao, S.-J. Multiple Transmission–Reflection Infrared Spectroscopy for High-Sensitivity Measurement of Molecular Monolayers on Silicon Surfaces. *J. Phys. Chem. A*. **2008**, *112*, 12372-12377. https://doi.org/10.1021/jp804553x

203. Liu, H.-B.; Xiao, S.-J.; Chen, Y.-Q.; Chao, J.; Wang, J.; Wang, Y.; Pan, Y.; You, X.-Z.; Gu, Z.-Z. Grazing Angle Mirror-Backed Reflection (GMBR) for Infrared Analysis of Monolayers on Silicon. *J. Phys. Chem. B*. **2006**, *110*, 17702-17705. https://doi.org/10.1021/jp063467q

204. Webb, L. J.; Rivillon, S.; Michalak, D. J.; Chabal, Y. J.; Lewis, N. S. Transmission Infrared Spectroscopy of Methyl- and Ethyl-Terminated Silicon(111) Surfaces. *J. Phys. Chem. B*. **2006**, *110*, 7349-7356. https://doi.org/10.1021/jp054618c

205. Hoffmann, H.; Mayer, U.; Brunner, H.; Krischanitz, A. Reflection-Absorption Infrared Spectroscopy of Self-Assembled Monolayers on Gold and Silicon Surfaces. *Vib. Spectrosc*. **1995**, *8*, 151-157. https://doi.org/10.1016/0924-2031(94)00037-H

206. Khalilzadeh-Rezaie, F.; Oladeji, I. O.; Cleary, J. W.; Nader, N.; Nath, J.; Rezadad, I.; Peale, R. E. Fluorine-Doped Tin Oxides for Mid-Infrared Plasmonics. *Opt. Mater. Express*. **2015**, *5*, 2184-2192. https://doi.org/10.1364/Ome.5.002184

207. Forbes, M. D. E.; Lewis, N. S. Real-Time Measurements of Interfacial Charge Transfer Rates at Silicon/Liquid Junctions. *J. Am. Chem. Soc.* **1990**, *112*, 3682-3683. https://doi.org/10.1021/ja00165a076

208. Acres, R. G.; Ellis, A. V.; Alvino, J.; Lenahan, C. E.; Khodakov, D. A.; Metha, G. F.; Andersson, G. G. Molecular Structure of 3-Aminopropyltriethoxysilane Layers Formed on Silanol-Terminated Silicon Surfaces. *J. Phys. Chem. C*. **2012**, *116*, 6289-6297. https://doi.org/10.1021/jp212056s

209. Webb, L. J.; Michalak, D. J.; Biteen, J. S.; Brunschwig, B. S.; Chan, A. S. Y.; Knapp, D. W.; Meyer, H. M.; Nemanick, E. J.; Traub, M. C.; Lewis, N. S. High-Resolution Soft X-Ray Photoelectron Spectroscopic Studies and Scanning Auger Microscopy Studies of the Air Oxidation of Alkylated Silicon(111) Surfaces. *J. Phys. Chem. B*. **2006**, *110*, 23450-23459. https://doi.org/10.1021/jp063366s

210. Masato, O.; Yoshihiro, N.; Kazushi, M. Surface Modification of N-Si(111) Electrodes with Brominated and Sulfonylated Alkyl Chains and Their Photoelectrochemical Characteristics. *Chem. Lett*. **2006**, *35*, 1360-1361. https://doi.org/10.1246/cl.2006.1360

211. Peczonczyk, S. L.; Brown, E. S.; Maldonado, S. Secondary Functionalization of Allyl-Terminated GaP(111)a Surfaces Via Heck Cross-Coupling Metathesis, Hydrosilylation, and Electrophilic Addition of Bromine. *Langmuir*. **2014**, *30*, 156-164. https://doi.org/10.1021/la403558k

212. Isenberg, N.; Grdinic, M. A Modern Look at Markovnikov's Rule and the Peroxide Effect. *J. Chem. Ed*. **1969**, *46*, 601-605. https://doi.org/10.1021/ed046p601

213. Yang, M.; Zhou, Y.; Zeng, Y.; Jiang, C.-S.; Padture, N. P.; Zhu, K. Square-Centimeter Solution-Processed Planar $CH_3NH_3PbI_3$ Perovskite Solar Cells with Efficiency Exceeding 15%. *Adv. Mater*. **2015**, *27*, 6363-6370. https://doi.org/10.1002/adma.201502586

214. Parsons, R., *Manual of Symbols and Terminology for Physicochemical Quantities and Units, Appendix III, Electrochemical Nomenclature*; International Union of Pure and Applied Chemistry: London, **1973**, p 499-516.

215. Chopra, T. P.; Longo, R. C.; Cho, K.; Chabal, Y. J. Ammonia Modification of Oxide-Free Si(111) Surfaces. *Surf. Sci*. **2016**, *650*, 285-294. https://doi.org/10.1016/j.susc.2016.01.002

216. Cui, N.-Y.; Liu, C.; Yang, W. XPS and AFM Characterization of the Self-Assembled Molecular Monolayers of a 3-Aminopropyltrimethoxysilane on Silicon Surface, and Effects of Substrate Pretreatment by UV-Irradiation. *Surf. Interface Anal*. **2011**, *43*, 1082-1088. https://doi.org/10.1002/sia.3698

217. Chidsey, C. E. D.; Liu, G. Y.; Rowntree, P.; Scoles, G. Molecular Order at the Surface of an Organic Monolayer Studied by Low Energy Helium Diffraction. *J. Chem. Phys*. **1989**, *91*, 4421-4423. https://doi.org/10.1063/1.456776

218. Burwell, R. L. The Cleavage of Ethers. *Chem. Rev*. **1954**, *54*, 615-685. https://doi.org/10.1021/cr60170a003

219. Geng, W.; Tong, C.-J.; Tang, Z.-K.; Yam, C.; Zhang, Y.-N.; Lau, W.-M.; Liu, L.-M. Effect of Surface Composition on Electronic Properties of Methylammonium Lead Iodide Perovskite. *J. Materiomics*. **2015**, *1*, 213-220. https://doi.org/10.1016/j.jmat.2015.07.005

220. Xu, X.; Li, K.; Yang, Z.; Shi, J.; Li, D.; Gu, L.; Wu, Z.; Meng, Q. Methylammonium Cation Deficient Surface for Enhanced Binding Stability at TiO2/CH3NH3PbI3 Interface. *Nano Res*. **2017**, *10*, 483-490. https://doi.org/10.1007/s12274-016-1307-3

221. Lindroos, V.; Motooka, T.; Franssila, S.; Paulasto-Krockel, M.; Tilli, M.; Airaksinen, V.-M., *Handbook of Silicon Based Mems Materials and Technologies*, Second Edition ed.; William Andrew Publishing: Boston, **2015**, p xvii-xviii.

222. Olthof, S. Research Update: The Electronic Structure of Hybrid Perovskite Layers and Their Energetic Alignment in Devices. *APL Mater*. **2016**, *4*, 091502. https://doi.org/10.1063/1.4960112

223. Grimm, R. L.; Bierman, M. J.; O'Leary, L. E.; Strandwitz, N. C.; Brunschwig, B. S.; Lewis, N. S. Comparison of the Photoelectrochemical Behavior of H-Terminated and Methyl-Terminated Si(111) Surfaces in Contact with a Series of One-Electron, Outer-Sphere Redox Couples in CH₃CN. *J. Phys. Chem. C*. **2012**, *116*, 23569-23576. https://doi.org/10.1021/jp308461q

224. Connelly, N. G.; Geiger, W. E. Chemical Redox Agents for Organometallic Chemistry. *Chem. Rev.* **1996**, *96*, 877-910.

225. Bard, A. J.; Faulkner, L. R., Electrochemical Methods: Fundamentals and Applications, 2nd. ed.; Wiley: New York, **2001**.

226. Memming, R., Semiconductor Electrochemistry; Wiley-VCH: New York, **2007**.

227. Lewis, N. S. A Quantitative Investigation of the Open-Circuit Photovoltage at the Semiconductor/Liquid Interface. *J. Electrochem. Soc.* **1984**, *131*, 2496-2503. https://doi.org/10.1149/1.2115347

228. Mailoa, J. P.; Bailie, C. D.; Johlin, E. C.; Hoke, E. T.; Akey, A. J.; Nguyen, W. H.; McGehee, M. D.; Buonassisi, T. A 2-Terminal Perovskite/Silicon Multijunction Solar Cell Enabled by a Silicon Tunnel Junction. *Appl. Phys. Lett.* **2015**, *106*. https://doi.org/10.1063/1.4914179

229. Bush, K. A., et al. 23.6%-Efficient Monolithic Perovskite/Silicon Tandem Solar Cells with Improved Stability. *Nat. Energy*. **2017**, *2*. https://doi.org/10.1038/nenergy.2017.9

230. Mahmood, K.; Sarwar, S.; Mehran, M. T. Current Status of Electron Transport Layers in Perovskite Solar Cells: Materials and Properties. *RSC Adv.* **2017**, *7*, 17044-17062. https://doi.org/10.1039/C7RA00002B

231. Ren, X.; Yang, D.; Yang, Z.; Feng, J.; Zhu, X.; Niu, J.; Liu, Y.; Zhao, W.; Liu, S. F. Solution-Processed Nb:SnO₂ Electron Transport Layer for Efficient Planar Perovskite Solar Cells. *ACS Appl. Mater. Interfaces*. **2017**, *9*, 2421-2429. https://doi.org/10.1021/acsami.6b13362

232. Jiang, C.-S., et al. Carrier Separation and Transport in Perovskite Solar Cells Studied by Nanometre-Scale Profiling of Electrical Potential. *Nat. Commun.* **2015**, *6*, 8397. https://doi.org/10.1038/ncomms9397

233. Serpetzoglou, E.; Konidakis, I.; Kakavelakis, G.; Maksudov, T.; Kymakis, E.; Stratakis, E. Improved Carrier Transport in Perovskite Solar Cells Probed by Femtosecond Transient Absorption Spectroscopy. *ACS Appl. Mater. Interfaces*. **2017**, *9*, 43910-43919. https://doi.org/10.1021/acsami.7b15195

234. NREL. Best Research Cell Efficiencies. https://www.nrel.gov/pv/cell-efficiency.html (accessed February 28, 2019).

235. Chen, M.; Ju, M.-G.; Carl, A. D.; Zong, Y.; Grimm, R. L.; Gu, J.; Zeng, X. C.; Zhou, Y.; Padture, N. P. Cesium Titanium(IV) Bromide Thin Films Based Stable Lead-Free Perovskite Solar Cells. *Joule*. **2018**, *2*, 558-570. https://doi.org/10.1016/j.joule.2018.01.009

236. Bansal, S.; Aryal, P. Evaluation of New Materials for Electron and Hole Transport Layers in Perovskite-Based Solar Cells through SCAPS-1d Simulations. *IEEE 43rd Photovoltaic Specialists Conference (PVSC)*. **2016**; pp 0747-0750.

237. Zhu, Y.; Deng, K.; Sun, H.; Gu, B.; Lu, H.; Cao, F.; Xiong, J.; Li, L. TiO_2 Phase Junction Electron Transport Layer Boosts Efficiency of Planar Perovskite Solar Cells. *Adv. Sci.* (Weinheim, Ger.). **2018**, *5*, 1700614-1700614. https://doi.org/10.1002/advs.201700614

238. Zhao, Y.; Zhang, H.; Ren, X.; Zhu, H. L.; Huang, Z.; Ye, F.; Ouyang, D.; Cheah, K. W.; Jen, A. K. Y.; Choy, W. C. H. Thick TiO_2-Based Top Electron Transport Layer on Perovskite for Highly Efficient and Stable Solar Cells. *ACS Ener. Lett.* **2018**, *3*, 2891-2898. https://doi.org/10.1021/acsenergylett.8b01507

239. Pan, X.; Yang, M.-Q.; Fu, X.; Zhang, N.; Xu, Y.-J. Defective TiO_2 with Oxygen Vacancies: Synthesis, Properties and Photocatalytic Applications. *Nanoscale*. **2013**, *5*, 3601-3614. https://doi.org/10.1039/C3NR00476G

240. Jones, T. W., *et al*. Lattice Strain Causes Non-Radiative Losses in Halide Perovskites. *Energy Environ. Sci.* **2019**, *12*, 596-606. https://doi.org/10.1039/C8EE02751J

241. Wang, Y.; Zhao, H.; Mei, Y.; Liu, H.; Wang, S.; Li, X. Carbon Nanotube Bridging Method for Hole Transport Layer-Free Paintable Carbon-Based Perovskite Solar Cells. *ACS Appl. Mater. Interfaces.* **2019**, *11*, 916-923. https://doi.org/10.1021/acsami.8b18530

242. Wantana, K.; Aniwat, P.; Bunlue, S.; Alongkot, T.; Anusit, K.; Pisist, K. Study of Thin Film Coating Technique Parameters for Low Cost Organic Solar Cells *Fabrication Mater. Today: Proc.* **2017**, *4*, 6626-6632. https://doi.org/10.1016/j.matpr.2017.06.177

243. Li, F.; Li, Y.; Wei, G.; Wang, Y.; Li, S.; Cheng, Y. Circularly Polarized Luminescence of Chiral Perylene Diimide Based Enantiomers Triggered by Supramolecular Self-Assembly. *Chem. Eur. J.* **2016**, *22*, 12910-12915. https://doi.org/doi:10.1002/chem.201601328

244. Wakizaka, D.; Fushimi, T.; Ohkita, H.; Ito, S. Hole Transport in Conducting Ultrathin Films of PEDOT/PSS Prepared by Layer-by-Layer Deposition Technique. *Polymer*. **2004**, *45*, 8561-8565. https://doi.org/10.1016/j.polymer.2004.10.007

245. Li, M.; Chao, Y.-H.; Kang, T.; Wang, Z.-K.; Yang, Y.-G.; Feng, S.-L.; Hu, Y.; Gao, X.-Y.; Liao, L.-S.; Hsu, C.-S. Enhanced Crystallization and Stability of Perovskites by a Cross-Linkable Fullerene for High-Performance Solar Cells. *J. Mater. Chem. A*. **2016**, *4*, 15088-15094. https://doi.org/10.1039/C6TA06152D

246. Kiel, J. W.; Eberle, A. P. R.; Mackay, M. E. Nanoparticle Agglomeration in Polymer-Based Solar Cells. *Phys. Rev. Lett.* **2010**, *105*, 168701. https://doi.org/10.1103/PhysRevLett.105.168701

247. Zhou, L.; Chang, J.; Liu, Z.; Sun, X.; Lin, Z.; Chen, D.; Zhang, C.; Zhang, J.; Hao, Y. Enhanced Planar Perovskite Solar Cell Efficiency and Stability Using a Perovskite/PCBM Heterojunction Formed in One Step. *Nanoscale*. **2018**, *10*, 3053-3059. https://doi.org/10.1039/C7NR07753J

248. Shin, W. S.; Jeong, H.-H.; Kim, M.-K.; Jin, S.-H.; Kim, M.-R.; Lee, J.-K.; Lee, J. W.; Gal, Y.-S. Effects of Functional Groups at Perylene Diimide Derivatives on Organic Photovoltaic Device Application. *J. Mater. Chem.* **2006**, *16*, 384-390. https://doi.org/10.1039/B512983D

249. Ganesamoorthy, R.; Vijayaraghavan, R.; Ramki, K.; Sakthivel, P. Synthesis, Characterization of Bay-Substituted Perylene Diimide Based D-A-D Type Small Molecules and Their Applications as a Non-Fullerene Electron Acceptor in Polymer Solar Cells. *J. Sci.: Adv. Mater. Devices*. **2018**, *3*, 99-106. https://doi.org/10.1016/j.jsamd.2017.11.005

250. Tautz, F. S.; Sloboshanin, S.; Schaefer, J. A.; Scholz, R.; Shklover, V.; Sokolowski, M.; Umbach, E. Vibrational Properties of Ultrathin PTCDA Films on Ag(110). *Phys. Rev. B*. **2000**, *61*, 16933-16947. https://doi.org/10.1103/PhysRevB.61.16933

251. Scholz, R.; Friedrich, M.; Salvan, G.; Kampen, T. U.; Zahn, D. R. T.; Frauenheim, T. Infrared Spectroscopic Study of the Morphology of 3,4,9,10-Perylene Tetracarboxylic Dianhydride Films Grown on H-Passivated Si(111). *J. Phys. Condens. Matter*. **2003**, *15*, S2647-S2663. https://doi.org/10.1088/0953-8984/15/38/005

252. Schmidt, A.; Schuerlein, T. J.; Collins, G. E.; Armstrong, N. R. Ordered Ultrathin Films of Perylenetetracarboxylic Dianhydride (PTCDA) and Dimethylperylene-bis(Dicarboximide) (Me-PTCDI) on Cu(100): Characterization of Structure and Surface Stoichiometry by LEED, TDMS, and XPS. *J. Phys. Chem*. **1995**, *99*, 11770-11779. https://doi.org/10.1021/j100030a023

253. Jiang, K.; Wu, F.; Yu, H.; Yao, Y.; Zhang, G.; Zhu, L.; Yan, H. A Perylene Diimide-Based Electron Transport Layer Enabling Efficient Inverted Perovskite Solar Cells. *J. Mater. Chem. A*. **2018**, *6*, 16868-16873. https://doi.org/10.1039/C8TA06081A

254. Heo, J. H.; Lee, S.-C.; Jung, S.-K.; Kwon, O. P.; Im, S. H. Efficient and Thermally Stable Inverted Perovskite Solar Cells by Introduction of Non-Fullerene Electron Transporting Materials. *J. Mater. Chem. A*. **2017**, *5*, 20615-20622. https://doi.org/10.1039/C7TA06900F

255. Zhang, H.; Xue, L.; Han, J.; Fu, Y. Q.; Shen, Y.; Zhang, Z.; Li, Y.; Wang, M. New Generation Perovskite Solar Cells with Solution-Processed Amino-Substituted Perylene Diimide Derivative as Electron-Transport Layer. *J. Mater. Chem. A*. **2016**, *4*, 8724-8733. https://doi.org/10.1039/C6TA03119F

256. Kelber, J.; Bock, H.; Thiebaut, O.; Grelet, E.; Langhals, H. Room-Temperature Columnar Liquid-Crystalline Perylene Imido-Diesters by a Homogeneous One-Pot Imidification–Esterification of Perylene-3,4,9,10-Tetracarboxylic Dianhydride. *Eur. J. Org. Chem*. **2011**, *2011*, 707-712. https://doi.org/doi:10.1002/ejoc.201001346

257. Akers, K.; Aroca, R.; Hor, A. M.; Loutfy, R. O. Molecular Organization in Perylenetetracarboxylic Dianhydride Films. *J. Phys. Chem*. **1987**, *91*, 2954-2959. https://doi.org/10.1021/j100295a061

258. Grabchev, I.; Bojinov, V.; Petkov, C. Infrared Absorption Studies of Some New 1,8-Naphthalimides. *Chem. Heterocyl. Compd*. (N.Y., NY, U.S.). **2003**, *39*, 179-183. https://doi.org/10.1023/a:1023760106439

259. Zaitsev, N. L.; Jakob, P.; Tonner, R. Structure and Vibrational Properties of the PTCDA/Ag(111) Interface: Bilayer Versus Monolayer. *J. Phys. Condens. Matter*. **2018**, *30*, 354001. https://doi.org/10.1088/1361-648x/aad576

260. Ozser, M. E.; Mohiuddin, O. Synthesis, Photophysical, Sructural and Electronic Properties of Novel Regioisomerically Pure 1,7-Disubstituted Perylene-3,4,9,10-

Tetracarboxylic Monoimide Dibutylester Derivatives. *J. Mol. Struct*. **2018**, *1158*, 145-155. https://doi.org/10.1016/j.molstruc.2018.01.023

261. Zheng, Y.; Jradi, F. M.; Parker, T. C.; Barlow, S.; Marder, S. R.; Saavedra, S. S. Influence of Molecular Aggregation on Electron Transfer at the Perylene Diimide/Indium-Tin Oxide Interface. *ACS Appl. Mater. Interfaces*. **2016**, *8*, 34089-34097. https://doi.org/10.1021/acsami.6b10731

262. Zheng, Y.; Giordano, A. J.; Shallcross, R. C.; Fleming, S. R.; Barlow, S.; Armstrong, N. R.; Marder, S. R.; Saavedra, S. S. Surface Modification of Indium–Tin Oxide with Functionalized Perylene Diimides: Characterization of Orientation, Electron-Transfer Kinetics and Electronic Structure. *J. Phys. Chem. C*. **2016**, *120*, 20040-20048. https://doi.org/10.1021/acs.jpcc.6b06812

263. Bhowmick, D. K.; Stegemann, L.; Bartsch, M.; Strassert, C. A.; Zacharias, H. Fluorescence Properties of Perylene and Pyrene Dyes Covalently Linked to 6H-SiC(0001) and Silicate Surfaces. *J. Phys. Chem. C*. **2016**, *120*, 3275-3288. https://doi.org/10.1021/acs.jpcc.5b09900

264. Ulman, A. Formation and Structure of Self-Assembled Monolayers. *Chem. Rev*. **1996**, *96*, 1533-1554. https://doi.org/10.1021/cr9502357

265. Faucheux, A.; Gouget-Laemmel, A. C.; Henry de Villeneuve, C.; Boukherroub, R.; Ozanam, F.; Allongue, P.; Chazalviel, J.-N. Well-Defined Carboxyl-Terminated Alkyl Monolayers Grafted onto H–SI(111): Packing Density from a Combined AFM and Quantitative IR Study. *Langmuir*. **2006**, *22*, 153-162. https://doi.org/10.1021/la052145v

266. Tetsassi Feugmo, C. G.; Champagne, B.; Caudano, Y.; Cecchet, F.; Chabal, Y. J.; Liégeois, V. Towards Modelling the Vibrational Signatures of Functionalized Surfaces: Carboxylic Acids on H–Si(111) Surfaces. *J. Phys. Condens. Matter*. **2012**, *24*, 124111. https://doi.org/10.1088/0953-8984/24/12/124111

267. Xu, C.; Goodman, D. W. Adsorption and Reaction of Maleic Anhydride on Mo(110), Monolayer Pd(111)/Mo(110), and Multilayer Pd(111)/Mo(110). *Langmuir*. **1996**, *12*, 1807-1816. https://doi.org/10.1021/la950290a

268. Wojciechowski, K.; Leijtens, T.; Siprova, S.; Schlueter, C.; Hörantner, M. T.; Wang, J. T.-W.; Li, C.-Z.; Jen, A. K. Y.; Lee, T.-L.; Snaith, H. J. C$_{60}$ as an Efficient N-Type Compact Layer in Perovskite Solar Cells. *J. Phys. Chem. Lett*. **2015**, *6*, 2399-2405. https://doi.org/10.1021/acs.jpclett.5b00902

269. Mizuguchi, J.; Tojo, K. Electronic Structure of Perylene Pigments as Viewed from the Crystal Structure and Excitonic Interactions. *J. Phys. Chem. B*. **2002**, *106*, 767-772. https://doi.org/10.1021/jp012909p

270. Sato, K.; Mizuguchi, J. N,N′-Diphenylperylene-3,4:9,10-Bis(Dicarboximide). *Acta Cryst. E*. **2006**, *62*, 5008. https://doi.org/doi:10.1107/S1600536806041845

271. Extance, A. The Reality Behind Solar Power's Next Star Material. *Nature*. **2019**, *570*, 429-432.

272. Matebese, F.; Taziwa, R.; Mutukwa, D. Progress on the Synthesis and Application of Cuscn Inorganic Hole Transport Material in Perovskite Solar Cells. *Materials*. **2018**, *11*, 2592.

273. Wu, J.-l.; Huang, W.-K.; Chang, Y.-C.; Tsai, B.-C.; Hsiao, Y.-C.; Chang, C.-Y.; Chen, C.-T.; Chen, C.-T. Simple Mono-Halogenated Perylene Diimides as Non-Fullerene Electron Transporting Materials in Inverted Perovskite Solar Cells with ZnO Nanoparticle Cathode Buffer Layers. *J. Mater. Chem. A*. **2017**, *5*, 12811-12821. https://doi.org/10.1039/C7TA02617J

274. Lewis, A., et al. In-Depth Analysis of Defects in TiO_2 Compact Electron Transport Layers and Impact on Performance and Hysteresis of Planar Perovskite Devices at Low Light. *Sol. Energy Mater. Sol. Cells*. **2020**, *209*, 110448. https://doi.org/10.1016/j.solmat.2020.110448

275. Peng, J., et al. Interface Passivation Using Ultrathin Polymer–Fullerene Films for High-Efficiency Perovskite Solar Cells with Negligible Hysteresis. *Energy Environ. Sci*. **2017**, *10*, 1792-1800. https://doi.org/10.1039/C7EE01096F

276. Carl, A. D.; Grimm, R. L. Covalent Attachment and Characterization of Perylene Monolayers on Si(111) and TiO_2 for Electron-Selective Carrier Transport. *Langmuir*. **2019**, *35*, 9352-9363. https://doi.org/10.1021/acs.langmuir.9b00739

277. Gao, W.; Zielinski, K.; Drury, B. N.; Carl, A. D.; Grimm, R. L. Elucidation of Chemical Species and Reactivity at Methylammonium Lead Iodide and Cesium Tin Bromide Perovskite Surfaces Via Orthogonal Reaction Chemistry. *J. Phys. Chem. C*. **2018**, *122*, 17882-17894. https://doi.org/10.1021/acs.jpcc.8b05352

278. Madhusudan Reddy, K.; Manorama, S. V.; Ramachandra Reddy, A. Bandgap Studies on Anatase Titanium Dioxide Nanoparticles. *Mater. Chem. Phys*. **2003**, *78*, 239-245. https://doi.org/10.1016/S0254-0584(02)00343-7

279. Maheu, C.; Cardenas, L.; Puzenat, E.; Afanasiev, P.; Geantet, C. UPS and UV Spectroscopies Combined to Position the Energy Levels of TiO_2 Anatase and Rutile Nanopowders. *Phys. Chem. Chem. Phys*. **2018**, *20*, 25629-25637. https://doi.org/10.1039/C8CP04614J

280. Duhm, S.; Gerlach, A.; Salzmann, I.; Bröker, B.; Johnson, R. L.; Schreiber, F.; Koch, N. Ptcda on Au(111), Ag(111) and Cu(111): Correlation of Interface Charge Transfer to Bonding Distance. *Org. Electron*. **2008**, *9*, 111-118. https://doi.org/10.1016/j.orgel.2007.10.004

281. Wijeyasinghe, N., et al. Copper(I) Thiocyanate (Cuscn) Hole-Transport Layers Processed from Aqueous Precursor Solutions and Their Application in Thin-Film Transistors and Highly Efficient Organic and Organometal Halide Perovskite Solar Cells. *Adv. Funct. Mater*. **2017**, *27*, 1701818. https://doi.org/10.1002/adfm.201701818

282. Schulz, P.; Edri, E.; Kirmayer, S.; Hodes, G.; Cahen, D.; Kahn, A. Interface Energetics in Organo-Metal Halide Perovskite-Based Photovoltaic Cells. *Energy Environ. Sci*. **2014**, *7*, 1377-1381. https://doi.org/10.1039/C4EE00168K

283. Schulz, P.; Cahen, D.; Kahn, A. Halide Perovskites: Is It All About the Interfaces? *Chem. Rev*. **2019**, *119*, 3349-3417. https://doi.org/10.1021/acs.chemrev.8b00558

284. DeBenedetti, W. J. I.; Hines, M. A. Breaking π–π Interactions in Carboxylic Acid Monolayers on Rutile $TiO_2(110)$ Leads to Unexpected Long-Range Ordering. *J. Phys. Chem. C*. **2019**, *123*, 8836-8842. https://doi.org/10.1021/acs.jpcc.8b11501

285. Ahmed, Z.; George, L.; Hiltunen, A.; Lemmetyinen, H.; Hukka, T.; Efimov, A. Synthesis and Study of Electrochemical and Optical Properties of Substituted Perylenemonoimides in Solutions and on Solid Surfaces. *J. Mater. Chem. A*. **2015**, *3*, 13332-13339. https://doi.org/10.1039/C5TA02241J

286. Ishimaru, Y.; Yoshiki, M.; Hatanaka, T. The Effect of Dopant Concentration on the Native Oxide Growth on Silicon Wafer Surface. *MRS Proceedings*. **1992**, *259*, 405. https://doi.org/10.1557/PROC-259-405

287. Dymshits, A.; Henning, A.; Segev, G.; Rosenwaks, Y.; Etgar, L. The Electronic Structure of Metal Oxide/Organo Metal Halide Perovskite Junctions in Perovskite Based Solar Cells. *Sci. Rep*. **2015**, *5*, 8704. https://doi.org/10.1038/srep08704

288. Henke, B. L. Ultrasoft X-Ray Reflection, Refraction and Production of Photoelectrons (100–1000 eV Region). *Phys. Rev. A*. **1972**, *A6*, 94-104&. https://doi.org/10.1103/PhysRevA.6.94

289. Kittel, C., Introduction to Solid State Physics, 8th ed.; Wiley, **2004**.

290. Blum, A. On Crystalline Character of Transparent Solid Ammonia. *Radiation Effects*. **1975**, *24*, 277-279. https://doi.org/10.1080/00337577508240819

291. Atkins, P.; Jones, L.; Laverman, L., *Chemical Principles: The Quest for Insight*; W.H. Freeman: New York, **2016**.